Department of Civil Engineering

Simulation of transport, evaporation, and combustion of liquids in large-scale fire incidents

Topi Sikanen

Aalto University

DOCTORAL DISSERTATIONS

Aalto University publication series
DOCTORAL DISSERTATIONS 254/2017
VTT SCIENCE 169

Simulation of transport, evaporation, and combustion of liquids in large-scale fire incidents

Topi Sikanen

A doctoral dissertation completed for the degree of Doctor of Science (Technology) to be defended, with the permission of the Aalto University School of Engineering, at a public examination held at the lecture hall R1 (Rakentajanaukio 4 A, Espoo) of the school on 19th January 2018 at 12:00.

Aalto University
School of Engineering
Department of Civil Engineering

Supervising professor
Prof. Simo Hostikka, Aalto University, Finland

Thesis advisor
Prof. Simo Hostikka, Aalto University, Finland

Preliminary examiners
Prof. Andre Marshall, University of Maryland, USA
Dr. Tarek Beji, Ghent University, Belgium

Opponents
Prof. Jennifer Wen, University of Warwick, UK

Aalto University publication series
DOCTORAL DISSERTATIONS 254/2017

VTT SCIENCE 169

ISBN 978-952-60-7784-0 (printed)
ISBN 978-952-60-7785-7 (pdf)
ISSN-L 1799-4934
ISSN 1799-4934 (printed)
ISSN 1799-4942 (pdf)
http://urn.fi/URN:ISBN:978-952-60-7785-7

ISBN 978-951-38-8599-1 (printed)
ISBN 978-951-38-8598-4 (pdf)
ISSN-L 2242-119X
ISSN 2242-119X (printed)
ISSN 2242-1203 (pdf)
http://urn.fi/URN:ISBN:978-951-38-8598-4

Unigrafia Oy
Helsinki 2017

Finland

Publication orders (printed book):
topi.sikanen@vtt.fi

441 697
Printed matter

Aalto University

Abstract

Aalto University, P.O. Box 11000, FI-00076 Aalto www.aalto.fi

Author
Topi Sikanen

Name of the doctoral dissertation
Simulation of transport, evaporation, and combustion of liquids in large-scale fire incidents

Publisher School of Engineering

Unit Department of Civil Engineering

Series Aalto University publication series DOCTORAL DISSERTATIONS 254/2017

Field of research Fire Safety

Manuscript submitted 8 September 2017 **Date of the defence** 19 January 2018

Permission to publish granted (date) 13 November 2017 **Language** English

☐ **Monograph** ☒ **Article dissertation** ☐ **Essay dissertation**

Abstract

Combustible liquids are often present in large quantities in industrial facilities and in transportation. Leaks, vessel ruptures, transportation accidents and terrorist attacks involving liquids may lead to large scale fire incidents. Analyses of such incidents are needed in the safety analyses of nuclear power plants and other critical infrastructure. However, large scale incidents may be outside the area of validity of empirical models. Development and validation of numerical simulation methods are therefore needed.

This thesis has two objectives. The first is to develop and validate spray boundary conditions that can be used to model spray injection of water mist systems or for modeling liquid dispersal. The second is to predict burning rates of liquid pool fires starting from first principles. Large eddy simulation is used for the Eulerian gas phase solution and Lagrangian particle tracking for the sprays.

The spray model is developed and validated using data from experiments on high-pressure water mist nozzles and liquid-filled missile impacts. Suitable droplet size distributions and initial velocities for use in spray simulations are determined from experimental data. The spray structure and entrainment into the sprays are predicted with reasonable accuracy. The conclusion is that liquid dispersal from missile impacts can be simulated using the same spray models as for water mist sprays.

The burning rate of the liquid pool is calculated on the basis of vapor pressure and a mass transfer calculation at the liquid surface. One dimensional heat transfer by conduction and radiation within the liquid is considered. Effective absorption coefficients are determined for use with a one-dimensional radiation transport equation. An enhanced thermal conductivity model accounts for in-depth convective heat transfer. The conclusion is that inclusion of spectrally resolved radiation calculations and of lateral convection may be necessary for predicting the temporal development of the burning rate.

Finally, the models are applied to the full-scale simulation of an airplane impact on a nuclear island. The predicted fireball lifetimes and sizes compare favorably with available empirical correlations. A significant amount of the fuel involved accumulates on the surfaces around the impact point.

Keywords fireball, pool fire, spray, plane crash

ISBN (printed) 978-952-60-7784-0 **ISBN (pdf)** 978-952-60-7785-7

ISSN-L 1799-4934 **ISSN (printed)** 1799-4934 **ISSN (pdf)** 1799-4942

Location of publisher Helsinki **Location of printing** Helsinki **Year** 2017

Pages 180 **urn** http://urn.fi/URN:ISBN:978-952-60-7785-7

Tekijä
Topi Sikanen

Väitöskirjan nimi
Nesteiden kuljettumisen, haihtumisen ja palamisen simulointi suurissa onnettomuuksissa

Julkaisija Insinööritieteiden korkeakoulu

Yksikkö Rakennustekniikka

Sarja Aalto University publication series DOCTORAL DISSERTATIONS 254/2017

Tutkimusala Paloturvallisuus

Käsikirjoituksen pvm 08.09.2017 **Väitöspäivä** 19.01.2018

Julkaisuluvan myöntämispäivä 13.11.2017 **Kieli** Englanti

☐ **Monografia** ☒ **Artikkeliväitöskirja** ☐ **Esseeväitöskirja**

Tiivistelmä

Palavia nesteitä esiintyy usein suurissa määrin teollisuuslaitoksissa ja liikenteessä. Vuodot, astian repeytymät, liikenneonnettomuudet ja terrori-iskut voivat johtaa suuriin palavan nesteen onnettomuuksiin. Tällaisten vaaratilanteiden vaikutusten arviointia tarvitaan ydinvoimaloiden ja muiden kriittisten infrastruktuurien turvallisuusanalyyseissa. Tällaiset onnettomuusskenaariot voivat kuitenkin olla empiiristen mallien pätevyysalueen ulkopuolella. Tämän vuoksi tarvitaan numeeristen simulointimenetelmien kehittämistä ja validointia.

Tällä opinnäytetyöllä on kaksi tavoitetta. Ensimmäinen tavoite on kehittää ja validoida vesisuihkureunaehto, jota voidaan käyttää vesisumujärjestelmien simuloinnissa tai nesteiden leviämisen mallintamiseen. Toinen tavoite on ennustaa nestealtaiden palamisnopeudet lähtien fysikaalisista perusteista. Kaasufaasin simuloinnissa käytetään suurten pyörteiden menetelmää (LES) ja pisaroiden simulointiin LE (Lagrangian-Eulerian) -menetelmää.

Suihkumalli kehitetään ja validoidaan käyttäen koetuloksia, jotka saadaan korkea-paineisilla vesisumuttimilla ja vedellä täytetyillä missiileillä tehdyistä kokeista. Kokeellisista tuloksista määritetään oikeat pisarakokojakaumat ja lähtönopeudet, joita käytetään simulaatioissa. Malli ennustaa vesisuihkujen rakenteen ja ilman laahautumisen kohtuullisella tarkkuudella. Johtopäätöksenä on, että törmäyksen aiheuttamaa nesteen leviämistä voidaan simuloida käyttämällä samoja suihkumalleja kuin vesisumu-jen suihkujenkin simuloinnissa.

Nestemäisen altaan palamisnopeus lasketaan höyrynpaineen ja massansiirtomallin perusteella nestepinnalla. Malli ottaa syvyyssuunnassa huomioon johtumisesta aiheutuvan lämmönsiirron ja lämpösäteilyn absorption nesteessä. Mallia varten kehitetään tehollisia absorptiokertoimia. Konvektio nesteessä pyritään ottamaan huomioon tehollisen lämmönjohtavuuden avulla. Johtopäätöksenä on, että säteilyn aallonpituusriippuvuuden ja nesteen liikkeen huomioiminen voi olla tarpeen palamisnopeuden ajallisen kehityksen ennustamiseksi.

Kehitettyjä malleja sovelletaan ydinvoimalaitokseen kohdistuvan lentokonetörmäyksen simulointiin. Ennustetut tulipallon kestoajat ja halkaisijat vastaavat melko hyvin empiirisiä malleja. Merkittävä määrä polttoainetta kertyy törmäyspisteen ympärillä oleville pinnoille.

Avainsanat tulipallo, allaspalo,suihku, lentokonetörmäys

ISBN (painettu) 978-952-60-7784-0 **ISBN (pdf)** 978-952-60-7785-7

ISSN-L 1799-4934 **ISSN (painettu)** 1799-4934 **ISSN (pdf)** 1799-4942

Julkaisupaikka Helsinki **Painopaikka** Helsinki **Vuosi** 2017

Sivumäärä 180 **urn** http://urn.fi/URN:ISBN:978-952-60-7785-7

Preface

The work in this thesis was carried out at VTT Technical research center of Finland between 2010 and 2017. Parts of this work were also carried out at the National Institute of Standards and technology in Gaithersburg, MD, USA.

My career as a Fire Scientist began when I applied for a Master's thesis position at VTT. Initially, the subject was going to be statistical, i.e. risk analysis of forest fire smoke or something to that effect (I forget). However, on my first day, the subject had changed, and I was asked if I wanted to develop a model for firebrands in FDS. I thought to myself "How hard can it be?". This illustrates very well how little I knew of fluid dynamics or of Fire.

My ten years at VTT have certainly been a learning experience. Each project and paper seems to lead to new questions and problems. Perhaps one of the most important lessons has been that papers do not need to (and seldom do) solve all of the world's problems. Instead, they are a description of work done up to that point.

I thank Simo Hostikka for agreeing to be the supervisor and instructor for this thesis in 2013. Serious progress on the thesis began under his supervision. I also thank Esko Mikkola, who was my master's thesis instructor and initially also agreed to be the instructor for my PhD thesis. I am sincerely grateful to the pre-examiners for their valuable comments.

Thank you to people at Kemistintie 3 for the great work ambiance, and for making it an easy and pleasant place to work. A very special thank you goes to the "fire people" still left at VTT: Anna, Tuula , Antti, Terhi, Timo and Jukka. I am grateful to our team leader Eila Lehmus for her encouragement and for arranging financial support for the finalization of this thesis. I am also grateful to Dr. Kevin McGrattan for the opportunity to spend a year as a guest researcher at the National Institute of Standards in Gaithersburg, MD.

I thank the IRSN for providing the experimental data for our use. Special thanks go to Pascal Boulet (Université de Lorraine) for arranging the measurements of the spectral absorption data used in Paper IV.

Finally, the financial sponsors of this work need to be acknowledged. The State Nuclear Waste Management Fund (VYR), Technical Research Centre of Finland (VTT) and Nordic Nuclear Safety Research (NKS) have financed this work. The work in Paper I was sponsored by the Finnish Funding Agency for Technology and

Innovation (Tekes), Marioff Corporation Oy, Rautaruukki Oyj, YIT Kiinteistötekniikka Oy and Insinööritoimisto Markku Kauriala Ltd.

List of publications

This thesis is based on the following original publications which are referred to in the text as I–V. The publications are reproduced with kind permission from the publishers.

I Sikanen, T., Vaari, J., Hostikka, S., and Paajanen, A. (2014). Modeling and simulation of high pressure water mist systems. *Fire Technology*, *50*(3), 483-504. http://dx.doi.org/10.1007/s10694-013-0335-8

II Hostikka, S., Silde, A., Sikanen, T., Vepsä, A., Paajanen, A., and Honkanen, M. (2015). Experimental characterisation of sprays resulting from impacts of liquid-containing projectiles. *Nuclear Engineering and Design*, 295, 388-402. https://doi.org/10.1016/j.nucengdes.2015.09.008

III Sikanen, T. and Hostikka, S. (2017). Numerical simulations of liquid spreading and fires following an aircraft impact. *Nuclear Engineering and Design*, *318*, 147-162. https://doi.org/10.1016/j.nucengdes.2017.04.012

IV Sikanen, T., and Hostikka, S. (2016). Modeling and simulation of liquid pool fires with in-depth radiation absorption and heat transfer. *Fire Safety Journal*, *80*, 95-109. https://doi.org/10.1016/j.firesaf.2016.01.002

V Sikanen, T., and Hostikka, S. (2017). Predicting the Heat Release Rates of Liquid Pool Fires in Mechanically Ventilated compartments. *Fire Safety Journal,* 91, 266-275. https://doi.org/10.1016/j.firesaf.2017.03.060

Author's contributions

Publication I: "Modeling and simulation of high pressure water mist systems."

The author wrote the paper and was responsible for the modeling and simulation of the experiments. The author also developed the spray boundary condition used for spray simulations. Co-authors were responsible for conducting the experiments and gave comments and feedback on the manuscript.

Publication II: "Experimental characterisation of sprays resulting from impacts of liquid-containing projectiles."

The author only analyzed the droplet distributions resulting from impacts of liquid filled missiles and participated in the writing of the article. Markus Honkanen conducted the direct imaging measurements of droplet size. Ari Vepsä was responsible for conducting the missile impact experiments. Ari Silde analyzed the spray front propagation. Simo Hostikka was the lead author of the paper.

Publication III: "Numerical Simulations of Liquid Spreading and Fires."

The author was responsible for writing the paper and performed all the simulations. Co-author developed the model of the nuclear island and gave comments and feedback on the manuscript.

Publication IV: "Modeling and simulation of liquid pool fires with in-depth radiation absorption and heat transfer."

The author was responsible for writing the paper and performed the modeling and simulation. The author also developed the methods for determining effective absorption coefficients and effective thermal conductivities. Co-author gave comments and feedback on the manuscript.

Publication V: "Predicting the Heat Release Rates of Liquid Pool Fires in Mechanically Ventilated compartments."

The author was responsible for writing the paper and designed and conducted the simulations. Co-author gave comments and feedback on the manuscript.

Contents

List of symbols

α	Droplet volume fraction (-)
c	Total molar concentration (mol/m^3)
C	Empirical coefficient (-)
c_p	Specific heat capacity (kJ/kg·K)
D	Diffusion coefficient (m^2/s)
d	Droplet diameter (m)
$\boldsymbol{g}$	gravitational acceleration vector
h	Sensible enthalpy (kJ/kg)
	or convective heat transfer coefficient (W/ m^{2}K)
h_m	Mass transfer coefficient (m/s)
Δh_v	Latent heat of evaporation (kJ/kg)
Δh_g	$\Delta h_v + \int_{T_0}^{T_b} c_p(T)dT$. Total heat of evaporation (kJ/kg)
I	Intensity (W/Sr· m^2)
k	Thermal conductivity (W/ m^2·K)
	or sub-grid kinetic energy (m^2/s^2)
κ	Absorption coefficient (1/m)
μ	Dynamic viscosity (Pa·s)
ν	Kinematic viscosity (m^2/s)
ρ	Density (kg/m^3)
R	Universal gas constant R=8.3144598 (kg /m^2 s^2 K mol)
	or droplet radius (m)
$\boldsymbol{\tau}$	Stress tensor

τ	Characteristic time (s)
T	Temperature (K)
$\boldsymbol{u}$	Velocity (m/s)
$\boldsymbol{V}$	Particle velocity (m/s)
p	Pressure (Pa)
$\boldsymbol{J}$	Mass flux tensor
L	Characteristic length (m)
M	Mass (kg)
N	Number of moles (mol)
$\dot{\boldsymbol{q}}''$	Heat flux vector
Y	Mass fraction (kg/kg)
X	Volume fraction (mol/mol)
$\langle\cdot\rangle$	Expected value
$\langle x \vert y\rangle$	Expected value of x conditional on y
$\|\|\boldsymbol{x}\|\|$	Vector norm $\|\|\boldsymbol{x}\|\| = \sqrt{\sum_1^3 x_i^2}$.

Superscripts

(i)	i:th particle property
S	Property evaluated at a surface
∞	Property evaluated in “free stream” or ambient conditions
$@p$	Property evaluated at particle position
$''$	Flux (-/m^2)
$'''$	Volumetric term (-/m^3)
$\cdot$	Rate (-/s)

Subscripts

α	Species α
b	Boiling temperature or blackbody intensity
f	Fuel

g	Gas phase property
l	Liquid phase property
λ	At wavelength λ
o	Oxidizer
t	Turbulent
r	Radiant

1. Introduction

1.1 Motivation and background

Liquid fuel spills present a potential fire hazard in many situations. The fuel dispersal leading to the formation of the spill may be a result of e.g. a pipe burst, vessel rupture, transport accidents, arson or terrorist attacks. Depending on the dispersal process, these incidents may lead to fireballs, pool fires, or spill fires. Evaluation of the consequences of such incidents is needed in the safety analyses of critical infrastructure.

The most important parameter in determining the impact of a fire on its surroundings is the heat release rate (HRR). The heat release rates of spill fires and pool fires are known to depend on the pool size. The pool size, in turn, depends on the fuel dispersal process. Spill fire sizes and heat release rates have been studied extensively. However, the conditions involved in the incident, such as the geometry, wind and oxygen concentration, as well as the fuel dispersal process, may be outside the domain of validity of traditional empirical methods.

For example, aircraft impacts must be considered in safety analyses of nuclear power plants (NPPs) [1]. Initially, the impact was envisioned to be from a small aircraft or possibly a fighter plane. Following the September 11 terrorist attacks in 2001, these analyses have been extended to assume the impact of a large commercial aircraft [2].

Such an aircraft can damage safety-related structures and components through mechanical impact and fire. Fires induced by an airplane impact may influence the NPP by three different mechanisms. Initially, a large fireball is created by the fuel cloud erupting from the breaking fuel tanks. This fireball has a duration of a few seconds and can be a hundred meters in diameter [3]. The most serious threat from a fireball to its surroundings is thermal radiation. The dose of thermal radiation received by a target is dependent on the size and duration of the fireball.

Only a fraction of the fuel carried by the plane will burn in the initial fireball [4]. The remaining part of the fuel will accumulate and burn in pools near the aircraft impact position. The size and burning rate of the pool fire depend on the geometry, properties of the roof and ground surfaces, and possible fire suppression activities.

The third mechanism involves the penetration of aviation fuel inside the plant through openings. These openings may exist beforehand (e.g. for ventilation) or be

created by the aircraft impact. Even if the amount of penetrated fuel is small, it can cause a rapid ignition of existing fire loads and result in internal fires.

Each portion of the problem touches on a widely researched problem in fire safety science: pool fires, fireballs and spray flames. However, the conditions are well outside the region of validity of most correlations. Because of this, their analysis would require the use of simulation software.

Fire safety analyses are commonly carried out using computational fluid dynamics (CFD) software. Although CFD models could in theory be used to predict the HRR of fires, this is usually predicted using correlations. The capability of CFD models the burning rates hinges on their ability to predict the important phenomena such as radiative heat transfer to the surface, fuel dispersion and suppression activities.

The methods developed in this thesis can be applied in more general settings than just nuclear safety. For example, pool fires are a significant fire hazard in all industries, not just the nuclear industry, and not only after a plane crash. Fireballs, on the other hand, can be formed from ruptures of pressure vessels or pipelines. Water mist is, of course, a widely used method of fire suppression.

The issues faced when modeling the sprays from liquid-filled missiles and water mist systems are the same. The first problem is characterization of the initial spray in terms of droplet sizes, velocities, and shape. The second problem is the simulation of spray transport. Correct prediction of the two-way coupling between the gas phase and the spray is crucial for successful simulations of either phase. From the computational standpoint, the simulation of high-pressure water mist systems and the simulation of liquid dispersal from missile impacts are both just simulations of high-speed sprays. The droplet sizes are similar in both cases, and even the droplet velocities are of the same magnitude.

1.2 Objectives and scope of the thesis

The purpose of this thesis is to develop numerical models for the transport, evaporation, and combustion of liquids present in large-scale fire incidents. The modeling efforts are limited to developing the sub models and boundary conditions for an existing CFD code Fire Dynamics Simulator (FDS), and to demonstrating their applications for fire safety problems. Each paper of this thesis aims to improve one aspect of the modeling.

The objectives of Paper I are

1. the development of a spray boundary condition for use in high-pressure water mist simulations,
2. validation of the spray model in FDS for simulations of high-speed liquid sprays, and
3. modeling dense spray effects in an LES context.

The objectives of Paper II are (the contribution of the author)

1. characterization of the initial spray from impacts of liquid-filled missiles.

The objective of Paper III is to “develop and validate a computational fluid dynamics (CFD) methodology for predicting the spreading and combustion of liquid fuel released upon an aircraft impact.” This overall objective is broken down into smaller goals:

1. development and validation of the spray boundary condition describing the fuel release.
2. validation of FDS predictions of fireball diameters and lifetimes.
3. investigation of the amount of liquid fuel left unburnt in the initial fireball following a crash
4. evaluation of the adequacy of physical separation based on a full-scale simulation study of aircraft impact on a nuclear island.

The objectives of Paper IV are

1. prediction of the liquid surface evaporation rate using a boundary condition based on an engineering mass transfer expression,
2. development of an appropriate technique for the specification of the liquid phase radiation absorption coefficients,
3. investigation of the importance of in-depth heat transfer in laboratory scale (0.5-3 meters) pool fires, and
4. validadtion of the proposed modeling approach using experimental results for different fuels.

The objectives of Paper V are

1. validation of the modeling methodology proposed in Paper II for the simulations of pool fires in mechanically ventilated compartments, and
2. further investigation of the in-depth heat transfer effects on the development of liquid pool fire burning rates.

Figure 1.1 visualizes the goals and contributions of this thesis.

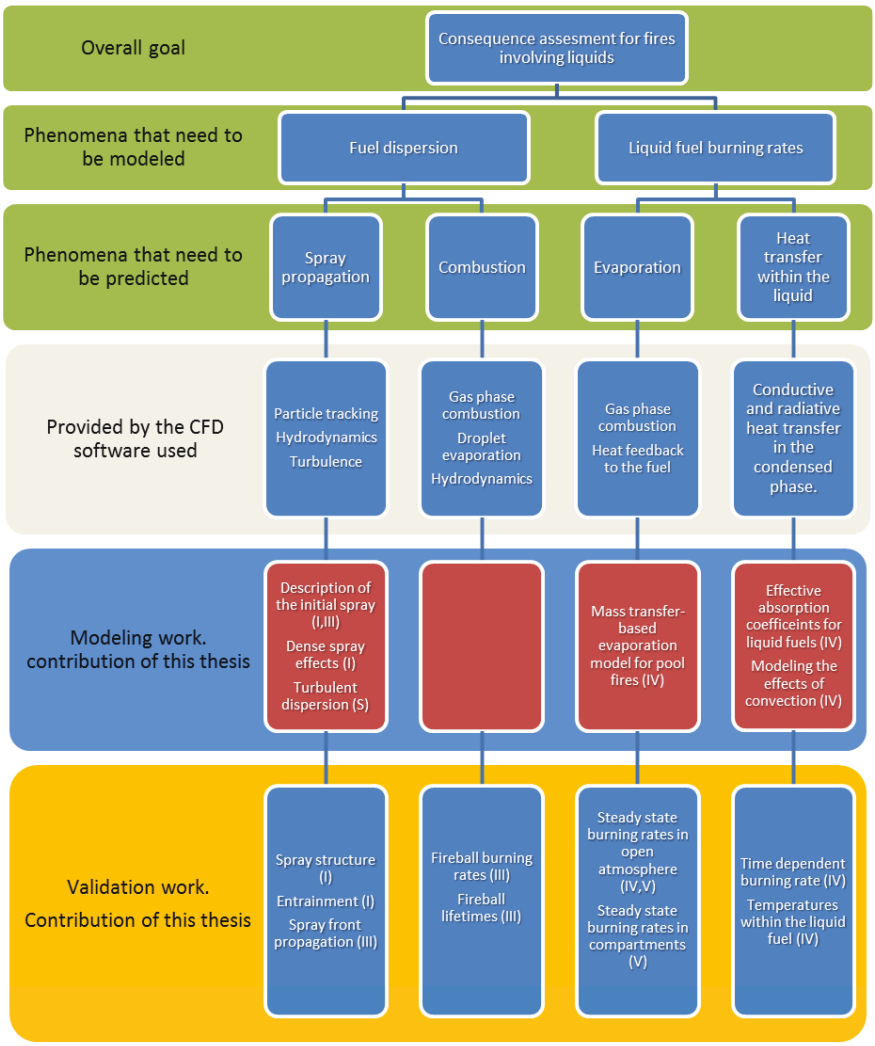

Figure 1.1 **Hierarchical chart illustrating the overall goal and contribution of this thesis. The Roman numerals in parentheses (I-V) indicate the paper in which the issue is discussed. The marking (S) indicates that additional work is described in this thesis summary.**

1.3 Outline

The main text of this thesis summary is organized as follows.

Section 2 presents a literature review of fire modeling in general, and of modeling of pool fires and liquid sprays in particular.

Section 3 describes the models used and developed in Papers I-V. The first part of the section presents an overview of the governing equations of the CFD software. The rest of the section describes the methods developed in Papers I-V.

Section 4 divides the results of the research into spray modeling, liquid pool fire modeling, and risk analysis. The sections on spray and pool fire modeling further divide the results into verification and validation. Papers I-V describe the Validation work. This thesis summary adds a description of the verification work.

Section 5 summarizes the conclusions from the research.

Section 6 presents suggestions for future research topics.

2. Literature review

2.1 Governing equations

2.1.1 Governing equations for the gas phase

The governing equations of compressible viscous follow from the conservation of mass, momentum, species, and enthalpy. The mass conservation equation is

$$\frac{D\rho}{Dt} = \dot{m}''', \tag{1}$$

where ρ is the density, $\dot{m}'''$ is the mass source term due to e.g. evaporation, and $\frac{D\phi}{Dt} = \frac{\partial\phi}{\partial t} + (\boldsymbol{u}\cdot\nabla)\phi$ is the substantial derivative. The conservation of momentum can be written as

$$\frac{D\rho\boldsymbol{u}}{Dt} = \rho\boldsymbol{g} - \nabla p + \nabla\cdot\boldsymbol{\tau} + \boldsymbol{f}. \tag{2}$$

In the momentum equation, the body force term $\boldsymbol{f}$ accounts for external forces acting on the fluid. Conservation of species is written as

$$\frac{D\rho Y_\alpha}{Dt} = \nabla\cdot\boldsymbol{J}_\alpha, \tag{3}$$

where Y_α is the mass fraction of species α. The species mass flux $\boldsymbol{J}_\alpha$ accounts for the diffusion mass flux. Finally a conservation equation for the sensible enthalpy[1] h is given by:

$$\frac{D\rho h}{Dt} = \frac{Dp}{Dt} + \nabla\cdot\dot{\boldsymbol{q}}''. \tag{4}$$

The heat flux vector $\dot{\boldsymbol{q}}''$ includes heat transport by conduction and radiation. The system of equations (1)-(4) is closed by the equation of state. For most fire situations, the ideal gas equation of state is sufficient.

$$p = \frac{\rho RT}{W}; W = \frac{1}{\sum_\alpha Y_\alpha/W_\alpha}. \tag{5}$$

With a different choice for the equation of state, equations (1)-(4) are equally valid for describing the motion of liquids.

2.1.2 Radiation

Radiation transport is usually the dominant heat transfer mechanism in fires. In a non-scattering medium, the radiation transport equation (RTE) in direction $\boldsymbol{s}$ is given by

$$\boldsymbol{s}\cdot\nabla I_\lambda = \kappa_\lambda I + \kappa_\lambda I_{b,\lambda}. \tag{6}$$

[1] This equation may also be written in terms of temperature, enthalpy, energy or sensible energy (see e.g. [130]).

Here, κ_λ, $I_{b,\lambda}$ and I_λ are the absorption coefficient, black body intensity and intensity at the wavelength λ. The radiation transport gives rise to a source term in the energy equation:

$$-\nabla \cdot \dot{q}_r'' = \int_0^\infty \kappa\left[U - 4\pi I_{b,\lambda}(\boldsymbol{x})\right] d\lambda \,;\, U = \int_{4\pi} I_\lambda(\boldsymbol{x}, \boldsymbol{s}') ds' \,. \tag{7}$$

From a numerical standpoint, the above equation is problematical. Equation (7) involves a double integral: one over the solid angle and another over all the wavelengths. In most fire applications, the gray gas assumption is invoked, removing the wavelength dependence.

2.1.3 Governing equations of dispersed phase

Equations governing the motion of a single particle are quite well known by now. Several books [5–7] and review articles [8–10] have been written on the subject. Maxey and Riley [11] derived an expression for the forces acting on a rigid spherical particle in non-uniform flow

$$\frac{d m_p \boldsymbol{v}}{dt} = F_D + F_G + F_P + F_H + F_L. \tag{8}$$

On the LHS, m_p and $\boldsymbol{v}$ are the mass and the velocity of the particle**.** The force terms appearing on the RHS are the drag force, gravitational acceleration, pressure gradient force, the Basset history force and lift force. The linear decomposition of forces in Eq. (8) is not always valid, since there may be non-linear interactions between the forces. These interactions are poorly understood and are usually neglected [8]. The last three terms are generally found to be negligible when the density of the particles is much higher than that of the carrier phase [8,9,12]. This type of model is commonly called a “quasi-steady drag” model since the unsteady terms are ignored.

If the droplet does not affect the carrier phase, the model is described as one-way coupled. In sprays, the influence of the droplets on the carrier phase usually needs to be taken into account. Typically, Lagrangian particle models only consider two-way coupling of the gas phase and the dispersed phase. The two-way coupling means that each particle interacts with the carrier fluid individually. Momentum lost from a particle is gained by the fluid and vice versa.

If the spray is dense enough, the droplets may start to travel in each other’s wakes. The Lagrangian-Eulerian model cannot capture these effects for two reasons: First, the Lagrangian particles have no volume in the Eulerian space, preventing the model from seeing effects that take place in the length scale of the droplet diameter. Secondly, the effects of this length scale would be sub-grid scale in most practical simulations. Therefore, these effects need to be modeled. This kind of modeling is sometimes called three-way coupling.

These aerodynamic interactions are often assumed to become important when the average droplet spacing is less than ten droplet diameters [8]. Ten droplet spacings correspond approximately to a droplet volume fraction $\alpha = 0.01$. Volume fractions as high as this can sometimes be achieved inside the sprays considered

in this thesis. If the spray was even more dense, particle-particle collisions or four-way coupling would need to be considered.

2.1.4 Governing equations for liquid evaporation

Equations (1)-(4), with the appropriate equation of state, describe the motion of both gases and liquids. At the interfaces of liquids and gases, such as on the surface of a liquid droplet or on the surface of a liquid pool, models are needed for the interfacial fluxes. This section discusses evaporation mostly from the perspective of pool fires. The discussion in this section is equally valid for evaporation from liquid droplets. In practice, droplets are usually much smaller than the computational grid, leading to somewhat different models of evaporation.

In a binary mixture of gases A and B, the molar flux of A relative to species B, in the z - coordinate direction, is [13]

$$\dot{N}_A'' = cD_{A,B}\frac{\partial X_A}{\partial z} + X_A\left(\dot{N}_A'' + \dot{N}_B''\right). \tag{9}$$

Here $D_{A,B}$ is the binary diffusion coefficient of A in B, X is the volume fraction of a species, and c is the total molar concentration. In the case of evaporation from a surface, we can take species A to be our evaporating species and B to be air. We will furthermore assume that the molar flux of air at the evaporating surface is zero, $\dot{N}_B'' = 0$. The evaporated molar flux from the surface can then be calculated from

$$\dot{N}_A'' = \frac{c}{1-Y_F^s} D_F \left(\frac{\partial X_A}{\partial n}\right)^s = cu_S. \tag{10}$$

Here u_S is the Stefan velocity, the velocity caused by the evaporation, D_F is the binary diffusion coefficient of the evaporating species in the ambient air, and n denotes surface normal direction. Terms marked with the superscript s are evaluated at the surface.

For an ideal gas the volume fraction can be calculated from the Clausius-Claypeyron relation for the partial pressure of saturated vapor:

$$X_A = \frac{p^{sat}(T)}{p_0} = \exp\left[-\frac{\Delta h_v}{R}\left(\frac{1}{T} - \frac{1}{T_b}\right)\right]. \tag{11}$$

On the liquid side, full Navier-Stokes equations would be needed to capture all the physics involved in predicting the surface temperature T^s. In numerical simulations, one of the main difficulties involved in the solution of Equation (10) is evaluation of the vapor volume fraction gradient $(\partial X_F/\partial z)^s$. The length scales involved become very small as the surface is approached. In order to resolve the concentration boundary layer, increasingly fine grids are needed.

In numerical simulations, the near wall grid resolution is often reported in terms of non-dimensional distance y^+. This is the distance from the surface to the first grid cell center divided by the local viscous length scale, δ_ν [14]:

$$\mathrm{y}^+ = \frac{1}{2}\frac{\delta \mathrm{n}}{\delta_\nu};\ \delta_\nu = \frac{\mu}{\rho u_\tau};\ u_\tau = \sqrt{\tau_w/\rho}. \tag{12}$$

Here $\tau_w = \mu\partial|\boldsymbol{u}|/\partial n$ is the viscous stress evaluated at the wall, and u_τ is the friction velocity. For a direct evaluation of the volume fraction gradient, a near wall grid resolution of $y^+ = 1$ is needed. Such grid resolutions are often infeasible. Therefore, the near wall gradients need to be modeled.

A commonly used approximation is based on the "film theory" (See, e.g. [13, pp 554-580]). If we assume that the vapor mass flux is constant within a thin film near the boundary, Equation (10) may be integrated over the film thickness δ to give

$$\dot{N}'' = c\frac{D_F}{\delta} log\left(\frac{1-X_f^\infty}{1-X_f^s}\right). \quad (13)$$

Here X_f^∞ is the "free stream" volume fraction of the evaporating species.

In the literature on spray evaporation Equation (13) is often written in terms of mass fractions instead of volume fractions. The difference between formulations based on molar fractions and mass fractions is in the assumptions needed for integrating Eq. 9. When molar fractions are used the assumption is that the total molar concentration and diffusivity stay constant. This is true in isothermal systems with constant pressure. If mass fractions are used, the total density of the gas mixture is held constant. Neither of these assumptions can be rigorously defended, but the former assumptions are perhaps slightly less restrictive.

Equation (13) still requires an estimate for the film thickness δ. This can be done e.g. by relating the film thickness to a mass transfer coefficient:

$$\frac{D_F}{\delta} = \frac{ShD_F}{\mathrm{L}} = h_m \ . \quad (14)$$

In the above, Sh is the Sherwood number, h_m is the mass transfer coefficient, and L is the characteristic length. Models based on film theory are commonly used to predict droplet evaporation (See, e.g. [7, pp. 9-29]). Droplets are usually much smaller than the grid size in CFD codes, and the "free stream" values and the length scale L have natural definitions. This is not the case when Eq. (13) is applied as a wall model in CFD.

In wall-bounded flows, a commonly used method for approximating the wall normal gradients is to use mixing length arguments to derive an analytical profile for the scalar near the wall. In the traditional flat plate boundary layer theory, this gives rise to the log-law velocity and scalar profiles. One problem with using the log-law for evaporation problems is the non-zero wall normal velocity or "blowing." Blowing changes the shapes of the near wall velocity and concentration profiles. The overall effect of blowing is to decrease the convective heat flux to the wall and to reduce the wall shear stress. [15, pp. 414-493]

Desoutter et al. [16] attempted to derive wall models that would account for the effect of blowing. They performed DNS simulations of the boundary layer above an evaporating liquid film in turbulent channel flow. By introducing new scaling for the variables, they were able to recover the traditional log law behavior of the boundary layer in the presense of evaporation. However, the parameters of their wall-law were found to be case dependent, reducing the usefulness of the approach.

Perhaps due to the above-described difficulties in wall modeling, many pool fire models ignore the boundary layer resistance to mass transfer (e.g. [17,18]). Instead,

they assume that the amount evaporated is ultimately determined by the energy balance at the surface [18]

$$\dot{m}'' = \frac{\dot{q}''_{net}}{\Delta h_g}. \tag{15}$$

The exact way in which $\dot{q}''_{net}$ is calculated varies from author to author. In the context of pool fire modeling, this approach can be justified by examining equation (10). The volume fraction of the evaporated species X_A grows as the surface temperature approaches boiling point. Consequently, the denominator in equation (10) tends towards zero and the mass flux grows without bound. When the surface temperature is near the boiling point, evaporation mass flux is limited only by the amount of incoming heat flux. However, blowing tends to decrease the incident convective heat flux and this effect may be important if convection heat transfer is the dominant mode of heat transfer.

2.2 Spray characterization

2.2.1 Structure and breakup of sprays

Liquid sprays are used in many industrial processes, including combustion, coating and fire suppression to name just a few. Regardless of the particular application, the efficiency of the system depends on the properties of the spray. For purposes of numerical simulations, the important properties of the sprays are the initial droplet velocity and size distribution.

The processes that lead to formation of a spray from a continuous jet or sheet of liquid are called atomization or breakup processes. **Figure 2.1** shows a close-up picture of the spray atomization processes in a Spraying Systems LN-02 water mist nozzle. Spray formation is often broken down into two steps. The first step is the primary atomization. Typically, primary atomization is achieved by injecting a jet or sheet of liquid into a gas. The shear between the gas and the injected liquid causes instabilities to form on the liquid surface. These instabilities grow until the continuous liquid is broken into fragments. [19]

The fragments produced by the primary atomization are often relatively large and may be deformed by the aerodynamic forces acting on them. If the deformation is sufficient, the fragments may become unstable and break up into smaller pieces. This process is called secondary breakup [20]. The breakup of the droplets continues as long as the aerodynamic forces are strong enough to overcome the surface tension forces holding the droplet together. The balance between surface tension and inertia is usually reported in terms of

$$We = \frac{\rho V^2 d}{\sigma}, \tag{16}$$

where V is the velocity of the fragment (or droplet), d is the diameter of the droplet and σ is the surface tension. The critical Weber number at which breakup processes begin is between 10 and 20 [7, p.144].

The breakup of water jets has been a subject of active research for many years, and the results of the research have been presented in many reviews on the subject [20–22].

From a practical standpoint, the structure of a spray resulting from the primary and secondary atomization depends on several factors. First is the existence of disturbances in the initial liquid flow. Second is the liquid surface tension. Due to differences in surface tension, different fluids may produce different sized droplets, even if they are generated by the same nozzle.

Simulation of all the primary and secondary atomization is usually not feasible. Sometimes a stochastic model is used to account for the entire spray formation process [23–26]. In other cases the breakup processes may be modeled by deterministic models, with the stochastic component stemming from the droplet motion. The modeling of spray atomization is still an active research topic.

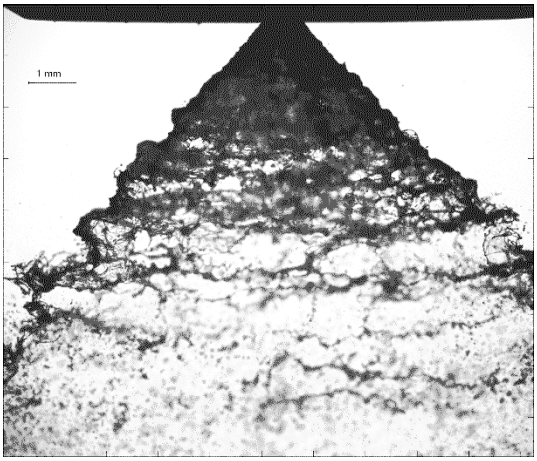

Figure 2.1 Close-up image of a Spraying Systems LN-02 water mist spray, showing primary and secondary atomization processes occurring. Picture from the Tampere University of Technology.

2.2.2 Water mist sprays

Commercially available sprinklers may differ substantially in the spray pattern they produce as well as in droplet sizes and velocities of the sprays. Water mist is a particular type of fire suppression spray that is characterized by small droplet size (99% of the spray volume is composed of droplets that are under 1000 microns in diameter [27]).

The usual way of characterizing sprinkler sprays is by measuring spray dispersion patterns. The dispersion patterns are measured by placing collection bins on the floor and measuring the water flux into each bin. Sprinklers are usually designed with a certain shape of dispersion pattern in mind. This kind of data is not useful for the development of spray models for use in CFD. Experimental

uncertainties and low resolution also diminish the usefulness of the data for validation purposes.

Measurements in the near field of the spray are needed for use in simulations. This has been recognized in the research community, and progress has been made in the detailed characterization of fire sprinkler sprays [28,29]. However, these efforts have mostly focused on traditional sprinkler sprays and not on water mists. Detailed measurements of water mist sprays have been conducted with PDPA and using direct imaging techniques [30–34]. Since water mist is often produced by pressure-swirl type nozzles, a significant amount of research is available on the spray structure and droplet size in the context of combustion applications.

2.2.3 Sprays from liquid-filled missile impacts

In addition to spray nozzles, the spray may be a result of a transportation accident or a tank rupture. From the perspective of this thesis, the most important class of transportation accidents is aircraft impacts. In a plane crash, the fuel dispersal process is similar to the spray formation process in a pressure-atomized spray. Tieszen [35] summarized the process as follows: First, due to the rapid deceleration of the crashing plane, liquid fuel is ejected from the tanks through ruptures formed because of the crash. What follows is the primary breakup phase, in which the discharged liquid sheets undergo atomization due to the instabilities generated by aerodynamic drag. The resulting liquid fragments are usually so large that the aerodynamic forces deform them. The deformation increases until the fragment breaks up into smaller droplets.

Unlike the spray formation from a nozzle, the spray formation from a liquid tank impact is not very well characterized. The ejection velocity of the liquid is unknown, and the size and shape of the initial liquid sheets are uncertain. Fragments of the impacting structure may also interfere with the spray.

Experimental data on the sprays formed by aircraft impact are scarce. The focus of experimental research has usually been on either crash worthiness of tanks (castor tanks or fuel tanks) or the effect of the impact on structures. Sandia National Laboratories conducted a full-scale test, in which a Phantom F-4 aircraft carrying 4.8 tons of water impacted a reinforced concrete target [36–38]. They did not make detailed measurements of water dispersal, but video footage shows the propagation of the spray cloud (See **Figure 2.2**). However, at least part of the cloud seen in the footage is made up of dust particles and debris of the impacting plane.

Figure 2.2 Still images from the video clips of the Phantom F-4 test by Sandia National Laboratories

VTT conducted a series of experiments with liquid-filled missiles impacting on a concrete block. Droplet size distributions were measured using a direct imaging method, and the resulting spray shapes were recorded on high-speed video. The results of the spray characterization experiments are reported in a paper by Silde et al. [39] and in Paper II.

Very few attempts at predicting the liquid dispersal process are available in the open literature. Brown et al. [40,41] coupled a transient dynamics code Presto with a low-Mach number fire code Fuego to predict the liquid dispersion from the high-speed impact tests of Jepsen [42]. They used Smoothed Particle Hydrodynamics (SPH) to predict the motion of liquid within the tank on impact. The particles from the SPH solution were then transferred to the fire code once the distance between the particles dropped below a certain threshold level. They found that their model was able to reproduce the observed liquid dispersal patterns reasonably well. Brown et al. did not compare the droplet size predictions with experimental results [41].

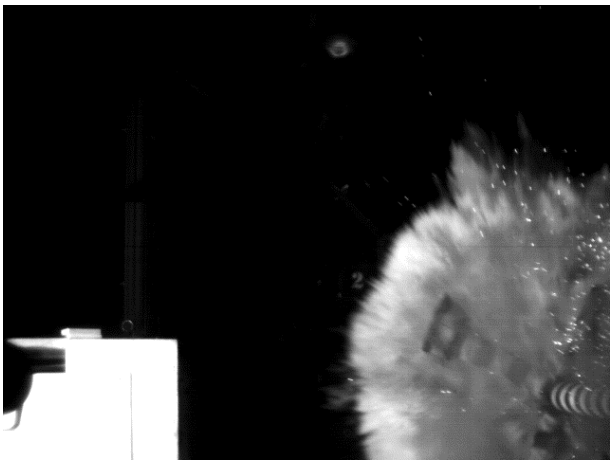

Figure 2.3 Spray front in the IMPACT experiments.

2.3 Modeling liquid pool fires

2.3.1 Physical mechanisms

Pool fires have been studied for decades, and the results have been collected in several review articles [43–46]. The result of such studies has usually been an empirical or semi-empirical correlation for the steady state burning rate of a pool fire as a function of the pool size. A recent example is a study by Ditch et al. [47], in which the authors correlated the incident radiation on the pool surface with the fuel heat of gasification and smoke point. The ambient temperature, radiation level, side wind and vitiation of the atmosphere in situations of practical interest may significantly differ from those in experimental conditions. Furthermore, the transient nature of the analyses may require knowledge of the time-dependent burning rate, not just the peak or steady-state value.

Figure 2.4 illustrates the main heat transfer mechanisms in a burning liquid pool. The heat from the flame is transported to the liquid by thermal radiation and convection. Heat conduction takes place between the vessel and the liquid. The size of the pool dictates which mode of heat transfer dominates, although the type of fuel also plays a role [44,45]. For very small pool diameters, conduction through the vessel walls dominates the heat transfer. For slightly larger pool fires, convective transport is the primary mode, and for large pool fires, radiative transport dominates. The exact diameters at which these transitions between dominant heat transfer mechanisms occur are fuel dependent. For low sooting fires such as methanol, transition to the radiation dominated regime occurs at larger diameters compared to sootier fuels [47].

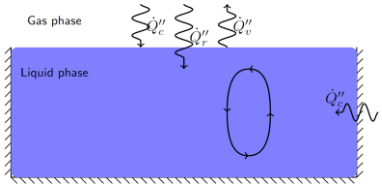

Figure 2.4 Heat transfer mechanisms in evaporation.

The capability of CFD models to predict the burning rates of liquid pool fires hinges on their ability to predict the heat feedback to the fuel surface. It is also not certain that the liquid side modeling capabilities in commonly used CFD software are up to the task. Wall-modeling for LES is also still an active research area. It is therefore necessary to develop sub-models for the CFD fire models that can predict the pool fire dynamics and burning rate during the simulation.

2.3.2 Pool fires in open atmosphere

Several authors have attempted to predict the burning rates of pool fires using either laminar or RANS equations fully coupled with the liquid phase. Prasad [48] solved

the laminar form of Navier-Stokes equations for a small 1 cm methanol pool fire. His model included heat transfer within the liquid by conduction but ignored in-depth radiation and convection. Snegirev et al. [17] predicted the burning rates of a wide range of acetone pool fires. They solved the Favre averaged governing equations together with the standard k-ε turbulence model. They used a Monte Carlo method to solve the weighted average of gray gases form of the RTE and included a model for turbulence radiation interaction. Novozhilov and Koseki [49] included one-dimensional heat transfer within the liquid in their model. The liquid evaporation rate was calculated based on a mass transfer calculation. They did not account for the blowing effect on the boundary layer. Pretrel et al. [18] attempted to reproduce the oscillatory behavior of a liquid pool fire in a mechanically ventilated compartment.

LES prediction of the pool burning rate of a methanol pool fire was performed by Hostikka et al. [50] In their model, the liquid evaporation rate was calculated iteratively over the course of the simulation to maintain an equilibrium fuel vapor pressure in the first gas-phase cell above the liquid boundary. The heat transfer inside the liquid layer was calculated using a one-dimensional heat conduction solver, ignoring the effects of convection and radiation. In the results, only the steady state burning rate value was observed, paying no attention to the temporal development. The main weakness of this kind of evaporation model is that the realized vapor concentration is highly sensitive to the spatial resolution.

Paper IV of this thesis presents simulations of an ethanol pool fire experiment conducted by Thomas et al. [51], who also reported simulations with FDS version 4. More recently, the same experiment was simulated using FDS version 6 [52]. They used the liquid pool boundary condition developed in this work. The evaporation model in FDS 4 maintained saturation pressure in the first grid cell above the evaporating surface, whereas in FDS 6 the evaporative mass flux is based on a mass transfer calculation. Despite the considerable differences in the evaporation models of FDS 4 and FDS 6, both models gave similar results. Neither model was able to reproduce the transient development of the burning rate.

In the light of the discussion in Section 2.1.4, the similarity in results of FDS 4 and FDS 6 is not surprising. Once the liquid heats up to a temperature near its boiling point, the boundary layer resistance to mass transfer is negligible and the evaporation rate is determined by prediction of incoming heat flux.

The mass transfer model developed in this thesis may be expected to differ from the equilibrium approach of FDS 4 in situations where the liquid temperature is below boiling point. These situations include pools evaporating in the absence of flame and liquid pool fires during the initial heat up phase. Modeling the evaporation in the latter case is likely to require detailed modelling of the internal heat transfer within the liquid

In paper IV, we investigated the hypothesis that the slowly growing burning rate is related to heat transfer within the liquid fuel.

2.3.3 Pool fires in confined spaces

The burning rates in confined spaces, possibly coupled with mechanical ventilation, can be significantly different from those measured in open atmosphere. These differences are caused by e.g. air vitiation and heat radiation from hot walls and the hot gas layer. Empirical correlations have been proposed to relate the open atmosphere burning rate to the burning rate in compartments [53,54].

Suard et al. [55] related the total pool burning rate to the pool size and local oxygen concentration according to empirical correlations. Three experiments with hydrogenated tetrapropylene fuel in a mechanically ventilated compartment were used to validate the model. Wahlqvist and Hees used a similar methodology of modifying the experimentally observed burning rate for compartment fire conditions [56]. Such approaches cannot be considered to be fully coupled, since they still rely on knowledge of the burning rate in open atmosphere.

Ventilation systems may also give rise to a new kind of dynamics in the fire: burning rate oscillations [18,57]. The oscillatory phenomenon is explained as a coupling process between the heat release rate and inlet flow rate. These two variables are coupled through the compartment pressure. During oscillations, a phenomenon of “ghosting flame" is seen, in which the flame moves away from the pool and towards the air inlet. The prerequisites for the oscillatory phenomenon are under-ventilated conditions and high enough temperatures to allow combustion at low oxygen concentrations.

A numerical and experimental study was carried out by Pretrel et al. [18] on the oscillatory phenomenon. Simulations with the CFD code ISIS successfully predicted the two dominant low frequencies of the oscillatory behavior of the fuel MLR.. However, the amplitude of the oscillations was substantially under predicted. FDS simulations of a heptane pool fire from the same set of experiments had similar results [58].

2.3.4 Heat transfer within the liquid phase

In the liquid phase of a pool fire, the dominant modes of transport are convection (fluid movement) and radiation. The heat to the surface is provided by conduction and convection from both the liquid phase and the gas phase. Therefore, the liquid side convection can have a major effect on the heat balance on the liquid surface

There are several possible sources of fluid movement within the fuel. One source is the uneven burning rate of fuel, which will cause it to flow towards regions of high burning rates. The second source is the hot walls of the pool, where heat transferred through the pool walls creates natural convection currents. The third source is in-depth radiation absorption. During pool combustion, the pool surface is cooled by evaporation and the liquid is internally heated by absorption of radiation. Uneven heat flux to the liquid surface may also give rise to convective currents. Higuera [59] numerically explored a liquid layer with a cold bottom plate heated non-uniformly from above. For liquids with Prandtl numbers near unity, both thermocapillary and buoyant flows were induced.

Studies have also been conducted to determine the spectra of emitted radiation [60] and to characterize the radiation absorption by gases within the flame [61]. Heat transfer within the liquid phase of a pool fire has received less attention. In modeling efforts, the heat transfer is often ignored. In experiments, steps are often taken to minimize the effect of in-depth radiation absorption and convection. For example, rocks or glass beads may be placed in the fuel pan to reduce the heat transfer within the pool [47,62]. In [62], Suo-Anttila et al. investigated the effect of convection in the liquid phase by removing the rocks from the pan. They found the effect to be negligible. The in-depth absorption by semi-transparent fuels has been studied for PMMA [63], polymer films [64] and liquid pool fires [60]. Most of the research related to the in-depth radiation absorption in liquids considers the boil-over of liquid pool fires on water [65]. The effect of in-depth radiation absorption on evaporation of fuel droplets has also been studied [66].

Vali et al. at the University of Alberta conducted detailed studies of the liquid side convection in laboratory scale methanol pool fires [67–70]. They found that there is a nearly constant temperature region directly below the surface of a pool fire. In this region, convection driven by heated pool walls is the primary mode of heat transfer. They also noted that varying the temperature of the pool boundary affected the burning rate. The importance of the initial temperature of the liquid fuel on pool fire dynamics has been noted previously by Hayasaka et al. [71] and Chen et al. [72]. Chen et al. recorded the temperature gradient within the fuel. They found that the initial temperature affected the temporal development of the burning rate but did not significantly influence the steady state burning rate.

Depending on the fuel, the penetration depth of thermal radiation can vary considerably. In fuels that are optically very thick in the infrared region, a thin layer on the surface absorbs the majority of the thermal radiation. In this case, the radiation can be taken into account as a boundary condition of the liquid's internal heat transfer problem. If the liquid is not optically thick, the in-depth absorption may need to be included as an internal source term of the heat conduction/convection problem. Additionally, the re-radiation of the fuel and vessel must be considered to ensure the conservation of energy in the case of optically thin fuels and high temperatures. In liquid spills, the layer thickness is often of similar magnitude or smaller than the absorption thickness in liquids.

2.4 Fireballs

Fireball may be defined as " fire, burning sufficiently rapidly for the burning mass to rise into the air like a cloud or ball." [73]. Ignition of dust or vapor clouds or releases of flammable gases from pressurized containers will often result in a fireball. Various types of transportation accidents can also result in fireballs, as vessels containing liquid fuel burst and disperse their contents into the surrounding atmosphere. An important class of accidents that may result in a fireball are boiling liquid expanding vapor explosions (BLEVEs). A BLEVE occurs when a vessel containing pressurized

liquid is heated until it bursts [3]. The difference between a vapor cloud explosion and a fireball is that in fireballs there is little mixing of fuel and air before ignition.

Fireballs have relatively short lifetimes, during which they pass through three distinct stages: growth, steady burning, and burnout. In the growth phase, air is entrained into the fireball and the diameter, $D(t)$, of the fireball increases. The rate of increase depends on the release type. If the fireball results from a high momentum release, such as pressurized vessel burst, $D(t) \propto t^{1/4}$. If the fireball is buoyancy dominated, $D(t) \propto t^2$ [74]. During the steady state burning phase, the diameter of the fireball is relatively constant; the fireball begins to lift off and starts to form the familiar mushroom cloud shape. During the burnout phase, the fireball diameter remains the same, but the flame becomes translucent and finally disappears.

Knowledge of fireball size, duration, and height are critical for estimating the hazard caused by the fireball. Several empirical correlations exist for determining the diameters and lifetimes of fireballs. The review by Abbassi and Abbassi [3] is an excellent calculation methods used to model BLEVEs. These methods can also be used to analyze fireballs from aircraft impacts. However, they cannot be used to estimate the fraction of the unburnt fuel. Baum and Rehm [4] proposed a model for the global energy release rate of fireballs and used it to characterize the energy releases during the 2001 WTC attacks in New York. They used video footage from the attacks for calibrating the model. They concluded that only a fraction of the fuel carried by the planes burned in the initial fireballs. Thus, the majority of the aviation fuel was available to accelerate the fires in the buildings. Apart from the efforts of Baum and Rehm, the fraction of fuel left unburnt has not attracted much attention.

Large scale fireballs are difficult to study experimentally. As a result, very few well-documented experiments are available in open literature. The most commonly cited experiment was conducted by The Federal Institute of Material Research and Testing (BAM) in Germany [75,76]. They exposed a 45 m^3 tank partially filled with 10 m^3 of liquefied propane to an open pool fire. The resulting fireball was around 100 meters in diameter and had a duration of 7 seconds.

Numerical studies are much more common. Fireballs resulting from vertical fuel gas releases were investigated numerically by Makhviladze et. a [77]. Makhviladze et al. [78] extended this model to investigate two-phase fuel releases from pressurized containers of liquefied gas. Their model solves two-dimensional Favre-averaged Navier--Stokes equations by using the standard k-ε turbulence model and an infinitely fast one-step reaction. The dispersed phase is treated in a Lagrangian fashion. They assumed a monodisperse droplet size distribution with the initial velocities of the droplets derived from Bernoulli's law. They compared the predicted lifetimes of fireballs with the experimental correlation of Roper et. al. [79], and the transient shapes and sizes of the fireballs with the experiments of Hasegawa and Sato [80]. Makhviladze [81] used this model to analyze total loss of containment scenarios for BLEVEs. They also investigated the overpressures that would occur in such events.

Yakush et al. [82] compared RANS and LES predictions of the fireball lifetime with the empirical correlation of Roper [79]. They used Fire Dynamics Simulator

(FDS) version 4 for the LES calculations. FDS was found to underestimate the fireball lifetimes. The fuel release was modeled with a gas inflow boundary condition. Hu [83] used a modified version of FDS to investigate deflagrations of premixed fuel vapor clouds. High-speed jets were not considered. Instead, the vapor clouds were created by slowly injecting gas into the simulation domain. Luther et. al. [84] used FDS version 5 to determine the spreading and extent of the fireball around a generic NPP. They also modeled the fuel insertion by using a gas inflow boundary condition. Shelke et al. [85] used FireFoam to simulate the fireball from the BAM BLEVE experiment and from a plane crash.

In the above fireball simulations, the fuel inlet boundary condition consisted of either a vertical spray or injection of fuel gas from a boundary patch. Initial velocities of the gas and droplets have been based on, for example, the theoretical calculations of flash evaporation. When multiphase models have been used, droplet sizes have been assumed to be monodisperse. The possibility of fuel droplets raining out of the fireball has usually been neglected. Ignoring the raining out of droplets may be justified because of the highly volatile nature of liquids such as liquefied natural gas (LNG) and propane that are being considered.

2.5 Numerical methods

2.5.1 Large eddy simulation

Due to the wide range of length scales present in a turbulent flow, direct solution of equations (1)-(4) is prohibitively expensive. For example, in a 1-meter wide pool fire with a heat release rate of 1 MW, the largest eddies are of the order of 0.5 m. On the other hand, the flame sheet thickness, which characterizes the length scale over which reactions occur, is of the order of 1 mm [86]. Such grid resolutions are not feasible with current hardware and will not be in the foreseeable future.

In large eddy simulation (LES), only the large energy-containing flow structures are resolved, and smaller structures are modeled. Formally this is achieved by low-pass filtering of the governing equations:

$$\bar{\phi}(\boldsymbol{x},t) = \int_V G(\boldsymbol{x}-\boldsymbol{y})\phi(\boldsymbol{x},t)d\boldsymbol{y}. \tag{17}$$

Here ϕ is a variable (such as pressure or velocity) and G is a filter kernel. If density is not constant, favre filtering $\tilde{\phi} = \overline{\rho\phi}/\bar{\rho}$ may be used. The real value of a variable is then related to the value available in an LES by the relation $\phi = \tilde{\phi} + \phi'$. Here $\tilde{\phi}$ is the resolved, filtered value and ϕ' the unresolved fluctuation. The filtering operation is rarely applied explicitly. The numerical grid itself functions as a low pass filter and this is usually the only filtering considered.

As a result of the application of the low-pass filter, new unclosed terms appear in the governing equations. These are the product of applying the filtering operator to nonlinear parts of Equations (1)-(4). These new terms correspond to the effects of the unresolved scale on the solution, and their closures are called subgrid-scale

models (sgs models). The turbulent stress tensor is commonly closed with gradient diffusion type models

$$\tau = \overline{\boldsymbol{u}\boldsymbol{u}} - \overline{\boldsymbol{u}}\,\overline{\boldsymbol{u}} = \nu_t \boldsymbol{S}|\boldsymbol{S}|, \tag{18}$$

where ν_t is turbulent viscosity. Other models available for the subgrid scales stresses include models based on approximate-deconvolution, scale-similarity and Taylor expansion (see, e.g. [14,87])

In two-way coupled flows, the dispersed phase affects the large scales of the flow. The particles may enhance or modulate the turbulence. However, only a few researchers have proposed modifications to turbulence closures that account for the existence of the dispersed phase [88–92].

Finally, the filtered emission and absorption terms in the radiation transport equation need modeling. Often, the Optically Thin Fluctuation model is evoked allowing one to write:

$$\overline{\kappa I} = \bar{\kappa}\bar{I} \tag{19}$$

However, the absorption-emission correlation $\overline{\kappa T^4}$ cannot be ignored.

In addition to the terms discussed here, filtering of the governing equations also gives rise to unclosed terms in the governing equations of the dispersed phase. These terms will be discussed in Section 2.5.3.

2.5.2 Statistical description of spray

This section reviews the statistical framework that forms the basis for most spray models used in CFD codes. The theoretical framework provides justification for the spray models discussed in this thesis. The implications of the statistical description are discussed at the end of this section.

Williams [93] defined spray as any system of liquid or solid particles in a gas, where there are so many particles that only a statistical description of their behavior is feasible. All of the sprays considered in this thesis are included in this definition. One of the earliest attempts at complete statistical description of a spray is also due to Williams [94]. He derived an evolution equation for the droplet density function (ddf), defined as $f(\boldsymbol{x}, \boldsymbol{v}, r, t)$. The density function describes the probability of finding a droplet within a volume of the phase space. The discussion of the spray equation here follows [95], see [96–99] for more detailed derivations.

Suppose that the spray is made up of an ensemble of N_s droplets which can all be described using M variables. The state of particle i is then represented by a vector $\boldsymbol{\Phi}^{\boldsymbol{i}} = \{\phi_1^i, \ldots, \phi_M^i\}$. We then define the probability $P(\boldsymbol{\psi}, t)$ that describes the probability of finding a particle at position $\boldsymbol{\psi}$ in the phase space, e.g. a droplet with certain velocity and radius at a certain position, at a time instant t. For the sprays considered in this thesis, the properties of the sprays can be described by position,velocity, radius and temperature of the droplets. The state space is then $\boldsymbol{\psi} = [\boldsymbol{V}, R, T]$.

The modeled pdf is governed by the evolution equation

$$\frac{\partial P}{\partial t} + \nabla_{\boldsymbol{v}} \cdot [\boldsymbol{A}(\boldsymbol{v}, r, T)P] + \frac{\partial}{\partial r}\left[\dot{R}(\boldsymbol{v}, T, r)P\right] + \frac{\partial}{\partial T}\left[\dot{T}(\boldsymbol{v}, T, r)P\right] = 0 \tag{20}$$

Here $\boldsymbol{A}$, $\dot{R}$ and $\dot{T}$ denote the conditional expectation $\langle \dot{\psi}_j | \boldsymbol{\psi} = \boldsymbol{\phi} \rangle$ with $\dot{\psi}_j$ = $\boldsymbol{V}$,R or T. Here, $\dot{\psi}_j$ is the rate of change of property ψ_j and the brackets $\langle \dot{\psi}_j | \boldsymbol{\psi} = \boldsymbol{\phi} \rangle$ denote the expectation of $\dot{\psi}_j$ conditional on the particles being found in state $\boldsymbol{\psi} = \boldsymbol{\phi}$.

Equation (20) is an exact, but unclosed, hyperbolic partial differential equation for the joint probability $P(\boldsymbol{\psi}, t)$. Due to the high dimensionality of the problem, the solution of Equation (20) with the usual finite volume and finite difference type methods is difficult. The equation is commonly solved using particle methods. If the continuous phase equations are solved in the Eulerian frame, the resulting method is called Lagrangian - Eulerian (LE). LE methods represent the spray by an ensemble *surrogate* of droplets $\{\boldsymbol{X}^{(i)}(t), \boldsymbol{V}^{(i)}(t), R^{(i)}(t), 1 \dots N_S(t)\}$. The properties of the surrogate droplets evolve according to:

$$\frac{d\boldsymbol{X}^{(i)}}{dt} = \boldsymbol{V}^{(i)} \tag{21}$$

$$\frac{d\boldsymbol{V}^{(i)}}{dt} = \boldsymbol{A}^{(i)} \tag{22}$$

$$\frac{dR^{(i)}}{dt} = \dot{R}^{(i)} \tag{23}$$

$$\frac{dT^{(i)}}{dt} = \Theta^{(i)} \tag{24}$$

Here, $\boldsymbol{A}^{(i)}$, $\boldsymbol{V}^{(i)}$, $\dot{R}^{(i)}$ and $\Theta^{(i)}$ are the modeled acceleration, velocity, vaporization rate and heating rate of the i:th surrogate particle. From the perspective of the work in this thesis, the main implications of the statistical description of sprays are [97,98]:

1. Primary atomization cannot be modeled with the spray equation that underlies LE methods. Instead, the initial spray needs to be described at a boundary where the primary atomization has finished.
2. The correspondence between real droplets in a spray and the surrogate droplets is only on the level of the conditional expected values. This gives considerable freedom in modeling the evolution equations of the surrogate drops. Particularly, this provides the possibility of using statistical models and adding random terms to the equations.
3. The point particle assumption has not been invoked in the derivation of Equation (20). As a result, Equation (20) is also valid for dense flows. LE methods can be used to model dense sprays. The influence of the volume fraction can be modeled through the expected drag.

2.5.3 Lagrangian-Eulerian particle models

In most engineering applications, the unsteady forces acting on a particle are negligible. The equation of motion of a rigid spherical particle is:

$$\frac{d\boldsymbol{V}^{(i)}}{dt} = \frac{\widetilde{\boldsymbol{u}} - \boldsymbol{V}^{(i)}}{\tau_p} + \boldsymbol{g} \tag{25}$$

Where the particle response time τ_p is given by

$$\tau_p = \frac{3}{8}\rho_g C_D \left\|\widetilde{\boldsymbol{u}} - \boldsymbol{V}^{(i)}\right\| / \rho_p R^{(i)} \tag{26}$$

When solving Equation(25), we need to make some approximations. The first approximation is the continuous phase properties at the particle location, also called forward interpolation. The second is the method used to project the particle forces and mass source terms back to the Eulerian grid.

The most common approach for the forward interpolation is to use linear interpolation. However, simple linear interpolation does not preserve the divergence and curl of the interpolated velocity field. As inertial particles preferentially concentrate in regions of flow with high strain and low vorticity [100], such interpolation errors could lead to errors in predictions of particle concentration.

Perhaps a more serious problem with the simple approach is that, in LES, only the low-pass filtered values $\widetilde{\boldsymbol{u}}$ are available. The fluctuating quantities $\boldsymbol{u}'$ need to be modeled. Bellan and O'Kong [101] considered three types of models for the velocity seen by the particle: baseline, a deterministic and a stochastic model. Their baseline model directly utilized the low pass filtered velocity. Their assesmentwas that, for the purpose of calculating drop source terms, the random model performed most poorly and the deterministic model was the best.

Some authors have proposed Langevin-type equations for the fluid properties seen by the particle [96,102,103]. These models require solution of an extra set of ODEs for the fluctuating components.

Park et al. [104] developed a dynamic subgrid-scale model for the velocity seen by the particle. They used an approximate deconvolution method together with a differential filter to estimate the unresolved velocity seen by the particles. They developed a dynamic procedure to determine the filter width Δ.

On the other hand, Bini and Jones [95,96] developed a model for the acceleration experienced by a particle in turbulent flow. Their model could reproduce the non-Gaussian acceleration PDF's observed in direct numerical simulations.

3. Methods

In this section, the methods used in the present work are reviewed. The simulation tool used in this thesis is the Fire Dynamics Simulator (FDS)[2]. The equations solved by FDS are reviewed in Section 3.1. The rest of this section reviews the modeling contributions from this thesis.

3.1 Description of the computational tool

3.1.1 Gas phase

FDS solves the Navier-Stokes equations in a form suitable for low-Mach number, thermally driven flows. The turbulence model in FDS is Large Eddy Simulation (LES). The low pass filtered equations of Low-Mach buoyancy-driven flow are given by [105]

$$\frac{\partial \rho}{\partial t} + \nabla \cdot \rho \boldsymbol{u} = \dot{m}''' \tag{27}$$

$$\frac{\partial \rho \boldsymbol{u}}{\partial t} + \nabla \cdot \rho \boldsymbol{u}\boldsymbol{u} = -\nabla \tilde{p} + \nabla \cdot \tau + (\rho - \rho_0)\boldsymbol{g} + \boldsymbol{f}_b \tag{28}$$

$$\frac{\partial \rho Y_\alpha}{\partial t} + \nabla \cdot \rho Y_\alpha \boldsymbol{u} = \nabla \cdot \boldsymbol{J}_\alpha + \dot{m}_\alpha''' \tag{29}$$

$$\frac{\partial \rho h_s}{\partial t} + \nabla \cdot \rho h_s \boldsymbol{u} = \frac{D\bar{p}}{Dt} + \dot{q}''' - \nabla \cdot \dot{\boldsymbol{q}}'' \tag{30}$$

$$\tau = \rho(\nu + \nu_t)\left((\nabla \boldsymbol{u} + \nabla \boldsymbol{u}^T) - \tfrac{2}{3}(\nabla \cdot \boldsymbol{u})\right) \tag{31}$$

$$\dot{\boldsymbol{q}}'' = \rho c_p (k + k_t)\nabla T + \textstyle\sum_\alpha \rho D_\alpha h_\alpha \nabla Y_\alpha + \dot{\boldsymbol{q}}_{\boldsymbol{r}}'' \tag{32}$$

$$\rho = \frac{\bar{p}\bar{W}}{RT};\ W = \frac{1}{\sum_\alpha Y_\alpha / W_\alpha} \tag{33}$$

Here the over bars denoting the low-pass filtering operation have been omitted for clarity. The low-Mach number approximation enables us to split the pressure into background pressure $\bar{p}$ and perturbation pressure $\tilde{p}$. Only the background pressure appears in the equation of state. Formally the low-Mach number equations can be derived from the compressible Navier-Stokes equations by expanding the variables in powers of the Mach number [106].

[2] Availble form https://pages.nist.gov/fds-smv/

Unless otherwise indicated, the turbulent viscosity is given a modified version of the model proposed by Deardorff [107]. The eddy viscosity is calculated from:

$$\mu_t = \rho C_{dea} \Delta \sqrt{k_{sgs}};\ k_{sgs} = \frac{1}{2}\|\boldsymbol{u}'\|;\ \boldsymbol{u}' = \overline{\boldsymbol{u}} - \overline{\overline{\boldsymbol{u}}}. \tag{34}$$

Here Δ is the filter width and C_{dea}=0.1 is an empirical constant. The main difference between the above model and the usual one-equation turbulence closures is that the sgs kinetic energy is obtained by a scale similarity argument. In addition to the default Deardorff model, the dynamic Smagorinsky model [108,109] is also used.

3.1.2 Radiation

The contribution of thermal radiation to the energy equation is computed from

$$-\nabla \cdot \dot{q}_r'' = \kappa[U - 4\pi I_b(\boldsymbol{x})];\ U = \int_{4\pi} I(\boldsymbol{x}, \boldsymbol{s}')ds'\ . \tag{35}$$

In the above, $I(\boldsymbol{x}, \boldsymbol{s}')$ is the spectrally integrated intensity in the direction $\boldsymbol{s}'$ at the location $\boldsymbol{x}$, $I_b(\boldsymbol{x})$is the source term, and κ is the absorption coefficient. The intensity I is obtained as a solution to the radiation transport equation (RTE):

$$\boldsymbol{s} \cdot \nabla I_\lambda = [\kappa + \kappa_d + \sigma_d]I + \kappa I_b + \kappa_d I_{b,d} + \frac{\sigma_d}{4\pi}\int_{4\pi} \Phi(\boldsymbol{s}, \boldsymbol{s}')I(\boldsymbol{x}, \boldsymbol{s}')ds'. \tag{36}$$

Here κ_d is the droplet absorption coefficient, $\sigma_d$is the droplet scattering coefficient, and $I_{b,d}$ is the emission term of the droplets. The scattering phase function $\Phi(\boldsymbol{s}, \boldsymbol{s}')$ gives the scattered intensity fraction from the direction $\boldsymbol{s}'$ to $\boldsymbol{s}$.

The mean absorption coefficient κ is tabulated as a function of the gas species and soot concentration by using the narrow-band model RadCal [110]. The absorption coefficient is given by

$$\kappa = \min\left[\kappa_p, \kappa_{eff}\right] \tag{37}$$

where κ_p is the planck mean absorption coefficient, and the effective absorption coefficient is solved from

$$\int_0^\infty I_\lambda\,(S) = \frac{\sigma}{\pi}[e^{-\kappa_{eff}S}T_{rad}^4 + (1 - e^{-\kappa_{eff}S})T^4] \tag{38}$$

Here T_{rad} is the assumed temperature of incident radiation. It is taken to be 900 ºC, corresponding to typical flame emission temperatures. The path length S is set to five times the nominal cell size. In engineering practice, the attainable grid resolutions are usually of the order of five grid cells across the plume. The effective mean absorption coefficient approaches the Planck mean absorption coefficient as the path length decreases. During simulations, the absorption coefficients are obtained by table lookup. The absorption and scattering coefficients of the liquid droplets are based on Mie theory [111]. The scattering integral is approximated as a sum of isotropic and forward components [112]. The RTE is solved using the Finite Volume Method for radiation [113].

As was discussed in Section 2.5.1, the source term in Eq. (36) requires modeling. In FDS the source term is computed as follows:

$$I_b(\boldsymbol{x}) = C\ \frac{\sigma T(\boldsymbol{x})^4}{\pi}\ \ C = \max\left[1, \frac{\int_{\dot{q}'''>0} \chi_r \dot{q}''' + \kappa U\ dV}{\int_{\dot{q}'''>0} \sigma \kappa T^4\ dV}\right] \tag{39}$$

This method aims to ensure that the fraction of energy released from flames as radiation is globally equal to the radiant fraction χ_r.

3.1.3 Combustion

For all simulations in this thesis, the gas phase combustion is treated as a single step irreversible reaction of fuel and oxidizer:

$$Fuel + Air \rightarrow Products\ . \tag{40}$$

The chemical heat source term in Equation (30) is given by

$$\dot{q}''' = \dot{m}_f''' \Delta h_c\ , \tag{41}$$

where Δh_c is the heat of combustion of the fuel. The rate of combustion is given by a model similar to the eddy dissipation concept (EDC) model [114]

$$\dot{m}_f''' = -\rho \min \frac{\left(Y_f, \frac{Y_o}{s}\right)}{\tau_{mix}}\ , \tag{42}$$

where Y_f and Y_o are the mass fractions of the fuel and oxidizer, respectively. The mixing time scale τ_{mix} is based on the local flow field [115].

FDS contains a simple extinction model based on the concept of critical flame temperature. For each computational cell, the extinction is determined by two criteria: The first rule suppresses the combustion if the temperature in the computational cell does not exceed a user defined auto ignition temperature. The second rule considers a stoichiometric pocket of fuel, air, and products in a computational cell. If the combustion energy of this fuel is not sufficient to increase the temperature of the gas mixture above the critical flame temperature, the combustion reaction is again suppressed. Both the critical flame temperature T_{CFT} and auto ignition temperature T_{AIT} are user-defined constants

3.1.4 Evolution equations for the Lagrangian particles

FDS uses the LE method for the description of the dispersed phase. Buoyancy, lift, and forces arising from fluid acceleration are neglected. With these assumptions, the motion of a single computational droplet is governed by

$$\frac{d\boldsymbol{V}^{(i)}}{dt} = \tau_p^{-1}\left[\boldsymbol{u}^{@\boldsymbol{p}} - \boldsymbol{V}^{(i)}\right] + \boldsymbol{g}. \tag{43}$$

The drag coefficient C_D is given by

$$C_D = \begin{cases} \frac{24}{Re} & Re < 1 \\ 24(0.85 + 0.15Re_D^{0.687}) & 1 \leq Re < 1000 \\ 0.44 & 1000 \leq Re \end{cases} \quad (44)$$

The mass of the particle evolves according to the pair of ODEs:

$$\frac{dM^{(i)}}{dt} = Ah_m\left(Y_\alpha^S - Y_{\alpha,g}^{@p}\right), \quad (45)$$

$$M^{(i)}c_p\frac{dT^{(i)}}{dt} = A\mathrm{h}\left(T_g^{@p} - T^{(i)}\right) + \dot{q}_r + \frac{dM^{(i)}}{dt}\Delta h_v. \quad (46)$$

As discussed earlier, each droplet represents several real droplets with the same properties. The fluid properties are interpolated at the droplet position using tri-linear interpolation. The backward interpolation is performed using a variant of the Particle-In-Cell (PIC) method, in which the mean particle source terms in Eqs (27)-(30) are calculated as the summation of the individual contributions of each particle in the control volume surrounding a grid node

The quasi-steady drag approximation is employed here, and it can be justified on the grounds of the large density difference between the carrier phase and the dispersed phase. The grid resolutions used in most fire simulations are also too coarse to resolve the pressure gradients and mean shear forces in Eq. (8). The errors caused by the numerical discretization are likely to be much larger.

3.1.5 Condensed phase heat transfer model

The FDS condensed phase heat transfer model is used in modeling the liquid phase in papers IV and V. FDS calculates the heat transfer in the solid phase based on conduction and radiation. The model is applied on a cell-by-cell basis. This section describes the model as it is applied to liquid pool fires.

The FDS solid phase model solves the one-dimensional heat conduction equation for the liquid fuel given by

$$\begin{aligned} &\rho c_p\frac{\partial T_l}{\partial t} = \frac{\partial}{\partial x}k_l\frac{\partial T_l}{\partial x} + \dot{q}''' \\ &-\mathrm{k}\left(\frac{\partial T_l}{\partial x}\right)^S = h\left(T_g - T_l^S\right) - \Delta h_v\dot{m}'' \\ &h = \max\left[1.52\left|T_g - T_l^S\right|^{\frac{1}{3}}, \frac{k_g Nu}{L}\right] \\ &Nu = 0.037Re^{4/5}Pr^{1/3}. \end{aligned} \quad (47)$$

Here ρ, c_p, k_l, *and* Δh_v are the fuel density, specific heat, thermal conductivity, and evaporation heat, respectively. The subscripts l and g refer to the liquid and gas phases. The superscript S denotes the liquid surface.

The heat source term $\dot{q}''$ in Equation 47 accounts for the effect of the in-depth absorption of radiation and therefore radiation is not accounted for in the surface boundary condition. The radiation heat transfer within the one-dimensional layer is

calculated using a “two-flux” model in which the radiative intensity is assumed to be constant in the “forward” and “backward” hemispheres. The forward radiative heat flux into the fuel is

$$\frac{d\dot{q}^+}{dx} = \kappa(\sigma T^4 - \dot{q}^+). \tag{48}$$

A corresponding formula can be written for the backward flux $\dot{q}^-$. The heat source term in Equation 47 is the difference between the forward and backward fluxes

$$\dot{q}''' = \frac{d\dot{q}^+}{dx} - \frac{d\dot{q}^-}{dx}. \tag{49}$$

Boundary condition at the fuel surface is given by

$$\dot{q}^+|_{x=0} = \dot{q}''_{in} + (1-\varepsilon)\dot{q}^-, \tag{50}$$

where ε is the fuel emissivity and $\dot{q}''_{in}$ is the incoming radiative flux.

3.2 Spray modeling

3.2.1 Overview

In order to correctly predict the spray dispersion, the characteristics of the initial spray must be accurately determined. This means that the droplet size distribution, initial velocity, and shape of the initial spray need to be described. For the present methodology, this means developing appropriate spray boundary conditions.

Section 3.2.2 discusses how to determine suitable droplet size distributions for use with the spray boundary conditions developed in Papers I and III.

Section 3.2.3 reviews the spray boundary condition for simulation of water mist sprays, developed in Paper I. Section 3.2.4 discusses the spray boundary condition for liquid dispersal from aircraft and liquid-filled projectile impacts, developed in Papers II and III.

Section 3.2.5 describes the three-way coupling model presented in Paper I. Additionally, Section 3.2.6 describes a turbulent dispersion model that was not presented in Papers I-V.

3.2.2 Droplet size distributions

The classical approach for modeling the droplet size distributions is to fit an analytical distribution to the experimental data. Several choices for the droplet size distribution are available in the literature (see e.g. [116]). This thesis considers only three different analytical distributions: the Rosin-Rammler distribution, the lognormal distribution and the combination of the Rosin-Rammler and log-normal distributions. These three distributions were chosen because they are available for modeling the droplet size distributions in FDS.

The Rosin-Rammler distribution was initially developed for modeling the size distribution of coal particles, but has been widely used for modeling spray droplet size distributions [116]. The lognormal distribution is usually considered as a model for the Cumulative Number Fraction (CNF). Here it is used as a model for the Cumulative Volume Fraction (CVF) instead. The combination of these two distributions, called Rosin-Rammler-lognormal distribution, has been found to describe the droplet sizes in sprinkler sprays and is commonly used among fire safety engineers.

The Rosin-Rammler distribution is described by the CVF:

$$F(d) = 1 - exp\left[-0.693\left(\frac{d}{d_m}\right)^{\gamma}\right]. \tag{51}$$

CVF of the lognormal distribution is given by:

$$F(d) = \frac{1}{\sqrt{2\pi}}\int_0^{\mathrm{d}} \frac{1}{\sigma d'} exp\left[-\frac{log\left(\frac{d'}{d_m}\right)^2}{2\sigma^2}\right] dd'. \tag{52}$$

The Rosin-Rammler-lognormal combination:

$$F(d) = \begin{cases} 1 - exp\left[-0.693\left(\frac{d}{d_m}\right)^{\gamma}\right] & , d > d_m \\ \frac{1}{\sqrt{2\pi}}\int_0^{d} \frac{1}{\sigma d'} exp\left[-\frac{log\left(\frac{d'}{d_m}\right)^2}{2\sigma^2}\right] dd' & , d \le d_m \end{cases}, \tag{53}$$

where d_m is the volumetric median diameter of the size distribution (half of the volume of the particles is in droplets smaller than this).

The numerical algorithm draws the droplet diameter from the cumulative number fraction (CNF), defined as

$$f(d) = \frac{\int_0^d F\prime(d\prime){d'}^{-3} dd\prime}{\int_0^{\infty} F\prime(d\prime){d'}^{-3} dd\prime}. \tag{54}$$

Since the numerical algorithm picks the droplet sizes from the CNF, the CNF was also used in the parameter estimation in Papers I and II. The distribution parameters were found by least squares fit of Eq. (54) to the experimentally determined cumulative number distribution. The difference between using CVF or CNF for parameter estimation is that the former places more weight on large droplets, whereas the latter emphasizes the smaller drop sizes. This point was discussed extensively by Ditch et al. [117].

From the perspective of the work described in this thesis summary, it is important that the spray boundary condition is situated far enough from the nozzle so that all atomization processes have finished and the droplet distribution can be considered to be stable. Consequently, the droplet size distribution should also be determined sufficiently far from the spray inlet.

Ideally, the droplet size distribution would be determined at a position at which the breakup processes have finished but the entrainment into the spray and turbulent mixing has not had time to affect the measured distributions significantly.

However, finding this distance may be difficult. Measurements further away from the nozzle can be used if the effect of the entrainment and mixing on the droplet size distributions is taken into account. This can be done by using appropriate averaging of distributions measured at several positions.

Unlike the initial droplet size distributions, the initial velocities and flux densities should be determined as close to the location of the spray boundary condition as possible. Measurements of fluxes and velocities further away from the spray inlet can be used for validation.

3.2.2.1 Water mist nozzles

In Paper I, the droplet size distributions of three high-pressure water mist nozzles, called A, B, and C, were characterized based on data from NFPA750 characterization experiments. Measurements and the calculation of gross cumulative volume (GRV) distribution were in accordance with the NFPA750 standard, except that one measurement point was added in the center of the spray. The measured nozzles (called A, B, and C in Paper I) produced a relatively narrow cone with a dense core. The central point was included to capture this dense core of the spray better.

The GRV distribution was calculated as

$$GRV(d_j) = \frac{\sum(R_{i,j} \times A_i \times v_i)}{\sum(A_i \times v_i)}. \quad (55)$$

where $GRV(d_j)$ is the cumulative volume fraction of all droplets equal to or less than d_j, and $R_{i,j}$ is the cumulative volume fraction of droplets equal to or less than d_j at location i. A_i and v_i are the cross-sectional area and the mist flux at location i.

The Gross CFN was calculated similarly. The parameters for the Rosin-Rammler-Lognormal distribution (Eq. (53)) were found by least squares fitting of the CNF defined by Eq. (54). Table 3.1 lists the FDS simulation parameters for the A, B, and C nozzles from Paper I. The K-factor is based on manufacturer info, whereas the spread angle θ was visually approximated from photographs of the spray.

Table 3.1 FDS Simulation parameters for nozzles A, B, and C from Paper I.

Nozzle	K (l/min/bar^{½})	θ (°)	d_m (μm)	γ
A	0.200	10	83	2.90
B	0.433	12	79	2.26
C	0.767	14	116	1.98

3.2.2.2 Sprays from liquid-filled missiles

The model is based on qualitative observations and quantitative characterization of the sprays resulting from high-speed impacts of water-filled missiles. Paper II describes the details of the experimental campaign and analysis methods. In this case, only a single measurement point was available. However, unlike the water mist sprays, the spray behavior was transient. Each experiment produced a slightly different droplet size distribution.

In all the tests, the spray concentration was found to follow a similar time dependence. The concentration peaks soon after the spray reaches the measurement position. A relatively long and dilute tail follows this initial front. Between 60% and 90% of the spray mass was found to pass the measurement position within the first 50 ms after the spray reached the measurement location.

Based on these observations, the experimental data was split into the “spray front” and “continuous” spray. In the analysis, the first 15 ms of the observations were assumed to belong to the spray front. The spray front contained approximately 20% of the total mass of the spray (approximated from measured volume fractions). The continuous spray is the rest of the spray. Table 5 shows the resulting size parameters.

The fitted distribution functions cannot capture all the features of the experimentally determined distributions. In particular, the experimental distributions had a sharp spike at the small particle diameters, followed by a long tail. The lognormal distribution function can reproduce this behavior most accurately. The Rosin-Rammler distribution significantly overpredicts the number of very small particles. In experiments SFP2-7, the continuous part of the spray contained large droplets, which increased the estimates of the volumetric median diameter d_m.

Table 5. Fitted distribution parameters.

Experiment		Distribution					
		Rosin-Rammler		Rosin-Rammler-Log-normal		Log-normal	
		d_m (μm)	γ	d_m (μm)	γ	d_m (μm)	σ
SFP 2-5	Whole	80	0.89	78	0.86	77	1.12
	Front	90	1.03	87	0.98	85	0.98
	Continuous	80	0.87	78	0.85	77	1.14
SFP 7-12	Whole	101	1.04	99	1.01	98	0.96
	Front	84	1.42	82	1.33	80	0.76
	Continuous	105	1.01	103	0.98	101	0.98
All	Whole	85	0.93	83	0.89	82	1.08
	Front	88	1.09	85	1.03	84	0.94
	Continuous	86	0.90	84	0.87	83	1.10

3.2.3 Spray boundary condition for water mist nozzles

As was discussed in Section 2.5.2, the Eulerian-Lagrangian particle model is not applicable in the solid region of the spray. Therefore, we did not attempt to model the atomization processes of the spray. Instead, we injected droplets to the simulation on a section of a spherical surface at distance R from the nozzle. The section of the surface that launches the droplets is determined by the elevation angle θ. **Figure 3.1** illustrates the spray boundary condition. All atomization processes (primary and secondary) are assumed to have finished at this position. The size distribution of the inserted droplets then represents a stable size distribution, measured far from the spray inlet.

The spray boundary condition developed in Paper I assumes a Gaussian profile for the initial droplet volume fraction. Experimentally measured and predicted liquid volume fractions in a pressure atomized spray [21] achieve a Gaussian-like profile between 12.5 and 50 nozzle diameters from the inlet. If the spray boundary condition is very close to that of the jet inlet, the assumptions behind the Gaussian profile are less valid.

For large-scale simulations of fire suppression systems, it is critical that the spray boundary condition injects the correct amount of momentum along with the correct volume of water into the system. The momentum works as a driving force for large-scale mixing in the compartment. In Paper I, a simple relationship between the initial velocity of the droplet and the operating pressure of the nozzle was assumed:

$$v_0 = C\sqrt{\frac{2p}{\rho}}. \tag{56}$$

Here p is the operating pressure of the nozzle, and ρ is the density of the liquid. In Paper I, we gave the discharge coefficient C the value 0.95. This value is not based on measurement and we did not carry out an extensive sensitivity analysis. All the droplets are given the same initial speed in the direction of the surface normal.

Note that the spray boundary condition defined here ignores deceleration of particles between the real injection point and the injection point in the simulation. The initial velocity defined by Eq. (56) ensures that the correct amount of momentum is injected into the simulation. Another approach would be to calculate the correct velocity of the droplets at distance corresponding to the spray boundary condition. In this approach, the gas phase velocity at the spray boundary condition should also be increased in order to conserve momentum.

The former approach is more complex than the one adopted in this thesis. The difference in the two approaches would likely be most important for small particles. However, small particles quickly reach their terminal velocity and therefore, the choice of using initial velocities defined by Eq. (56) simply causes the particle to slow down farther away from the nozzle than in reality. This effect is likely to be important only in the immediate vicinity of the spray boundary condition.

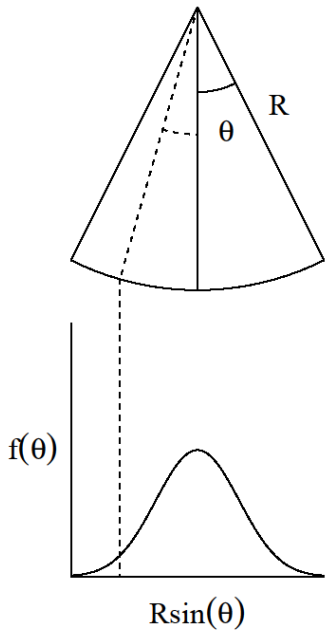

Figure 3.1. Illustration of the spray boundary condition for water mist spray simulations

The initial position of a particle is picked randomly from the conical section described previously. The variable flux density within the spray is implemented by defining a probability density function for the initial position that depends on the latitude θ but not longitude φ. The joint probability of the initial latitude and longitude is

$$p(\theta,\varphi) = p(\theta)p(\varphi) = \frac{1}{2\pi}\sin\theta\, f(\theta) \tag{57}$$

Here the longitude is assumed to be independent of the latitude. If the function $f(\theta)$ is taken to be unity, the resulting mass flux is uniform. Prior to the implantation of the spay boundary condition in Paper I, FDS used uniform distribution to pick the latitude θ. This corresponds to a flux distribution $f(\theta) = \sin\theta^{-1}$.

The exponential shape of the mass flux is implemented by using the probability density function

$$f(\theta) = exp\left[-\beta\left(\frac{\theta-\theta_\mu}{\theta_{max}-\theta_{min}}\right)^2\right], \text{ where} \tag{58}$$

$$\theta_\mu = \begin{cases} 1/2(\theta_{max}+\theta_{min}) & \theta_{min} \neq 0 \\ 0 & \theta_{min} = 0 \end{cases}$$

The spread parameter $\beta = 5$ was chosen so that the simulations best fit the nozzle characterization experiments. In Paper I we did not attempt to provide a theoretical estimate for β. The following discussion is an addition to the discussion in Paper I.

For the case where $\theta_{min} = 0$ (full cone spray), an estimate for the spread parameter β can be derived using the theory of turbulent round jets. We approximated the profiles of velocity and scalar density in a round jet with an exponential distribution

$$c(x,r) = c_0 exp\left[-\frac{r^2}{2r_{1/2}^2}\right]. \tag{59}$$

Here r is the radial coordinate in the jet and $r_{1/2}$ is jet half-width. For a turbulent round jet, $dr_{1/2}\backslash dx \approx 0.1$ [13 p.111]. The jet width at distance x is then $r_{1/2} = x/10$. On the other hand, $r = x \tan\theta \approx x\,\theta$. Substituting gives

$$c(x,r) = c_{max} exp[-50\theta^2] = c_{max} exp\left[-50\theta_{max}^2\left(\frac{\theta}{\theta_{max}}\right)^2\right]. \tag{60}$$

The estimate of β is then $50\theta_{max}^2 = 2.37$. This is approximately half of the value used in Paper I. It is possible that nozzles A, B and C considered in Paper I place more water at the center of the jet by construction.

3.2.4 Spray boundary for liquid-filled missiles

Our model of an aircraft impact only describes the liquid dispersal from ruptured fuel tanks. The deformation of the missile and ejection of debris are ignored. The fuel dispersal process is modeled as a high-speed spray boundary condition. The model is based on qualitative observations and quantitative characterization of the sprays resulting from high-speed impacts of water-filled missiles [118].

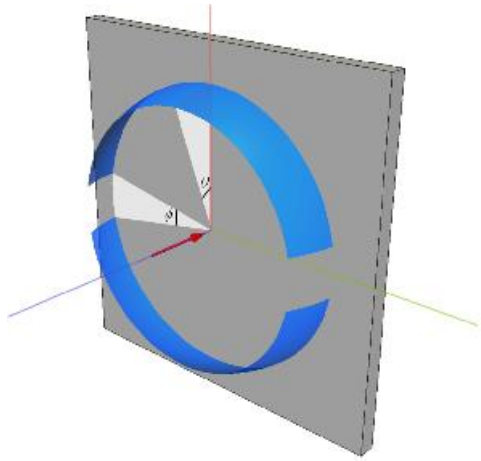

Figure 3.2. Illustration of the spray boundary condition for aircraft impact simulations

Droplets enter the simulation at a randomly selected position on a spherical surface at distance R from the impact location. All droplets have the same initial speed, but the diameter of the droplets is randomly selected. Based on the analysis in Paper III, the initial speed of the inserted particles is 1.8 times the speed of impact.

Figure 3.2 illustrates the shape and parameters of the spray injection surface. The surface consists of two elements of a spherical surface, representing fuel released upwards and downwards. Visual observations from the Sandia experiments revealed that no fuel is released in the directions of the wings. The gaps in the injection surface account for the effect of the wings. The distance between the spherical surface and impact location should be greater than or equal to the characteristic length scale of missile deformation and primary liquid ejection. The particle distribution should represent a stable particle size distribution.

3.2.5 Three-way coupling between droplets and gas

As discussed in Section 2.5.3, in dense sprays the wakes behind individual droplets may start to influence other droplets. In Paper I, we presented a model for the drag reduction in dense sprays.

We base our model on the analytical formula developed by [119]. The model builds on the idea that in a configuration in which two particles with the same diameter are directly in line, the hydrodynamic force on the trailing particle can be calculated using drag correlations for an isolated sphere. However, the reference velocity in this calculation needs to be correctly defined. The authors employed the well-known analytical results for the wake of a sphere in laminar flow [119 p. 349]. They developed the following analytical formula for the hydrodynamic force to the second sphere.

$$C_D = C_{D_0}\frac{F}{F_0}, \tag{61}$$

where C_{D_0} is the single droplet drag coefficient and F/F_0 is the hydrodynamic force ratio of trailing droplet to single droplet:

$$\frac{F}{F_0} = \bar{W}\left[1 + \frac{Re}{16\left(\frac{L}{d}-\frac{1}{2}\right)^2}\, exp\left(-\frac{Re}{16\left(\frac{L}{d}-\frac{1}{2}\right)}\right)\right], \tag{62}$$

where Re is the single droplet-Reynolds number, L is the distance between the droplets and $\bar{W}$is the non-dimensional, non-disturbed wake velocity at the center of the trailing droplet

$$\bar{W} = 1 - \frac{C_{D_0}}{2}\left[1 - exp\left(-\frac{Re}{16\left(\frac{L}{d}-\frac{1}{2}\right)}\right)\right], \tag{63}$$

In our implementation, the separation distance L/d between droplet centers is calculated from the local droplet volume fraction, α, and local average droplet diameter $\langle d\rangle$

$$\frac{L}{d} = \langle d\rangle\left(\frac{\pi}{6\alpha}\right)^{\frac{1}{3}}, \tag{64}$$

Eq. (64) gives the separation distance for evenly distributed spherical particles of diameter $\langle d\rangle$.

The hydrodynamic force predicted by Eq. (62) can be compared with the numerical results of Prahl et al. [121]. According to their study, Eq. (62) significantly underestimates the drag reduction at small drop-to-drop distances, where the wake is not fully developed, and (63) does not hold. At greater distances the two results are similar, the present correlation showing more drag reduction. The sprays considered in this paper are relatively dilute, and hence these short separation distances are not expected to be important.

3.2.6 Turbulent dispersion

Turbulent dispersion models were not used in Papers I-V. However, in Paper I, some features of the simulation results were credited to the turbulent mixing of particles. In this thesis summary, the effect of turbulent dispersion on water mist sprays is studied using the model developed by Bini and Jones [95,96]. The particle velocity evolves according to

$$d\boldsymbol{V}^{(i)} = \tau_p^{-1}\left[\boldsymbol{V}^{(i)} - \boldsymbol{u}^{@\boldsymbol{p}} -\right]dt + \boldsymbol{g}dt + \sqrt{\frac{k_{sgs}}{\tau_t}}\,d\boldsymbol{W}_t \text{ , with } \tau_t = \frac{\tau_p^{1.6}}{\left(\frac{\Delta}{\sqrt{k_{sgs}}}\right)^{0.6}} \tag{65}$$

Here $d\boldsymbol{W}_t = \sqrt{\Delta t}\boldsymbol{\xi}$,with $\boldsymbol{\xi} \sim N(0,1)$, is an increment of the Wiener vector process. The subgrid scale kinetic energy is approximated from

$$k_{sgs} = (\mu_t/\rho C_{dea}\Delta)^2, \tag{66}$$

This model is easy to implement, as it does not require the solution of additional ODEs for the turbulent velocity seen by the particle. Note that this model of turbulent dispersion is isotropic. Bini and Jones [95] developed an anisotropic version of the model, but this was not pursued here.

3.3 Modeling liquid pool fires

3.3.1 Mathematical model

The liquid pool fire model utilized In Papers IV and V is based on treating the liquid fuel as a semi-transparent solid with evaporation at the fuel surface. Heat transfer in the liquid is calculated using the condensed phase model in FDS, described in section 3.1.5. In Paper IV the earlier [50], equilibrium-based, mass transfer model was replaced by a mass transfer expression.

In Paper IV, the mass flux from the surface is calculated by a simple approach based on film theory. The molar flux in Eq. (13) can be related to mass flux using the ideal gas relation $c = P/RT$. The mass flux is then given by

$$\dot{m}'' = h_m \frac{\bar{p} W_f}{RT} log\left(\frac{X_f^{\infty} - 1}{X_f^{S} - 1}\right); \; X_f^{S} = exp\left[-\frac{\Delta h_v W}{R}\left(\frac{1}{T_S} - \frac{1}{T_b}\right)\right] \quad (67)$$

Here $h_m = ShD_{f,g}/L$ is the mass transfer coefficient and $\rho_{f,g}$ and X_G are the density of the fuel vapor and the volume fraction of fuel vapor in the grid cell adjacent to the pool surface, W is the molar mass of the fuel gas and R is the universal gas constant. D_f is the binary diffusivity of the vapor and the Sherwood number is given by

$$Sh = 0.037 Sc^{\frac{1}{3}} Re^{\frac{4}{5}}; \; Re = max\left[5 \cdot 10^5, \frac{\rho u L}{\mu}\right] . \quad (68)$$

The Reynolds number is calculated based on the conditions in the cell adjacent to the surface. In the above, *L* is some characteristic length. Note that the Reynolds number is bounded from below, which ensures a non-zero mass flux from liquid fuels and thus circumvents the need to model the ignition process. The Reynolds number varies over time through the gas speed dependence, and so do the Sherwood and mass transfer numbers.

Papers IV and V did not present alternative methods for determining the mass transfer coefficient. In Paper IV, we briefly discussed the effect of mass transfer coefficient on predicted evaporation rates and concluded that because of the log term in Eq. (67), the importance of the mass transfer coefficient rapidly decreases as the liquid temperature approaches boiling point. The rest of this section adds to the discussion presented in Papers IV and V.

The Sherwood number in Eq. (67) and the Nusselt number in Eq. (47) represent average mass and heat transfer coefficients for a horizontal flat plate. The situation at the pool surface could perhaps more realistically be described as natural or mixed convection.

The use of flat plate correlations can be justified from two perspectives. Firstly, as discussed above, the mass transfer coefficient is important only in the initial phases of a pool fire, when surface temperature is far below boiling temperature. Secondly, the gas phase flow in pool fires is not driven by the temperature difference between the liquid surface and gas. Instead it is driven by heat generation outside the boundary layer. As such, the use of traditional natural convection based correlations is questionable. From the point of view of the pool surface, the situation is close to forced convection, where the entrainment in to the flame is driving the flow.

A simple alternative for the mass transfer coefficient can be derived using the viscous wall units given by Eq. (12). Assume that the non-dimensional film thickness δ^+ is constant. The mass transfer coefficient can then be related to the non-dimensional film thickness by

$$\delta = \frac{\delta^+ \nu}{u_\tau};\ h_m = \frac{D_F u_\tau}{\delta^+ \nu}. \tag{69}$$

We could, for example, assume that the film thickness is equal to the laminar sublayer thickness, $\delta^+ = 5$. However, in the following discussion δ^+ is treated as a fitting parameter.

Figure 3.3 shows predicted evaporation velocities for toluene, calculated from Eq. (67). The mass transfer coefficient was calculated using Eq. (69). The black dots in **Figure 3.3** correspond to the wind tunnel data of Reijnhardt and Rose [122]. In their experiments, they measured the evaporation rate of toluene in a wind tunnel. The pool was a square with 0.25 m side length. In their toluene evaporation experiments, the friction velocity derived from measurements directly in front of the pool was 0.43 m/s.

The fitting parameter $\delta^+ = 21.16$ produced the best fit to the data. The corresponding value of the mass transfer coefficient for this case is $h_m = 0.01$ m/s. The mass transfer coefficient used in Paper II gives $h_m = 0.034$ for this case.

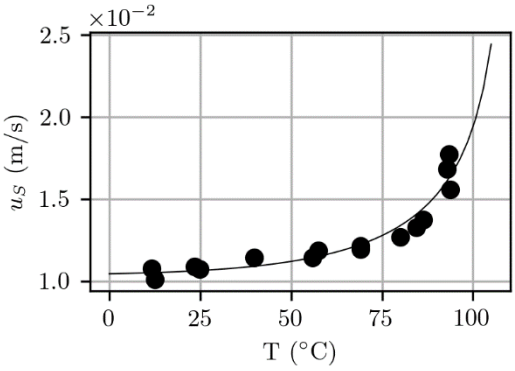

Figure 3.3 The normalized evaporation rate of toluene as a function of temperature. The solid line is computed from Eqs. (67) **and** (69) **with** $D_F = 7.69 \cdot 10^{-6}\ m^2/s$ **(toluene at 20 ºC)** ,$\nu = 1.50 \cdot 10^{-5}\ m^2/s$ **(air at º20 C) and** δ^+**=21 (curve fit). Black dots correspond to experimental data from wind tunnel experiments** [122,123] **with** $u_\tau = 0.43\ m/s$.

The experimental data shows the importance of accounting for convective mass transfer. As the fluid temperature approaches boiling point, the mass flux increases exponentially. The log-term in Eq. (67) can capture this increase in evaporation rate quite well. This data was not used for validation of the evaporation model in Paper II and is reported here to highlight the effect of convection on mass transfer.

Note that the evaporation model used for droplets, Eq. (45), does not contain the logarithmic term appearing in in Eq. (67). **Figure 3.3** shows that the effect of blowing is only important near the boiling point. For the sprays considered in this thesis the liquids are injected at room temperature (20 ºC) and into similar ambient temperatures. Therefore, the effect of the logarithmic term is expected to be negligible.

The heat transfer coefficient in Equation (47) does not consider the effect of nonzero wall transpiration. The effect of blowing is to reduce the convective heat flux to the boundary [15]. The pool fires considered in this thesis are relatively large (0.5-3 meters in diameter), and radiation is the dominant heat transfer mode. For smaller pool fires the effect of blowing on convective heat transfer may have to be considered.

3.3.2 Effective absorption coefficients for in-depth radiation absorption

Absorption of thermal radiation in semi-transparent media is highly dependent on the wavelength of the radiation. A spectrally resolved (line-by-line) solution of Eq. (68) would be prohibitively expensive. It would also be unwarranted, as fire models often assume the gas to behave as a gray medium, and thus, the spectrum of incoming radiation is not known.

Paper II presents a method for determining effective absorption coefficients. The procedure is as follows:

1. Start with spectrally resolved absorption coefficients κ_λ for a liquid.
2. Calculate the transmitted fraction of radiation at distance x from the liquid surface by

$$\dot{q}^+_{ex}(x) = \int_0^\infty \dot{q}^+_{\lambda,ex}(\tau)d\lambda \tag{70}$$

$$\dot{q}^+_{\lambda,ex} = E_{b,\lambda}(T_\infty)2E_3(\tau) + E_{b,\lambda}(T(x))2\int_0^\infty E_2(\tau')d\tau' \tag{71}$$

Here, $\tau = \kappa x$ is the optical thickness, $T(x)$ and T_∞ are the temperatures of the liquid and the external source. $E_{b,\lambda}(T_\infty)$ is the black body emissive power at wavelength λ

$$E_{b,\lambda}(T) = \frac{2hc^2}{\lambda^5}\frac{1}{exp\left\lfloor\frac{hc}{k_B\lambda T}\right\rfloor - 1} \tag{72}$$

where c,k_B and h are the speed of light, the Boltzmann constant and the Planck constant, respectively. E_2 and E_3 are exponential integrals of the second and third kind, respectively

3. Optimize to find a value for absorption coefficient κ that minimizes some error metric between the predicted flux $\dot{q}^+$ from the solution of Eq. (48) and the flux calculated from Eq. (70) .

Three choices need to be made in this process:

1. Choice of optimization metric.
2. The path length L at which the flux $\dot{q}^+$is matched or over which the heat source distribution $\dot{q}'''$ is matched.
3. The spectrum of the incoming radiation.

We investigated two optimization metrics in Paper II. The first one tries to produce an accurate flux at the bottom of the liquid layer $x = L$, thus giving a good estimate for the amount of energy absorbed by the liquid. The absorption cofficients corresponding to this criterion are given by:

$$\kappa = \arg\min\left[\frac{\dot{q}^+(L)}{\dot{q}^+(0)} - \frac{\dot{q}^+_{ex}(L)}{\dot{q}^+_{ex}(0)}\right]. \tag{73}$$

The absorption coefficients determined by the above criterion produce an accurate flux at the bottom boundary only at the beginning of the simulation. As the liquid layer thickness decreases, the flux will be increasingly inaccurate.

The second, alternative criterion attempts to reproduce the distribution of radiant flux over the entire thickness of the liquid layer. This choice should provide more accurate distribution of temperature inside the liquid, but it may not conserve the

energy as well as the first criterion. The absorption coefficients corresponding to the second criterion are given by:

$$\kappa = \arg\min\left[\int_0^L \left(\frac{\dot{q}^+(x)}{\dot{q}^+(0)} - \frac{\dot{q}^+_{ex}(x)}{\dot{q}^+_{ex}(0)}\right)^2 dx\right]. \tag{74}$$

This second criterion is less sensitive to the choice of the path length L than the first.

In Paper II, the former method was termed M1 (for Method 1), and the latter was named M2 (Method2). **Figure 3.4** shows the transmitted fraction of radiation as a function of path length for liquid heptane. The continuous black line corresponds to the solution of Eq. (70). The dotted line shows the predicted flux $\dot{q}^+$ from solution of Eq. (50) using the two different methods of determining the absorption coefficient.

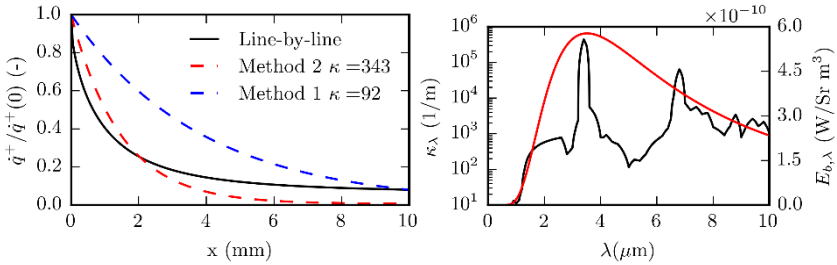

Figure 3.4 Left: Results from a simulation of radiation transport in heptane. Comparison of line-by-line solution and the two approaches for determining the effective absorption coefficient. Right: The absorption coefficient spectra of heptane with black body emissive power imposed (in red).

Figure 3.4 shows that neither method of determining the absorption coefficient can reproduce the exact attenuation of radiation predicted by Eq. (70). In order to correctly capture the long tail of the attenuation, the wavelength dependency of radiation would need to be addressed in some way. The line-by-line solution in **Figure 3.4** also shows that for heptane, most of the absorption of thermal radiation takes place within 4 mm of the fuel surface. However, a fraction of the incoming radiation (approximately 10% for heptane) may penetrate deep into the liquid layer.

3.3.3 Modeling the effects of convection in the liquid phase

As discussed in Section 2, accurate description of the liquid phase in pool fires would require solving the full Navier-Stokes equation with radiation heat transfer within the liquid. Such an approach is very complex and time-consuming. In Paper II, we explored an alternative approach of adjusting the thermal conductivity to take into account the internal convection. The Nusselt number gives the non-dimensional heat flux due to convective and conductive motions at an arbitrary plane in the liquid:

$$Nu = \frac{\dot{q}''_{conv}}{\rho c_p k \Delta T}. \tag{75}$$

If we assume that heat conduction can model the heat transfer by convection with an effective conductivity k_{eff}, Eq. (75) becomes

$$Nu = \frac{k_{eff}}{k}. \tag{76}$$

In Paper IV, we assumed that in large pool fires the primary source of convective motions is buoyancy generated by in-depth radiation absorption. We then calculated an effective thermal conductivity that reproduces the heat flux through the liquid layer at the surface of the fuel. We calculated the Nusselt number from a correlation for an internally heated horizontal plane layer with an isothermal top boundary and a thermally insulated bottom boundary[124]:

$$Nu = 0.338 Ra_i^{0.227}. \tag{77}$$

Here Ra_i is the internal Rayleigh number:

$$Ra_i = \frac{g\beta \dot{q}''' H^5}{k\nu\alpha}, \tag{78}$$

where β is the coefficient of thermal expansion of liquid, $\dot{q}'''$ is the volumetric heat source and H is a characteristic length scale. In the denominator, α is the thermal diffusivity of the liquid. Correlation (78) is derived for a case in which the internal heating is uniform. However, heat source distribution due to the absorption of radiation is approximately exponential. A Rayleigh number corrected for this distribution type is given by [125]

$$Ra_{i,corr} = \frac{g\beta \dot{q}''' H^5}{k\nu\alpha} \frac{\eta^2}{Q(\eta)} \left[1 - \left(1 + \frac{1}{\eta}\right) exp\left(-\frac{1}{\eta}\right)\right]. \tag{79}$$

Here $\eta = 1/\kappa$ is the length scale associated with the source distribution. The normalization constant $Q(\eta)$ in Eq. (79) is calculated from

$$Q(\eta) = \int_0^H \exp\left[-\frac{z}{\eta}\right] dz = \eta \left[1 - \exp\left(-\frac{H}{\eta}\right)\right]. \tag{80}$$

The effective thermal conductivity model described above is likely to work better for relatively thin layers of fuel. In thin layers, convection can be thought to cause mixing through the whole layer. In deeper pools, the convective currents are likely to involve only a part of the liquid. Table 3.3 lists the thermophysical properties of the liquid considered in Paper II.

Table 3.2 gives calculated Nusselt numbers for the situation considered in Paper IV (Table 5). For this case $\dot{q}''' = 20\ kW/m^2$ and the layer thickness H is 1 cm. It can be seen that for most liquids the Rayleigh numbers are O(10^7) and the Nusselt numbers are O(10). Therefore, we conclude that the heat transfer through the fuel would be greatly enhanced by convection.

A significant source of uncertainty in calculating the effective thermal conductivity is the characteristic length scale. We take the characteristic length H to be the depth of the liquid layer, which is constantly changing as the fuel is consumed. Furthermore, Eq. (78) also depends on knowing the volumetric heating rate.

Table 3.2 Nusselt numbers calculated from Eqs. (77)-(80). Ra_i is the internal Rayleigh number for uniform heating given by Eq. (78). $Ra_{i,corr}$ is the corrected Rayleigh number given by Eq. (79).

fuel	κ (1/m)	η (mm)	Ra_i 10^8	$Ra_{i,corr}$ 10^7	Nu based on Ra_i	Nu based on $Ra_{i,corr}$
Methanol	1000	1	1.6	1.6	25	15
Ethanol	1140	9	1.1	0.99	23	13
Water	1345	7	5.9	0.044	12	6
Benzene	162	6	2.1	7.9	26	21
Heptane	335	3	3.4	8.8	29	22
Toluene	289	4	2.2	6.3	26	20

Table 3.3 Thermophysical parameters of the liquids considered.

	k	ν	β	ρ	c_p
	W/m	m^2/s 10^{-7}	$1/K$ 10^{-3}	kg/m3	kJ/kg K
Heptane	0.14	5.57	1.24	675	2.24
Ethanol	0.17	13.9	1.09	789	2.72
Methanol	0.20	7.08	1.18	791	2.51
Toluene	0.15	6.34	1.08	867	1.72
Benzene	0.17	6.88	1.25	873.8	1.92
Water	0.58	8.9	0.21	1000	4.19

The corrected Rayleigh number in Eq. (79) is based on non-dimensional analysis, in which all length scales are scaled by the liquid layer height H. The length scale η used in Paper IV (Eq. (81)) is not normalized. Using a normalized length scale $\eta = 1/\kappa H$, the normalization constant $Q(\eta)$ in Eq. (79) is calculated from

$$Q(\eta) = \int_0^1 \exp\left[-\frac{z}{\eta}\right] dz = \eta\left[1 - \exp\left(-\frac{1}{\eta}\right)\right]. \quad (81)$$

Table 3.4 compares the Rayleigh numbers and Nusselt numbers calculated using the normalized length scale. The Nu values calculated here are approximately three times higher than those calculated in Paper II. This does not affect the conclusions of Paper II, as the order of magnitude remains the same.

Table 3.4 Nusselt numbers calculated from Eqs. (77)- (79) and (81). $Ra_{i,corr,new}$ is the corrected Rayleigh number given by Eq. (79) and the normalization constant given in Eq. (81). Nu_{orig} is the Nusselt number calculated using the original normalization constant given by Eq. (80).

fuel	κ (1/m)	η (-)	$Ra_{i,corr,new}$ 10^7	$Nu_{orig.}$	Nu_{new}	$\frac{Nu_{orig.}}{Nu_{new}}$
Heptane	335	0.30	8.83	7.9	21.5	2.7
Ethanol	1140	0.09	0.992	4.6	13.1	2.8
Methanol	1000	0.10	1.59	5.1	14.6	2.8
Toluene	289	0.35	6.27	7.4	19.9	2.7
Benzene	162	0.62	7.95	8.7	21.0	2.4
Water	1345	0.07	0.04	2.3	6.4	2.8

4. Results and discussion

4.1 Overview

This section includes a summary of the most important results described in Publications I-V and some additional results that provide more insight into the results reported in the Papers. The published results are divided into Spray modeling, Liquid pool fire modeling, and Risk analysis. For each subject, the results are divided into verification, validation, and application.

The verification of computational software is a process in which an attempt is made to ascertain the quality of the implementation. The verification can be performed by calculating simple problems for which an analytical solution is known. The validation of a model is the process in which the predictions of the model are compared with experiments, and the predictive uncertainty is quantified.

One could argue that if the model agrees well with experimental results, this should be seen as proof that the model is correctly implemented. However, invariably there are discrepancies between the model predictions and experimental results. It is then important to determine whether this is due to inaccuracies in the models themselves or to their incorrect implementation . It is also possible that good results can be obtained even after an incorrect implementation of a model. In each case, incorrect conclusions will be drawn concerning the capability of the model. Therefore it is important to consider both verification and validation.

In Paper I, we validated the basic implementation of the LE method in FDS using data from high-pressure water mist experiments. We investigated the capability of FDS to predict the drop size, velocity, droplet flux and number concentration profiles within the spray cone. The effects of turbulence modeling on the predictions of the spray dynamics were assessed. Prediction of air entrainment by high-speed water sprays was validated using experiments in rectangular channels with open ends. In Paper III, the spray boundary condition for aircraft and liquid missile impacts was developed. Predictions of liquid front velocities were compared with experimental results. Predicted spray shapes were visually compared with still images from experiments.

Paper III presented an application of the developed models for risk analysis. As a contribution to the validation work, Paper III compared the predicted lifetimes and diameters of fireballs from two-phase releases.

In Papers IV and V we presented validation of the pool evaporation model. Paper IV considered pools in the open atmosphere and investigated the effects of in-depth heat transfer on temporal development of the burning rate. Paper V focused on pool fires in mechanically ventilated compartments. Paper V also compared the predicted temperatures in the liquid phase of a pool fire with experimental observations.

This thesis summary also reports some additional results, that were not included in Papers I-V. These additional results are the verification tests and results from the turbulent dispersion model described in section 3.2.6.

4.2 Spray modeling

4.2.1 Verification

The verification of the particle tracking solver in FDS involves checking that the two-way coupling between the phases works correctly. The momentum transfer between particles and gas is verified by test cases that consider a 1 m by 1 m by 1 m channel with periodic boundary conditions on the x-faces and FREE_SLIP walls on the y- and z-faces. Static droplets are placed in the center of the channel, so that they form a surface perpendicular to the flow direction. Gravity is set to zero Assuming that the droplets are of uniform diameter and the drag coefficient and gas density are constant, the velocity in the channel decays according to

$$u = \frac{u_0}{1+Bu_0 t};\ B = \frac{1}{2}\frac{\sum C_D \pi r_d^2}{V}. \tag{82}$$

where V is the volume of the channel, r_d is the droplet radius, and u is the gas velocity in the x-direction. The summation is over all N particles. The common parameters used in all the simulations are: C_D = 10, r_d = 0.005 m.

Table 4.1 lists the initial velocities, u_0 and particle numbers. **Figure 4.1** shows comparisons of computed and analytical results, indicating that the current integration scheme accurately predicts the amount of momentum transferred from droplets to the gas phase. The FDS verification suite includes this case (with the name `particle_drag_A-F`). In cases A-C there is one particle per computational cell, while in cases D-F there are ten.

Table 4.1. Parameters for the particle momentum transfer tests.

Case	u_0	N
A	10	16
B	50	16
C	100	16
D	50	1600
E	100	1600
F	150	1600

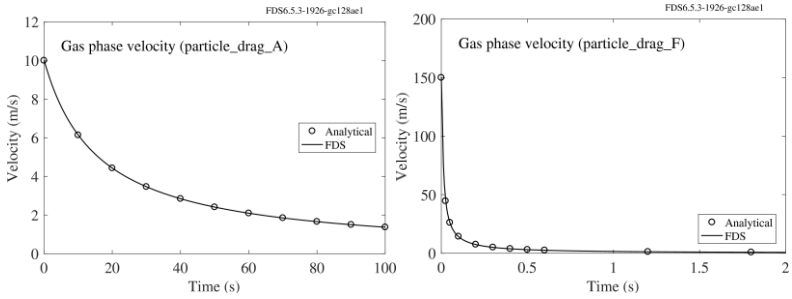

Figure 4.1 Comparison of FDS predictions and analytical solutions in the particle drag test cases A and F.

Another simple verification test is prediction of the particle terminal velocity. The particle reaches its terminal velocity when the drag force and gravitational force exactly match, leading to velocity:

$$V_{term} = \sqrt{\frac{2m_p g}{\rho A_{p,eff} C_D}}. \tag{83}$$

This equation needs to be solved implicitly, since, especially for small droplets, the terminal velocity is low, and the corresponding drag coefficient is non-linearly dependent on the velocity.

Table 4.2 lists errors in terminal velocity predictions for a range of particle sizes. There is a significant error in predicting the terminal velocities of very small droplets. The integration method employed in FDS holds the drag coefficient constant over a time step. When Re<1, as is the case for droplets smaller than 100 μm, drag coefficient varies rapidly as a function of velocity. The terminal velocity of very small droplets is also low. The uncertainty in predicting the gas phase velocity is likely to be an order of magnitude greater than the error in the terminal velocity. This verification case is slightly modified from the particle terminal velocity (`terminal_velocity`) case in FDS verification suite.

Table 4.2 Error in terminal velocity predictions.

d (μm)	Re	V_{term} Eq. (59)	V_{term} FDS	error (%)
1	2.14E-06	3.12E-05	1.99E-03	6288
10	2.02E-03	3.03E-03	1.76E-03	-42
100	1.87E+00	2.80E-01	2.81E-01	<1
1000	2.62E+02	3.92E+00	3.93E+00	<1
10000	1.05E+04	1.57E+01	1.58E+01	<1

4.2.2 Simulation of nozzle characterization experiments

The NFPA 750 nozzle characterization experiments in Paper I were modeled using a rectangular computational area 1.5 m high, 0.5 m wide and 0.5 m deep. The computational area was open on all sides. The nozzles were placed 0.1 m from the top of the computational domain, and the measurements were made 1 meter below the nozzle. The simulation results corresponded to droplet properties averaged over a sphere with 1 cm radius centered at the measurement location.

FDS is a continuously developed code, and the simulation results in Paper I are several years old at the time of writing this thesis. For this reason, the simulations have been rerun with a newer version of the code. There are some small differences in the results, but the conclusions made in Paper I still hold. Here, only results for nozzle B are shown. The results for the other nozzles are similar.

Figure 4.2 shows a grid convergence study for mean drop velocity, droplet flux and mean drop size d_{10}. In Paper I, discretization intervals of 1, 2 and 4 cm were investigated. Here, the simulations were also carried out with a 0.5 cm discretization. The spatial resolution had a strong effect on the simulation results. In Paper I, the difference between 1 and 2 cm discretization intervals was deemed insignificant, but there was a considerable difference between 4cm and 2cm grids. However, **Figure 4.2** shows that results on a 0.5 cm grid differ significantly from those on the 1cm grid. The results on 0.5cm grid are within experimental uncertainty. However, the large difference in results on the two finest grids points to issues with grid convergence. Section 4.2.5 discusses this issue in more detail.

The velocities and fluxes tend to be over-predicted except on the finest grid. In Paper I, this effect was attributed to the turbulence model and especially to the increased turbulent dispersion of particles when using the Dynamic Smagorinsky model.

A distinct feature of the experimental data is the flat diameter profile. Entrainment into the spray tends to produce a V-shaped profile of average diameter. Smaller droplets have shorter response times and are quickly drawn into the center of the jet. The FDS simulations with the default Deardorff model predict the usual V-shaped average diameter profile.

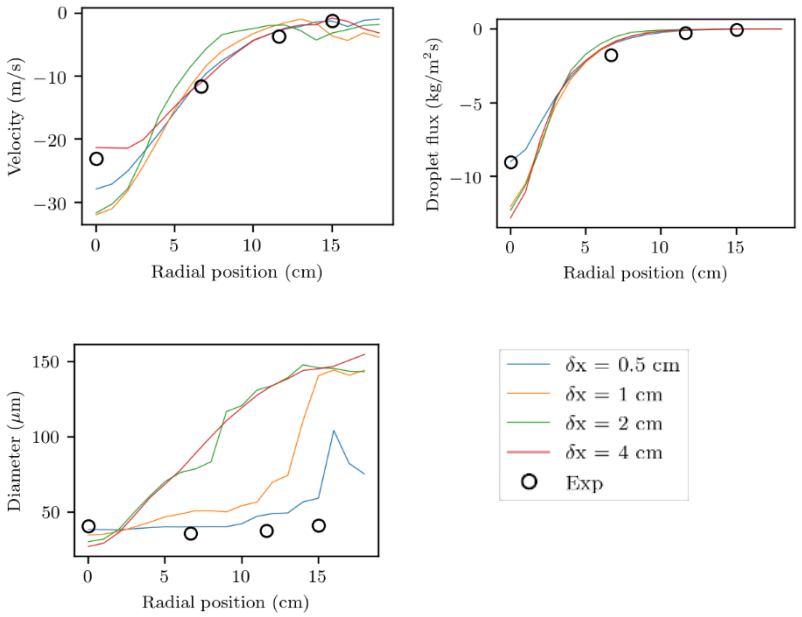

Figure 4.2 Comparison of predicted and experimental velocity, droplet flux and average diameter profiles in the NFPA tests of micro nozzle B from Paper I. Recreated here using FDS version 6.5.3 and the Deardorff turbulence model.

The sensitivity of the results to the initial velocity and the offset parameter was also investigated. Initial velocity could be varied at least 10% without a significant impact on the results. Varying the offset parameter between 5 cm and 15 cm also had a negligible effect.

4.2.2.1 Effect of the drag reduction model

We investigated the effect of the drag reduction caused by three-way coupling on the water spray characteristics by running the nozzle characterization tests with and without the drag reduction model described in Section 3.2.5. The model had a very modest effect on the results. The most noticeable effect was a slight flattening of the droplet diameter profile when the drag reduction model was included. The droplet volume fractions in the densest parts of the spray were just slightly over $\alpha>0.01$ for all nozzles. These results indicate that droplet-droplet aerodynamic interactions are not significant in modeling water mist systems created with the nozzles of this study. The drag reduction model was used in all simulations of Paper I.

4.2.2.2 Effect of the turbulent dispersion model

In Paper I, the dynamic Smagrorinsky model was found to perform better than the default Deardorff model. The better performance of the dynamic Smagrorinsky model was attributed to the increased gas phase mixing with the model. Here this hypothesis is further investigated. The turbulent dispersion model described in Section 3.2.6 was implemented in FDS version 6.5.3.

Figure 4.3 shows the velocity, diameter and mist flux profiles in the NFPA characterization experiments with and without the turbulent dispersion model. The model has only a modest effect on the velocity profiles. The relative velocity between the droplets and the gas quickly relaxes towards the terminal velocity of the droplets. Further away from the nozzle, the jet motion is driven by the gas momentum, and the droplets act as tracers.

The turbulent dispersion model has a greater effect on the droplet flux curves and average diameter profiles. The dynamic Smagorinsky model and the turbulent dispersion model together with the Deardorff model have similar effects. On coarse grids the flux profiles are flattened but, as the grid is refined, the flux profiles converge towards the experimental data. Notably, models produce a flatter diameter distribution compared to the default Deardorff model (See **Figure 4.2**). This provides more evidence that the flat diameter distributions observed for nozzles A, B and C are caused by turbulent mixing of the droplets, with smaller droplets being more easily ejected from the core of the spray

The results presented in this section support the conclusions made in Paper I. The differences between the Deardorff model and the dynamic Smagorinsky model are to a great extent caused by increased turbulent dispersion of droplets when the latter model is used. An advantage of the turbulent dispersion model investigated here is that it is computationally cheaper than the dynamic Smagorinsky model.

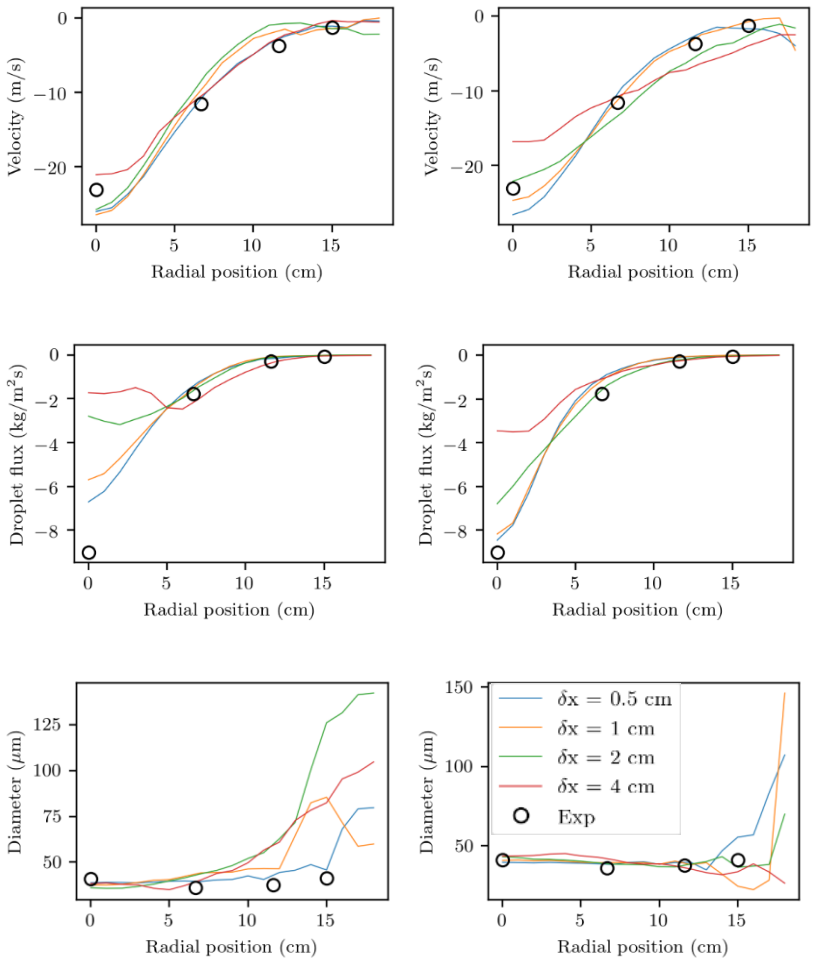

Figure 4.3 Comparison of predicted and experimental velocity, droplet flux and average diameter profiles in the NFPA tests of micro nozzle B from Paper I. On the right, results using the Dynamic Smagorinsky model. On the left, results using the Deardorff model and the turbulent dispersion model described in Section 3.2.6.

4.2.3 Air entrainment

Correct prediction of air entrainment is crucial for predicting the penetration capability of water mist sprays. The air entrainment results indicate the accuracy of simulations in which the capability of the water mist to penetrate to the vicinity of the fire and to mix the gas space is important. Air entrainment into sprays is also important for predicting the dispersion of liquids from liquid jets. Small droplets

behave almost as flow tracers. The air entrained into the spray jet carries the droplets further than they could travel on their own.

The multi-orifice nozzles were modeled by positioning several single orifice models with different orientations at one point in the computational domain. The center nozzle points in the axial direction and the perimeter nozzles are equally spaced and at the same angle in relation to the center nozzle. The smaller the perimeter angle, the more parallel are the orifices in the spray head. Details can be found in Paper I.

Comparisons of the air entrainment simulations to the experimental results are shown in **Figure 4.4**. Figure a) shows the centerline velocities for the single-orifice spray heads. The center line and close-to-the-wall velocities for the multi-orifice spray heads are shown in Figures b and c, respectively.

Of the single-orifice nozzles, the entrainment for nozzle B is predicted within the experimental uncertainty. For nozzle C, the velocities in the channel are overestimated by about 20%, and for nozzle A the velocities are underestimated by a similar amount. For the multi-orifice spray heads, the agreement with the experiment is good on the centerline of the channel. The difference between these spray heads is the amount of x-momentum injected into the simulation.

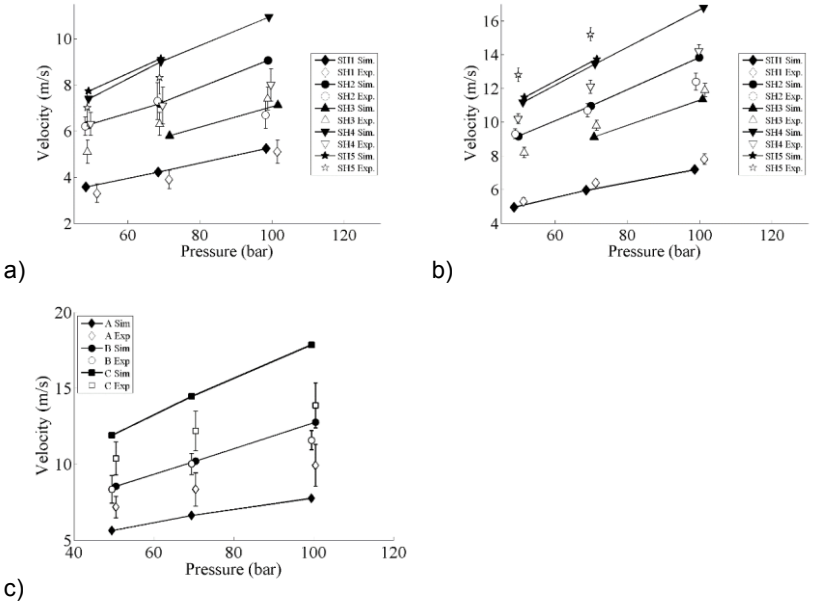

Figure 4.4 Comparison of measured and predicted velocities in the air entrainment tests. Velocity at the channel center for single orifices in a). Center and wall velocity for multi-orifice heads in b) and c). Random noise is introduced to x-values to avoid symbol overlap.

4.2.4 Liquid sprays from missile impacts.

In paper III, the FDS spray model was validated both by quantitative comparisons of the spray front velocity data and qualitative comparisons of spray shapes. Details of the simulation models can be found in Paper III. Details of the experiments and analysis of the experimental results can be found in Paper II.

Figure 4.5 compares the predicted spray front velocities to the velocities determined from experiments. The shaded areas in the graphs correspond to the minimum and maximum velocities at a given time instant, while including experimental uncertainty (+-25 m/s). The circles represent the median velocity from all directions. The predicted velocities were close to the median of the experimentally observed velocities. Near the impact location, the propagation velocity tended to be overestimated. This behavior can be explained by the effect of the missile fragments on the propagation of the jets.

The spray propagation velocity was highest in the directions in which it was unimpeded by shell fragments. The spray boundary condition does not account for projectile fragments; therefore the simulated liquid front propagation velocities were more closely related to the maximum (unimpeded) liquid front velocities. In cases in which the missile deformation had a smaller effect, the predicted liquid front velocities were close to the median velocity.

Further away from the impact location, entrainment into the individual jets caused the jets to spread and merge with nearby jets. This merging smoothed the edge of the spray pattern and consequently decreased the variability in propagation speed between directions. Therefore, the good correspondence between the simulation and the median velocities at later stages indicated that the entrainment in the sprays was correctly predicted.

The results show that the sprays from missile impacts can be simulated using the same methods as are used in simulations of water mist sprays. When the droplet size and initial velocity were correctly prescribed, the spray propagation predictions fell within the range of experimental uncertainty. This was true especially far away from the impact location, where the effects of missile fragments on spray propagation had diminished. Note that the initial velocity estimate was derived from the same experimental data that was used for the validation of the spray front propagation experiments. It is unclear whether this relation holds for other missile impact scenarios.

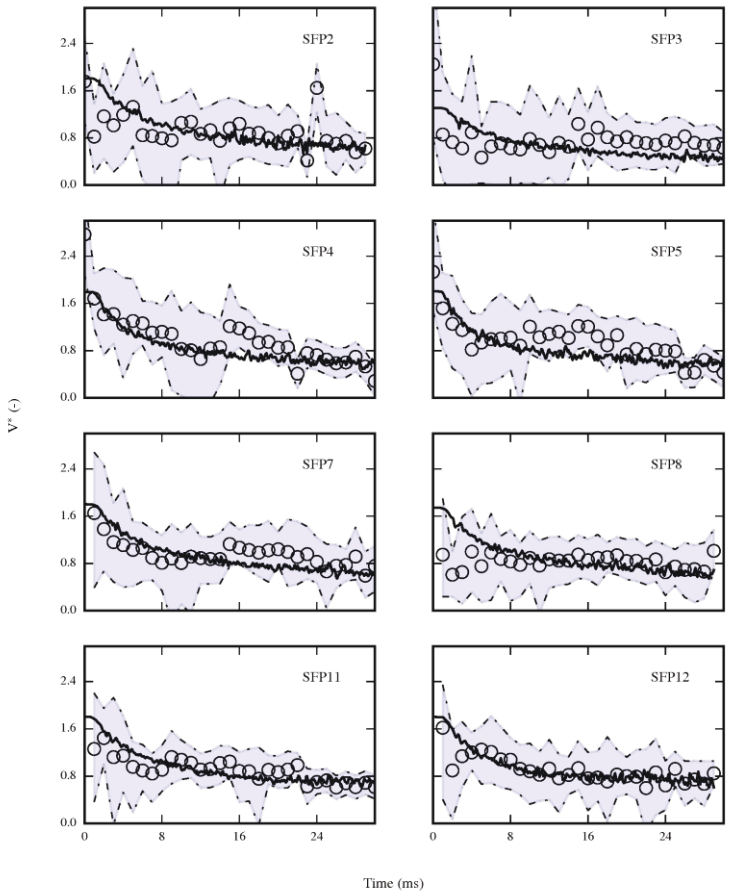

Figure 4.5 Comparison of predicted spray front propagation velocities with experimental observations. The open circles show the median of the experimental data, while the shaded area shows the minimum and maximum of the observed velocities including the experimental uncertainty (+/- 25 m/s).

4.2.5 Grid resolution requirements

Grid resolution is perhaps the most important parameter in a CFD study. In LES, the grid should be fine enough to resolve the so-called “energy-containing eddies”. In LES, the filter width should lie well within the inertial subrange of the kinetic energy spectrum. The existence and location of the inertial subrange are not known a priori. Using arguments based on model spectra of isotropic turbulence, Pope [14,126] showed that if the SGS model corresponds to under 20 % of the total kinetic energy in the simulation, the filter width is well in the inertial subrange of the kinetic energy spectrum. The turbulence resolution can then be monitored by inspecting the ratio of unresolved kinetic energy to the total kinetic energy:

$$M(\boldsymbol{x}) = \frac{K_{SGS}}{K_{RES}+K_{SGS}}, K_{RES} = \frac{1}{2}\left\|\langle\overline{\boldsymbol{u}}(\boldsymbol{x}) - \langle\overline{\boldsymbol{u}}(\boldsymbol{x})\rangle\rangle\right\|^2 \ , \tag{84}$$

where K_{RES} is the resolved portion of the turbulent kinetic energy (TKE), and K_{SGS} is the sgs kinetic energy.

Figure 4.6 shows the measure of turbulence resolution $M(\boldsymbol{x})$ defined by Eq. (84) for the simulations of nozzle B from Paper I. The left graph in **Figure 4.6** shows the turbulence resolution when using the Deardorff model, while the graph on the right shows the same metric when using the dynamic Smagorinsky model. For the dynamic Smagorinsky model, over 60% of the turbulent kinetic energy is resolved on all grid resolutions. With both models, a 1 cm grid is needed for the resolution metric to reach the "Pope criterion" of MTR<0.2.

The results in **Figure 4.6** agree with the prior analysis of Section 4.2.2. On the coarsest grid, the sgs model accounts for almost all of the TKE. Therefore, without the turbulent dispersion model, the droplets do not see the gas phase turbulence, leading to the weaker dispersion of particles from the jet centerline observed with the Deardorff model.

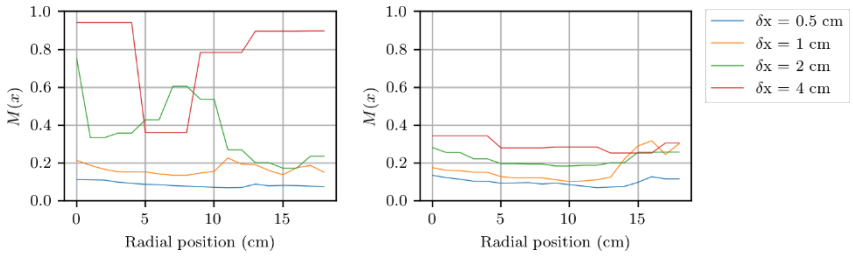

Figure 4.6 Measure of turbulence resolution in the simulations of NFPA tests of micro nozzle B from Paper I. Left: Deardorff model Right: Dynamic Smagorinsky model.

Subramaniam [99] pointed out that, as usually implemented, LE methods are not convergent. Traditional LE methods use a fixed number of particles to describe the spray. When the grid is refined, the number of computational particles per grid cell decreases. As a result of this, the statistical error in estimated source terms in each grid cell increases. This may lead to a counter-intuitive result where the error in predictions increases as the grid is refined. Garg et al. [127] formulated a model for the error in interphase momentum transfer

$$\epsilon = \frac{a}{\sqrt{N_p}} + \frac{b(\delta x)}{N_p} + \frac{c}{\delta x^p}. \tag{85}$$

The terms on the right-hand side represent statistical estimation error, bias error, and discretization error. Equation (85) highlights the dependence of the error in two-way coupling on both the grid size and the number of particles.

The large differences between the 0.5 cm and 1 cm grid shown by **Figure 4.2** may be related to the above described estimation error. In the simulations discussed in section 4.2.2, the number of particles used to describe the spray was held constant for all grid resolutions. This would lead to increased stochastic error in estimating the two-way coupling terms and therefore possibly increasing the resolved turbulence. This increased turbulence in turn would have a reducing effect on the velocities and fluxes similar to the effect of using the dynamic Smagorinsky model.

It was found in Paper I that the grid resolution had a large effect on the simulation results. For multi-orifice spray heads, it is important that each of the individual orifices discharges within a different computational cell. This implies that the offset parameter and grid resolution need to be selected so that there are separate spray jets for each orifice. This is challenging to achieve if the perimeter angle of the spray nozzles is small. Furthermore, the number of Lagrangian particles used to describe the spray needs to be sufficiently high. The greater the number of particles used to describe the spray, the smoother is the predicted droplet density field.

4.3 Liquid pool fire modeling

4.3.1 Verification

A straightforward test for the liquid evaporation model is to see whether, given an imposed heat flux, the correct amount of liquid is evaporated. After the initial heat up phase, it is expected that the liquid will evaporate at a rate equal to $\dot{q}'' = \dot{q}''/(\Delta h_g)$. Here Δh_g is the sensible enthalpy of evaporation, $\Delta h_g = \Delta h_v + \int_{T_0}^{T_b} c_p dT$. To decrease the initial transients involved, the in-depth radiation transfer is ignored.

Figure 4.7 shows the results of the mass conservation test. The model does not exactly conserve mass. This is possibly due to the remeshing procedure used in the condensed phase solver. Apart from the initial transient, the evaporation rate is relatively close to being correct. Note that errors in the prediction of the surface temperature in the simulation will cause the evaporation rate to differ from the theoretical value. Inaccuracy in calculating the mass transfer coefficient partly causes the difference in the evaporation rate. The surface temperature does not reach the boiling point of the liquid and the effective Δh_g value in the simulation will differ from the exact one.

Figure 4.7 also shows the evaporation rate of water in the ASTM flame spread apparatus and a mass conservation test of water evaporating under 50 kW/m^2 heat flux. While not strictly a verification test, it is simple enough to be used for checking the accuracy of the model implementation. The theoretical evaporation rate is within 3 % of the steady portion of the experimentally measured evaporation rate. The peak evaporation rate predicted by the evaporation model coincides with this value.

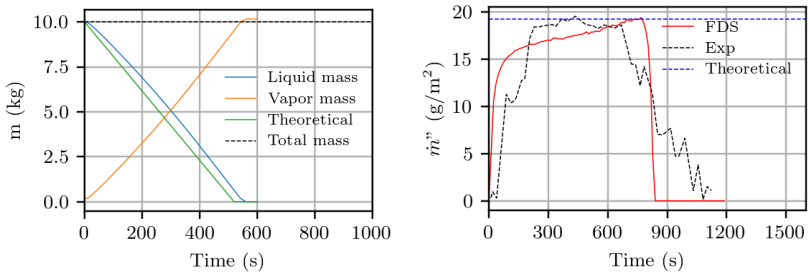

Figure 4.7 Verification of the liquid evaporation model. On the left: Mass conservation test for the evaporation model. On the right: the experimental rate of water vaporization in the ASTM flame propagation device.

4.3.2 Validation of steady state burning rate predictions

In Paper IV and Paper V, the steady state burning rates of pool fires in open atmosphere and compartments were compared with experiments. **Figure 4.8** shows a summary of the results for large pool fires in open atmosphere. In addition to experimental data, **Figure 4.8** compares the predictions with the correlations [43,47]:

$$\dot{m}'' = \frac{\dot{q}''_{in}}{\Delta h_g};\ \dot{q}''_{in} = 12.5 + 68.3\, y_s^{1/4}\left(1 - exp\left[-\left(\frac{4}{3}\Delta h_g D\right)^{3/2}\right]\right). \quad (86)$$

$$\dot{m}'' = 0.001\frac{\Delta \mathrm{h}_c}{\Delta h_g};\ \Delta h_g = \Delta h_v + \int_{T_0}^{T_b} c_p dT \quad (87)$$

The simulation results follow the general trends in burning rates for large pool fires. Except for methanol and butane, the burning rates are over-predicted compared to experimental data. Grid resolution effects at least partly cause the over-prediction. Section 4.3.4 discusses these effects in more detail.

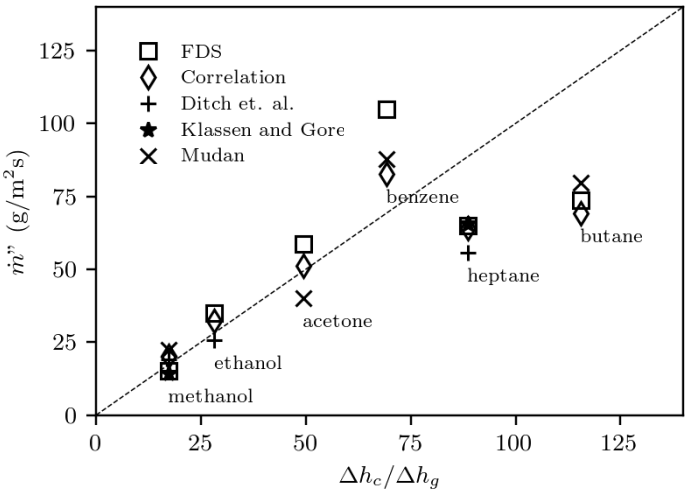

Figure 4.8 Comparison of predicted pool fire burning rates in open atmosphere with correlations and experimental measurements. Experimental data from Mudan [43]**, Klassen and Gore** [128]**, and Ditch et al.** [47]**. The dashed line is Eq.** (87) **and the diamonds correspond to the correlation given by Eq.**(86)**. Figure reproduced from Paper IV.**

Paper V studied the effect of decreased oxygen concentration on the steady state burning rates of TPH pool fires. **Figure 4.9** summarizes the results. The predicted burning rates are averaged over the steady state burning portion. The model predictions tend to be slightly higher than the experimental data. In one case, burning rate oscillations appeared in the simulations. In this case, the averaged burning rate is lower than in the experiments since the averaging is made over the oscillations. **Figure 4.9** also shows the correlation [53]

$$\frac{\dot{m}''}{\dot{m}_0''} = 10X_{O_2} - 1.1, \tag{88}$$

where $\dot{m}_0''$ is the burning rate of the pool fire in open atmosphere, and X_{O_2} is the oxygen volume fraction near the pool base.

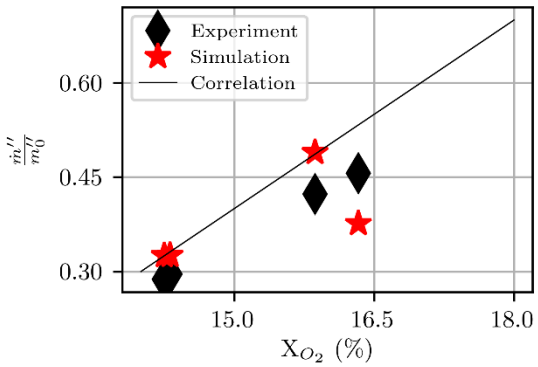

Figure 4.9 Predicted steady state burning rates of TPH pool fires in a mechanically ventilated compartment as a function of oxygen concentration near the flame base.

The appearance of burning rate oscillations in the compartment simulations is an apparent failure of the model. On the other hand, the result indicates that all the physics required to replicate the oscillations observed in other experiments [18] is included in the present FDS.

Overall, the steady state burning rates were predicted with accuracy similar to empirical correlations. Neither the 1-meter pool models nor the TPH pool models considered the effect of convection. This indicates that in-depth transport is likely to be important mostly in the initial heat up phase of the pool fire and possibly near the end. The next section discusses the effects of heat transfer within the liquid.

4.3.3 Effect of liquid side heat transfer

In Paper II, we tested the effects of in-depth absorption of radiation and heat transfer using data for water evaporation and an ethanol pool fire. **Figure 4.10** presents results using two methods for determining the effective absorption coefficient (M1 and M2) and results from ignorining in-depth absorption of radiation (M3). Thermal conductivity was either the molecular value of thermal conductivity or the effective thermal conductivity defined in section 3.3.3. The thermal conductivity values are calculated with the corrected method of determining the effective thermal conductivity.

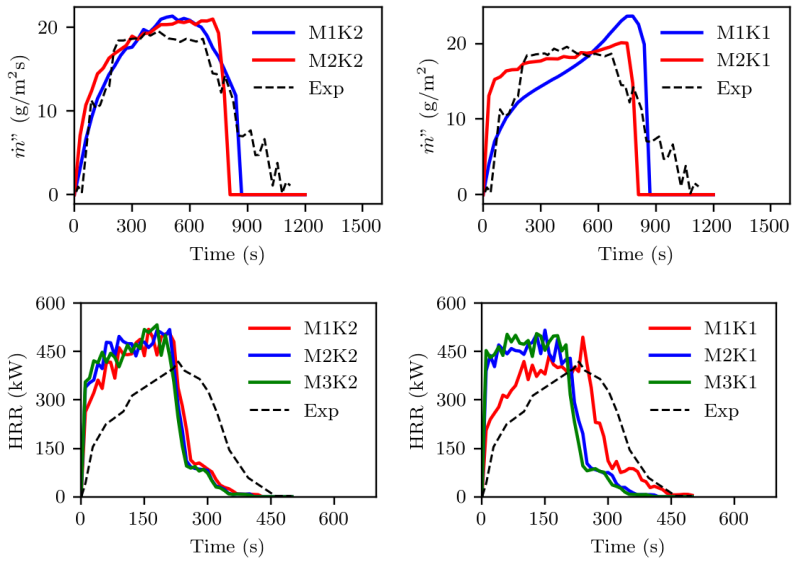

Figure 4.10 Top: Evaporation rate of water in an ASTM E2058 fire propagation apparatus. Bottom: Heat release rate of a large ethanol pool fire case from Victoria University [51]**. Left column: models with modified thermal conductivity. Right column: Models using the molecular thermal conductivity.**

The mean absorption coefficient that produces the more realistic heat source distribution (M2) does not reproduce the gradually increasing heat release rate of the ethanol pool fire. The evaporation rate of water in the fire propagation apparatus is also steady. Method 1 (M1) produces slowly increasing evaporation rates in both cases. This method attempts to model the fraction of radiation passing through the liquid layer correctly. The lower absorption coefficient associated with Method M1 leads to radiation absorption deeper in the liquid.

Ignoring in-depth radiation (M3) absorption gives virtually identical results to method M2. This is likely a result of the relatively high value of absorption coefficient for ethanol. For radiation from ethanol flames, ethanol liquid is optically thick. The results could be different for other liquid fuels and thinner layers.

Liquid phase temperature data were not available for either experiment. **Figure 4.11** shows profiles of liquid temperature in the water evaporation simulations. Liquid temperature is on the y-axis and height from the bottom of the pool on the x-axis. The models that produce gradually increasing burning rates in the ethanol pool fire case (M1K2 and M1K1) produced unphysical temperature distributions in the water evaporation case. The increasing temperature gradient near the liquid surface caused the increasing trend in burning rates seen in Figure 4.10. In a real pool fire, liquid convection could have a similar effect of changing the temperature gradient by transporting heat deeper into the liquid.

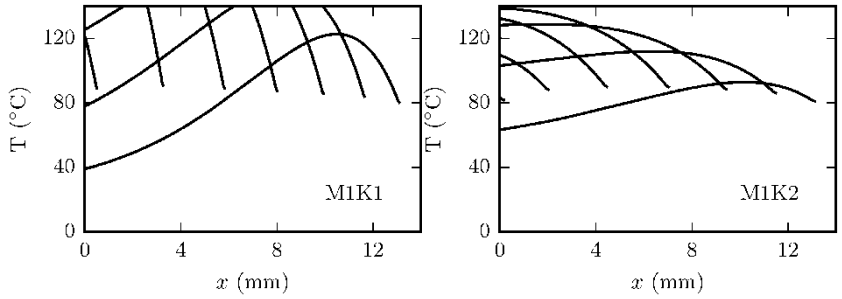

Figure 4.11 Predicted temperature profiles within the liquid in the simulation of water evaporation. Unphysical temperatures in the liquid phase in the water evaporation experiments.

In Paper IV, the predicted temperatures within a TPH pool are compared to the measured temperatures. **Figure 4.12** displays the results from a simulation of a TPH fire in open atmosphere. The absorption coefficient was calculated using method M2 with data for DTE-medium oil because data for TPH was not available. The results show that the presently employed models are not capable of capturing the thermal gradient within the liquid. The heat penetration depth in the liquid is much thicker than is predicted by the model. The inaccuracy in the prediction of heat penetration is at least partly caused by the use of the absorption coefficient for DTE-Medium Oil.

Liquid temperatures in the simulation do not reach the specified boiling temperature. This is due to over-prediction of the mass transfer coefficient. Various stages in the burning rate of the pool fire can be matched with the development of the temperature gradient in the liquid. Up to around 300 seconds, the burning rate increases very gradually, as the surface slowly reaches boiling temperature.

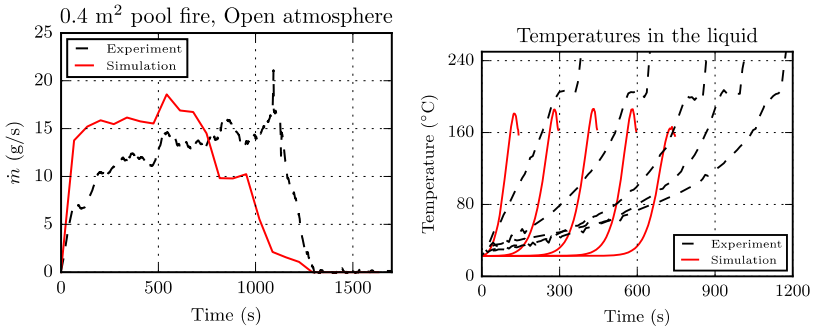

Figure 4.12 Left: Burning rate of a TPH pool fire in open atmosphere. Right: temperatures within the liquid. Experimental data from the PRISME SOURCE S3 experiment.

The peak evaporation rates for the liquid evaporation and pool fire cases are close to the experimental values. The models are not able to reproduce the transient features of the evaporation rate. The simulations and the experimental data show that the transient features are related to the heat transfer within the liquid.

From the results, it seems apparent that the boundary layer resistance to mass transfer may only be significant when the liquid temperature is far from the boiling point. This is the case during the initial stages of pool fire burning and flame spread. Using a more accurate mass transfer model together with the one-dimensional, "transparent solid" - approximation is problematic. If the flame produces a very uneven radiative heat flux to the surface, a one-dimensional model will result in an uneven surface temperature and therefore an uneven burning rate. However, it seems improbable that significant differences in surface temperature could persist in a real pool fire. The uneven burning rate and heat flux would tend to mix the top layer of fuel, producing a uniform surface temperature.

4.3.4 Grid resolution requirements

The grid convergence tests in Paper II showed that for square heptane pool fires in open atmosphere and with 0.5 to 3-meter side length, the predicted burning rate on the coarsest grid was up to 40% higher than on the finest grid. However, full grid convergence could not be achieved in the burning rate prediction simulations.

In order to assess the role of the gas phase modeling in the grid dependence of burning rates, we carried out pool fire simulations with specified fuel mass flux. These cases were identical to the burning rate prediction simulations, except that the evaporation was specified, not predicted. The mass flux was calculated from the correlation [44]:

$$\dot{m}'' = \dot{m}''_{\infty}(1 - \exp(-\kappa\beta D)). \quad (89)$$

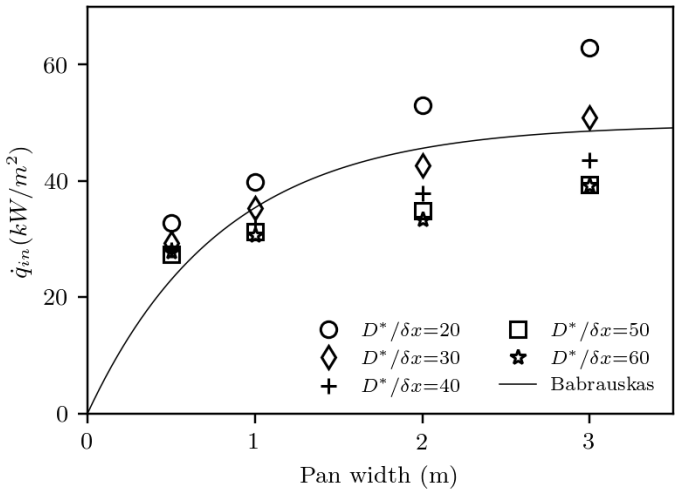

Figure 4.13 Convergence of incident heat flux as a function of grid size for different size burners.

For buoyancy dominated flows, such as flames from a pool fire, the grid resolution between two models can be compared using the Plume Resolution Index (RI) [129]. The RI is defined as

$$RI = \frac{D^*}{\delta x}\ , \tag{90}$$

where δx is the nominal size of a mesh cell, and $D^*$is a characteristic fire diameter

$$D^* = \left[\frac{\dot{Q}}{\rho_\infty c_p T_\infty \sqrt{g}}\right]^{\frac{2}{5}}. \tag{91}$$

Here $\dot{Q}$ is the total heat release rate of the fire. D^* is related to the characteristic fire power Q^* via the relation $\mathrm{Q}^* = (\mathrm{D}^*/\mathrm{D})^{5/2}$, where D is the physical diameter of the fire. D^* can be viewed as a measure of the integral length scale in the flame. The near wall grid resolution can be monitored in terms of y^+.

We measured the average incident heat flux to the burner surface at different grid resolutions and for various burner sizes. **Figure 4.13** shows the results of the grid convergence study. The solid line corresponds to the expected incident heat flux $\dot{q}_{in}{}'' = \dot{m}''/\Delta h_g$. Incident heat flux predictions converge around $D^*/\delta x = 50$ for larger pool fires and at about $D^*/\delta x = 40$ for smaller pool fires. This is in line with experimental findings, in which the ratio of integral length scale to the pool size is found to get smaller as the pool size increases.

Grid convergence results in Paper IV showed that in compartment fire scenarios the burning rate predictions are less sensitive to the grid resolution. Since only a limited number of experiments with a single fuel were considered, no general conclusions can be made from this observation. However, the results from Paper II

and Paper IV suggest that the primary source of grid sensitivity of the burning rate predictions lies in predicting the radiative heat flux to the surface.

4.4 Risk analysis

4.4.1 Motivation

The stated goal of this thesis is to produce models for simulation of large scale incidents. Paper III presents an application of the methods developed in this thesis. The application part of Paper III studied the physical extent of the flames and smoke generated by the combustion of jet fuel from the impact of a commercial aircraft on an NPP reactor building. The goal was to investigate how far from the impact point the flames can reach to cause a possible threat to the components of the plant. In addition to the assessment of physical separation, the amount of fuel that does not burn in the initial fireball was recorded.

We conducted the risk analysis in two parts. The first part examined the effects of mean droplet size and impact height on the amount of accumulated fuel. After this, simulations of aircraft impact on a full-scale model of a nuclear island were conducted.

4.4.2 Validation of predicted fireball lifetimes and diameters

The threat posed by a fireball is proportional to its size, shape and lifetime. Therefore, for risk analysis purposes it is important that these aspects can be accurately predicted. Paper IV compared the predicted fireball lifetimes and diameters with empirical correlations. The relevant length and time scales of fireballs, based on dimensional analysis, are given by [77]:

$$L_* = \left(\frac{\mathrm{M}\Delta h_c}{\rho_\infty c_p T_\infty}\right)^{\frac{1}{3}},\ U_* = \sqrt{L_* g} \text{ and } t_* = \sqrt{L_*/g}. \tag{92}$$

Here M is the fuel mass and Δh_c is the heat of combustion. Roper et. al. determined an experimental correlation for fireball lifetimes resulting from vertical fuel releases [79]. The correlation, stated in terms of the fireball length and timescales in Eq. (92) , is:

$$\frac{t_*}{t_{FB}} = 0.22 + 0.01 Fr^{\frac{1}{2}};\ Fr = \left(\frac{U_0}{U_*}\right)^2. \tag{93}$$

Numerical simulations were performed in a domain of $4L_* \times 4L_* \times 8L$, and fuel was inserted in the time interval $t_{in} = [0{,}0.1t_{FB}]$. The domain was discretized with $220 \times 220 \times 550$ cells. The droplet size distribution was based on liquid missile impact experiments. However, very large droplets were observed to rain out of the fireball before they evaporate. Therefore the width parameter was increased to decrease the number of very large droplets. The fuel insertion was modeled as a

vertical fuel spray with a spray angle of 15º. Nine simulations were performed with fuel masses of 10, 1000, or 10,000 kg and initial velocities of 50, 200, or 300 m/s.

We defined the end of the fireball lifetime as the time at which 95 % of the fuel is burned. The start of the fireball lifetime was taken as $0.5t_{in}$. This definition of the start of the fireball lifetime was also used by Roper et. al. They defined the end of the fireball lifetime as the time when flames were no longer visible.

Figure 4.14 compares the simulation results with Eq. (92). Overall, the simulated results showed good agreement with the correlation. The predicted fireball lifetimes were within 15% of the values predicted by Eq. (92). Despite the low-Mach number limitation of FDS, there were no significant deviations from the general trend, even for cases in which the droplets were inserted at 300 m/s.

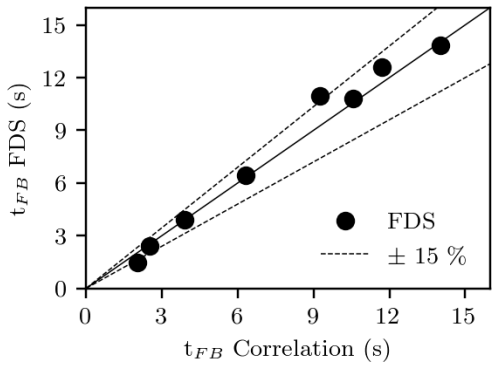

Figure 4.14 Comparison of predicted Fireball lifetimes with correlation.

Figure 4.15 shows the contours of the gas temperature at the midplane of a fireball. The contours are shown at time instants t_{FB} = 0.3, 0.6, and 0.9 and for an initial velocity V_0 = 200 m/s. The top of **Figure 4.15** shows the results for the case with M = 10,000 kg, and the bottom shows the results for the case with M = 10 kg. At the early stages of the fireball development, the hot gas cloud was still shaped like a jet. At about halfway through its lifetime, the fuel jet decelerated, and its movement was now controlled by buoyancy. In the final stages, the cloud rolled up in a vortex, reaching its final size. The vortex roll up started earlier for the M = 10,000 kg case owing to the lower Froude number. If the 1000 ºC contour is taken as the fireball edge, the maximum fireball diameter can be visually approximated from **Figure 4.15** to be $\sim 1.2L_*$. This falls within the range given by correlations for fireball diameter.

The threat posed by a fireball is related to the dose of thermal radiation absorbed by the target under investigation. The thermal radiation dose is determined by the duration and diameter of the fireball. The results from Paper III, summarized in this

section, show that FDS can predict these parameters within 20 % of experimental correlations.

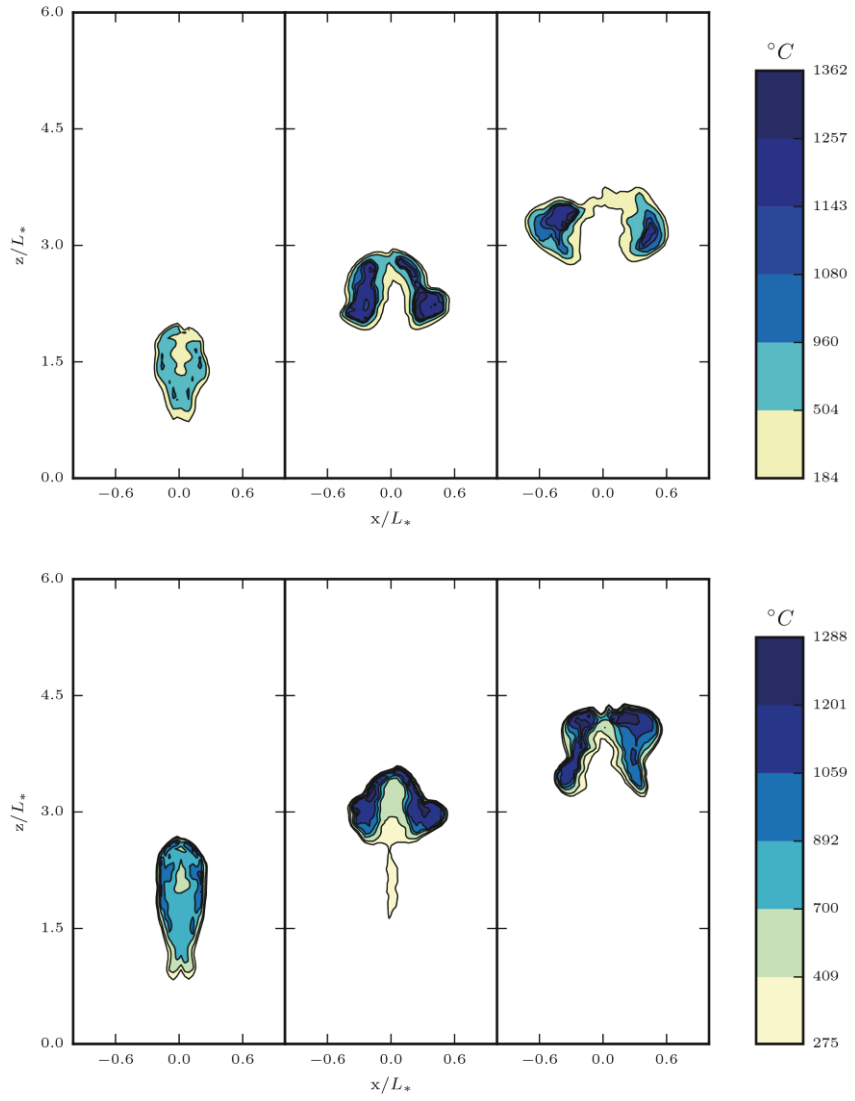

Figure 4.15 Instantaneous temperature contours for fireballs with U_{ini} = 200 m/s at time instants t/t_{FB} = 0.3,0.6,0.9. Top: M = 10,000 kg. Bottom: M = 10 kg

4.4.3 The effect of impact height and droplet size on pooling fraction

An important aspect of the fires resulting from an aircraft impact is the fraction of the fuel that does not burn in the initial fireball. We call this quantity “the pooling fraction”. The specific amount of remaining fuel depends on both the droplet size and impact height. The closer the impact location is to the ground, the larger the pooling fraction. Because smaller droplets evaporate faster than larger droplets, a lower average droplet diameter results in smaller pooling fractions. Paper III presents a sensitivity study considering the relationship between impact height and pooling fraction.

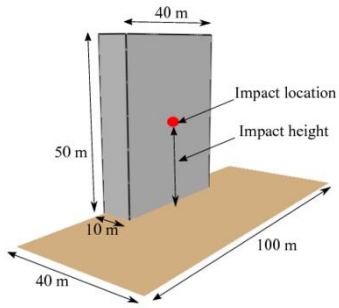

Figure 4.16 Simulation domain used for the pooling fraction sensitivity analysis.

Some numerical experiments were carried out to quantify the effect of impact height and droplet size on the pooling fraction. The simulation domain consisted of a rectangular building 40 meters wide and 50 meters high. The impact location on the building was varied. **Figure 4.17** illustrates the simulation model and impact locations. 10 000 kg of fuel was released in 0.1 seconds. Grid resolution was 1.0 meter.

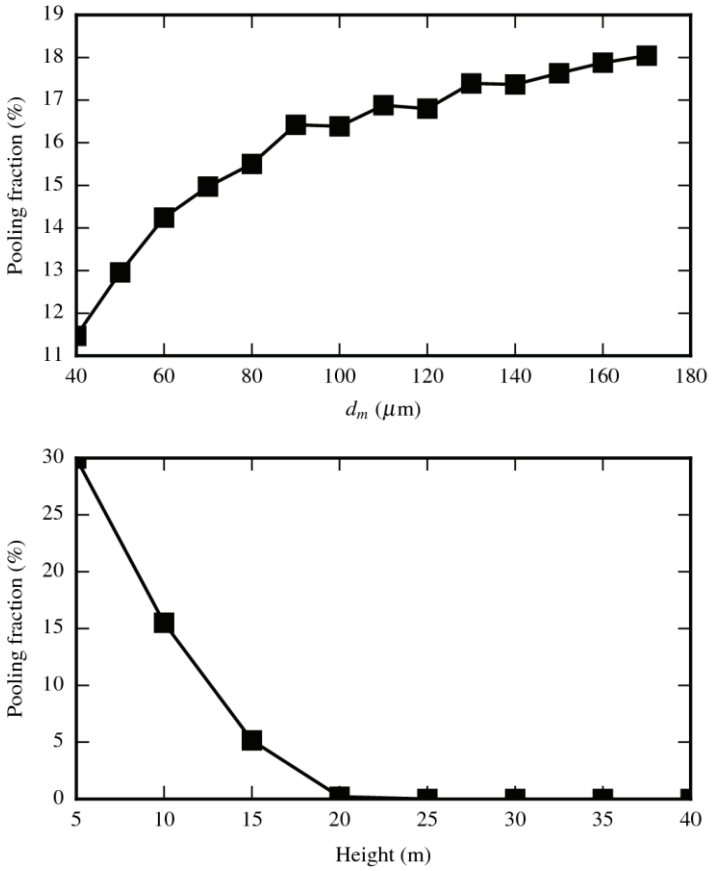

Figure 4.17 Sensitivity of pooling fraction to droplet size and to impact height.

The bottom graph in **Figure 4.17** shows the pooling fraction as a function of the impact height for the droplet distribution with $d_m = 80\,\mu m$. As the impact location moves closer to the ground, the fraction of fuel left unburnt increases significantly. At a height of 5 m, the pooling fraction is almost 30%. For impact heights above 20 m, the pooling fraction is practically zero.

The median volumetric diameter has a more modest effect (see the top graph in **Figure 4.17**). For an impact height of 10 m, the pooling fraction varies between 11 % and 18 % for median diameters in the range of 40 μm to 180 μm. The growth of the pooling fraction tapers off at just below 20%.

Two conclusions can be made from these results. The first is that with realistic droplet size distributions a significant fraction of the fuel ejected from a plane may accumulate in pools. The second conclusion is that the pooling fraction is more sensitive to the geometry surrounding the impact location than to the droplet size.

When the impact location is closer to the ground, the liquid jets do not have time to evaporate before impact.

4.4.4 Simulation of a plane impact on a nuclear island

The simulation model of the NPP included the reactor building (cylindrical shape with a diameter of 56 m), four auxiliary buildings attached to the reactor building, part of the diesel building, and part of the turbine hall (details of the model can be found in Paper III).

The impact scenario was the horizontal impact of a commercial aircraft, carrying 10 tons of fuel, at a speed of 125 m/s in the direction normal to the reactor building wall. The impact height was 35 m from the ground and approximately 10 m from the roof of the auxiliary building. Five different impact positions were considered, and the effect of wind was investigated by assuming either 10m/s wind speed or no wind (See **Figure 4.18**). Eight possible wind directions were considered.

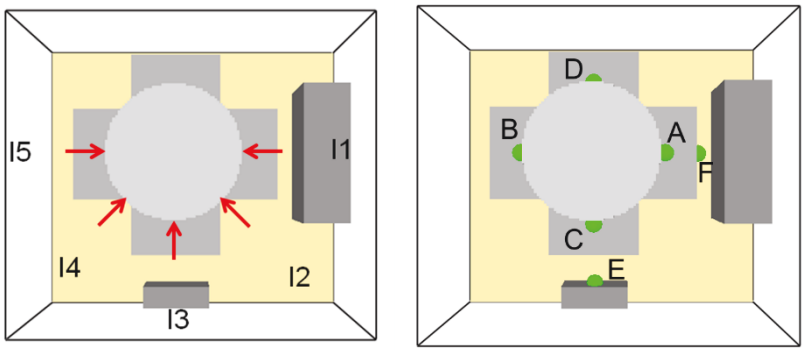

Figure 4.18 Impact locations and monitoring points used in the simulation of plane impact on a nuclear island.

Gas temperature, gas velocity, and fuel gas volume fraction were monitored at six locations denoted A-F. The maximum observed value of each monitored quantity over the entire simulation was recorded for each measurement location. This observed value was then used to indicate whether the conditions at the measurement point can be considered hazardous. **Figure 4.18** shows an overview of the simulation model and the monitoring locations.

In the analysis of the simulations, we treated the impact location and wind direction and measurement location as random variables. This allowed us to derive probability density functions for seeing threatening conditions in a randomly selected spot on the main building. The placement of the monitoring locations A--D around the dome also allowed us to determine the sufficiency of physical separation.

The simulation results showed that direct contact with the flame was limited to a region of the building complex that covered less than half of the reactor building perimeter. Flames lasting longer than about one second were observed in a sector that reached 45º - 90º in both directions from the direction of the incoming aircraft.

The probability of any individual target at the height of the roofs of the auxiliary buildings and close to the reactor building becoming engulfed by flames was between 25% and 50%. For objects placed at two opposite sides of the reactor building, physical separation was realized. **Figure 4.19** illustrates the conclusions drawn from the simulations.

In addition to the gas phase quantities, we also investigated the amount of fuel deposited on the reactor building. In the majority of the simulations, the amount of accumulated fuel was between10 and 30% of the total amount. In 40% of the simulated scenarios, the amount of fuel burning on the surfaces was more than 20%. The fuel accumulated on the roof near the impact location and also on the reactor dome.

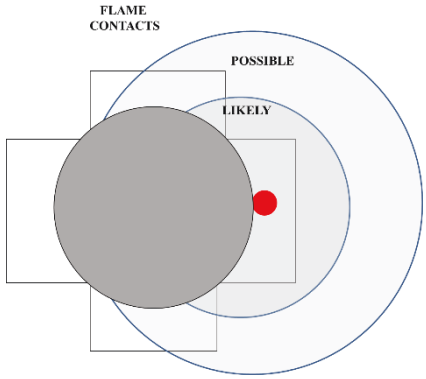

Figure 4.19 Possible and likely regions of aircraft impact flame contact around the NPP reactor building in the case of a horizontal impact at a height of 35 m and releasing 10 t of fuel.

5. Conclusions

Papers I-V present modeling and validation of three fire-related phenomena: liquid transport in a spray, rapid spray combustion, and liquid pool burning. Paper I deals with water sprays formed by high-pressure water mist nozzles. Papers II and III discuss liquid sprays from missile impacts. Despite the apparent differences in the formation mechanisms of the sprays, the droplet sizes and speeds were relatively similar. Both types of sprays can be simulated using the LE method, when the spray boundary condition is correctly defined.

The correct prediction of air entrainment into liquid sprays is crucial for successful predictions of spray penetration and dispersion. The correct amount of air entrainment is predicted if the spray boundary condition is defined appropriately.

Firstly, the droplets need to have the correct initial velocity. In this work, the initial velocity of the droplets accounted for all of the momentum of the injected liquid. This ensures that the correct amount of momentum is inserted. Modifying initial velocity of the gas phase at the spray boundary condition was not necessary.

Secondly, the droplet size distribution can be selected to represent a stable size distribution further away from the nozzle. In fact, any other choice would necessitate the use of secondary breakup models.

In Paper III, we applied the developed models to simulations of airplane impact on a nuclear island. Based on the results of these simulations we made the following conclusions:

1. The simulated fireballs resulted in locally high temperatures and velocities but only for a short duration. Physical separation was realized for targets situated on opposite sides of the building.
2. Droplet size and the geometry surrounding the impact location have a significant effect on the pooling fraction. Lower impact location and larger average droplet size lead to larger pooling fractions.
3. Up to 20 % of the fuel involved in the crash accumulated on the surfaces of the target building. The subsequent burning of this fuel may then be a significant hazard to the safety of the NPP and should not be ignored. The pool fire models developed in this thesis could be directly applied to predict the consequences of the resulting pool fires.

Papers IV and V showed that the steady state burning rates in compartments and open atmosphere could be predicted with accuracy similar to empirical correlations.

The grid resolution requirements for accurate burning rate predictions of open pool fires are very demanding. Accurate steady state burning rates could be predicted in compartment fire scenarios on relatively coarse grids. Together, these results suggest that the key to easing the grid resolution requirements lies in the modeling of the radiation transport.

Paper IV showed that the in-depth heat transfer, in the form of the in-depth radiation absorption and enhanced heat transfer in the liquid due to convective motions, might be important in predicting the detailed dynamics of the fire. However,

the models employed are not capable of accounting for all the phenomena in the liquid.

The gray gas approximation of the radiation transport cannot correctly predict the transport of radiation through the liquids. This prediction could be improved by resolving the wavelength dependence of absorption and re-radiation. In the current model, heat transfer is one dimensional. In real liquids, the heat transfer by convection in the lateral direction could play a significant role. Better models for the internal heat transfer may be needed to capture the dynamics of pool fires correctly. A better evaporation model may also be needed in conjunction with the improved heat transfer models.

6. Future work

The results presented in this thesis support the conviction of previous researchers that radiation modeling is the key factor in predicting burning rates in CFD simulations. One avenue that should be explored is spectrally resolved solutions of the radiative transfer equations. This would be required for prediction of both the heat feedback to the fuel surface and the radiation heat transfer within the liquid. For a liquid layer a few millimeters thick, a significant portion of the incident radiation will pass through the layer. In such cases, the modeling of in-depth radiation transport and heat transfer to the substrate is likely to be the key in predicting the burning rate.

The mass transfer resistance to evaporation is relatively unimportant for predicting the steady state burning rates of deep pools, but could have a significant effect in cases in which it is attempted to predict the formation of flammable clouds from liquid spills. A better model based on e.g. wall functions could help in this respect. Better experimental data is needed for liquid evaporation from surfaces under relevant conditions.

There are still several open questions concerning the heat transfer mechanisms in pool fires. It would be interesting to see the results of studies in which full 3D predictions of heat transfer through the pan and within the liquid were coupled with gas phase solution. Such simulations could offer insight into the mechanisms of lip height effects and radiation absorption within the fuel.

The characterization of the initial spray is still an open research question. Highly resolved measurements near the spray inlet would be required to validate the Gaussian profile assumption made in section 3.2.3.

The grid resolution requirements of predictive pool fires and spray simulations are still prohibitive for everyday engineering use. The effect of the subgrid scales on particle motion is likely to be important, considering the coarse resolutions used in engineering calculations of suppression systems. Turbulent dispersion models such as the one discussed in this work could be pursued.

The number of computational droplets used to describe the spray may also be a limiting factor in engineering applications. Droplet density control algorithms could be explored to alleviate these problems.

References

[1] NS-G-1.5, External Events Excluding Earthquakes in the Design of Nuclear Power Plants, International Atomic Energy Agency, Vienna, 2003

[2] NEI 07-13, Methodology for Performing Aircraft Impact Assessments for New Plant Designs. Revision 8p, Nuclear Energy Institute,Washington,DC, 2011.

[3] T. Abbasi, S.A. Abbasi, The boiling liquid expanding vapour explosion (BLEVE): mechanism, consequence assessment, management., J. Hazard. Mater. 141 (2007) 489–519. doi:10.1016/j.jhazmat.2006.09.056.

[4] H.R. Baum, R.G. Rehm, A simple model of the World Trade Center fireball dynamics, Proc. Combust. Inst. 30 (2005) 2247–2254. doi:10.1016/j.proci.2004.08.125.

[5] C. Crowe, J. Schwarzkopf, M. Sommerfeld, Y. Tsuji, Multiphase Flows with Droplets and Particles, 2nd ed. CRC Press, 2012.

[6] E.E. Michaelides, Particles, bubbles & drops: their motion, heat and mass transfer, World Scientific, New Jersey, 2006.

[7] W.A. Sirignano, Fluid Dynamics and Transport of Droplets and Sprays, 2nd ed., Cambridge University Press, New York, 2010.

[8] E., Loth, Numerical approaches for motion of dispersed particles, droplets and bubbles, Prog. Energy Combust. Sci. 26 (2000) 161–223. doi:10.1016/S0360-1285(99)00013-1.

[9] F. Mashayek, R.V.R. Pandya, Analytical description of particle/droplet-laden turbulent flows, Prog. Energy Combust. Sci. 29 (2003) 329–378. doi:10.1016/S0360-1285(03)00029-7.

[10] E.E. Michaelides, Hydrodynamic Force and Heat/Mass Transfer From Particles, Bubbles, and Drops—The Freeman Scholar Lecture, J. Fluids Eng. 125 (2003) 209. doi:10.1115/1.1537258.

[11] M.M.R. Maxey, J. Riley, Equation of motion for a small rigid sphere in a nonuniform flow, Phys. Fluids. 26 (1983) 883–889. doi:10.1063/1.864230.

[12] V. Armenio, V. Fiorotto, The importance of the forces acting on particles in turbulent flows, Phys. Fluids. 13 (2001) 2437–2440. doi:10.1063/1.1385 390.

[13] R.B. Bird, W.E. Stewart, E.N. Lightfoot, Transport Phenomena, Wiley, New

York, 1960.

[14] S.B. Pope, Turbulent Flows, Cambridge University Press, Cambridge, UK, 2000.

[15] F. White, Viscous Fluid Flow, 3rd ed., McGraw-Hill, Singapore, 2006.

[16] G. Desoutter, C. Habchi, B. Cuenot, T. Poinsot, DNS and modeling of the turbulent boundary layer over an evaporating liquid film, Int. J. Heat Mass Transf. 52 (2009) 6028–6041. doi:10.1016/j.ijheatmasstransfer.2009.06.039.

[17] A.Y. Snegirev, Statistical modeling of thermal radiation transfer in buoyant turbulent diffusion flames, Combust. Flame. 136 (2004) 51–71. doi:10.1016/j.combustflame.2003.09.005.

[18] H. Pretrel, S. Suard, L. Audouin, Experimental and numerical study of low frequency oscillatory behaviour of a large-scale hydrocarbon pool fire in a mechanically ventilated compartment, Fire Saf. J. 83 (2016) 38–53. doi:10.1016/j.firesaf.2016.04.001.

[19] M. Gorokhovski, M. Herrmann, Modeling Primary Atomization, Annu. Rev. Fluid Mech. 40 (2008) 343–366. doi:10.1146/annurev.fluid.40.111406.102200.

[20] D.R. Guildenbecher, C. López-Rivera, P.E. Sojka, Secondary atomization, Exp. Fluids. 46 (2009) 371–402. doi:10.1007/s00348-008-0593-2.

[21] G. Faeth, L.P. Hsiang, P.K. Wu, Structure and breakup properties of sprays, Int. J. Multiph. Flow. 21 (1995) 99–127. doi:10.1016/0301-9322(95)00059-7.

[22] C. Dumouchel, On the experimental investigation on primary atomization of liquid streams, Exp. Fluids. 45 (2008) 371–422. doi:10.1007/s00348-008-0526-0.

[23] J. Pozorski, S.V. Apte, Filtered particle tracking in isotropic turbulence and stochastic modeling, Int. J. Multiph. Flow. 35 (2009) 118–128. doi:10.1016/j.ijmultiphaseflow.2008.10.005.

[24] M. Bini, W.P. Jones, Large Eddy Simulation of an evaporating acetone spray, Int. J. Heat Fluid Flow. 30 (2009) 471–480. doi:10.1016/j.ijheatfluidflow.2009.03.005.

[25] W.P. Jones, S. Lyra, A.J. Marquis, Large Eddy Simulation of evaporating kerosene and acetone sprays, Int. J. Heat Mass Transf. 53 (2010) 2491–2505. doi:10.1016/j.ijheatmasstransfer.2010.01.028.

[26] A. Irannejad, F. Jaberi, Large eddy simulation of turbulent spray breakup and evaporation, Int. J. Multiph. Flow. 61 (2014) 108–128. doi:10.1016/j.ijmultiphaseflow.2014.01.004.

[27] NFPA 750, Standard on Water Mist Fire Protection Systems, Natl. Fire Prot. Assoc., 2015.

[28] E.D. Link, S.J. Jordan, T.M. Myers, P.B. Sunderland, A.W. Marshall, Spray dispersion measurements of a sprinkler array, Proc. Combust. Inst. 36 (2017) 3305–3311. doi:10.1016/j.proci.2016.06.056.

[29] T.M. Myers, A.W. Marshall, A description of the initial fire sprinkler spray, Fire Saf. J. 84 (2016) 1–7. doi:10.1016/j.firesaf.2016.05.004.

[30] P.E. Santangelo, Experiments and modeling of discharge characteristics in water-mist sprays generated by pressure-swirl atomizers, J. Therm. Sci. 21 (2012) 539–548. doi:10.1007/s11630-012-0579-5.

[31] P.E. Santangelo, Characterization of high-pressure water-mist sprays: Experimental analysis of droplet size and dispersion, Exp. Therm. Fluid Sci. 34 (2010) 1353–1366. doi:10.1016/j.expthermflusci.2010.06.008.

[32] X. Huang, X.S. Wang, G.X. Liao, Characterization of an effervescent atomization water mist nozzle and its fire suppression tests, Proc. Combust. Inst. 33 (2011) 2573–2579. doi:10.1016/j.proci.2010.06.001.

[33] B.P. Husted, P. Petersson, I. Lund, G. Holmstedt, Comparison of PIV and PDA droplet velocity measurement techniques on two high-pressure water mist nozzles, Fire Saf. J. 44 (2009) 1030–1045. doi:10.1016/j.firesaf.2009.07.003.

[34] D. Sheppard, J.F. Widmann, R.M. Lueptow, Non-Intrusive Measurements in Fire Sprinkler Sprays Using Phase Doppler Interferometry and Particle Image Velocimetry, in: Proc. Fire Suppr. Detect. Res. Appl. Symp., The Fire Protection Research Foundation, Quincy, Massachusetts, 2001.

[35] S.R. Tieszen, Post-crash fuel dispersal, in: Work. Aviat. Fuels with Improv. Fire Saf., Washington, DC, 1997: p. 107.

[36] W.A. Von Riesemann, R.L. Parrish, D.C. Bickel, S.R. Heffelfinger, K. Muto, T. Sugano, H. Tsubota, N. Koshika, M. Suzuki, S. Ohrui, Full scale aircraft impact test for evaluation of impact forces-Part 1, (1989).

[37] K. Muto, T. Sugano, H. Tsubota, N. Koshika, M. Suzuki, S. Ohrui, W.A. von Riesemann, D.C. Bickel, R.L. Parrish, R.D.M. Tachau, Full-scale aircraft impact test for evaluatioin of impact force: Part 2: Analysis of results, (1989).

[38] T. Sugano, H. Tsubota, Y. Kasai, N. Koshika, C. Itoh, K. Shirai, W.A.A. von Riesemann, D.C.C. Bickel, M.B.B. Parks, Local damage to reinforced concrete structures caused by impact of aircraft engine missiles Part 2. Evaluation of test results, Nucl. Eng. Des. 140 (1993) 407–423. doi:10.1016/0029-5493(93)90121-O.

[39] A. Silde, S. Hostikka, A. Kankkunen, Experimental and numerical studies of liquid dispersal from a soft projectile impacting a wall, Nucl. Eng. Des. 241 (2011) 617–624. doi:10.1016/j.nucengdes.2010.07.033.

[40] A.L. Brown, Impact and Fire Modeling Considerations Employing SPH Coupling to a Dilute Spray Fire Code, in: ASME 2009 Summer Heat Transf. Conf., ASME, San Francisco, 2009, 161–171. doi:10.1115/HT2009-88493.

[41] A.L. Brown, K.E. Metzinger, G.J. Wagner, Predictions of Transport Accident Fires Using Coupled Structural Dynamics and Computational Fluid Dynamics, Fire Saf. Sci. 11 (2014) 584–597.

[42] R.A. Jepsen, T. O'Hern, B. Demosthenous, E. Bystrom, M. Nissen, E. Romero, S.S. Yoon, Diagnostics for liquid dispersion due to a high-speed impact with accident or vulnerability assessment application, Meas. Sci. Technol. 20 (2009) 25401. doi:10.1088/0957-0233/20/2/025401.

[43] K.S. Mudan, Thermal radiation hazards from hydrocarbon pool fires, Prog. Energy Combust. Sci. 10 (1984) 59–80. doi:http://dx.doi.org/10.1016/0360-1285(84)90119-9.

[44] V. Babrauskas, Estimating large pool fire burning rates, Fire Technol. 19 (1983) 251–261. doi:10.1007/BF02380810.

[45] T. Steinhaus, S. Welch, R.O. Carvel, J.L. Torero, Large-scale pool fires, Therm. Sci. 11 (2007) 101–118.

[46] P. Joulain, The behavior of pool fires: State of the art and new insights, Symp. Combust. 27 (1998) 2691–2706. doi:http://dx.doi.org/10.1016/S0082-0784(98)80125-2.

[47] B.D. Ditch, J.L. de Ris, T.K. Blanchat, M. Chaos, R.G.B. Jr., S.B. Dorofeev, Pool fires – An empirical correlation, Combust. Flame. 160 (2013) 2964–2974. doi:http://dx.doi.org/10.1016/j.combustflame.2013.06.020.

[48] K. Prasad, C. Li, K. Kailasanath, C. Ndubizu, R. Ananth, P.A. Tatem, Numerical modelling of methanol liquid pool fires, Combust. Theory Model. 3 (1999) 743–768. doi:10.1088/1364-7830/3/4/308.

[49] V. Novozhilov, H. Koseki, CFD prediction of pool fire burning rates and

flame feedback, Combust. Sci. Technol. 176 (2004) 1283–1307. doi:10.1080/00102200490457484.

[50] S. Hostikka, K.B. McGrattan, A. Hamins, Numerical Modeling of Pool Fires using Large Eddy Simulation and Finite Volume Method for Radiation, in: Fire Saf. Sci. -- Proc. Seventh Int. Symp., International Association for Fire Safety Science, 2002, 383–394.

[51] I.R. Thomas, K. a. M. Moinuddin, I.D. Bennetts, The Effect of Fuel Quantity and Location on Small Enclosure Fires, J. Fire Prot. Eng. 17 (2007) 85–102. doi:10.1177/1042391506064908.

[52] S. Ebrahim Zadeh, T. Beji, B. Merci, Assessement of FDS 6 Simulation Results for a Large-Scale Ethanol Pool Fire, Combust. Sci. Technol. 188 (2016) 571–580. doi:10.1080/00102202.2016.1139367.

[53] M.J. Peatross, C.L. Beyler, Ventilation Effects On Compartment Fire Characterization, Fire Saf. Sci. 5 (1997) 403–414.

[54] J.G. Quintiere, Fire behavior in building compartments, Proc. Combust. Inst. 29 (2002) 181–193. doi:10.1016/S1540-7489(02)80027-X.

[55] S. Suard, M. Forestier, S. Vaux, Toward predictive simulations of pool fires in mechanically ventilated compartments, Fire Saf. J. 61 (2013) 54–64. doi:10.1016/j.firesaf.2013.08.010.

[56] J. Wahlqvist, P. van Hees, Implementation and validation of an environmental feedback pool fire model based on oxygen depletion and radiative feedback in FDS, Fire Saf. J. 85 (2016) 35–49. doi:10.1016/j.firesaf.2016.08.003.

[57] Y. Utiskul, J.G. Quintiere, A.S. Rangwala, B.A. Ringwelski, K. Wakatsuki, T. Naruse, Compartment fire phenomena under limited ventilation, Fire Saf. J. 40 (2005) 367–390. doi:10.1016/j.firesaf.2005.02.002.

[58] T. Beji, B. Merci, Blind Simulation of Periodic Pressure and Burning Rate Instabilities in the Event of a Pool Fire in a Confined and Mechanically Ventilated Compartment, Combust. Sci. Technol. 188 (2016) 504–515. doi:10.1080/00102202.2016.1139365.

[59] F.J. Higuera, Steady thermocapillary-buoyant flow in an unbounded liquid layer heated nonuniformly from above, Phys. Fluids. 12 (2000) 2186–2197.

[60] J.M. Suo-Anttila, T.K. Blanchat, A.J. Ricks, A.L. Brown, Characterization of thermal radiation spectra in 2 m pool fires, Proc. Combust. Inst. 32 (2009) 2567–2574.

[61] K. Wakatsuki, G. Jackson, J. Kim, A. Hamins, M. Nyden, S. Fuss, Determination of Planck Mean Absorption Coefficients for Hydrocarbon Fuels, Combust. Sci. Technol. 180 (2008) 616–630.

[62] J.M. Suo-Anttila, T.K. Blanchat, Hydrocarbon characterization experiments in fully turbulent fires: results and data analysis, Albuqueque, New Mexico, 2011. doi:10.2172/1018470.

[63] S.I. Stoliarov, S. Crowley, R.E. Lyon, G.T. Linteris, Prediction of the burning rates of non-charring polymers, Combust. Flame. 156 (2009) 1068–1083.

[64] P.T. Tsilingiris, Comparative evaluation of the infrared transmission of polymer films, Energy Convers. Manag. 44 (2003) 2839–2856.

[65] B. Broeckmann, H. Schecker, Heat transfer mechanisms and boilover in burning oil-water systems, J. Loss Prev. Process Ind. 8 (1995) 137–147.

[66] S.S. Sazhin, W.A. Abdelghaffar, E.M. Sazhina, S.V Mikhalovsky, S.T. Meikle, C. Bai, Radiative heating of semi-transparent diesel fuel droplets, J. Heat Transfer. 126 (2004) 105-109.

[67] A. Vali, D.S. Nobes, L.W. Kostiuk, Effects of altering the liquid phase boundary conditions of methanol pool fires, Exp. Therm. Fluid Sci. 44 (2013) 786–791. doi:10.1016/j.expthermflusci.2012.09.023.

[68] A. Vali, D.S. Nobes, L.W. Kostiuk, Transport phenomena within the liquid phase of a laboratory-scale circular methanol pool fire, Combust. Flame. 161 (2014) 1076–1084. doi:http://dx.doi.org/10.1016/j.combustflame.2013.09.028.

[69] A. Vali, D.S. Nobes, L.W. Kostiuk, Fluid motion and energy transfer within burning liquid fuel pools of various thicknesses, Combust. Flame. 162 (2015) 1477–1488. doi:10.1016/j.combustflame.2014.11.013.

[70] A. Vali, D.S. Nobes, L.W. Kostiuk, Quantifying the Conduction Pathways in a Laboratory-Scale Methanol Pool Fire, Combust. Sci. Technol. 187 (2015) 765–779. doi:10.1080/00102202.2014.965811.

[71] H. Hayasaka, Unsteady burning rates of small pool fires, in: 5th Symp. Fire Saf. Sci., 1997, 499–510.

[72] B. Chen, S.-X. Lu, C.-H. Li, Q.-S. Kang, V. Lecoustre, Initial fuel temperature effects on burning rate of pool fire, J. Hazard. Mater. 188 (2011) 369–374. doi:http://dx.doi.org/10.1016/j.jhazmat.2011.01.122.

[73] C. and W. Van den Bosch, ed., Methods for the Calculation of Physical Effects: Due to Releases of Hazardous Materials (liquids and

Gases),'yellow Book'. CPR 14E, 3., Committee for the Prevention of Disasters, The Hague, 2005.

[74] J.A. Fay, D.H. Lewis, Unsteady burning of unconfined fuel vapor clouds, Symp. Combust. 16 (1977) 1397–1405. doi:10.1016/S0082-0784(77)80424-4.

[75] C. Balke, W. Heller, R. Konersmann, J. Ludwig, Study of the failure limits of an undergrate-fired railway tank car filled with liquefied petroleum gas - Final report of BAM project number 3215, Federal Institute for Materials Research and Testing (BAM), Berlin, Germany. 1999.

[76] B. Droste, U. Probst, W. Heller, Impact of an Exploding LPG Rail Tank Car Onto a Castor Spent Fuel Cask, Int. J. Radioact. Mater. Transp. 10 (1999) 231–240. doi:10.1179/rmt.1999.10.4.231.

[77] G.M. Makhviladze, J.P. Roberts, S.E. Yakush, Numerical Modelling of Fireballs from Vertical Releases of Fuel Gases, Combust. Sci. Technol. 132 (1998) 199–223. doi:10.1080/00102209808952015.

[78] G.M. Makhviladze, J.P. Roberts, S.E. Yakush, Combustion of two-phase hydrocarbon fuel clouds released into the atmosphere, Combust. Flame. 118 (1999) 583–605. doi:10.1016/S0010-2180(99)00026-7.

[79] F. Roper, J. Arno, H.C. Jaggers, The Effect of Release Velocity and Geometry on Burning Times for Non-Premixed Fuel Gas Clouds, Combust. Sci. Technol. 78 (1991) 315–338. doi:10.1080/00102209108951754.

[80] K. Hasegawa, K. Sato, Experimental investigation of the unconfined vapour-cloud explosions of hydrocarbons, 1978.

[81] G.M. Makhviladze, S.E. Yakush, Modelling of Formation and Combustion of Accidentally Released Fuel Clouds, Process Saf. Environ. Prot. 83 (2005) 171–177. doi:10.1205/psep.04242.

[82] S.E. Yakush, G.M. Makhviladze, Large Eddy Simulation of Hydrocarbon Fireballs, Proc. Eur. Combust. Meet. (2005).

[83] Z. Hu, A. Trouve, Numerical Simulation of Explosive Combustion Following Ignition of a Fuel Vapor Cloud, Fire Saf. Sci. 9 (2008) 1055–1066.

[84] W. Luther, W.C. Müller, FDS simulation of the fuel fireball from a hypothetical commercial airliner crash on a generic nuclear power plant, Nucl. Eng. Des. 239 (2009) 2056–2069. doi:10.1016/j.nucengdes .2009.04.018.

[85] A.V. Shelke, N.K. Maheshwari, B. Gera, R.K. Singh, CFD Analysis of

Hydrocarbon Fireballs, Combust. Sci. Technol. 189 (2017) 1440–1466. doi:10.1080/00102202.2017.1296433.

[86] V.R. Lecoustre, P.G. Arias, S.P. Roy, Z. Luo, D.C. Haworth, H.G. Im, T.F. Lu, A. Trouvé, Direct numerical simulations of non-premixed ethylene–air flames: Local flame extinction criterion, Combust. Flame. 161 (2014) 2933–2950. doi:10.1016/j.combustflame.2014.05.016.

[87] P. Sagaut, Large Eddy Simulation for Incompressible Flows, Springer, 2001.

[88] S. Yuu, T. Ueno, T. Umekage, Numerical simulation of the high Reynolds number slit nozzle gas-particle jet using subgrid-scale coupling large eddy simulation, Chem. Eng. Sci. 56 (2001) 4293–4307. doi:10.1016/S0009-2509(01)00050-1.

[89] V. Sankaran, S. Menon, LES of spray combustion in swirling flows, J. Turbul. 3 (2002) N11. doi:10.1088/1468-5248/3/1/011.

[90] N. Bharadwaj, C.J. Rutland, S. Chang, Large eddy simulation modelling of spray-induced turbulence effects, Int. J. Engine Res. 10 (2009) 97–119. doi:10.1243/14680874JER02309.

[91] N. Bharadwaj, C.J. Rutland, A Large-Eddy Simulation Study of Sub-Grid Two-Phase Interaction in Particle-Laden Flows and Diesel Engine Sprays, At. Sprays. 20 (2010) 673–695. doi:10.1615/AtomizSpr.v20.i8.20.

[92] C.J. Rutland, Large-eddy simulations for internal combustion engines - a review, Int. J. Engine Res. 12 (2011) 421–451. doi:10.1177/1468087411407248.

[93] F.A. Williams, Combustion theory, The Benjamin/Cummings Publishing Company, Inc., 1985.

[94] F.A. Williams, Spray Combustion and Atomization, Phys. Fluids. 1 (1958) 541. doi:10.1063/1.1724379.

[95] M. Bini, W.P. Jones, Large-eddy simulation of particle-laden turbulent flows, J. Fluid Mech. 614 (2008) 207. doi:10.1017/S0022112008003443.

[96] M. Bini, W.P. Jones, Particle acceleration in turbulent flows: A class of nonlinear stochastic models for intermittency, Phys. Fluids. 19 (2007) 35104. doi:10.1063/1.2709706.

[97] S. Subramaniam, Statistical representation of a spray as a point process, Phys. Fluids. 12 (2000) 2413–2431. doi:10.1063/1.1288266.

[98] S. Subramaniam, Statistical modeling of sprays using the droplet distribution function, Phys. Fluids. 13 (2001) 624–642. doi:10.1063/1.1344893.

[99] S. Subramaniam, Lagrangian-Eulerian methods for multiphase flows, Prog. Energy Combust. Sci. 39 (2013) 215–245. doi:10.1016/j.pecs.2012.10.003.

[100] J.K. Eaton, J.R. Fessler, Preferential concentration of particles by turbulence, Int. J. Multiph. Flow. 20 (1994) 169–209. doi:10.1016/0301-9322(94)90072-8.

[101] N.A. Okongo, J.R. Bellan, Consistent large-eddy simulation of a temporal mixing layer laden with evaporating drops. Part 1. Direct numerical simulation, formulation and a priori analysis, J. Fluid Mech. 499 (2004) 1–47. doi:10.1017/S0022112003007018.

[102] J.-P. Minier, S. Chibbaro, S.B. Pope, Guidelines for the formulation of Lagrangian stochastic models for particle simulations of single-phase and dispersed two-phase turbulent flows, Phys. Fluids. 26 (2014) 113303. doi:10.1063/1.4901315.

[103] M. Breuer, F. Hoppe, Influence of a cost–efficient Langevin subgrid-scale model on the dispersed phase of large–eddy simulations of turbulent bubble–laden and particle–laden flows, Int. J. Multiph. Flow. 89 (2017) 23–44. doi:10.1016/j.ijmultiphaseflow.2016.10.007.

[104] G.I. Park, M. Bassenne, J. Urzay, P. Moin, A simple dynamic subgrid-scale model for LES of particle-laden turbulence, Phys. Rev. Fluids. 2 (2017) 44301. doi:10.1103/PhysRevFluids.2.044301.

[105] R.G. Rehm, H.R. Baum, The Equations of Motion for Thermally Driven, Buoyant Flows, J. Res. NBS. 83 (1978) 297–308.

[106] A. Majda, J. Sethain, The Derivation and Numerical Solution of the Equations for Zero Mach Number Combustion, Combust. Sci. Technol. 42 (2007) 185–205. doi:10.1080/00102208508960376.

[107] J.W. Deardorff, Stratocumulus-capped mixed layers derived from a three-dimensional model, Boundary-Layer Meteorol. 18 (1980) 495–527.

[108] M. Germano, U. Piomelli, P. Moin, W.H. Cabot, A dynamic subgrid-scale eddy viscosity model, Phys. Fluids A Fluid Dyn. 3 (1991) 1760–1765. doi:10.1063/1.857955.

[109] D.K. Lilly, A Proposed Modification of the Germano Subgrid-Scale Closure Method, Phys. Fluids A. 4 (1992) 633–635.

[110] W. Grosshandler, RadCal: A Narrow Band Model for Radiation Calculations in a Combustion Environment, Gaithersburg, Maryland, 1993.

[111] R. Siegel, J.R. Howell, Thermal Radiation Heat Transfer, 4th ed., Taylor & Francis, New York, 2002.

[112] S. Hostikka, K.B. McGrattan, Numerical modeling of radiative heat transfer in water sprays, Fire Saf. J. 41 (2006) 76–86.

[113] G.D. Raithby, E.H. Chui, A Finite-Volume Method for Predicting Radiant Heat Transfer in Enclosures with Participating Media, J. Heat Transfer. 112 (1990) 415–423. doi:10.1115/1.2910394.

[114] B.F. Magnussen, B.H. Hjertager, On mathematical modeling of turbulent combustion with special emphasis on soot formation and combustion, Symp. Combust. 16 (1977) 719–729. doi:10.1016/S0082-0784(77)80366-4.

[115] R. McDermott, K. McGrattan, J. Floyd, A Simple Reaction Time Scale for Under-Resolved Fire Dynamics, in: Fire Saf. Sci. -- Proc. 10th Int. Symp., University of Maryland, College Park, Maryland, USA, 2011, 809–820.

[116] E. Babinsky, P.E. Sojka, Modeling drop size distributions, Prog. Energy Combust. Sci. 28 (2002) 303–329. doi:10.1016/S0360-1285(02)00004-7.

[117] B. Ditch, H.Z. Yu, Water Mist Spray Characterization and Its Proper Application for Numerical Simulations., in: Fire Saf. Sci. 9, 2008:, 541–552. doi:10.3801/IAFSS.FSS.9-541.

[118] S. Hostikka, A. Silde, T. Sikanen, A. Vepsä, A. Paajanen, M. Honkanen, Experimental characterisation of sprays resulting from impacts of liquid-containing projectiles, Nucl. Eng. Des. 295 (2015) 388–402. doi:10.1016/j.nucengdes.2015.09.008.

[119] J. Ramírez-Muñoz, A. Soria, E. Salinas-Rodríguez, Hydrodynamic force on interactive spherical particles due to the wake effect, Int. J. Multiph. Flow. 33 (2007) 802–807. doi:10.1016/j.ijmultiphaseflow.2006.12.009.

[120] G.K. Batchelor, An Introduction to Fluid Dynamics, Cambridge University Press, Cambridge, UK, 1967.

[121] L. Prahl, A. Hölzer, D. Arlov, J. Revstedt, M. Sommerfeld, L. Fuchs, On the interaction between two fixed spherical particles, Int. J. Multiph. Flow. 33 (2007) 707–725. doi:10.1016/j.ijmultiphaseflow.2007.02.001.

[122] R. Reijnhart, R. Rose, Vapour cloud dispersion and the evaporation of volatile liquids in atmospheric wind fields-II. Wind Tunnel Experiments,

Atmos. Environ. 14 (1980) 759–762. doi:10.1016/0004-6981(80)90129-8.

[123] R. Reijnhart, J. Piepers, L.H. Toneman, Vapour cloud dispersion and the evaporation of volatile liquids in atmospheric wind fields-I. Theoretical model, Atmos. Environ. 14 (1980) 751–758. doi:10.1016/0004-6981(80)90129-8.

[124] F.A. Kulacki, A.A. Emara, Steady and transient thermal convection in a fluid layer with uniform volumetric energy sources, J. Fluid Mech. 83 (1977) 375–395.

[125] Y. Tasaka, Y. Takeda, Effects of heat source distribution on natural convection induced by internal heating, Int. J. Heat Mass Transf. 48 (2005) 1164–1174.

[126] S.B. Pope, Ten questions concerning the large-eddy simulation of turbulent flows, New J. Phys. 6 (2004) 1–24.

[127] R. Garg, C. Narayanan, D. Lakehal, S. Subramaniam, Accurate numerical estimation of interphase momentum transfer in Lagrangian-Eulerian simulations of dispersed two-phase flows, Int. J. Multiph. Flow. 33 (2007) 1337–1364. doi:10.1016/j.ijmultiphaseflow.2007.06.002.

[128] M. Klassen, J.P. Gore, Structure and radiation properties of pool fires, 1994.

[129] K. McGrattan, S. Hostikka, R. McDermott, J. Floyd, C. Weinschenk, K. Overholt. Fire Dynamics Simulator, User's Guide, National Institute of Standards and Technology, Gaithersburg, Maryland, USA and VTT Technical Research, Centre of Finland, Espoo, Finland, 6th ed., 2013 https://github.com/firemodels/fds/releases/download/FDS6.5.3/FDS_User_Guide.pdf

[130] T. Poinsot, D. Veynante, Theoretical and Numerical Combustion, 2nd ed., R.T. Edwards, Inc., Philadelphia, Pennsylvania, 2005.

II

Nuclear Engineering and Design 295 (2015) 388–402

Contents lists available at ScienceDirect

Nuclear Engineering and Design

journal homepage: www.elsevier.com/locate/nucengdes

Experimental characterisation of sprays resulting from impacts of liquid-containing projectiles

Simo Hostikka[a,*], Ari Silde[b], Topi Sikanen[b], Ari Vepsä[b], Antti Paajanen[b], Markus Honkanen[c]

[a] Aalto University, Espoo, Finland
[b] VTT Technical Research Centre of Finland Ltd, Espoo, Finland
[c] Pixact Oy, Tampere, Finland

HIGHLIGHTS

- Detailed characterisation of sprays resulting from the impacts of water-filled metal projectiles on a hard wall.
- Experimental measurements of spray speed, direction and droplet size.
- Detailed analysis of overall spray evolution.
- The spray characterisation information can be used in CFD analyses of aircraft impact fires.

ARTICLE INFO

Article history:
Received 24 March 2015
Received in revised form 26 August 2015
Accepted 17 September 2015
Available online 13 November 2015

ABSTRACT

Modelling and analysing fires following aircraft impacts requires information about the behaviour of liquid fuel. In this study, we investigated sprays resulting from the impacts of water-filled metal projectiles on a hard wall. The weights of the projectiles were in the range of 38–110 kg, with 8.6–68 kg water, and the impact speeds varied between 96 and 169 m/s. The overall spray behaviour was observed with high-speed video cameras. Ultra-high-speed cameras were used in backlight configuration for measuring the droplet size and velocity distributions. The results indicate that the liquid leaves the impact position as a thin sheet of spray in a direction perpendicular to the projectile velocity. The initial spray speeds were 1.5–2.5 times the impact speed, and the Sauter mean diameters were in the 147–344 μm range. This data can be used as boundary conditions in CFD fire analyses, considering the two-phase fuel flow. The overall spray observations, including the spray deceleration rate, can be used for validating the model.

1. Introduction

Aircraft impacts have been included in the safety analyses of nuclear power plants (NPP) for a long time, but only recently have these analyses assumed the impact of a large commercial aircraft. The impact of such an aircraft can cause damage to the safety-related structures and components through mechanical impact and fire. Three different modes of influence can be identified in aircraft impact-induced fires: the first mode is a large fireball, caused by the ignition of the aircraft fuel cloud erupting from the breaking fuel tanks. The diameter of the fireball can be tens of metres and it lasts for a few seconds. The second mode of influence is the combustion of residual fuel as a pool fire in the vicinity of the impact location. The size and burning rate of the pool fire depend on the geometry and the properties of the surfaces below the pool. The duration of the pool fire depends on the amount of aviation fuel that did not burn in the initial fireball, the pool burning rate and the possible fire suppression activities. The third mode of fire influence is the penetration of aviation fuel inside the plant through existing openings, or mechanical damage caused by perforated aircraft components. Even if the mass of the penetrated fuel was relatively small, it would cause a rapid ignition of existing internal fire loads, such as electrical cables. Experimental data and simulation capabilities of the high-speed fuel dispersal mechanisms are needed to develop engineering methods for protection against aircraft impact-induced fires.

Tieszen (1997) has summarised and classified the major fuel dispersal processes in the context of an aircraft crash as follows: the first stage is fuel leakage from the ruptured tank due to the inertial and gravitational forces. Because the deceleration of the plane

* Corresponding author. Tel.: +358 504471582.
E-mail address: simo.hostikka@aalto.fi (S. Hostikka).

http://dx.doi.org/10.1016/j.nucengdes.2015.09.008
0029-5493/

occurs very rapidly and the impact forces are enormous, the fuel spills out from the ruptured tanks and disperses to surroundings. The next stage is known as the primary break-up phase, where the liquid break-up and atomisation begins, due to the destabilising processes of aerodynamic drag and turbulence within the liquid core. The primary break-up phase is followed by the secondary break-up phase of flying droplets. Due to the interphase momentum transfer from the droplets, the surrounding air is accelerated to a speed that is close to the speed of the spray, and the droplets are decelerated correspondingly. Depending on the speed of a droplet relative to the surrounding gas, the secondary break-up can produce droplets of different sizes. The size distribution resulting from the break-up process can be either uni- or bi-modal in nature. The size and velocity distributions have an influence on the transfer distance of a droplet cloud. The rest of the liquid stream and partially atomised droplets may impact the targets or fall down due to gravitational forces. Flying structures and fragments of the aeroplane also affect the fuel dispersal processes.

Very few publications are available on full-scale aircraft crash tests including fuel. Early test series by FAA and NACA using belly-landing aircraft demonstrated that fuel spilled from ruptured tanks, forming a fine mist (droplet) cloud that can be ignited by several sources (Pinkel et al., 1953; Ahlers 1977; Johnson and Garodz, 1986). Experiences from numerous real crash incidents, such as the '9/11' terrorist attacks on the World Trade Centre September 11, 2001, support this observation. Furthermore, a film footage analysis of aircraft crash fireballs has indicated that these flame balls are very similar to the fireballs resulting from boiling liquid expanding vapour explosions, i.e. BLEVEs (Luther and Müller, 2009). However, none of the analysed accidents included impact on a rigid vertical structure, such as modern NPP.

Most of the published studies involving high-speed impacts of liquids have focused on the fracture and deformations of solid surfaces. The fate of the liquid has been investigated mostly in the length scale of an individual droplet impacting a surface, serving the purposes of process industry and manufacturing technologies, such as spray coating. In his work concerning droplet impacts on rigid surfaces, Knežević (2002) defined 'high-speed' droplet impact as an impact causing at least 5% compressibility in the liquid. This was obtained if the impact speed was in the order of 100 m/s or higher. The properties of the splash have in general been found to depend on the properties of the liquid and the target, air pressure and the initial speed prior to the impact. The velocity of the splashing droplets has been found to be several times higher than the impact velocity (Yarin, 2006). Field et al. (1989), for instance, made observations of 10–32 mm droplets hitting various rigid surfaces at a speed of 110 m/s, producing splashing jets with initial speeds of between 670 and 1170 m/s and splash angles (angle between wall tangent and splash direction) of between 10 and 19 degrees. They observed that a harder target material generally leads to smaller splash angles and higher spray speeds than softer materials.

Experimental scenarios that are qualitatively closer to the aircraft impact are often related to the crashworthiness of the vehicle fuel tanks. Fasanella and Jackson (2001) reported on a drop test of an aircraft fuel tank at speed of about 10 m/s. Anghileri et al. (2005) used various numerical tools, validated through drop tower tests, to investigate the liquid-structure interaction within a tank during impact on the ground. The aim of these studies was to ensure that the fuel tanks can withstand impacts at moderate speeds. They did not increase our knowledge of the fate of fuel in case of tank rupture.

Sandia National Laboratories have conducted a crash test where a Phantom F-4 aircraft carrying 4.8 tonnes of water was hit into a reinforced concrete target at a velocity of 215 m/s (von Riesemann et al., 1989; Muto et al., 1989; Sugano et al., 1993). Unfortunately, the liquid dispersal processes were not measured and documented in detail because the main aim of the tests was to study the impact forces versus time. However, the liquid spread process can be seen in the video clips taken from the test (Fig. 1). According to the video material, the initial liquid discharge velocity was about 280–330 m/s, i.e. 1.3–1.55 times the impact velocity. The liquid spread pattern seems be quite symmetrical, except the sideward direction. The spread direction calculated from the wall plane was about 0–30° ± 10° (0° is along the wall plane, 90° is directly backwards). The final size (diameter) of the cloud was 60–80 m.

Jepsen et al. (2009) investigated the usability of various experimental methods for the diagnostics of high-speed liquid dispersion. In addition to the numerous small-scale tests on individual drops, they discussed the use of photometric, PIV and PDPA measurements in a large-scale water-slug test with a water-filled 1.2 m diameter aluminium cylinder hitting a concrete wall at 105 m/s. The photometrics showed that the initial speed of the radially spreading cloud of water was slightly higher than the impact speed (110 m/s). The cloud in their experiment reached distances of 30–40 m from the impact point. A large-scale PIV, based on the high-speed video images, showed peak velocities of about 250 m/s, i.e. substantially higher than the values shown by photometrics. A PDPA measurement of the residual spray indicated a size distribution in the range of 6–13 μm, which was concluded to be a result of the secondary break-up or atomisation processes, expecting the break-ups mainly in the bag break-up regime. PDPA measurements did not succeed in capturing the droplets of the primary spray.

BLEVE-induced fireballs are traditionally analysed using analytical and empirical formulas (Abbasi and Abbasi, 2007). Such formulas can also be used in the analysis of aircraft impact fires and explosions. In order to take into account the geometrical aspects and details of the event dynamics, it is necessary to use computational fluid dynamics (CFD) tools for the analysis. Using the CFD tools for the task has three major challenges: the first is to collect the necessary input data for prescribing the boundary conditions for the aviation fuel spray. The second challenge is the development of numerical tools with a verified capability to simulate the extremely dynamic reactive flow involving several different length scales. The need to validate the simulation methods and tools forms the third challenge, because the experimental data on impacts with fuel-filled projectiles is not available. The validation must therefore be performed independently for different parts of the modelling methodology, using water-filled projectiles to validate the spray formation and transport calculations, for instance.

The purpose of this work is to contribute to the first and third of the above-mentioned challenges by characterising experimentally the liquid spray resulting from a high-speed impact of a liquid-containing projectile against a hard wall. The intended use of the results is the generation of model inputs and validation data for the CFD simulations of aircraft impact fires. The work has been done in the context of VTT's IMPACT experiments (Kärnä et al., 2004; Lastunen et al., 2007). The paper by Silde et al. (2011) provided an overview of the liquid experiments, but as the experimental methods have been improved from earlier attempts, they will be presented here in detail. The next section describes the experimental methods. The third section presents the experimental results in a form that can be utilised as model inputs (droplet size distribution, initial spray velocity) and validation (spray deceleration). Finally, some concluding remarks will be given.

2. Experimental methods

2.1. Impact facility

The facility for impact testing was designed and constructed in the early 2000s in the wake of the 9/11 terrorist attacks. The facility

Fig. 1. Still figures from the video clips of the Phantom F-4 test by Sandia National Laboratories. From https://share.sandia.gov/news/resources/video-gallery/index.html#rocketsled (accessed 12.03.15).

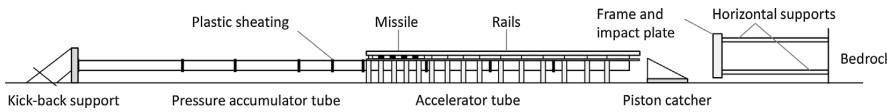

Fig. 2. Side view of the impact test facility.

was initially designed for the measurement of load-time functions generated by soft projectile impacts. Shortly afterwards, the facility was upgraded for testing concrete walls under impact loading. A side view of the test facility is shown in Fig. 2. Air pressure is used to accelerate the projectile to its target velocity. Pressure is gradually increased in a pressure accumulator tube (on the left) until it reaches a predefined, test-specific value. The pressure accumulator tube is separated from an acceleration tube (in the middle) by a flange with a set of plastic membranes taped on both of its sides. When the predetermined value of pressure is achieved, the plastic membranes are punctured and the released air pushes a piston, which is located inside the acceleration tube. The projectile is then pushed forward by a fin of this piston. The projectile travels on the rails above the acceleration tube. While the projectile continues its flight and ultimately hits the impact plate, the piston is stopped by a piston catcher before it hits the target.

The impact plate is placed between two halves of a steel frame resting on wooden planks. The frame itself is supported in the horizontal direction against the bedrock by four supports, called back pipes.

The facility has been designed for projectiles with mass up to 100 kg and diameter between 150 and 500 mm. Target walls have a square shape with a side-length of 2.1 m. The maximum impact velocity that can be reached depends mainly on the combined mass of the projectile and the piston. For example, with a 50 kg projectile and a 52 kg piston, the maximum speed is currently 165 m/s. A thorough description of the facility is given by Vepsä et al. (2012).

2.2. Liquid front observations

Three high shutter speed/high-speed video cameras (1000 frames per second) were used to observe the propagation of the water spray up to 3 m from the impact point. The camera positions within the facility are shown in Fig. 3. In three experiments (labelled 632, 652 and FP7), the camera positions differed slightly from those in the figure. At distances beyond 3 m, the liquid flow patterns were affected by the boundaries of the laboratory space. The facility was lit with 48,300 W halogen lamps with a luminous flux of 10,000 lm per lamp. The lamps were arranged in three patterns of 28, 18 and two lamps. In addition, three ETC PAR EA fixtures with 750 W (19,500 lm) HPL lamps were used in two patterns to focus more light on the most important regions of video imaging.

The radial position of the water front and the spread direction were measured from the still figures taken from the high-speed videos. The water front position was traced in nine different angular directions from the point of impact. Image analysis was used to find the exact location of the front (Fig. 4). Since the frame rate of the videos was known, the momentary velocity of the spray front could be estimated from the sequential still figures. The

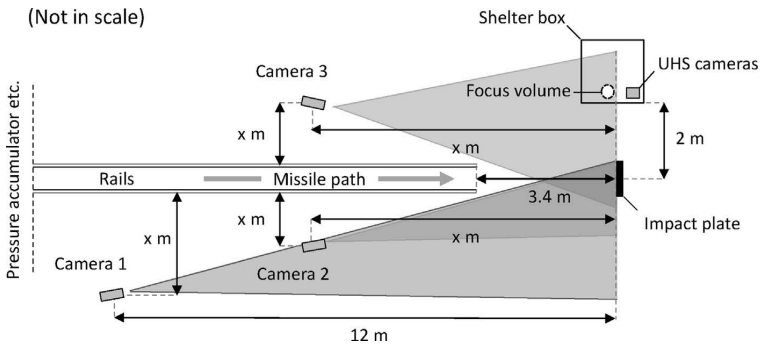

Fig. 3. Positions of the regular high-speed cameras and the ultra-high-speed (UHS) cameras. Fields of view of the regular high-speed cameras are indicated by areas highlighted in red, green and blue. The location of the focus volume of the ultra-high-speed cameras is indicated by the white dot. (For interpretation of the references to colour in this figure legend, the reader is referred to the web version of the article.)

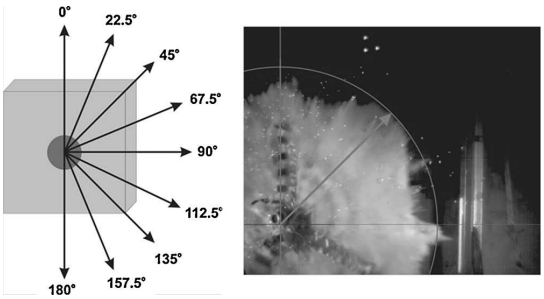

Fig. 4. Angular directions where the water front position was measured (left) and an example of measurement in an impact test (right).

uncertainty of the water front position measurement is estimated to be approximately ±0.1 m or less. This is caused by the factors which hinder clear sight of the water front in the still figures (e.g. limited amount of illumination, minimum available exposure time, limited figure resolution, shadows, mist, other impurities). The uncertainty may also vary slightly in different angular positions and at different moments. Because the period of the sequential still figures is as small as 1 ms, the uncertainty of the spray front position results in an uncertainty in the temporary velocity of the spray front of approximately ±25 m/s, or less. The nearest position where the liquid velocity could be reliably measured was about 0.2 m from the surface of the impacted projectile.

The water spread direction looking from the side of the target is also measured from the still figures of the high-speed videos (Fig. 5). In this method, a straight line is drawn from the centre line of the ruptured projectile to the leading edge of the water front a few milliseconds after the impact. The spread angle is calculated from the wall plane: 0° is along the wall plane and 90° is directly backwards. The uncertainty of the angular directions is estimated to be ±5° or less.

2.3. Spray characterisation

The local spray properties were characterised using two ultra-high-speed digital cameras recording images of flying droplets. The technical challenge of the measurement was related to the wide velocity and size ranges that needed to be observed simultaneously: the spray front was known to consist of large and fast droplets, while the spray following behind mainly consisted of small and relatively slow droplets. One of the cameras was therefore used for measuring the smallest droplets 12–750 μm in diameter, and the other for measuring the larger droplets in the size range of 50–2500 μm. The results of two cameras were combined to a single distribution, noticing the effective measuring volumes of both views.

Sharp still images of droplets were obtained with pulsed high-speed diode laser illumination. Backlight illumination was utilised

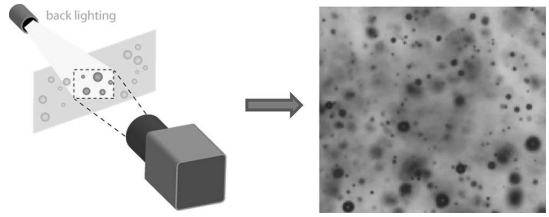

Fig. 6. Principle of backlight imaging.

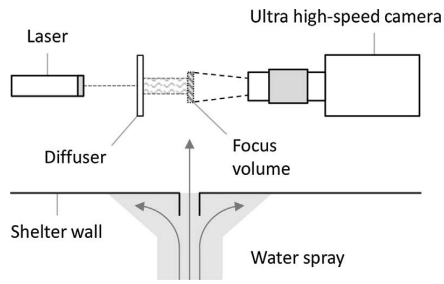

Fig. 7. Schematic drawing of the droplet imaging set-up. The size of the focus volume is greatly exaggerated for illustration purposes.

to obtain images of droplet silhouettes against a bright background. Fig. 6 shows the principle of the backlight illumination technique with a camera, backlight and flying droplets that cross the measuring volume. An example of an obtained image is shown on the right.

A schematic drawing of the droplet imaging set-up is shown in Fig. 7. The images were taken using two Photron Fastcam cameras (SA-1.1 and SA-X) at frame rates from 40,000 to 100,000 fps and image resolutions from 640 × 208 to 640 × 144 pixels. The cameras have 12-bit 1024 × 1024 pix CMOS sensors with a pixel size of 20 μm. The backlight was produced using Cavilux HF lasers from Cavitar Ltd at 810 nm wavelength and guided through an optical cable to the laser optics. A holographic diffuser was placed between the measurement plane and the laser optics to even out the backlight intensity. The lasers were triggered by the camera frame rate and a 200 ns long laser light pulse was shot once per image frame. The cameras started recording when the trigger signal from the pressure accumulator arrived. Both lasers and the cameras were placed inside a shelter box to protect them from the water spray and flying fragments of the projectile. The shelter box was positioned on the side of the impact position (Fig. 3) at distance of 2 m from the centre of the impact position and equipped with a 20 mm-wide vertical gap that allowed a sheet of water spray to enter the measurement volume between the lasers and the cameras. The total distance of the cameras from the centre of the impact point was 2.2 m.

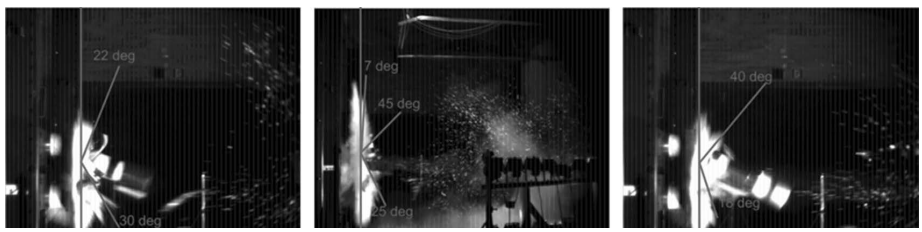

Fig. 5. Examples of the method to measure the water spread direction (side views). Note that each image is taken from a different test.

The SA-X camera was equipped with an Infinity K2-S long-distance microscope, including a CF-2 front lens and a 2× optical converter. With 640 × 144 pixel resolution and 100,000 Hz frame rate, this set-up produced a $3.2 \times 0.7\,mm^2$ field of view at a working distance of 110 mm, which corresponds to the scaling of 5.0 μm per image pixel. Therefore, droplets as small as 12 μm in diameter could be detected. The droplets smaller than 12 μm in diameter were visually observed in the images, but they were not analysed due to high level of imaging noise that disturbed the evaluation of single pixel objects. The depth of field of the microscopy images was about 4 mm and it halved for micro-droplets with a diameter of less than 30 μm. This means that the smallest droplets ($d < 30$ μm) where detected only when they were located inside the $3.2 \times 0.7 \times 2.0\,mm^3$ focusing range of the SA-X camera.

The SA-1.1 camera was equipped with a Nikon 100 mm macro lens. With 640 × 208 pixel resolution and a 40,000 Hz frame rate, this set-up produced a $12.8 \times 4.2\,mm^2$ field of view at a working distance of 130 mm, which corresponded to the scaling of 20.0 μm per image pixel or a magnification of 1.0×. Droplets larger than 50 μm in diameter were successfully analysed from the images of the SA-1.1 camera. Smaller droplets were also clearly visible with 1.0× magnification, but they appeared as 1-pixel dots in the image, whose size could not be evaluated. The lens aperture was set to $f^{\#} = 11$ to produce a depth of field of 12 mm.

A novel image analysis algorithm was utilised to detect the individual, in-focus droplets and to track their pathlines. In this method, the edges of the sharp, in-focus droplet images are detected with a Canny edge detector (Canny, 1986). An advanced Spoke filter (from Minor and Sklansky, 1981) was developed to locate the circular-like droplets based on the greyscale gradient directions along the droplet edge pixels. The region of each droplet image is analysed with a point-spread function approach presented by Fdida and Blaisot (2010). The detected in-focus droplets are tracked over time with an iterative version of the best-estimate tracking algorithm (Ouellette et al., 2006), which finds the best match for each droplet in three consecutive image frames. Matching is carried out iteratively to optimise the matching parameters to the current flow conditions (i.e. to the level of turbulence). We assume that the droplet size and the velocity remain unchanged over three image frames (i.e. 20–50 μs period of time).

The measurement set-up was calibrated prior to the measurements by taking images of micro-dots printed on a glass sheet at known depth locations. Images of the micro-dots were analysed with the droplet detection algorithm and the obtained dot size measurements were compared to the known dot sizes. The mean relative sizing error of all detections was 5.0% for high-magnification (4×) images and 3.4% for 1× magnification images. Sizing error increased slightly for smaller dot sizes and when moving the micro-dots away from the focal plane of the imaging system. The maximum sizing error was 10%, whereas the minimum was as small as 0.1%.

The effective depth of field of the imaging system decreased with decreasing droplet size. For both cameras, the smallest recognisable droplets had about one-third of the depth of field of large droplets (0.5–2 mm in diameter). This effect was taken into account by weighting the lowest size classes of the droplet size distributions accordingly.

For spray characterisation purposes, three different mean diameters were calculated from the data. The arithmetic d_{10}, Sauter d_{32} and volumetric d_{43} mean diameters are:

$$d_{10} = \frac{\sum_{i=1}^{N} d_i}{N}, \quad d_{32} = \frac{\sum_{i=1}^{N} d_i^E}{\sum_{i=1}^{N} d_i^z} \quad \text{and} \quad d_{43} = \frac{\sum_{i=1}^{N} d_i^4}{\sum_{i=1}^{N} d_i^E} \tag{1}$$

Here d_i is the diameter of ith detected droplet in the image. In addition to the mean diameters, the droplet flux and concentration were also determined. The droplet flux was calculated from the average number of detected droplets per image. The droplet concentration in turn represents the total volume of droplets per total measuring volume and it is presented in ppm.

The main disadvantage of the backlighting is that all the objects that cross the path between the camera and the light are seen in the image. The obtained images contained several blurry droplets that were located either behind or in front of the measuring volume. They hindered the visibility and caused underestimation of the droplet concentration.

Table 1
The four types of water-filled projectiles according to their test identifiers.

Material ↓/Geometry →	Cylindrical	Winged
Aluminium	632, 652	688, 689, 695, 696
Stainless steel	FP7, SFP1–5, SFP 7–12	–

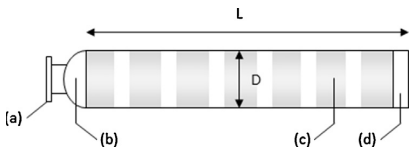

Fig. 8. The projectile construction consists of (a) a stainless steel collar, (b) a stainless steel end dome, (c) a hollow stainless steel cylinder and (d) an aluminium front cap.

2.4. Projectiles

The projectiles used in this work can be divided into four categories on the basis of the geometry (cylindrical or cylindrical with added wings) and the material used (aluminium or stainless steel). Table 1 provides the test identifiers of the tests used.

2.5. Cylindrical projectiles

In total, eight different versions of the cylindrical water-filled projectiles have been used in the tests. These versions differ by material, cross-sectional dimensions, total mass, mass of water, length of water tank and location of water tank.

A typical stainless steel projectile construction is shown in Fig. 8 as an example. This construction was used in tests SFP1–SFP5 and SFP7–SFP12. The projectile is made of a stainless steel (grade EN 1.4432) pipe (c) with an aluminium 'hat' (d) at the front and a stainless steel cap (b) at the back, to form a water tank. The aluminium hat is pushed inside the pipe and attached with only waterproof padding so that it will yield easily when the projectile hits the steel plate. The steel collar (a) at the back of the projectile is required for pushing the projectile with a fin attached to the piston. The projectiles were designed to break easily at the front due to internal water pressure and to release the water content into the surroundings. In general, the water tank tends to split into numerous long strips. The number of these strips depends on the ratio between the length of the water tank and its outer diameter, the wall thickness and the impact velocity. An example of a ruptured projectile is shown in Fig. 9.

In addition to the aforementioned differences between the projectile versions, the impact velocity was also varied with roughly three different levels used: ∼100, ∼125 and ∼137 m/s. The main characteristics of the projectiles are listed in Table 2 as realised in tests. If not otherwise mentioned, the material of the projectile was stainless steel, the water tank was located at the front of the projectile and it was completely filled with water.

The spray characterisation failed in tests SFP1, SFP9 and SFP10. In test SFP1, the ultra-high-speed cameras did not trigger. In tests

Table 2
The realised values of the projectile parameters in tests SFP1–5 and SFP7–12.

Test id.	Projectile properties						
	Version	Wall thickness (mm)	Inner diameter (mm)	Water tank length (mm)	Mass (kg)	Water mass (kg)	Impact velocity (m/s)
Tests with spray characterisation							
*SFP2	A	1.5	150	2155	50.52	37.1	97
**SFP3	B	1.5	150	2155	38.09	24.69	97
SFP4	C	1.5	150	1412	38.4	24.81	99
SFP5	C	1.5	150	1412	38.38	24.74	99
SFP7	D	1.5	200	1204	49.75	36.82	103
SFP8	E	2.0	200	1204	51.05	37.24	100
SFP11	D	1.5	200	1204	49.9	36.96	126
SFP12	E	2.0	200	1204	51.5	37	122
Tests without spray characterisation							
SFP1	A	1.5	150	2155	50.4	36.96	96
SFP9	D	1.5	200	1204	49.7	36.71	137
SFP10	E	2.0	200	1204	51.1	37.27	137
***632	G	5.0	240	1500	108.1	67.8	96
***652	H	5.0	240	~630	50.7	28.0	104
****FP7	I	3.0	250	559	51.93	24.66	135

* In test SFP2, a camera with 4× magnification malfunctioned.
** In test SFP3, the water tank was only filled to two-thirds of its volume.
*** In tests 632 and 652, the material of the projectile was aluminium.
**** In test FP7, the water tank was located at the centre of the projectile, 338 mm from the front. The impact velocity of the tank was roughly 102 m/s.

Fig. 9. A projectile after the test.

SFP9 and SFP10, the spray front hits the shelter wall so heavily that the gap in the measurement region was closed and only a few droplets arrived in the focus volumes of the cameras.

2.6. Winged projectiles

In addition to cylindrical projectiles, a projectile type that represents a whole aircraft was also designed. The purpose of these 3D projectiles was to incorporate the wings and the knife effect they may cause. A schematic drawing of the winged projectile is shown in Fig. 10. The projectile consists of a hollow, thin-walled cylindrical pipe simulating the fuselage of an aircraft, a trapezoidal thin-walled box below the pipe, simulating the wings, 200 mm-long 'claws', made out of 3 mm-thick steel sheets, below the wings, and a separate thick-walled steel pipe at the back. The purpose of the 'claws' was to keep the projectile on the rails of the launch pad during acceleration. The back part was added to increase the weight of the projectile. Both the projectile body and the wings were made of aluminium. The wings were made watertight and filled with water to simulate the fuel inside the wing tanks of an aircraft. These wings/water tanks tend to break into three large and a few smaller parts in the tests, as shown in Fig. 11. The main dimensions of the projectile, referred to in Fig. 10, are as follows:

- Projectile length: $l_p = 1130$ mm,
- Span width: $W = 1300$ mm,

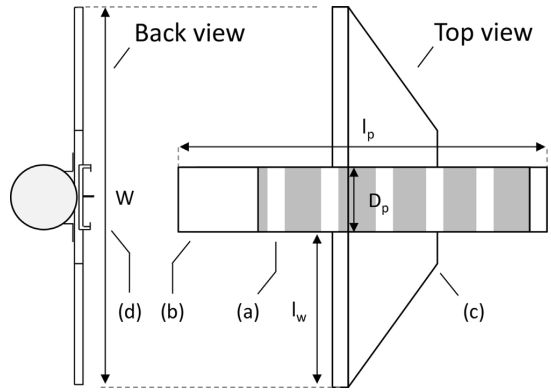

Fig. 10. Main components of the 3D projectile construction: the (a) aluminium pipe, (b) steel pipe section, (c) aluminium wings, and (d) steel claws.

Fig. 11. A 3D projectile after test 688.

- Length of the wings: $l_w = 350$ mm,
- Starting location of the wings: 350 mm from the front,
- Inner diameter of the pipe: $D_p = 200$ mm,
- Thickness of the pipe wall: $t_p = 4$ mm,
- Thickness of the wing material: $t_w = 3$ mm.

Table 3
The realised values of the projectile parameters in tests with winged projectiles.

Test ID	Mass (kg)	Water mass (kg)	Impact velocity (m/s)	Impact velocity of the water tank (m/s)
688	41.15	9.05	137	118
689	40.65	8.6	142	124
695	40.36	8.6	167	149
696	41.08	9.4	169	151

The test-specific values of the projectile mass, water mass, impact velocity and the estimated impact velocity of the water tank are shown in Table 3. The impact velocities of the water tank are lower than the projectile velocities because the wings were placed at a finite distance from the projectile front, and because the projectiles decelerated before the wings hit the impact plate. The impact velocities of the wing tanks were estimated assuming a constant rate of deceleration, knowing the impact duration when similar projectiles without wings were used.

3. Results and discussion

3.1. Spray imaging

Images of a typical liquid dispersion pattern from a cylinder projectile at three separate moments are illustrated in Fig. 12. The images were taken from test SFP5, where the impact velocity and the amount of liquid were 100 m/s and 25 L, respectively. High-speed liquid droplets and jets form stripes in the images due to the motion blur, especially in the vicinity of the projectile. The liquid dispersion occurs quite uniformly in all directions around the projectile, but the projectile fragments may cause perturbations of the liquid front, possibly increasing the folding and fingering of the front. As a result, the spray front can propagate at different velocities in different directions. In some directions, there are fragments impeding the spray propagation. There is also an issue with the projectile leaning to one side, leading to the faster spray front propagation in the opposite direction. The far-field images from test no. 652 show the liquid spray dispersing as several radial waves (Fig. 13). The propagation speeds of the sequential waves are approximately equal near the impact location, but later, the leading front of the cloud decelerates strongly and some waves coming from behind may pass the leading front. Based on the current data, it is not possible to definitively conclude whether the waves are produced during the eruption from the breaking tank or as a result of liquid–gas interactions.

A typical dispersion pattern from a winged projectile (impact velocity 137 m/s) is shown in Fig. 14. The total amount of water locating inside the wings was 8 L, with the cylindrical part of the projectile being empty. When the wings hit the wall, the leading edges of the wings are first ruptured open, and the liquid dispersion occurs primarily in vertical directions (i.e. in the normal directions of the wing surfaces). Compared to the cylindrical projectile tests, the vertical spread directions are pronounced, and only an insignificantly small amount of water is ejected sideways. This conclusion is also confirmed by images from another winged projectile test, where the impact velocity was 167 m/s (Fig. 15). The observed behaviour is consistent with the video material from the SNL Phantom F-4 experiments.

The earlier Phantom F-4 and cylinder experiments, conducted by SNL, have revealed that the liquid dispersion starts along the wall plane and a flat dispersion pattern is formed around the target (von Riesemann et al., 1989; Sugano et al., 1993; Jepsen et al., 2009). Side view images from selected tests of the current campaign show similar behaviour (Figs. 5 and 16). The ejection angle of the liquid, measured near the projectile, is in the range of 20–40° from the wall plane. This result was obtained for both the cylindrical and winged projectiles. Further away from the impact location, the spray angle is usually smaller. We assume that the spray angle is reduced over the course of the spray movement due to the one-sided air entrainment. Air entrainment is a fluid dynamic process of jets and plumes, where the viscous stress between the primary flow direction and the surrounding gas causes the movement of the gas towards and along the jet or the plume. In the impact scenario, the air can only be entrained into the spray from the direction of the arriving projectile, and horizontal momentum occurs only towards the wall. As a result, the spray is 'pushed' towards the wall, and the spread angle becomes smaller than what it is initially.

Fig. 17 shows the measured spray front velocities as a function of the distance from the projectile surface. Fig. 17(a) shows the velocities from tests SFP1-SFP12, i.e. with two different projectile diameters and different impact velocities. Each curve represents the median over the angular directions shown in Fig. 4. The differences between the velocities measured from individual tests are slightly bigger than the measurement uncertainty. In Fig. 17(b), the velocities from three selected tests are normalised by dividing the spray front velocity with the projectile impact velocity.

$$V^* = \frac{V_{\text{spray}}}{V_{\text{impact}}} \tag{2}$$

Correspondingly, the distance from the impact position is normalised with the projectile diameter

$$R^* = \frac{R}{D} \tag{3}$$

In most experiments, the highest spray velocities ($V^* \geq 2$) were obtained near the impact position. In some tests, however, the behaviour of the spray front velocity was not consistent, as illustrated in Fig. 17. The overall results indicate that the spray front velocity decreases as the time and distance from the impact target increase. In the tests presented in Fig. 17(b), the spray front decelerates to a level of projectile impact velocity ($V^* = 1$), first at $0.5 < R^* < 1$, but then it accelerates again. The spray front velocity fluctuations can, at least partially, be caused by the measurement uncertainty, but they can also be explained by the sequential waves of the spray: if the leading front decelerates enough, the following wave with a higher velocity may pass. This can be seen as a velocity jump, presented in Fig. 17.

Fig. 18 presents the normalised liquid front velocities in the region very close to the projectile in selected impact tests. In addition to the median values, average values with error bars indicating the standard deviation and the maximum measured values are plotted. The measurements indicate that the liquid velocity near the projectile is much higher than the impact velocity. Velocity ratios as high as 3–4 were detected in some tests, but mostly the average and median velocity ratios close to the impact point are between 1.5 and 2.5. The results also indicate that the velocity ratio is quite independent from the projectile impact velocity.

The spray front velocity data is summarised in Fig. 19. Each marker represents an average velocity from an individual test at a single distance. By linear extrapolation, the initial spray velocity becomes 1.7 ± 0.25 times the impact velocity, and the velocity decreases to the level of the impact velocity at distance $R^* \approx 4$.

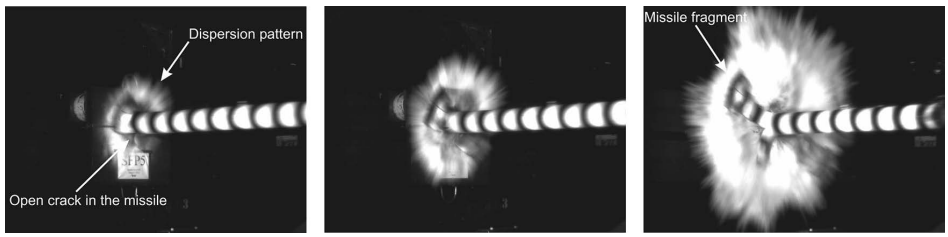

Fig. 12. Near-field liquid dispersion pattern in test SFP5 with an impact velocity of 100 m/s and 25 L of water. The time instances are 1, 2 and 5 ms after the impact.

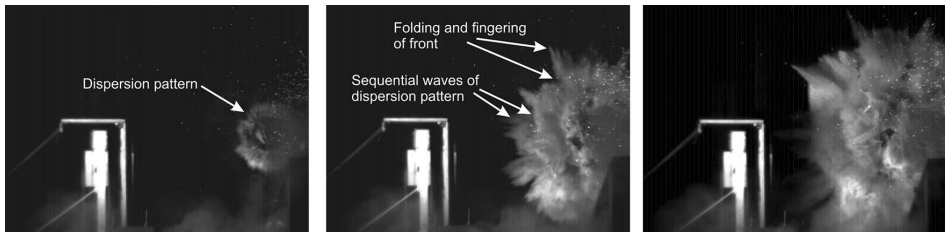

Fig. 13. Far-field liquid dispersion pattern in test no. 652 with an impact velocity 100 m/s and 28 L of water. The time instances are 2, 6 and 10 ms after the impact.

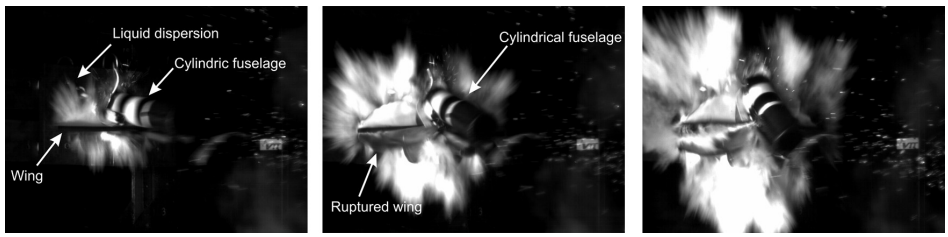

Fig. 14. Near-field liquid dispersion pattern from 3D projectile test no. 688 with an impact velocity of 137 m/s and 8 L of water. The time instances are 1, 3, and 5 ms after the impact.

Fig. 15. Far-field liquid dispersion pattern from 3D projectile test no. 695 with an impact velocity of 167 m/s and 8 L of water. The time instances are 1, 5 and 10 ms after the impact.

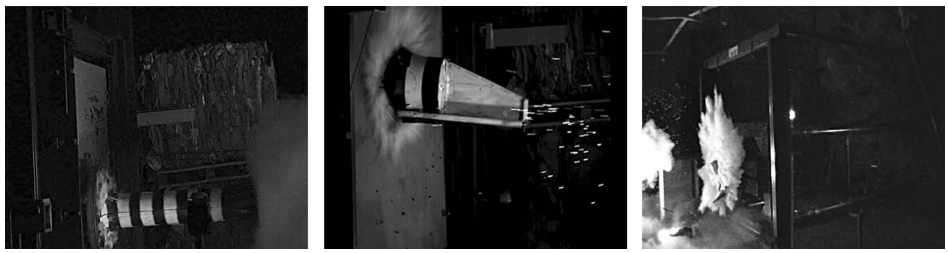

Fig. 16. Side view images of liquid dispersion pattern in selected VTT impact tests (note that each image is taken from different tests).

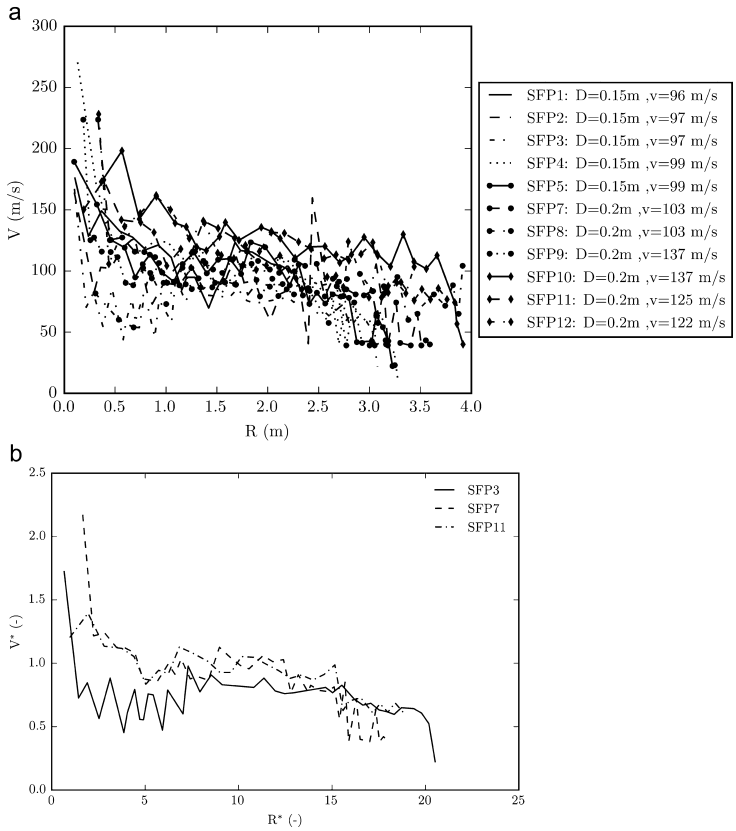

Fig. 17. Spray front velocities of tests SFP1-SFP12 (a), and the normalised velocities of three selected tests (b).

3.2. Droplet imaging

Images from the ultra-high-speed video cameras were used to analyse the general characteristics of the spray, droplet velocities and drop size distributions. When analysing the results, one must remember that the images were taken inside the protective box after the flow had entered through a 20 mm gap, which allowed only a small proportion of the spray to enter the measurement region. Both the radial spread and the ejection angle of the spray affected the amount of water that entered the measurement region.

Fig. 20 shows three individual images of the spray passing by the SA-1.1 camera in test SFP11. The first image was taken 0.6 ms after the first droplets were observed, representing the early part of the spray. The second image was taken 0.4 ms later and already represents a very dense part of the spray. Dozens of droplets could be detected from this image using the image analysis software, although with the naked eye it is difficult to observe any droplets at all. The third image was taken 24 ms after the arrival of the spray. It represents the bulk of the spray. Fig. 21 shows three images from test SFP12, taken by the SA-X camera. In these images, the initial spray front is seen as a dark area consisting of both in-focus and out-of-focus droplets.

Table 4 shows the main spray characteristics for test SFP2-SFP12. The droplet velocities are reported as the maximum velocity, the peak of mean velocity and the peak of rms velocity. Time series of the mean velocities and the rms velocities were computed with 15 ms time classes. The peak values of the mean and rms droplet velocities correspond to the maxima of these time series. Maximum droplet velocity is the maximum velocity of an individual droplet observed in the test. The mean droplet size is reported as the arithmetic mean, Sauter mean and the volumetric mean over the whole measurement period.

The maximum and peak mean droplet velocities are plotted as a function of the impact velocity in Fig. 22. There is almost no correlation between the average droplet velocity and the impact velocity, whereas there is an almost perfect correlation between the impact velocity and the maximum observed droplet velocity. The maximum observed droplet velocities most likely belong to large liquid fragments that are relatively sparse in the spray. Their effect on the average velocity is therefore very small. The average value is dominated by the small droplets, which in turn are likely to travel at velocities that are very close to their terminal velocities. The observed mean droplet velocities are thus heavily influenced by the local gas phase velocities. As far as the projectile wall thickness has any effect, the current sample size is too small for detecting this effect.

3.3. Droplet size distributions

Fig. 23 shows the time histories of the three mean diameters and the spray number concentration in three of the tests. The time in these figures starts when the spray front arrives in the measurement location. In all three tests, the initially high number concentration is followed by a long, relatively diluted tail. The

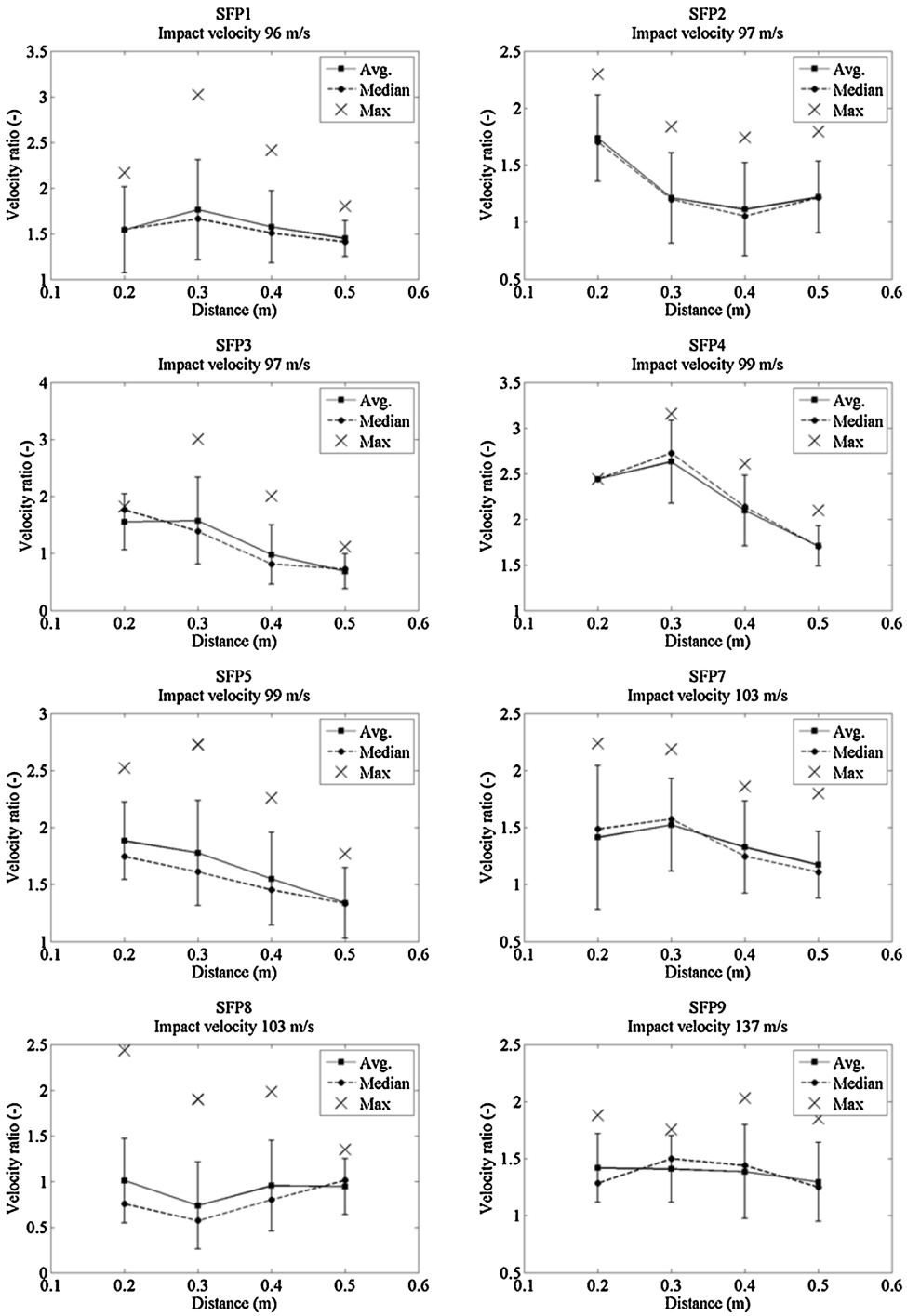

Fig. 18. Liquid front velocity near the projectile: median, average with error bars indicating the standard deviation and maximum values.

Table 4
Average droplet speed and size as function of projectile parameters.

Test ID	Water mass (kg)	Wall thick-ness (mm)	Impact velocity (m/s)	Maximum droplet velocity (m/s)	Peak mean droplet velocity (m/s)	Peak RMS droplet velocity (m/s)	d_{10} (μs)	d_{32} (μs)	d_{43} (μs)
SFP2	37.1	1.50	97.3	107	63.4	24.4	96	208	262
SFP3	24.7	1.50	96.6	103	39.0	12.3	78	180	152
SFP4	24.8	1.50	98.7	103	51.3	19.5	61	147	116
SFP5	24.7	1.50	99.3	101	24.0	14.8	55	153	190
SFP7	36.8	1.50	103	116	34.4	19.4	67	344	254
SFP8	37.2	2.00	99.7	100	26.3	18.4	53	253	183
SFP11	37.0	1.50	126	130	54.6	27.8	39	316	372
SFP12	37.0	2.00	122	127	43.3	24.0	49	237	223

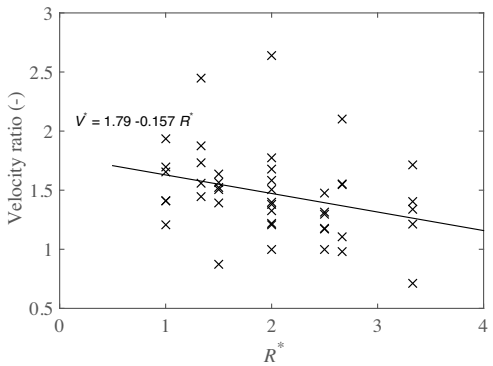

Fig. 19. Normalised velocity as a function of normalised distance from the impact location.

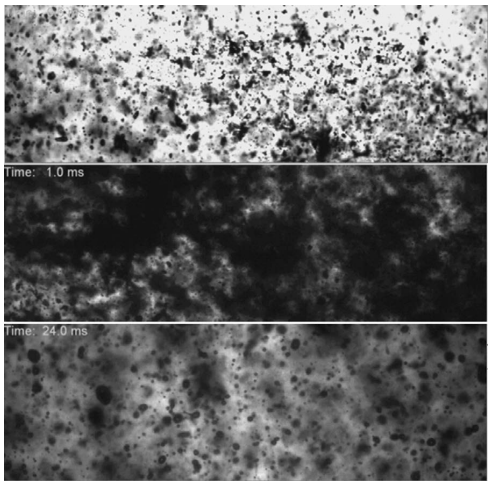

Fig. 20. Images from the ultra-high-speed video (larger image area) of test SFP11.

number mean diameter d_{10} shows a flat or decreasing trend for the three examined tests. The trends for the volume-weighted means d_{32} and d_{43} show a greater variance. The variance is lower for approximately the first 50 ms of observations. This phase is followed by a noisy phase indicating heterogeneous spray consisting of secondary spray fronts, residual mist and large water fragments. Both d_{32} and d_{43} place more weight on the large droplets. They are thus more sensitive to the existence of large liquid fragments, which can cause fluctuations in the resulting time series. In our experiments, even the smallest observed mean diameters were

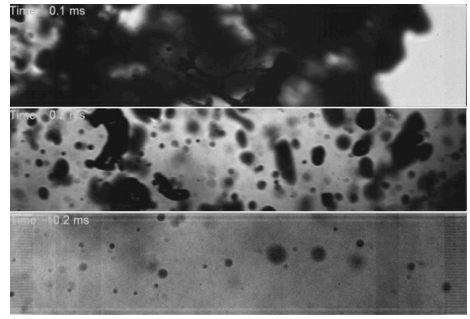

Fig. 21. Images from the ultra-high-speed video (larger image area) of test SFP12.

larger than the SNL results for the diameters of the residual mist droplets, being in the range of between 6 and 13 μm.

The plots in Fig. 24 show the time histories of the droplet velocity and the normalised cumulative mass flux in three selected tests. The normalised cumulative mass flux is calculated using the average droplet velocity and the measured concentration. The result is normalised using the accumulated observed mass from the whole duration of the measurements. This quantity can be used to approximate the fraction of the total spray volume that is contained by the various stages of the spray. In the three tests, between 60 and 90% of the spray mass passes the measurement location during the first 50 ms. The fluctuating parts of the diameter time series in Fig. 23 are thus related to the residual parts of the spray containing relatively little mass.

The classical approach for modelling the droplet size distributions is to fit an analytical distribution to the experimental data. Several choices for the droplet size distribution are available in the literature (see e.g. Babinsky and Sojka, 2002). Here we focused on three different analytical distributions: Rosin–Rammler distribution, the log-normal distribution and the combination of the Rosin–Rammler and log-normal distributions. These three distributions were chosen because they are available for modelling the droplet size distributions in the CFD software Fire Dynamics Simulator, which is commonly used in the fire safety engineering community (McGrattan et al., 2012).

The Rosin–Rammler distribution was originally developed for modelling the size distribution of the coal particles, but has been widely used for modelling spray droplet size distributions (Babinsky and Sojka, 2002). The log-normal distribution is usually considered as a model for the cumulative number fraction (CNF). Here it is used as a model for the cumulative volume fraction (CVF) instead. The combination of these two distributions, called Rosin–Rammler-log-normal distribution, has been found to describe the droplet sizes in sprinkler sprays, and is commonly used among fire safety engineers.

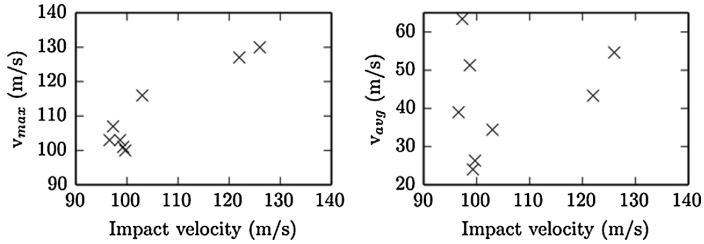

Fig. 22. Effect of impact velocity on measured droplet velocities. The maximum observed particle velocity on the left and the peak value of mean droplet velocity on the right.

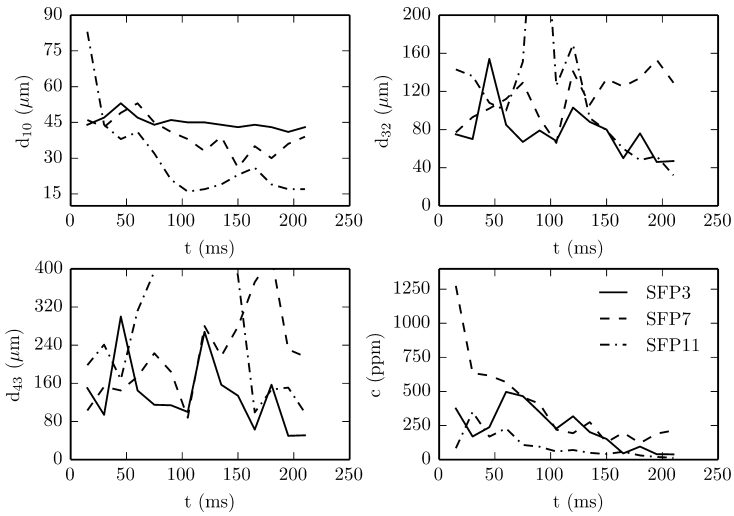

Fig. 23. Mean, Sauter mean, volumetric mean droplet diameters and the spray concentration as a function of time for three selected tests. Time starts from the moment the spray front arrives at the measurement location.

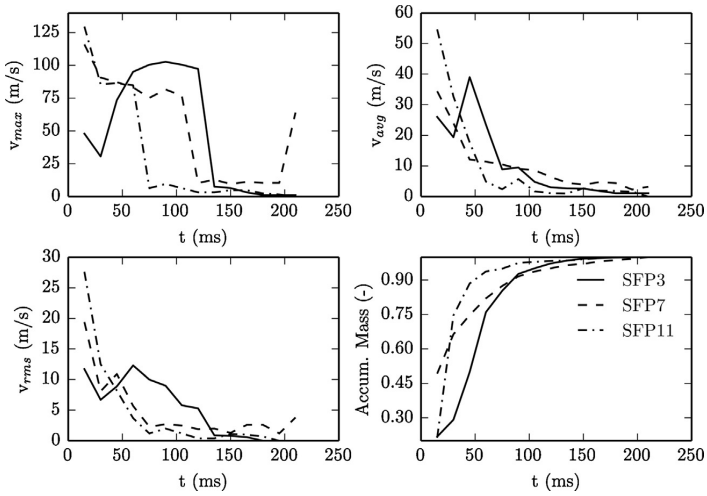

Fig. 24. Trends of measured droplet velocity at measurement location. Top left: maximum droplet velocity, top right: average droplet velocity. Bottom left: variance of droplet velocity. Bottom right: Normalised accumulated mass of water.

Table 5
Fitted distribution parameters.

Experiment		Distribution					
		Rosin–Rammler		Rosin–Rammler-Log-normal		Log-normal	
		d_m (μm)	γ	d_m (μm)	γ	d_m (μm)	σ
SFP 2-5	Whole	80	0.89	78	0.86	77	1.12
	Front	90	1.03	87	0.98	85	0.98
	Continuous	80	0.87	78	0.85	77	1.14
SFP 7-12	Whole	101	1.04	99	1.01	98	0.96
	Front	84	1.42	82	1.33	80	0.76
	Continuous	105	1.01	103	0.98	101	0.98
All	Whole	85	0.93	83	0.89	82	1.08
	Front	88	1.09	85	1.03	84	0.94
	Continuous	86	0.90	84	0.87	83	1.10

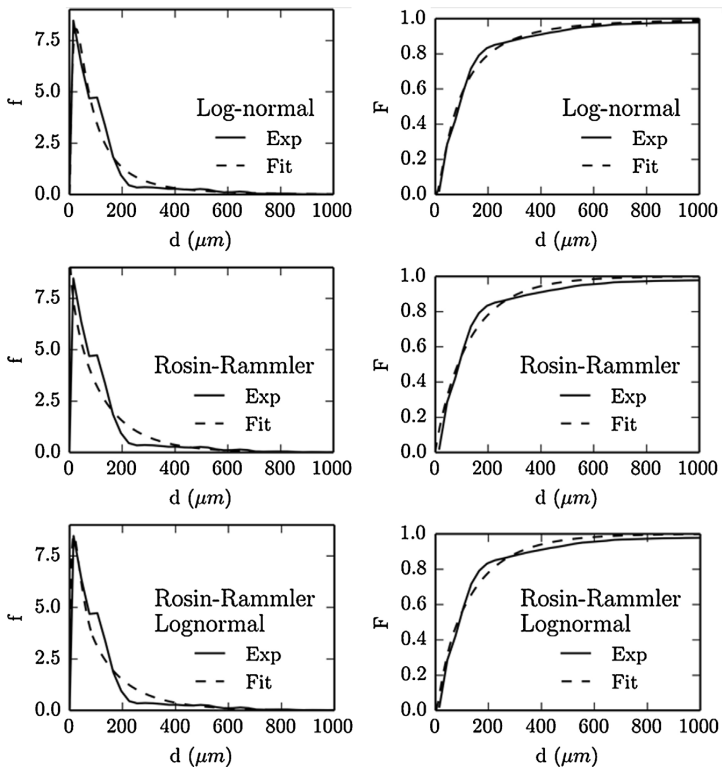

Fig. 25. Comparisons of fitted distributions with experimental data. On the left: probability density functions. On the right: cumulative density functions. Continuous lines show the experimental distributions averaged over all experiments. Dashed lines show the fitted distributions.

Rosin–Rammler distribution:

$$F(d) = 1 - \exp\left[-0.693\left(\frac{d}{d_m}\right)^{\gamma}\right] \tag{4}$$

Log-normal distribution:

$$F(d) = \frac{1}{\sqrt{2\pi}} \int_{\sigma d'}^{d'} \exp\left[\frac{\log\left(\frac{d'}{d_m}\right)^2}{2\sigma^2}\right] \tag{5}$$

Rosin–Rammler–Log-normal combination:

$$F(d) = \left\{ \begin{array}{ll} 1 - \exp\left[-0.693\left(\frac{d}{d_m}\right)^{\gamma}\right], & d > d_m \\ \frac{1}{\sqrt{2\pi}} \int_0^a \frac{1}{\sigma d'} \exp\left[-\frac{\log\left(\frac{d'}{d_m}\right)^2}{2\sigma^2}\right], & d > d_m \end{array} \right\} \tag{6}$$

where d_m is the volumetric median diameter of the size distribution (half of the volume of the particles is in droplets smaller than this).

In the analysis, the first 15 ms of the observations were assumed to belong to the spray front. Using this definition, the spray

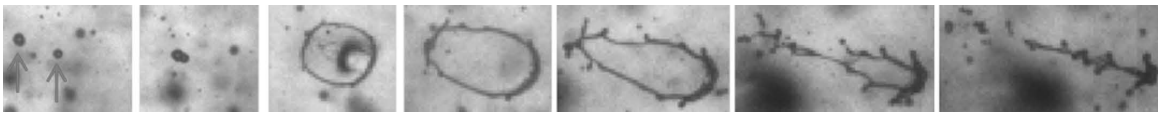

Fig. 26. Collision of two droplets with a velocity difference of 20 m/s (in SFP5). Time between each image is 20 μs.

front contained approximately 20% of the total mass of the spray (approximated from measured volume fractions). The continuous spray is the rest of the spray. The resulting size parameters are shown in Table 5.

Fig. 25 compares the fitted volumetric density distributions with the experimental data that was combined from all the experiments. The fitted distribution functions cannot capture all the features of the experimentally determined distributions. In particular, the experimental distributions have a sharp spike at the small particle diameters, followed by a long tail. The log-normal distribution function can reproduce this behaviour most accurately. The Rosin–Rammler distribution significantly over-predicts the number of very small particles. In experiments SFP2-7, the continuous part of the spray contained large droplets, which increased the estimates of the volumetric median diameter d_m.

The droplet size results can be analysed in the light of the existing literature of the spray atomisation process. The most important parameter for the droplet formation is the relative speed between the liquid and the surrounding gas. Although convenient for computational models, this parameter is difficult to determine from experiments where the observations are made for absolute droplet velocities without the knowledge of the speed of the gas moving along the spray. In the impact scenario, the spray front is penetrating into the (practically) still air, and thus the spray front speed measurements can be used to estimate the largest possible stable droplet size. According to one of the commonly used theoretical models for the secondary break-up (Reitz, 1987), the stable water droplet size at the speed of 170 m/s (corresponding to the initial spray from an 100 m/s impact) is about 30 μm. The 1 mm-sized droplets in the spray front statistics (Fig. 25) can be seen as an indication of much lower relative speeds (as low as 30 m/s). Alternatively, it can mean that the break-up process is unfinished, and the observed distribution is still developing. Indeed, the shapes of the first water fronts in Figs. 20 and 21 indicate that the water is still in the form of large fragments, not a mist consisting of spherical droplets. As the time scale of the break-up process (∼1 ms) is shorter than the travel time from the impact position to the measurement location (∼20 ms), the existence of large droplets at the measurement location indicates a complicated flow phenomenon where the first front of water always enters still air, meets a high drag and is then broken down to relatively small droplets of a few tens of microns. The momentum of these small droplets is low, and they are quickly decelerated and eventually passed by larger, faster-moving droplets. At the same time, the air speed within the impact spray is accelerated and the relative speed of the droplets leaving the impact position behind the initial front is significantly lower than the relative speed at the first front. The existence of the different droplet velocities is demonstrated in Fig. 26, which shows a sequence of images where two droplets (highlighted by the arrows in the first image) collide with a relative velocity of 20 m/s. The collision is caused by the velocity difference, and it is found to create plenty of micro-droplets. The time between each image is 20 μs.

Despite the uncertainties associated with the measured spray characteristics, the measured distributions can be used to serve as boundary conditions for the CFD analyses of the liquid spreading from impact scenarios. Making an analysis of the aircraft impact fires naturally requires a consideration of the effect of the liquid type on the spray formation process. However, the geometrical and other variations of the real impact scenarios are likely to dominate the uncertainties over the difficulties of prescribing droplet size and speed distributions for fuel droplets.

4. Conclusions

In this article, we presented the experimental characterisation of liquid sprays resulting from high-speed impacts of liquid-filled projectiles against a hard wall. The experiments were carried out using water-filled aluminium and stainless steel projectiles at speeds of between 96 and 169 m/s. The results provide us with the necessary data for analysing the consequences of such events in the context of nuclear power plant safety analyses. In practice, the results can be used to prescribe the boundary conditions for detailed CFD analyses of aircraft impact fires and to validate the simulation tools and methodologies.

The overall shape and speed of the liquid spray was investigated using high-speed video cameras. The images taken from the direction of arrival indicate that the cylindrical projectiles produce a very symmetrical spray. Adding liquid-filled 'wings' to the projectile increased the proportion of liquid leaving in vertical directions. The images taken from the side of the impact indicate that initially the spray is retained at angles of between 0 and 20–40° from the wall tangent. After some distance, the angle of spray propagation gets smaller, presumably due to the one-sided air entrainment. As a result, the global shape of the impact spray is a flat disc spreading in the direction of the target wall tangent. This observation was consistent with the larger scale results in the literature. Behind the leading spray front, the spray was found to consist of sequential waves following each other. It is not clear at the moment if the waves were generated in the eruption process or as a result of the liquid–gas interactions, but they have a clear role in the hydrodynamic process of fast spray penetrating into still air.

The speed of the liquid spray front was determined from the high-speed video images. The initial spray speed ranged between 1.5 and 2.5 times the impact velocity, being 1.7 ± 0.25 on average. The spray front deceleration rate was found to be about 16% when it travelled a distance of one projectile diameter. Dependence of the spray speed on the experimental parameters, such as the impact speed or the projectile wall material, could not be confirmed.

Time series of droplet size and velocity distributions in the spray were successfully measured using two ultra-high-speed cameras. The image sequences at 40,000–100,000 Hz were illuminated with pulsed diode lasers in backlight configuration. A two-camera approach allowed the size and velocity measurement of small and large droplets at the same time, with a size range of 12–2500 μm. We could, however, visually observe droplets that were even smaller than 10 μm in the images. Droplet concentration was also estimated, although the measurement clearly underestimated the droplet concentration in the dense spray front. It was impossible to analyse all droplets that passed the measurement volume, because the visibility of the measurement volume was often blocked by large liquid fragments.

The measurement results revealed many interesting details in the spray. The ratio of the maximum measured droplet velocity and the impact velocity was near unity for all test cases at the measurement location two metres from the impact point. The droplets within the spray front moved slightly more quickly in the case

of the thin-wall projectile in comparison to the thick-wall projectile. Higher impact velocity caused smaller droplets: the mean droplet diameter of 78 μm was obtained with the impact velocity of 97 m/s, whereas at 126 m/s the mean of 39 μm was achieved. The droplet velocities dropped quickly after the spray front and a turbulent flow regime was formed. Plenty of micro-droplets and large droplets were detected, indicating a high collision rate of droplets. All tests included secondary spray fronts that caused the scatter in the measured time trends.

The collected information about the initial droplet direction, speed and size distribution can be used to specify the boundary conditions for the CFD simulations investigating the dynamics of the aircraft impact fires. Such simulations are obviously very challenging, and careful verification and validation processes are needed to ensure the reliability of predictions. The collected information about spray propagation dynamics can be used for validation purposes.

To date, the only liquid to be used is water. More comprehensive validation of the simulation technologies requires well-documented experiments with projectiles filled with a well-characterised hydrocarbon fuel. For the full validation of the spray combustion calculations, experimental sprays should be ignited. The current results form a good basis for designing such experiments, although the safety aspects will certainly pose practical limitations. Other topics of future research include the mechanical conditions leading to the penetration of liquid through the structure, and the characterisation of the sprays in such situations.

Acknowledgements

We would like to thank all the VTT employees who contributed to the successful test campaigns over the years. Special thanks for experimental arrangements go to Ilkka Hakola, Matti Halonen, Jouni Hietalahti, Erkki Järvinen and Jukka Mäkinen from VTT, and Juha Juntunen and Leo Lapinluoma from VTT Expert Services Oy. This work was funded by the the State Nuclear Waste Management Fund (VYR) within the Finnish national research programmes for the nuclear safety (SAFIR).

Appendix A. Supplementary data

Supplementary data associated with this article can be found, in the online version, at http://dx.doi.org/10.1016/j.nucengdes.2015.09.008.

References

Abbasi, T., Abbasi, S.A., 2007. The boiling liquid expanding vapour explosion (BLEVE): mechanism, consequence assessment, management. J. Hazard. Mater. 141, 489–519.

Ahlers, R.H., 1977. Full-scale aircraft crash tests of modified jet fuel. In: No. FAA-NA-77-35. National Aviation Facilities Experimental Center, Atlantic City, NJ.

Anghileri, M., Castelletti, L.-M.L., Tirelli, M., 2005. Fluid-structure interaction of water filled tanks during the impact with the ground. Int. J. Impact Eng. 31 (2005), 235–254.

Canny, J.A., 1986. Computational approach to edge detection. IEEE Trans. Pattern Anal. Machine Intell. 8 (6), 679–698.

Babinsky, E., Sojka, P.E., 2002. Modeling drop size distributions. Prog. Energy Combust. Sci. 28 (4), 303–329.

Fasanella, E.L., Jackson, K.E., 2001. Crash simulation of a vertical drop test of a B 737 fuselage section with auxiliary fuel tank. In: Third Triennial International Fire & Cabin Safety Research Conference, Atlantic City, NJ, October 22–25, 2001.

Fdida, N., Blaisot, J.-B., 2010. Drop size distribution measured by imaging: determination of the measurement volume by the calibration of the point spread function. Meas. Sci. Technol. 21, 025501.

Field, J.E., Dear, J.P., Ogren, J.E., 1989. The effects of target compliance on liquid drop impact. J. Appl. Phys. 65 (2), 533–540.

Knežević, K.H., 2002. High-Velocity Impact of a Liquid Droplet on a Rigid Surface: The Effect of Liquid Compressibility, Doctoral thesis. Swiss Federal Institute of Technology, Zurich (DISS. ETH NO. 14826).

Kärnä, T., Saarenheimo, A., Tuomala, M., 2004. Impact loaded structures. In: SAFIR, the Finnish Research Programme on Nuclear Power Plants Safety. Interim Report. VTT Publications 2272, Espoo, pp. 113–122.

Jepsen, R.A., O'Hern, T., Demosthenous, B., Bystrom, E., Nissen, M., Romero, E., Yoon, S.S., 2009. Diagnostics for liquid dispersion due to a high-speed impact with accident or vulnerability assessment application. Meas. Sci. Technol. 20, 1–12.

Johnson, D., Garodz, L., 1986. Crashworthiness experiment summary - full-scale transport controlled impact demonstration program. In: No. DOT/FAA/CT-85/20. Federal Aviation Administration Technical Center, Atlantic City, NJ.

Lastunen, A., Hakola, I., Järvinen, E., Calonius, K., Hyvärinen, J., 2007. Impact Test Facility. In: International Conference on Structural Mechanics in Reactor Technology 19, Toronto, Paper # J08/2.

Luther, W., Müller, W.C., 2009. FDS simulation of the fuel fireball from a hypothetical commercial airliner crash on a generic nuclear power plant. Nuclear Engineering Design 239, 2056–2069.

McGrattan, K., McDermott, R., Floyd, J., Hostikka, S., Forney, G., Baum, H., 2012. Int. J. Comput. Fluid Dyn., 1–13.

Minor, L.G., Sklansky, J., 1981. The detection and segmentation of blobs in infrared images, systems, man and cybernetics. IEEE Trans. 11, 194–201.

Muto, K., Sugano, T., Tsubota, H., Kasai, Y., Koshika, N., Suzuki, M., Ohrui, S., von Riesemann, W.A., Bickel, D.C., Parrish, R.L., 1989. Full-scale aircraft impact test for evaluation of impact forces: Part 2: Analysis of results. In: International Conference on Structural Mechanics in Reactor Technology 10, Anaheim, CA.

Ouellette, N.T., Xu, H., Bodenschatz, E., 2006. A quantitative study of three-dimensional Lagrangian particle tracking algorithms. Exp. Fluids 40, 301–313.

Pinkel, I.I., Preson, G.M., Pesman, G.J., 1953. Mechanism of start and development of aircraft crash fires. National Advisory Committee for Aeronautics, naca-report-1133.

Reitz, R.D., 1987. Modeling atomization processes in high-pressure vaporizing sprays. Atomisation Spray Technol. 3, 309–337.

von Riesemann, W.A., Parrish, R.L., Bickel, D.C., Heffelfinger, S.R., Muto, K., Sugano, T., Tsubota, H., Koshika, N., Suzuki, M., Ohrui, S., , 1989. Full-scale aircraft impact tests for evaluation of impact forces: Part 1. Test plan, test method, and test results. In: International Conference on Structural Mechanics in Reactor Technology 10, Anaheim, CA.

Silde, A., Hostikka, S., Kankkunen, A., 2011. Experimental and numerical studies of liquid dispersal from a soft projectile impacting a wall. Nucl. Eng. Des. 241, 617–624.

Sugano, T., Tsubota, H., Kasai, Y., Koshika, N., Orui, S., von Riesemann, W.A., Bickel, D.C., Parks, M.B., 1993. Full-scale aircraft impact test for evaluation of impact force. Nucl. Eng. Des. 140, 373–385.

Tieszen, S.R., 1997. Post-crash fuel dispersal. In: Workshop on Aviation Fuels with Improved Fire Safety, PBD, Washington DC, November 19–20, 1997.

Vepsä, A., Saarenheimo, A., Tarallo, F., Rambach, J.-M., Orbovic, N., 2012. Impact tests for IRIS_2010 benchmark exercise. J. Disaster Res. 7 (5), 619–628.

Yarin, A.L., 2006. Drop Impact Dynamics: Splashing, Spreading, Receding Bouncing. Annu. Rev. Fluid Mech 38, 59–92, http://dx.doi.org/10.1146/annurev.fluid.38.050304.092144.

III

Nuclear Engineering and Design 318 (2017) 147–162

Contents lists available at ScienceDirect

Nuclear Engineering and Design

journal homepage: www.elsevier.com/locate/nucengdes

Numerical simulations of liquid spreading and fires following an aircraft impact

Topi Sikanen [a,*], Simo Hostikka [b]

[a] VTT Technical Research Centre of Finland Ltd, P.O. Box 1000, FI-02044 VTT, Finland
[b] Aalto University, Espoo, Finland

HIGHLIGHTS

- Methodology for simulating fires resulting from aircraft impact was developed.
- The methodology was validated using experimental data.
- Large scale simulations of aircraft impact on a nuclear island were conducted.
- The fraction of fuel available for subsequent fires was found to be significant.
- The pooling fraction was strongly affected by impact geometry.

ARTICLE INFO

Article history:
Received 22 July 2016
Received in revised form 4 April 2017
Accepted 7 April 2017
Available online 20 April 2017

Keywords:
Fireball
Plane crash
Physical separation
Fuel pooling
Nuclear power plant

ABSTRACT

In this paper, we present a methodology for predicting the spreading and combustion of liquid fuel released from an aircraft impact. Calculations were done with Fire Dynamics Simulator, and the aircraft impact was modeled as a spray boundary condition. The spray boundary condition was developed and validated by experiments using water-filled missiles. The predicted liquid front speeds were compared with water spray front propagation data, and the predicted lifetimes and diameters of fireballs were compared with experimental correlations. A full-scale simulation of the aircraft impact on a nuclear island was performed. The simulation results were used to assess the adequacy of physical separation in the case of aircraft impact. We concluded that 10%–20% of the fuel involved in the crash will accumulate in pools around the building.

1. Introduction

Safety analyses of nuclear power plants (NPPs) have long included aircraft impacts. Initially, the impact was envisioned to be from a small aircraft or possibly a fighter plane. Following the September 11 terrorist attacks on the World Trade Center in 2001, these analyses have been extended to assume the impact of a large commercial aircraft (e.g. NEI 07-13, 2011).

Such an aircraft can damage safety-related structures and components through mechanical impact and fire. Fires induced by an aircraft impact may influence the NPP by three different mechanisms. Initially, a large fireball is created by the fuel cloud erupting from the breaking fuel tanks. This fireball has a duration of few seconds and can be hundred meters in diameter. The most serious threat from a fireball to its surroundings is thermal radiation. The dose of thermal radiation received by a target is dependent on the size and duration of the fireball.

Only a fraction of the fuel carried by the plane will burn in the initial fireball. The remaining fraction of the fuel will accumulate and burn in pools near the aircraft impact position. The size and burning rate of the pool fire depend on the geometry, properties of the roof and ground surfaces, and possible fire suppression activities.

The third mechanism involves the penetration of aviation fuel inside the plant through openings. These openings may exist beforehand (e.g., for ventilation) or be created by the aircraft impact. Even if the amount of penetrated fuel is small, it can cause a rapid ignition of existing fire loads to result in internal fires.

The literature on aircraft impacts involving fuel is scarce. Early test series by the Federal Aviation Administration (FAA) and National Advisory Committee for Aeronautics (NACA) using belly-landing aircraft demonstrated that fuel spilled from ruptured tanks forms a fine mist cloud that can be ignited by several sources

* Corresponding author.
E-mail addresses: Topi.Sikanen@vtt.fi (T. Sikanen), simo.hostikka@aalto.fi (S. Hostikka).

http://dx.doi.org/10.1016/j.nucengdes.2017.04.012
0029-5493/

(Pinkel et al., 1952; Ahlers, 1977; Johnson and Garodz, 1986). Experiences from numerous real crash incidents such as the September 11 terrorist attacks support this observation. Luther and Müller (2009) analyzed the film footage of aircraft crash fireballs. They discovered that these fireballs are very similar to those resulting from boiling liquid expanding vapor explosions (BLEVEs). However, none of the analyzed accidents included an impact on a rigid vertical structure, such as modern NPPs.

Several experimental correlations exist for determining the diameters and lifetimes of fireballs resulting from BLEVEs. Abbasi and Abbasi (2007) gave an excellent review of the hand calculation methods used to model BLEVEs. These methods can also be used to analyze fireballs from aircraft impacts. However, they cannot be used to estimate the fraction of unburnt fuel.

Baum and Rehm (2005) proposed a model for the global energy release rate of fireballs. They calibrated their model by comparison with videos of the WTC fireballs and used it to estimate the fuel involved in the subsequent fires. They found that most of the fuel carried by the airplanes did not burn in the initial fireball and was available for fires that destroyed the buildings. This result was likely to have been a consequence of the airplane penetrating the outer wall of the building.

Considering the complexity of the three above mechanisms, their analyses cannot rely on empirical formulas derived from idealized situations but on transient numerical simulations of the fuel spray and combustion.

Fireballs resulting from vertical fuel gas releases were investigated numerically by Makhviladze et al. (1998). Makhviladze et al. (1999) extended this model to investigate two-phase fuel releases from pressurized containers of liquefied gas. Their model solves two-dimensional Favre-averaged Navier–Stokes equations by using the standard k-ϵ turbulence model and infinitely fast one-step reaction. The dispersed phase is treated in a Lagrangian fashion. They assumed a monodisperse droplet size distribution with the initial velocities of the droplets derived from Bernoulli's law. They compared the predicted lifetimes of fireballs with the experimental correlation of Roper et al. (1991), and they compared the transient shapes and sizes of the fireballs with the experiments of Hasegawa and Sato (1978). Makhviladze and Yakush (2005) used this model to analyze total loss of containment scenarios for BLEVEs. They also investigated the overpressures that would occur in such events.

Yakush and Makhviladze (2005) compared Reynolds-averaged Navier–Stokes (RANS) and large eddy simulation (LES) predictions of the fireball lifetime with the experimental correlation of Roper et al. (1991). They used Fire Dynamics Simulator (FDS) version 4 for the LES calculations. FDS was found to underestimate the fireball lifetimes. The fuel release was modeled with a gas inflow boundary condition. Hu and Trouve (2008) used a modified version of FDS to investigate deflagrations of premixed fuel vapor clouds. They did not consider high speed jets. Instead the vapor clouds were created by slowly injecting gas to the simulation domain. Luther and Müller (2009) used FDS version 5 to determine the spreading and extent of the fireball around a generic NPP. They also modeled the fuel insertion by using a gas inflow boundary condition.

In the above fireball simulations, the fuel inlet boundary condition consisted of either a vertical spray or injection of fuel gas from a boundary patch. Initial velocities of the gas and droplets have been based on, for example, the theoretical calculations of flash evaporation. When multiphase models have been used, droplet sizes have been assumed to be monodisperse. The possibility of fuel droplets raining out of the fireball has usually been neglected. This may be because of the highly volatile liquids such as liquefied natural gas (LNG) and propane that are being considered.

Analysis of footage of real aircraft crashes and the results of Baum and Rehm (2005) indicated that, in aircraft crashes, a significant amount of the fuel may not be burned in the initial cloud. In the case of an aircraft crash, part of the fuel released is traveling towards the ground and walls. The fuels involved are also less volatile. This means that fuel droplets may rain out of the burning cloud.

In some of the published analyses, such as that of Jeon et al. (2012), the amount of fuel burning as a pool has simply been assumed to be equal to the amount of fuel carried by the aircraft. This kind of assumption is conservative and well-justified if better information is not available. Predicting the amount of fuel available for pool fires requires accurate modeling of the fuel sprays from ruptured tanks of liquid fuel.

Brown et al. (2012) coupled a transient dynamics code Presto to a low-Mach number fire code Fuego in order to predict the liquid dispersion from a high speed impact. They used Smoothed Particle Hydrodynamics (SPH) to predict the motion of liquid within the tank on impact. The particles from the SPH solution were then transferred to the fire code once the distance between the particles dropped under a certain threshold level. They found that their model was able to reasonably reproduce the quantified results of the experiments of Jepsen et al. (2009). These results consists mainly of liquid dispersal patterns. Brown et al. (2014) noted that the method still lacks validation, especially concerning the evolution of droplet size.

The objective of this work was to develop and validate a computational fluid dynamics (CFD) methodology for predicting the spreading and combustion of liquid fuel released upon an aircraft impact. The model for liquid release is based on the experimental work of Hostikka et al. (2015). The experimentally determined droplet sizes and spray velocities were used to determine realistic spray boundary conditions for liquid insertion. We focused on the threat posed by the initial fireball and amount of fuel that collects on the target surfaces. The subsequent combustion of the pools was not considered.

This paper is organized as follows. First, the numerical model is presented. Next, the boundary condition describing the fuel release is presented with experimental data. The validation of the numerical model against experiments and correlations is given next. First, the shape and size of the droplet cloud predicted by the model is qualitatively compared with photographs from the Sandia F-4 impact experiments. The predicted spray front velocities are then compared with experimental data. The predicted lifetimes and diameters of the two-phase fireballs are compared with the experimental correlations. Finally, we present the results from a full-scale simulation of an aircraft impact on a nuclear island. The simulation results were used to evaluate the adequacy of physical separation. We also examine the fraction fuel that will burn as a pool.

2. Computational method

All simulations in this study were done by using FDS (McGrattan et al., 2013a, 2012; McDermott, 2014), which is an LES code that solves a form of the Navier–Stokes equations appropriate for a low-speed and thermally driven flow with an emphasis on smoke and heat transport from fires. The governing equations for momentum transport are discretized by second-order central finite differences on a Cartesian staggered grid. A two-stage explicit Runge–Kutta method is used for time-stepping. Radiative heat transfer is included in the model via the solution of the radiation transport equation (RTE) for a gray gas. The RTE is solved by a finite volume method. The governing equations are presented here for completeness. More detailed descriptions of the model and numerical procedure are given by McGrattan et al. (2013a, 2012) and McDermott (2014).

2.1. Gas phase model

The governing equations solved by FDS are the continuity, species mass conservation, momentum, energy, and ideal gas equations of state:

$$\frac{\partial \rho}{\partial t} + \nabla \cdot \rho \mathbf{u} = 0 \tag{1}$$

$$\frac{\partial \rho Y_\alpha}{\partial t} + \nabla \cdot \rho Y_\alpha \mathbf{u} = \nabla \cdot \rho((\nu + \nu_t)/\mathrm{Sc}_t)\nabla Y_\alpha + \dot{m}'''_\alpha + \dot{m}'''_{\alpha,b} \tag{2}$$

$$\frac{\partial \rho \mathbf{u}}{\partial t} + \nabla \cdot \rho \mathbf{u}\mathbf{u} = -\nabla \tilde{p} + \nabla \cdot \boldsymbol{\tau} + (\rho - \rho_0)\mathbf{g} + \mathbf{f}_b \tag{3}$$

$$\frac{\partial \rho h_s}{\partial t} + \nabla \cdot \rho h_s \mathbf{u} = \frac{D\bar{p}}{Dt} + \dot{q}''' - \nabla \cdot \dot{\mathbf{q}}'' \tag{4}$$

$$\boldsymbol{\tau} = \rho(\nu + \nu_t)\left((\nabla \mathbf{u} + \nabla \mathbf{u}^T) - \frac{2}{3}(\nabla \cdot \mathbf{u}) \right)\mathbf{I} \tag{5}$$

$$\dot{\mathbf{q}}'' = \left(\rho c_p(\nu + \nu_t)/\mathrm{Pr}_t\right)\nabla T + \sum_\alpha \rho((\nu + \nu_t)/\mathrm{Sc}_t)h_\alpha \nabla Y_\alpha + \dot{q}''_r \tag{6}$$

$$\rho = \frac{\bar{p}W}{RT}. \tag{7}$$

Here, ρ is the density, $\mathbf{u}$ is the velocity, Y_α is the mass fraction of the species α, $\dot{m}'''_\alpha$ is the reaction source term, and $\dot{m}'''_{\alpha,b}$ results from droplet evaporation. In Eq. (3), ρ_0 is the ambient density, $\mathbf{g}$ is the gravitational acceleration, τ is the stress tensor, and the term $\mathbf{f}_b$ accounts for the drag force exerted by Lagrangian particles. Because of the low-Mach number assumption, the total pressure p is split into the background pressure $\bar{p}$ and perturbation $\tilde{p}$. Only the background pressure is retained in the equation of state, where R is the universal gas constant and W is the molar mass of the gas mixture. In Eq. (4), h_s is the specific enthalpy, and $\dot{q}'''$ is the source term from the combustion reaction. The heat flux vector $\dot{\mathbf{q}}''$ represents the conductive, diffusive, and radiative heat fluxes.

The turbulent viscosity ν_t is based on the eddy viscosity model of Deardorff (1972). The turbulent Schimdt and Prandtl numbers (Sc_t and Pr_t) were assumed to be constant and equal to 0.5.

2.2. Combustion

Jet fuels are complicated mixtures of various hydrocarbon fuels. However, at the time of writing FDS was not able to handle multicomponent fuel evaporation. Therefore a single surrogate species was selected. All simulations in this study were performed by using n-heptane as a combustible liquid, which was evaporated into the gas phase heptane C_7H_{16}. The gas phase combustion was assumed to yield 1.5% soot and 0.8% carbon monoxide. The gas phase combustion was treated by a single-step mixing-controlled chemical reaction scheme using three lumped species: air, fuel, and products.

The chemical heat source term in Eq. (4) is obtained from

$$\dot{q}''' = \dot{m}'''_f \Delta h_c \tag{8}$$

where Δh_c is the heat of combustion of the fuel. The rate of combustion is given by a model similar to the eddy dissipation concept (EDC) model (Magnussen and Hjertager, 1977)

$$\dot{m}'''_f = -\rho \frac{\min\left(Y_f, Y_o/s\right)}{\tau_{mix}} \tag{9}$$

where Y_f and Y_o are the mass fractions of the fuel and oxidizer, respectively. The mixing time scale τ_{mix} is based on the local flow field (McDermott et al., 2011).

2.3. Radiative heat transfer

The contribution of thermal radiation to the energy equation is computed from

$$-\nabla \cdot \dot{q}''_r = \kappa[U - 4\pi I_b(x)]; \quad U = \int_{4\pi} I(x, s')ds' \tag{10}$$

where $I(x, s')$ is the spectrally integrated intensity in the direction s at the location x, I_b is the source term, and κ is the absorption coefficient. The intensity I is obtained as a solution to the radiation transport equation (RTE):

$$s \cdot \nabla I = -[\kappa + \kappa_d + \sigma_d]I + \kappa_d I_{b,d} + \kappa I_b + \frac{\sigma_d}{4\pi}\int_{4\pi} \Phi(s, s')\, I_\lambda(s')\, ds' \tag{11}$$

where κ_d is the droplet absorption coefficient, σ_d is the droplet scattering coefficient, and $I_{b,d}$ is the emission term of the droplets. $\Phi(s', s)$ is a scattering phase function that gives the scattered intensity fraction from the direction s' to s.

The mean absorption coefficient κ is tabulated as a function of the gas species and soot concentration by using the narrow-band model RadCal (Grosshandler, 1993). During simulations, the absorption coefficients are obtained by table lookup. The absorption and scattering coefficients of the liquid droplets are based on Mie theory (See e.g. Siegel and Howell, 2002). The scattering integral is approximated as a sum of isotropic and forward components (Hostikka and McGrattan, 2006). The RTE is solved using the Finite Volume Method for radiation with 104 control angles uniformly spanning the 4π solid angle.

In large-scale fire simulations, the flame sheets cannot be resolved, and the source term in Eq. (10) requires modeling. The source term is computed as follows:

$$I_b(x) = C\frac{\sigma T(x)^4}{\pi}; \quad C = \max\left[1, \frac{\sum_{\dot{q}'''_{ijk}>0}\left(\chi_r \dot{q}'''_{ijk} + \kappa_{ijk} U_{ijk}\right)dV}{\sum_{\dot{q}'''_{ijk}>0}\left(4\kappa_{ijk}\sigma T^4_{ijk}\right)dV}\right] \tag{12}$$

Here, the subscript $_{ijk}$ refers to the value in a computational cell. This ensures that the fraction of energy released as radiation is globally equal to the radiant fraction χ_r. For all simulations in this study, χ_r was assumed to be equal to 0.35.

2.4. Dispersed phase model

If buoyancy, lift, and forces arising from fluid acceleration are neglected, the equation of motion of a single spherical droplet is given by

$$\frac{\partial m_d \mathbf{u}_d}{\partial t} = m_d \mathbf{g} + \rho C_D \pi r_d^2 \|\mathbf{u}_{rel}\|\mathbf{u}_{rel} \tag{13}$$

On the left-hand side, m_d is the mass of the droplet, and $\mathbf{u}_d$ is the velocity of the droplet. On the right-hand side, $\mathbf{u}_{rel}$ is the relative velocity between the droplet and surrounding gas, r_d is the radius of the droplet, and C_D is the drag coefficient. The drag coefficient is given by

$$C_D = \begin{cases} \mathrm{Re}_d/24 & \mathrm{Re}_d < 1 \\ \frac{\mathrm{Re}_d}{24}\left(1 + 0.15\mathrm{Re}_d^{0.683}\right) & 1 < \mathrm{Re}_d < 1000 \\ 0.44 & \mathrm{Re}_d > 1000 \end{cases} \tag{14}$$

where $\mathrm{Re}_d = 2\|\mathbf{u}_{rel}\|r_d/\nu$ is the droplet Reynolds number.

The high-speed sprays considered in this study may sometimes lead to numerical instabilities in the simulations. To ensure that the momentum lost by the droplets is distributed correctly in the

gas, an additional CFL-like condition was placed on the global time step:

$$\Delta t \leqslant C min\left(\frac{u_{d,x}}{\delta x}, \frac{u_{d,y}}{\delta y}, \frac{u_{d,z}}{\delta z}\right) \tag{15}$$

Here, C is a user-defined constant between 1 and 0 and $u_{d,x}, u_{d,y}$, and $u_{d,z}$ are the three components of the droplet velocity $\mathbf{u}_d$.

The mass and energy transfer between the gas and liquid can be described by a coupled set of equations (Cheremisinoff, 1986):

$$\frac{dm_\mathrm{d}}{dt} = -A_\mathrm{d}\, h_\mathrm{m}\, \rho\, (Y_{\alpha,\ell} - Y_\alpha) \tag{16}$$

$$\frac{dT_\mathrm{d}}{dt} = \frac{1}{m_\mathrm{d}\, c_\mathrm{d}}\left[A_\mathrm{d}\, h\,(T - T_\mathrm{d}) + \dot{q}_\mathrm{r} + \frac{dm_\mathrm{d}}{dt}\, h_\mathrm{v}\right] \tag{17}$$

Here, A_d is the surface area of the liquid droplet, h_m is the mass transfer coefficient, c_p is the liquid specific heat, $\dot{q}_\mathrm{r}$ is the rate of radiative exchange, and h_v is the latent heat of vaporization of the liquid. The liquid equilibrium vapor mass fraction is obtained from the Clausius–Clapeyron equation (See e.g. Berry et al., 1980):

$$X_{\alpha,\ell} = \exp\left[\frac{h_\mathrm{v} W_\alpha}{R}\left(\frac{1}{T_\mathrm{b}} - \frac{1}{T_\mathrm{d}}\right)\right]; \quad Y_{\alpha,\ell} = \frac{X_{\alpha,\ell}}{X_{\alpha,\ell}(1 - W_\mathrm{a}/W_\alpha) + W_\mathrm{a}/W_\alpha} \tag{18}$$

where $X_{\alpha,\ell}$ is the equilibrium vapor volume fraction, W_α is the molecular weight of the gaseous species α, W_a is the molecular weight of air, and T_b is the boiling temperature of the liquid.

The heat and mass transfer coefficients in Eq. (17) are given by empirical relationships (Incropera and De Witt, 1996):

$$h_\mathrm{m} = \frac{\mathrm{Sh}\, D_{\ell\mathrm{g}}}{2r_d}; \quad \mathrm{Sh} = 2 + 0.6\, \mathrm{Re}_d^{\frac{1}{2}}\, \mathrm{Sc}^{\frac{1}{3}} \tag{19}$$

$$h = \frac{\mathrm{Nu}\, k}{2r_d}; \quad \mathrm{Nu} = 2 + 0.6\, \mathrm{Re}_d^{\frac{1}{2}}\, \mathrm{Pr}^{\frac{1}{3}} \tag{20}$$

Here, Sh is the Sherwood number, $D_{\ell\mathrm{g}}$ is the binary diffusion coefficient between the liquid vapor and air, Nu is the Nusselt number, and k is the thermal conductivity of the gas.

Due to the large number of droplets in a real spray, only a fraction of these droplets can be tracked in the computation. Therefore, each droplet in the simulation represents a large number (parcel) of real droplets with the same properties. A stratified sampling approach is used to ensure the coverage of the entire droplet size distribution.

3. Model of liquid dispersal from aircraft impact

3.1. Liquid insertion

Our model of an aircraft impact only considers the liquid dispersal from ruptured fuel tanks. The deformation of the missile and ejection of debris are ignored. The fuel dispersal process is modeled as a high-speed spray boundary condition. The model is based on qualitative observations and quantitative characterization of the sprays resulting from high-speed impacts of water-filled missiles (Hostikka et al., 2015).

Droplets are inserted into the simulation on a spherical surface at the distance R from the impact location. The initial position is randomly selected from this surface. All droplets have the same initial speed, but the diameter of the droplets is randomly selected.

Fig. 1 illustrates the shape and parameters of the surface where droplets are inserted. Because FDS cannot model the primary atomization of an ejected liquid, the distance between the spherical surface and impact location should be greater than or equal to the characteristic length scale of missile deformation and primary liquid ejection. Because the secondary breakup is not modeled, the particle distribution should represent a stable particle size distribution.

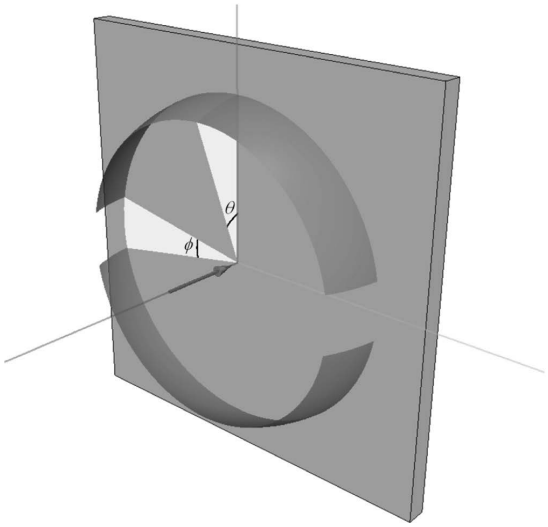

Fig. 1. Spray boundary condition used in simulations of missile and aircraft impacts.

A close examination of the Sandia F-4 impact video footage indicated that no liquid was expelled directly sideways, i.e., in the directions of the wings. Therefore, the pattern in Fig. 1 includes a gap in the spray boundary condition where the wings of the plane would be. The width of this gap is controlled by the angle ϕ, while the width of the droplet insertion band is controlled by θ. For missiles with no wings, the gap may be removed.

The liquid flux is evenly distributed between the two portions. The initial speed u_{ini} of the droplets is given for each portion separately and is assumed to be the same in all directions. The experimental data of Hostikka et al. (2015) indicated that the average droplet speed is 1.8 times the impact velocity at the impact location.

In the experiments of Hostikka et al. (2015), the spray angle θ varied between 7° and 40°. In some earlier experiments, Silde et al. (2011) reported the spray angle to be 15°. In the Sandia phantom crash experiments, the spray spreading angle was 25°. For the simulations in this study, the spray angle θ was assumed to be 25°.

The time during which the droplets are inserted into the simulation was determined from videos and depends on the size of the missile. In cases where video is not available, the liquid release time can be estimated from the impact velocity and liquid tank length.

3.2. Droplet size

Three distributions were fitted to selected portions of the data of Hostikka et al. (2015). The average droplet size distribution for all of the experiments was found to be best described by the log-normal cumulative volume function (CVF):

$$F(d) = \frac{1}{\sqrt{2\pi}} \int_0^d \frac{1}{\sigma \acute{d}} exp\left[-\frac{\left[\ln\left(\acute{d}/d_m\right)\right]^2}{2\sigma^2}\right] d\acute{d} \tag{21}$$

Here, d_m is the volumetric median diameter, while σ is the width parameter. The distribution parameters were found by least-squares fitting Eq. (21) to the experimentally determined

cumulative volume distribution. The best-fitting distribution had the parameters $d_m = 82$ μm and $\sigma = 1.08$. This size distribution was used for all simulations in this study unless stated otherwise.

Because the above mentioned data for the droplet size distributions was determined from experiments conducted with water, we needed to consider the effect of a varying surface tension on the droplet size distribution. Hydrocarbon fuels typically have lower surface tension than water.

The two important dimensionless numbers for analysis of spray atomization and droplet breakup are the droplet Weber number (We) and Ohnesorge number (Oh):

$$\mathrm{We} = \frac{\rho 2 u_{rel}^2 r_d}{\sigma_d} \quad \text{and} \quad \mathrm{Oh} = \frac{\mu_d}{\sqrt{\rho_d 2 r_d \sigma_d}}, \tag{22}$$

where σ_d is the liquid surface tension and μ_d is the dynamic viscosity of the liquid droplet.

Schmehl et al. (2000) proposed a correlation in terms of the corrected Weber number,which considers the viscosity effects, observed for Oh $\geqslant$ 0.1:

$$\mathrm{We}_{corr} = \frac{\mathrm{We}}{1 + 1.077\mathrm{Oh}^{1.6}} \tag{23}$$

The correlation gives the statistical mean diameter for a spray that is generated by breaking up an originally monodisperse spray. The ratio of the spray Sauter mean diameter d_{32} to the original drop diameter is

$$\frac{d_{32}}{d_0} = 1.5\mathrm{Oh}^{0.2}\mathrm{We}_{corr}^{-0.25} \tag{24}$$

Fig. 2 shows the predicted mean diameter at different relative velocities for water and jet fuel and two different initial drop sizes. Table 1 lists the liquid properties used for the comparison. The predicted water and jet fuel drop diameter were practically identical when the relative velocity was higher than 100 m/s. This means that the differences in the surface tension and dynamic viscosity between the two liquids cancel each other. As a result, the measured drop size distributions with water can be directly applied to full-scale computations simply by considering the effect of the speed.

4. Validation of the model of aircraft impact

4.1. SANDIA Phantom F-4

This section presents a qualitative comparison of the present model with photographic data from experiments. Sandia National Laboratories conducted a crash test where Phantom F-4 aircraft carrying 4.8 tons of water hit a reinforced concrete target at a velocity of 215 m/s (von Riesemann et al., 1989; Muto et al., 1989; Sugano et al., 1993). Unfortunately, the liquid dispersal processes were not measured and documented in detail. However, the video evidence from the experiments can be used for qualitative validation of the aircraft impact model by comparing the shapes and sizes of the predicted sprays.

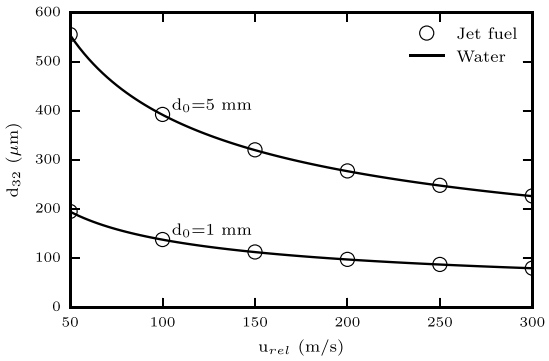

Fig. 2. Mean diameters for water and jet fuel sprays (Eq. (24)).

Table 1
Properties of water and jet fuel used for droplet size scaling with Eq. (24).

	Water	Jet fuel
σ_d 10^{-3} N/m	73	27
μ_d 10^{-3} Ns/m^2	1.04	2.00
ρ kg/m^3	1000	816

According to the video material, the initial liquid discharge velocity was in the range of 280–330 m/s, which is 1.3–1.55 times the impact velocity. The liquid spreading angle θ was determined from the videos to be 25°. There was a 15° opening for wings. In the model the diameter of the droplet insertion band was 3 m. The simulation model of the Sandia experiment was 45 m deep, 120 m wide, and 90 m high.

Fig. 3 visually compares the predicted spray shapes with photographs from the experiments. In the experiments, the liquid seemed to spread quite uniformly in all directions except directly sideways. The final size (diameter) of the cloud was 60–80 m.

The spray pattern predicted by FDS was very similar to that observed in the experiments. Water propagated fairly uniformly in all directions except parallel to the ground. This was by design because a gap corresponding to the wings was left in the droplet insertion pattern. Later in the simulation, the spray front started to develop "fingers", where parts of the spray propagated faster than the rest of the spray. The resulting spray shape closely resembled the experimentally observed spray shape. The final size of the droplet cloud in the simulations was comparable to the experimentally observed value.

The composition of the spray can not be determined from the photographs. It is likely that at least part of the visible spray is made up of dust and parts of the impacting plane. Small dust particles behave in a similar manner to the fine water mist particles. Therefore, the overall spray dynamics should be similar to water sprays.

4.2. Impact experiments with liquid-filled missiles

This section presents the validation of the spray boundary condition and droplet transport models against experimental data. The IMPACT experiments were a series of experiments with liquid-filled missiles that were carried out at the VTT Technical Research Centre of Finland, where stainless steel fluid-filled missiles were shot against a steel force plate with three impact velocities: 100, 125, and 137 m/s (Hostikka et al., 2015).

Two missiles with different wall thickness (1.5 and 2.0 mm) were used for each velocity. The amount of water inside the missile was 37 L in all tests. The distance and velocity of the water front was measured by using high-speed video images. The droplet size, velocity, and mass flux were measured by using ultrahigh-speed cameras with special optics to detect droplets as small as 10 μm.

Fig. 4 shows the domain used to simulate the IMPACT experiments. The initial speed was taken as 1.8 times the impact velocity. The droplet insertion time t_{insert} was calculated from the impact velocity assuming linear deceleration of the missile. There was no gap for wings in the droplet insertion pattern (see Fig. 1). The number of tracked parcels in the computation was adjusted so that

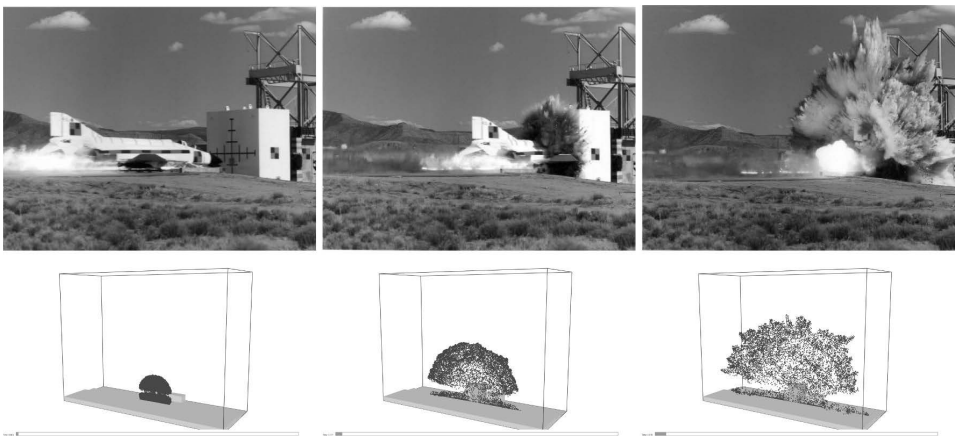

Fig. 3. Visual comparison of the Sandia F-4 impact experiment with a simulation. Images from https://share.sandia.gov/news/resources/video-gallery/index.html#rocketsled (accessed 12.03.15).

1,000,000 particles were inserted during the spray insertion. Table 2 lists the parameters of the simulated experiments.

Fig. 5 visually compares the simulated and observed spray shapes for test SFP5. This test was selected for comparison because of the relatively uniform spray pattern. The uniformity of the spray pattern indicated that the effect of the missile deformation on the spray propagation was small. The first row shows the comparison at $t = 10$ ms after impact. In the simulation the spray front was smooth in all directions, while in the experiments the spray had a serrated edge.

The differences between the simulation and experiment can be partly explained by the details of the impact. In the experiments, the water was pushed out through the deformed nose of the missile. The resulting liquid sheet was not perfectly uniform in shape. Furthermore, this liquid sheet may have exhibited fingering and jetting behavior before it underwent breakup to form droplets. The unevenness of the initial liquid sheet was reflected in the shape of the resulting spray. The spray boundary condition used in the simulations gave a uniform velocity and flux in all dimensions. This resulted in a much smoother spray, especially in the early stages.

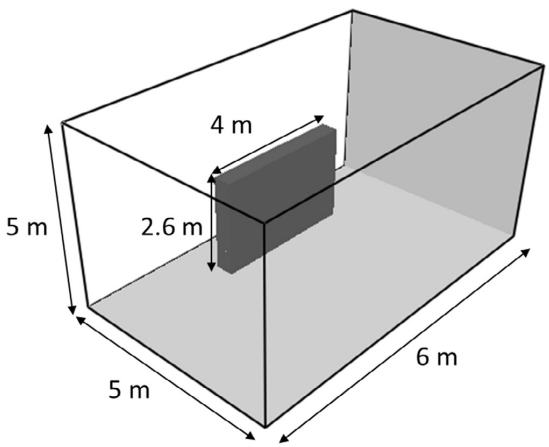

Fig. 4. Simulation domain for the IMPACT tests.

Table 2
Parameters for the simulations of the IMPACT experiments.

Exp. #	u_{ini} (m/s)	$\dot{m}$ (l/min)	$t_{insert}(s)$
SFP2	175	44,500	0.05
SFP3	127	29,600	0.05
SFP4	178	49,600	0.03
SFP5	179	49,500	0.03
SFP7	186	73,600	0.03
SFP8	179	74,500	0.03
SFP11	226	11,100	0.02
SFP12	220	11,100	0.02

The contours of the spray density in Fig. 5 show wavelike phenomena, where a denser part of the spray moved faster than the front edge of the spray. This behavior was also observed in the experiments, where a second spray front overtook the first spray front once the latter had slowed down. This can be observed as the jump in the experimental spray front velocities in Fig. 6. The last row of Fig. 5 shows the wave breaking up before it overtakes the spray edge.

Fig. 6 compares the predicted liquid front speed with the experimentally determined liquid front speeds. The radial position of the water front in several spread directions were measured from the still images taken with the high-speed videos. The water front position was traced in nine different angular directions from the point of impact. The uncertainty of the experimentally determined spray front velocity was approximately ±25 m/s or less.

The velocities were nondimensionalized by the impact velocity $V^* = V/V_{imp}$. The shaded areas in the figures correspond to minimum and maximum velocities at a given time instant while including experimental uncertainty (±25 m/s). The circles represent the median velocity from all directions. The simulated velocity was determined by differentiating the spray front position using central differences. The spray front position in turn was defined as the 99th percentile distance of all droplets from the impact location.

The simulated and observed velocity curves were quite noisy. For the simulated curve, this was caused by the method of determining the liquid front position as the 99th percentile of all droplet distances. Because the sprays did not propagate completely uniformly in all directions the 99th percentile may correspond to different directions for each time step. The simulation model did not reproduce the jump due to the wave phenomena, even though it was observed in the density contours of the sprays (see Fig. 5).

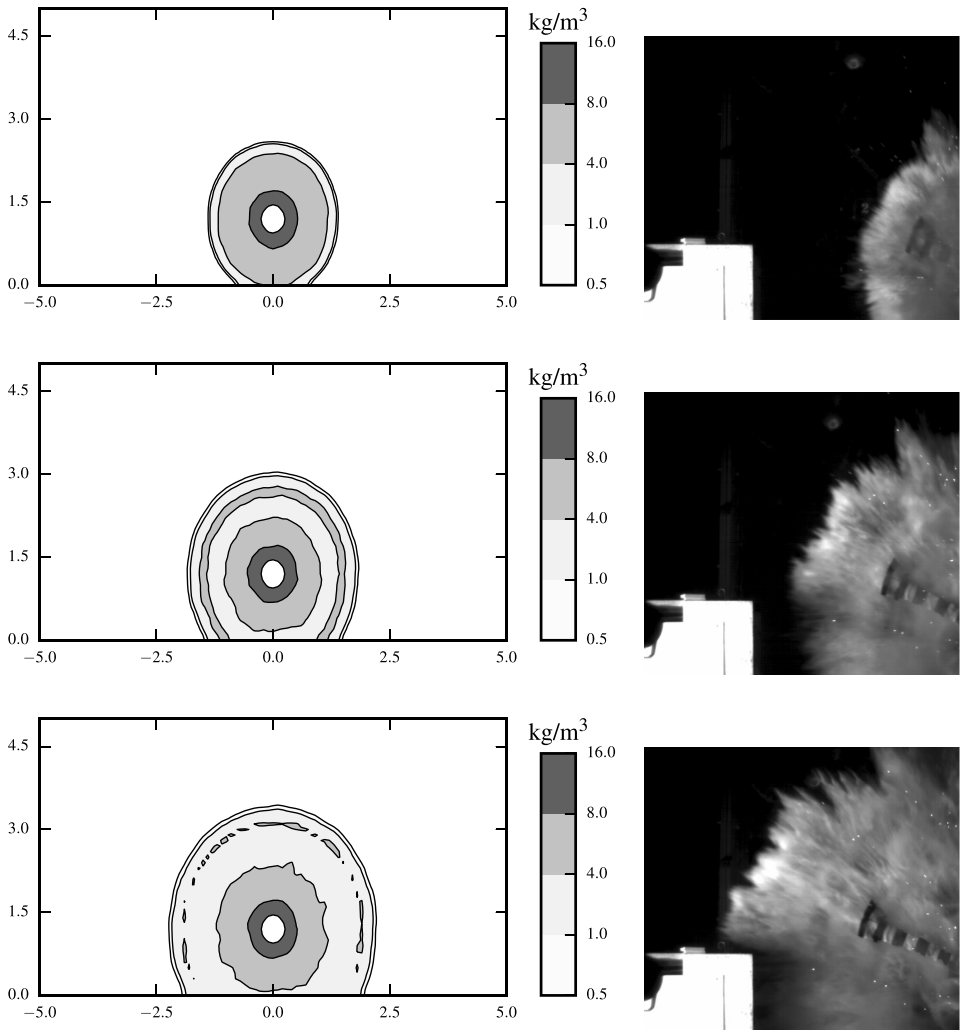

Fig. 5. Visual comparison of simulated and observed spray shapes in the SFP5 experiment at three time instants. Top row: $t = 10$ ms. Middle row: $t = 15$ ms. Bottom row: $t = 20$ ms. The left column shows the contours of the spray density on the impact plane. The right column shows the frames from high-speed video of the experiment.

The predicted velocities were close to the median of the experimentally observed velocities. Near the impact location (i.e., when t was small), however, the propagation velocity tended to be overestimated, and the liquid speeds were in many cases close to the maximum observed liquid front speeds. This behavior can be explained by the effect of the missile fragments on the propagation of the jets.

The spray propagation velocity was largest in the directions where it was unimpeded by missile fragments. The spray boundary condition does not account for missile fragments; therefore the simulated liquid front propagation velocities were more closely related to the maximum (unimpeded) liquid front velocities. The effect of missile fragments was most pronounced in experiment SFP8, where a large fragment of the missile impeded the sprays in the direction of the liquid front measurements. In this test, the resulting median liquid front velocities were significantly lower than those predicted by the simulations.

In cases where the missile deformation had a smaller effect, the predicted liquid front velocities fell within the scatter of the data. In these cases, the liquid front velocities near the impact location were close to the median velocity. This is expected because the initial velocity was based on linear fitting to the observed velocities.

Further away from the impact location (i.e., for large values of t), entrainment into the individual jets causes the jets to spread and merge with nearby jets. This smoothed the edge of the spray pattern and consequently decreased the variability in propagation speed between directions. Therefore, the good correspondence between the simulation and the median velocities at later stages indicates that the entrainment in the sprays was correctly predicted.

4.3. Fireball lifetimes and diameters

This section presents comparison of predicted fireball lifetimes and diameters with empirical correlations. Makhviladze et al.

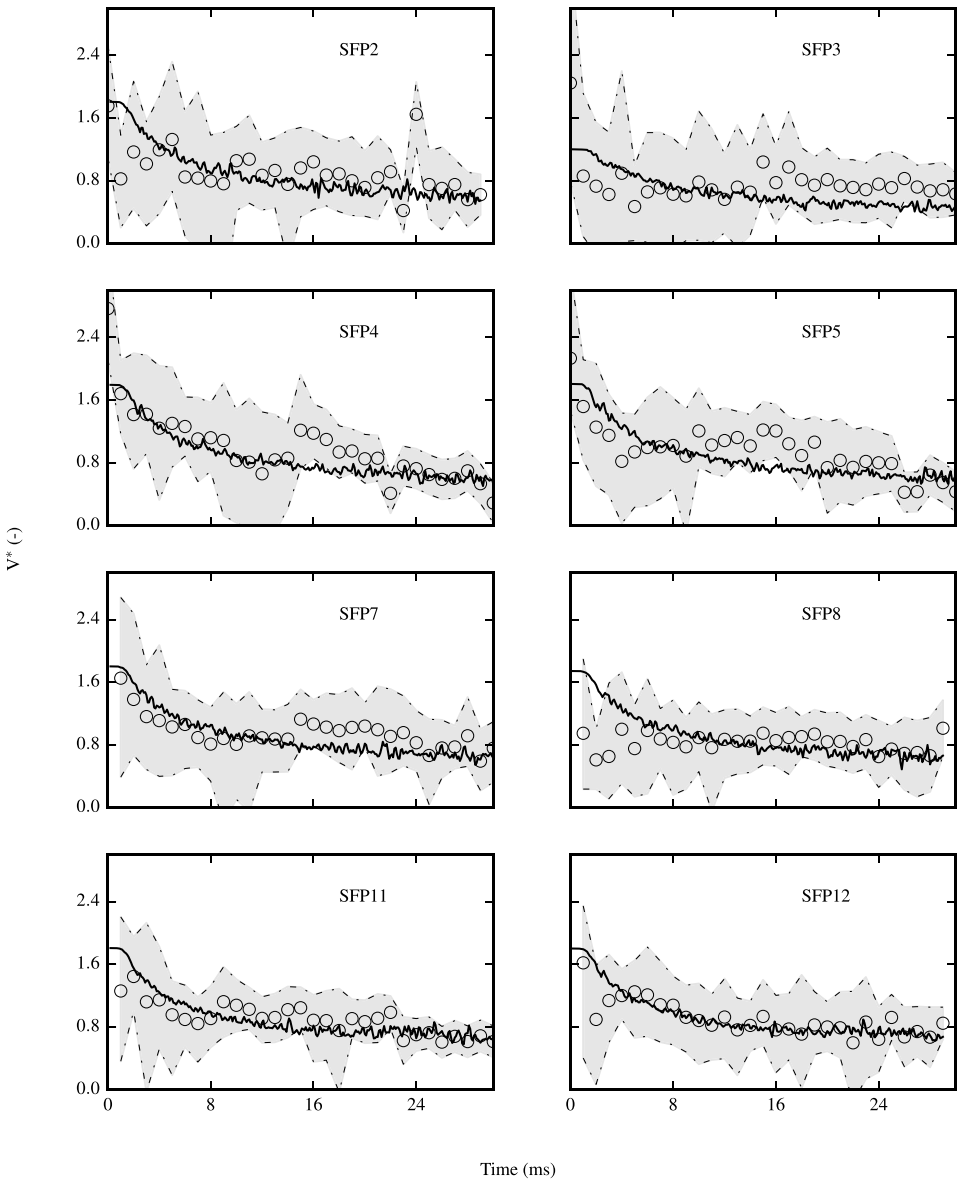

Fig. 6. Comparison of predicted liquid front propagation velocities with experimental data. Experiment SFP2-12. Continuous line: simulation result. Open symbols: median of experimental data. Shaded area: minimum and maximum of experimental data ±25 m/s.

(1998) used dimensional analysis to determine the relevant length and time scales of fireballs:

$$L_* = \left(\frac{M\Delta H_c}{\rho_0 c_{p,0} T_0}\right)^{\frac{1}{3}}, \quad U_* = \sqrt{L_* g}, \quad t_* = \sqrt{\frac{L_*}{g}} \tag{25}$$

Here, the subscript 0 refers to the properties of air at ambient conditions. The length scale L_* is close to experimentally determined fireball diameters. Roper et al. (1991) determined an experimental correlation for fireball lifetimes resulting from vertical fuel releases. Makhviladze et al. (1998) formulated the correlation in terms of the length and timescales in Eq. (25) as follows:

$$\frac{t_*}{t_{FB}} = 0.22 + 0.01\mathrm{Fr}^{\frac{1}{2}}; \quad \mathrm{Fr} = \left(\frac{U_{ini}}{U_*}\right)^2 \tag{26}$$

Numerical simulations were performed in a domain of $4L_* \times 4L_* \times 8L_*$, and fuel was inserted in the time interval $t_{in} = 0.1 t_{FB}$. The domain was discretized with $220 \times 220 \times 550$ cells. The droplet size followed the Rosin–Rammler–lognormal distribution (see McGrattan et al., 2013a) with a volumetric median diameter of 83 μm and spread parameter γ of 2.5. In numerical

experiments with the droplet distribution determined in Section 3.2, larger droplets were observed to rain out of the fireball before they had time to evaporate. Here, by selecting a different distribution the number of very large droplets was diminished and all droplets evaporated within the fireball. The fuel insertion was modeled as a vertical fuel spray with a spray angle of 15°. Nine simulations were performed with fuel masses of 10, 1000, or 10,000 kg and initial velocities of 50, 200, or 400 m/s.

In their experimental study, Roper et al. (1991) determined the end of the fireball lifetime as the moment when visible flames disappeared, and the start time of the fireball burning was taken to be the moment when half of the fuel mass was released. We defined the end of the fireball lifetime as the time at which 95% of the fuel is burned. The start of the fireball lifetime was taken as $\frac{1}{2}t_{in}$.

Fig. 7 compares the simulation results with Eq. (26). Overall, the simulated results showed good agreement with Eq. (26). The predicted fireball lifetimes were within 15% of the values predicted by Eq. (26). Despite the low-Mach number limitation of FDS, there were no significant deviations from the general trend, even for cases where the droplets were inserted at 400 m/s.

Fig. 8 shows the contours of the gas temperature at the midplane of a fireball. The contours are shown at the time instants t/t_{FB} = 0.3, 0.6, and 0.9 and for an initial velocity U_{ini} = 200 m/s. Fig. 8a shows the results for the case with M = 10,000 kg, and Fig. 8b shows the results for the case with M = 10 kg. At the early stages of the fireball development, the hot gas cloud was still shaped like a jet. At about half of its lifetime, the fuel jet decelerated, and its movement was now controlled by buoyancy. In the final stages, the cloud rolled up in a vortex. The vortex roll up started earlier for the M = 10,000 kg case owing to the lower Froude number. If the 1000 °C contour is taken as the fireball edge, the maximum fireball diameter can be visually approximated from Fig. 8 to be $D_{FB} \approx 1.2L_* \approx 5.86M^{0.33}$. Experimental correlations for the diameters of fireballs from flammable liquids range from $5.8M^{0.33}$ to $6.3M^{0.33}$ (Abbasi and Abbasi, 2007).

The grid resolution is an important parameter for CFD simulations. For buoyancy-dominated flows, a useful length scale is the characteristic fire diameter McGrattan et al. (2013c):

$$D^* = \left(\frac{\dot{Q}}{\rho_0 c_p T_0 \sqrt{g}}\right)^{\frac{2}{5}} \tag{27}$$

The quantity $\dot{Q}$ is the total heat release rate of the fire. By using Eq. (26), we can estimate the average heat release rate in a fireball. We can then use the ratio of D^* to grid resolution δx to compare grid resolutions. For the simulations presented in this paper, $\frac{D^*}{\delta x} \geqslant 15$. This grid size has been found adequate for a wide range of validation cases (McGrattan et al., 2013b).

The fireballs resulting from airplane impacts have fairly low Froude numbers because of the large amount of fuel involved. Therefore, using $\frac{D^*}{\delta x}$ as a grid size metric is warranted. Because of the vertical orientation of the spray and chosen particle size distribution, the fireball burning times are not very sensitive to the details of the spray insertion method. This is in line with the experimental results of Roper et al. (1991).

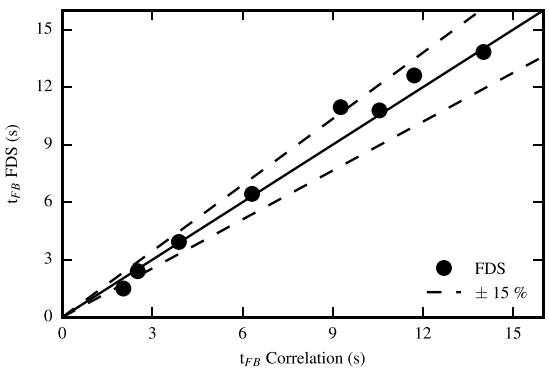

Fig. 7. Comparison of predicted fireball lifetimes with Eq. (26). The black dots show the simulation results. The dashed lines show ±15% deviation from exact correspondence.

4.4. Effect of the impact height and droplet size on the pooling fraction

An important aspect of the fires resulting from an aircraft impact is the fraction of fuel that does not burn in the initial fireball. We call this quantity the pooling fraction. The specific amount of remaining fuel depends on both the droplet size and impact height. The closer the impact location is to the ground, the larger the pooling fraction. Because smaller droplets evaporate faster than larger droplets, a lower average droplet diameter results in smaller pooling fractions.

A number of numerical experiments was run in order to quantify the effect of impact height and droplet size on the pooling fraction. The simulation domain consisted of a rectangular building 40 m wide and 50 m high. The impact location was varied on the building. The domain and impact locations are shown in Fig. 9. 10,000 kg of fuel was released in 0.1 s. Grid resolution was 1.0 m.

The bottom graph in Fig. 10 shows the pooling fraction as a function of the impact height for the droplet distribution with $d_m = 80$ μm. As the impact location moves closer to the ground, the fraction of fuel left unburnt increases significantly. At a height of 5 m, the pooling fraction is almost 30%. For an impact height of 20 m, the pooling fraction is practically zero.

The median volumetric diameter has a more modest effect. For an impact height of 10 m, the pooling fraction varies between 11% and 18% for median diameters in the range of 40 μm to 180 μm. The growth of the pooling fraction tapers off at just below 20%.

5. Simulation of a plane impact on a nuclear island

5.1. Overview

We studied the physical extent of the flames and smoke generated by the combustion of jet fuel from the impact of a commercial aircraft on an NPP reactor building. The goal was to investigate how far from the impact point the flames can reach to cause a possible threat to components of the plant.

The simulation model of the NPP included the reactor building (cylindrical shape with a diameter of 56 m), four auxiliary buildings attached to the reactor building, part of the diesel building, and part of the turbine hall (see Fig. 11). The computational domain had dimensions of a 135 m length, 120 m width, and 72 m height. All of the domain boundaries except the bottom boundary were open for flow. Two of the auxiliary buildings—the one next to the turbine hall and the other directly opposite—were 25 m tall. The other two auxiliary buildings were 20 m tall. The heights of the diesel building and turbine hall were 15 and 35 m, respectively. The spatial resolution of the CFD solver was 1.0 m.

The impact scenario was the horizontal impact of a commercial aircraft at a speed of 125 m/s in the direction normal to the reactor building wall. The impact height was 35 m from the ground and approximately 10 m from the roof of the auxiliary building. Five different impact positions were considered, as shown in Fig. 11a. Fig. 11b shows the six measurement locations.

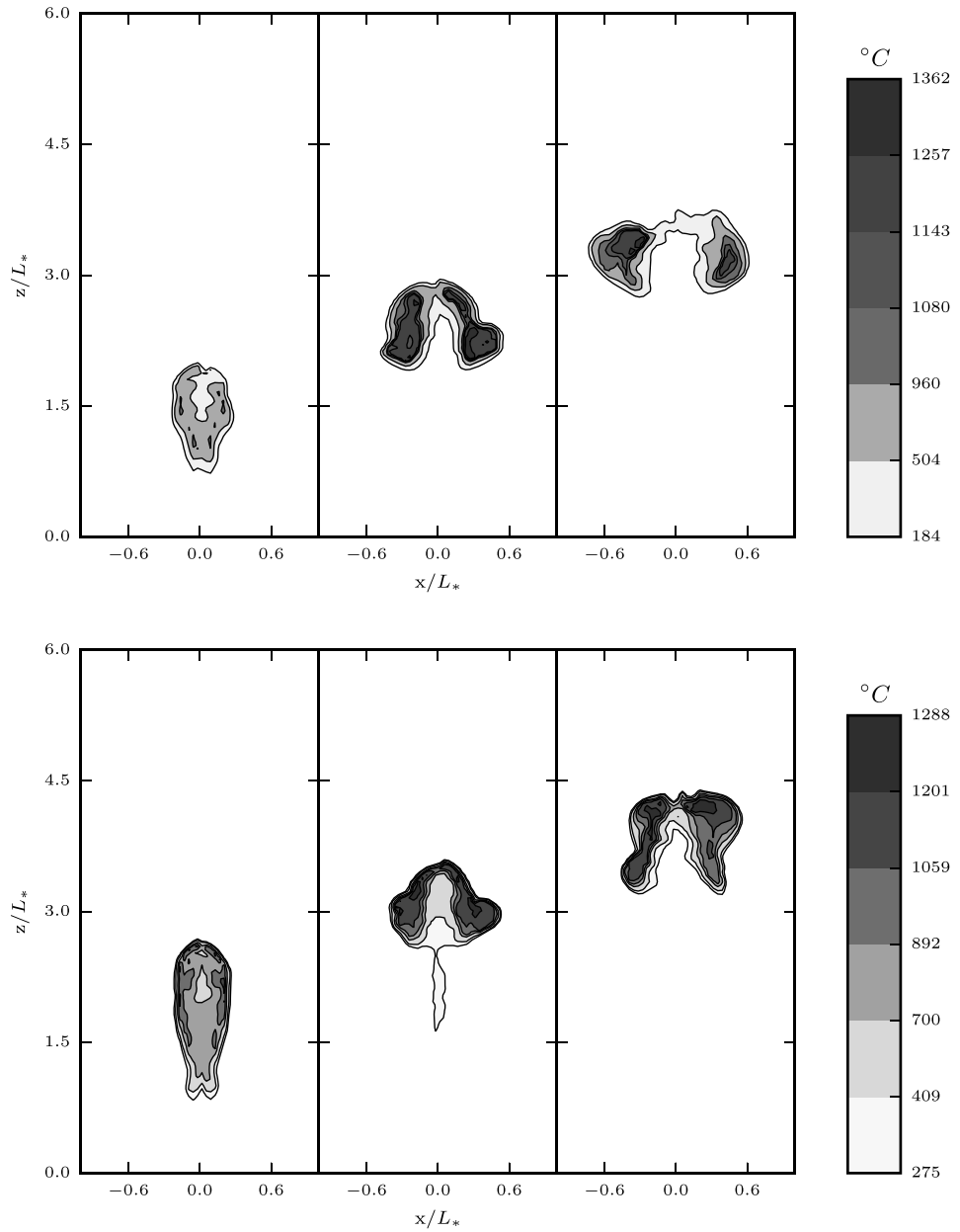

Fig. 8. Instantaneous temperature contours for fireballs with U_{ini} = 200 m/s at time instants t/t_{FB} = 0.3,0.6,0.9. Top: M = 10,000 kg. Bottom: M = 10 kg.

The effect of wind was investigated by assuming either 10 m/s wind speed or no wind. Eight possible wind directions were considered. These directions are shown in Fig. 11c. The wind velocity field was realized by a simple form of data assimilation of forcing the mean velocity inside the domain to a desired value. A total of 45 simulations were run.

The amount of jet fuel was assumed to be 10 metric tons, which corresponds roughly to the fuel contained in the tanks of one wing of a midsize commercial aircraft (Airbus A320). The fuel in the other wing and fuselage tanks was assumed to not contribute to the splash. The fuel was released at a distance of 3.0 m from the impact center with a speed of 250 m/s at an angle reaching from the wall tangent and following the empirical pattern observed in the Sandia Phantom F-4 experiment (see Section 4.1). The same lognormal droplet size distribution as that in the simulations of the Sandia experiments was used.

Four different quantities were monitored from the simulation results at six locations denoted as A–F (see Fig. 11). Locations A–

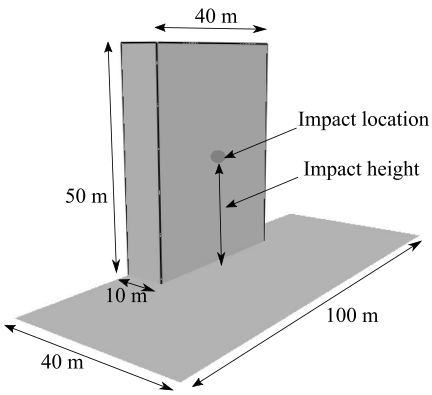

Fig. 9. Simulation model used for pooling fraction sensitivity analysis.

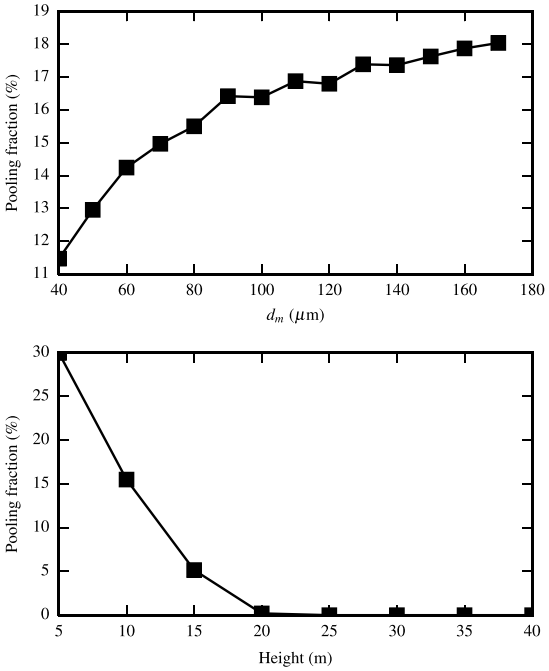

Fig. 10. Sensitivity of the pooling fraction to the impact height and droplet size. Top: Pooling fraction for different volumetric median diameters d_m and impact height z = 10 m. Bottom: Pooling fraction as a function of the impact height for d_m = 80 μm.

D were placed 3 m above the roof of the corresponding auxiliary building and 3 m from the reactor building wall. Location E was located close to the diesel building at a height of 10 m from the ground. Location F was between the first auxiliary building and turbine hall at a height of 20 m from ground level.

The quantities of interest were the gas temperature, gas velocity, and fuel gas volume fraction. In addition, the amount of fuel deposited on the reactor building was also recorded. The maximum observed value of each monitored quantity over the entire simulation was recorded for each measurement location. This observed value was then used to indicate if the conditions at the measurement point can be considered hazardous. Table 3 lists the quantities and their limit values.

5.2. Results

Fig. 12 qualitatively compares the flame and smoke spread patterns for the case with the impact position I1 and wind directions W1 and W5. At 0.5 s from the impact, the flame shape was still dominated by the spray pattern. One second after impact, the wind started to bend the flame to the downwind direction, which significantly affected the portion of the plant geometry that was engulfed in flames. About 4 s after impact, the flame developed to the lift-up phase, and the wind effect was mainly limited to the extent of the smoke spreading. Later, the flames were only visible above the pool fire that formed below the impact position, and their movement was mainly dominated by the large-scale turbulence. Smoke spreading is strongly influenced by the wind. The horizontal distance of the flame influence was estimated to be less than 50 m.

From a risk perspective, we are interested in the likelihood of seeing threatening conditions at any of the measurement locations. The impact location, wind direction, and measurement location were treated as random variables. The measurement locations were further divided into those around the dome (locations A–D) and those between the buildings. For these two groups, we determined the complementary cumulative distribution function

$$\overline{F}(t) = P(T > t) = 1 - F(t) \tag{28}$$

This gives the probability that a random variable takes on values larger than t. The cumulative distribution function $F(t)$ is approximated by the empirical cumulative distribution function

$$\widehat{F}(x) = \frac{1}{N}\sum_{i=1}^{N} I(x_i, x); \quad I(x_i, x) = \begin{cases} 1 & \text{if } x_i \leqslant x \\ 0 & \text{otherwise} \end{cases}. \tag{29}$$

Here, N is the number of observations in the sample, and x_i are the observations.

Fig. 13 shows the complementary cumulative distribution functions for each monitored quantity. The x-axis shows the range of observed values, and for each x-axis value the curves show the probability of seeing larger values.

The distributions of the monitored quantities had similar shapes for monitoring locations around the dome and between the reactor building and auxiliary buildings. At every measurement location, the most likely result was that the conditions did not appreciably differ from the ambient.

The highest temperatures were observed at locations around the dome. Here, temperatures exceeding 1200 °C were observed in approximately 20% of the cases. The maximum temperatures between the buildings were not as high. However, temperatures exceeding 600 °C were observed in 40% of the cases. Because the impact locations were around the dome, it is natural that the highest temperatures were observed around the dome.

The largest fuel gas volume fractions were observed around the dome. This is expected because these measurement locations were closest to the impact location. The majority of the unburnt fuel also accumulated around the dome.

The maximum velocity observed was 0.47 Mach. Velocities exceeding 40 m/s were observed in less than 20% of the cases. The gas velocities tended to be slightly faster between the buildings. The tails of the distribution were similar for locations around the dome and between buildings. For low velocities, the peaks were higher between the buildings.

Overall, threatening conditions were observed in less than 20% of the cases. In other words, for a randomly selected measurement location and randomly selected impact location, the probability of

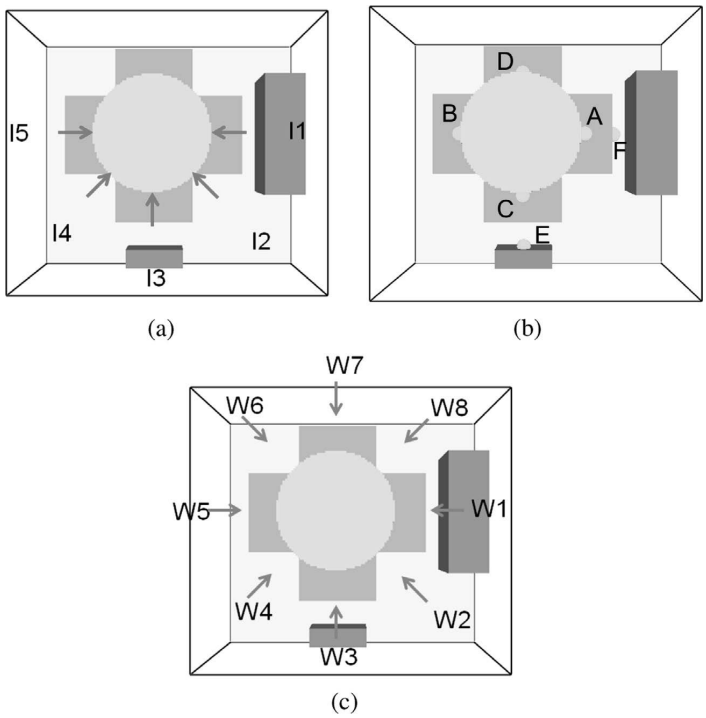

Fig. 11. Simulation model of the nuclear island: (a) impact locations. (b) measurement locations (c) wind directions.

Table 3
List of monitored quantities and limit values that indicate dangerous conditions.

Observed quantity	Limiting value
Gas temperature (T) 700 °C	for "flame" conditions
200 °C	for "smoke" conditions
Fuel gas volume fraction (X_f)	1% vol.
Gas velocity (V)	40 m/s

threatening conditions was less than 20%. These results indicate that only the measurement locations closest to the impact are significantly affected by the ensuing fireball.

The shortest times to reach the limit conditions for fuel concentration and velocity were on the order of a few hundredths of a second. For the temperature, the time was at least a few tenths of a second. At the locations close to the reactor building, the limit conditions were typically reached in less than 1 s. For location E, the time to reach the critical temperature was about 1 s; for F, it was about 2 s. These times only have meaning in the context of the current study because they were strongly dependent on the distances between the assumed impact and measurement locations.

Finally, Fig. 13 also shows the distribution of the pooling fraction in the simulations. In all simulations, more than 10% of the fuel collected on surfaces of the reactor building. In 40% of the simulated scenarios, the amount of fuel burning on the surfaces was more than 20%. The fuel accumulated on the roof near the impact location and also on the reactor dome. Any fuel deposited on the dome was assumed to eventually flow down to the roof.

6. Discussion

The results of the full-scale simulation exercise indicated that direct contact with the flame was limited to a region of the building complex that clearly covered less than half of the reactor building perimeter. Flames lasting longer than about one second were observed in a sector that reached 45° - 90° in both directions from the direction of the incoming aircraft. If the impact direction is treated as a random parameter, the probability of any individual target at the height of the roofs of the auxiliary buildings and close to the reactor building to become engulfed by flames is between 25% and 50%. For objects placed at two opposite sides of the reactor building, physical separation is clearly realized. These conclusions are summarized in Fig. 14, which shows the likely and possible regions of flame contact for one of the impact positions. The regions of thermal radiation and smoke influence can be larger. Overall, a significant fraction of the fuel involved will not burn in the initial fireball. Therefore, this aspect of the aircraft crash scenario should not be ignored.

As discussed in Section 4.4, the amount and distribution of fuel that accumulates on the surfaces strongly depends on the geometry of the problem and details of the droplet size. On the other hand, the development of the fireball itself is relatively insensitive to the details of the fuel injection. In their numerical experiments, Makhviladze et al. (1999) found that two-phase fireballs behave independent of the droplet size when the fuel mass is large enough. Roper et al. (1991) found that the fireball lifetime is insensitive to the geometry of the fuel injection. In both cases, very volatile liquids were discharged vertically away from surfaces. In such a configuration, the lifetime of a droplet is much shorter than the fireball lifetime. When sprays are oriented towards buildings or the ground, droplets may not have time to evaporate before they hit the ground or walls.

Based on the above, we can conclude that accurately modeling the fuel sprays is crucial for predicting the pooling fraction. FDS has previously been used for simulating high-speed two-phase flows in

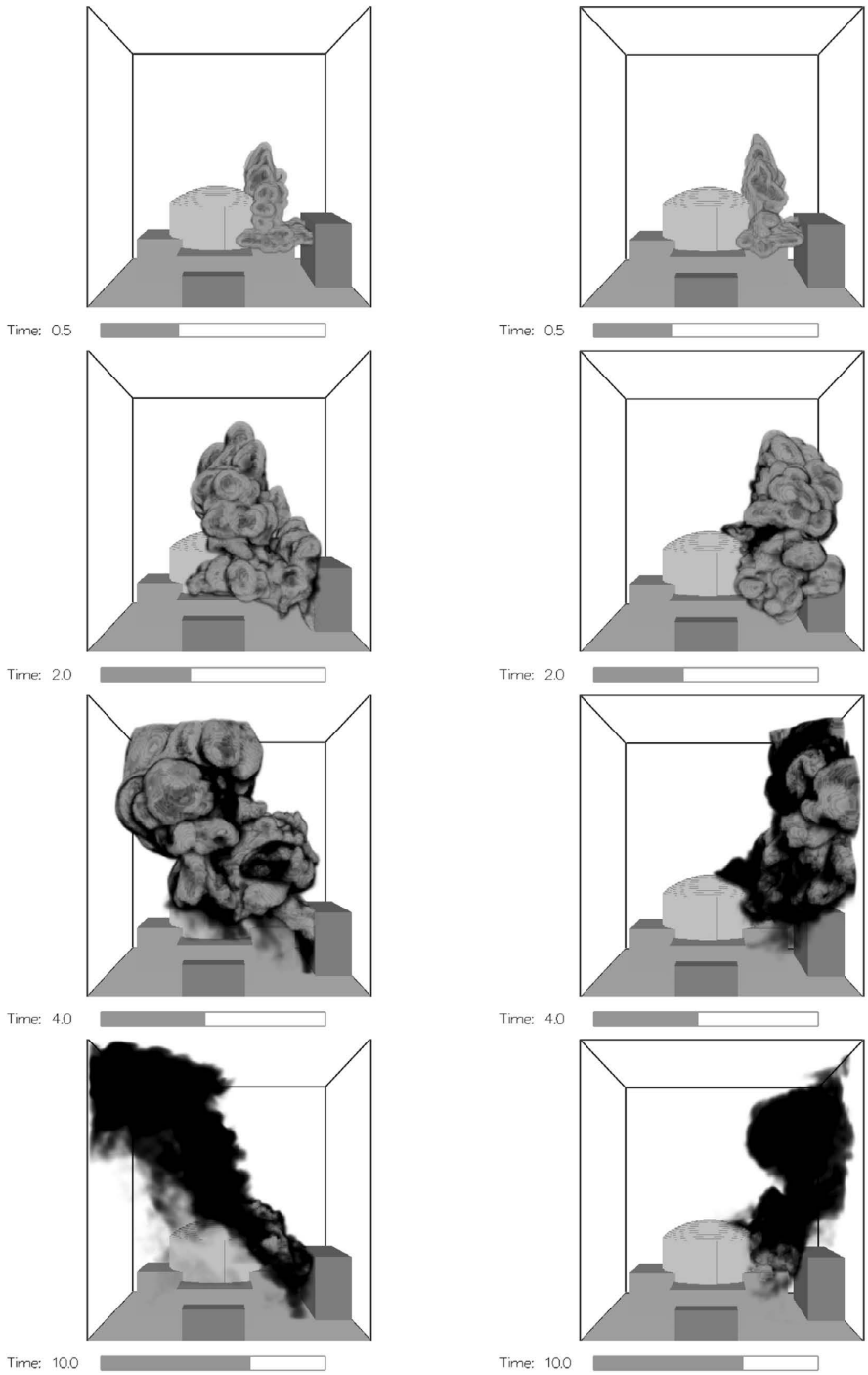

Fig. 12. Qualitative comparison of the flame and smoke spread patterns at 0.5, 2.0 and 4.0 and 10.0 s after impact. Left column: wind direction W1. Right column: wind direction W5. Impact location I1.

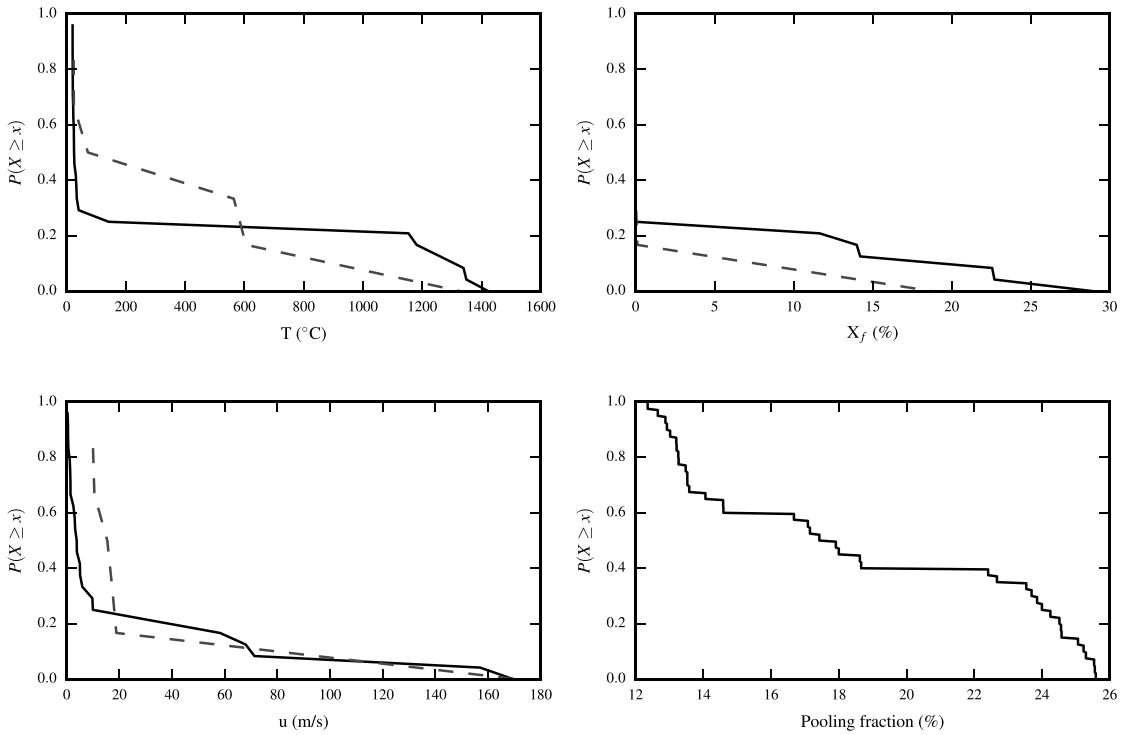

Fig. 13. Complementary cumulative distribution functions for peak values of the temperature, fuel mass fraction, gas velocity and pooling fraction. Continuous lines: Locations A–D, conditions around the dome. Dashed lines: Locations E–F, conditions between the reactor building and auxiliary buildings. The pooling fraction includes fuel deposited on all surfaces.

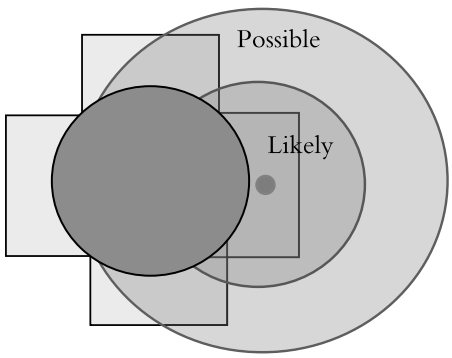

Fig. 14. Possible and likely regions of aircraft impact flame contact around the NPP reactor building in the case of a horizontal impact at a height of 35 m and releasing 10 t of fuel.

the context of high-pressure water mist systems (Vaari et al., 2012; Sikanen et al., 2013). For these sprays FDS predictions of spray structure and entrainment were found to be in reasonable agreement with experimental data. Droplet velocities in the water mist cases ranged from 95 to 132 m/s.

In this study, the FDS spray model found to predict the spray front propagation data from the IMPACT experiments with reasonable accuracy. A comparison with the SANDIA experiments also showed that the spray behavior was qualitatively correct at a large scale.

Authors are not aware of any validation work involving the high-speed reacting sprays such as considered in this study. Burning times of the vertical releases predicted by FDS where in satisfactory agreement with the empirical correlation of Roper et al. (1991). However, fireball lifetimes are typically much longer than the time needed to evaporate all droplets. Therefore, further validation work is needed for the droplet evaporation rate because this may significantly affect the pooling fraction predictions.

In the present study, we assumed that the liquid is ejected at 1.8 times the impact velocity. The assumed impact velocities were similar in magnitude to those observed in the IMPACT experiments. Aircraft can fly at higher speeds than the low speeds considered in this study and, depending on the assumed impact velocity, the initial velocities given to the droplets may approach or even exceed the speed of sound. This increases the uncertainty in two ways. First, the relation of the initial velocity as a function of the impact velocity is based on experimental data where droplet velocities were clearly subsonic. The drag on a body moving at supersonic speeds is significantly greater than that in the subsonic case. Therefore, it is not certain if the relationship between the impact velocity and initial velocity holds at these high impact velocities. For example, in the SANDIA Phantom experiments, the impact velocity was 215 m/s, but the initial velocity of the spray was less than 1.5 times the impact velocity. The second issue is that the present model for the dispersed phase does not include the effects of supersonic velocities.

The hydrodynamic model of FDS is based on the assumption of a low Mach number. The fast gas phase velocities resulting from supersonic speeds could result in large errors in the gas phase solution. The error induced by the incompressibility assumption scales with the square of the Mach number. The commonly used limit for validity of Ma = 0.3 then implies a 10% error level. Faster gas velocities lead to larger errors but should stay bounded until shockwaves are formed at near-supersonic speeds. In all simulations presented here, the maximum gas phase velocity was clearly subsonic. The largest Mach number encountered was Ma = 0.6.

Milton and Pianthong (2005) compared the predictions of subsonic empirical formulas for the velocity decay and penetration distance of conical liquid jets against the experimental measurements of supersonic (Ma = 5.3) water and diesel jets. They concluded that the use of sub-sonic formula leads to overestimation of the velocity decay and underestimation of the jet penetration distance, with errors being in the range 20–30%. Although the velocity decay profiles of the conical super-sonic jets of Milton and Pianthong (2005) are much steeper than those in Fig. 6, we can assume that the compressibility effects in our fuel splash jets with Ma = 1 are at most equally significant as in their study. More experiments with higher impact velocities would be needed to confirm the assumed droplet velocities and sizes in cases where the liquid speed approaches Ma = 1.

The region of maximum velocity is also limited in both space and time. Generally, large velocities are observed early in the simulation and near the droplet insertion location. In this region, the error from neglecting the impacting missile and its deformation should dominate. This effect can be observed in the data from the IMPACT experiments, where the deformation of the missile had a significant effect on the spray propagation near the impact location.

The model of liquid release after an aircraft impact presented here is based on experiments made with liquid-filled missiles. In airplanes, fuel is stored in several locations: mainly in the wings but also in the hull of the airplane. This distribution of fuel may result in a different pattern of dispersal from the one utilized in this paper. The effect of the plane geometry on the resulting droplet size is also unknown.

7. Conclusions

This paper presents a methodology for simulating the effects of airplane impact on a nuclear island. In our method, the fuel release is modeled as a spray boundary condition. This allows for prediction of both the effects of the initial fireball as well as the pooling fraction. All computations were done with the LES code FDS. Droplet sizes and initial velocities of droplets were based on experimental data from small scale experiments.

FDS predictions of spray cloud shapes were compared qualitatively with photographs from experiments. Quantitative comparisons experimental data and correlations showed that the model can accurately predict the propagation velocities of unreacting sprays as well as the lifetimes and diameters of fireballs. Further validation work is needed for high-speed two-phase spray flames because this study only considered non-reacting cases for validation. The uncertainty in predicting the evaporation rates of droplets in reacting sprays mostly affects the pooling fraction predictions.

Finally we presented results from simulations of airplane impact on a nuclear island and a sensitivity study of impact height and average droplet size. Based on the results of theses simulations presented in this paper we made the following conclusions:

1. The simulated fireballs resulted in locally high temperatures, velocities, and pressures but for only a short duration. In the case of airplane impact on a nuclear island. physical separation was realized for targets situated on opposite sides of the building.
2. Up to 20% of the fuel involved in the crash accumulated on the surfaces of the target building. The subsequent burning of this fuel may then be a significant hazard to the safety of the NPP and should not be ignored.
3. Droplet size and the geometry surrounding the impact location has a significant effect on the pooling fraction. Lower impact location and larger average droplet size lead to larger pooling fractions.

Possible future research topics are the effect of the spatial fuel distribution on the hazard posed to the NPP. Different plane configurations and fuel inlet geometries can also be investigated.

Acknowledgments

This work was funded by the State Nuclear Waste Management Fund (VYR) within the Finnish National Research Programme on Nuclear Safety (SAFIR).

References

Abbasi, T., Abbasi, S.A., 2007. The boiling liquid expanding vapour explosion (BLEVE): mechanism, consequence assessment, management. J. Hazard. Mater. 141, 489–519. http://dx.doi.org/10.1016/j.jhazmat.2006.09.056. URL http://www.sciencedirect.com/science/article/pii/S0304389406011290.

Ahlers, R.H., 1977. Full-Scale Aircraft Crash Tests of Modified Jet Fuel. FAA-NA-77-35. National Aviation Facilities Experimental Center. Atlantic City, NJ. URL http://oai.dtic.mil/oai/oai?verb=getRecord&metadataPrefix=html&identifier=ADA043843.

Baum, H.R., Rehm, R.G., 2005. A simple model of the World Trade Center fireball dynamics. In: Proceedings of the Combustion Institute 30, pp. 2247–2254. doi: http://dx.doi.org/10.1016/j.proci.2004.08.125.

Berry, S.R., Rice, S.A., Ross, J., 1980. Physical Chemistry. John Wiley and Sons, New York.

Brown, A.L., Metzinger, K.E., Wagner, G.J., 2014. Predictions of transport accident fires using coupled structural dynamics and computational fluid dynamics. Fire Safety Sci. 11, 584–597.

Brown, A.L., Wagner, G.J., Metzinger, K.E., 2012. Impact, fire, and fluid spread code coupling for complex transportation accident environment simulation. J. Therm. Sci. Eng. Appl. 4, 021004.

Cheremisinoff, N., 1986. Encyclopedia of fluid mechanics. Gas-Liquid Flows, vol. 3. Gulf Publishing Company, Houston, Texas.

Deardorff, J., 1972. Numerical investigation of neutral and unstable planetary boundary layers. J. Atmos. Sci. 29, 91–115.

Grosshandler, W., 1993. RadCal: A narrow band model for radiation calculations in a combustion environment. NIST Technical Note 1402. National Institute of Standards and Technology. Gaithersburg, Maryland.

Hasegawa, K., Sato, K., 1978. Experimental investigation of the unconfined vapour-cloud explosions of hydrocarbons. Technical Memorandum of Fire Research Institute No. 12. Fire Research Institute, Fire Defence Agency, Japan.

Hostikka, S., McGrattan, K., 2006. Numerical modeling of radiative heat transfer in water sprays. Fire Saf. J. 41, 76–86. http://dx.doi.org/10.1016/j.firesaf.2005.09.003.

Hostikka, S., Silde, A., Sikanen, T., Vepsä, A., Paajanen, A., Honkanen, M., 2015. Experimental characterisation of sprays resulting from impacts of liquid-containing projectiles. Nucl. Eng. Des. 295, 388–402. http://dx.doi.org/10.1016/j.nucengdes.2015.09.008. URL http://www.sciencedirect.com/science/article/pii/S002954931500401X.

Hu, Z., Trouve, A., 2008. Numerical simulation of explosive combustion following ignition of a fuel vapor cloud. Fire Saf. Sci. 9, 1055–1066. URL http://www.iafss.org/publications/fss/9/1055.

Incropera, F.P., De Witt, D.P., 1996. Fundamentals of Heat and Mass Transfer. John Wiley and Sons, New York.

Jeon, S.J., Jin, B.M., Kim, Y.J., 2012. Assessment of the fire resistance of a nuclear power plant subjected to a large commercial aircraft crash. Nucl. Eng. Des. 247, 11–22. http://dx.doi.org/10.1016/j.nucengdes.2012.02.003. URL http://www.sciencedirect.com/science/article/pii/S0029549312000805.

Jepsen, R.A., O'Hern, T., Demosthenous, B., Bystrom, E., Nissen, M., Romero, E., Yoon, S.S., 2009. Diagnostics for liquid dispersion due to a high-speed impact with accident or vulnerability assessment application. Measure. Sci. Technol. 20, 025401. URL http://stacks.iop.org/0957-0233/20/i=2/a=025401.

Johnson, D., Garodz, L., 1986. Crashworthiness Experiment Summary - Full-Scale Transport Controlled Impact Demonstration Program. DOT/FAA/CT-85/20.

National Aviation Facilities Experimental Center. Atlantic City, NJ. URL http://oai.dtic.mil/oai/oai?verb=getRecord&metadataPrefix=html&identifier=ADA173861.

Luther, W., Müller, W.C., 2009. FDS simulation of the fuel fireball from a hypothetical commercial airliner crash on a generic nuclear power plant. Nucl. Eng. Des. 239, 2056–2069. http://dx.doi.org/10.1016/j.nucengdes.2009.04.018. URL http://www.sciencedirect.com/science/article/pii/S0029549309002167.

Magnussen, B., Hjertager, B., 1977. On mathematical modeling of turbulent combustion with special emphasis on soot formation and combustion. Proceedings of the Sixteenth Symposium (International) on Combustion. Combustion Institute, Pittsburgh, Pennsylvania, pp. 719–729.

Makhviladze, G., Roberts, J., Yakush, S., 1999. Combustion of two-phase hydrocarbon fuel clouds released into the atmosphere. Combust. Flame 118, 583–605. http://dx.doi.org/10.1016/S0010-2180(99)00026-7.

Makhviladze, G., Yakush, S., 2005. Modelling of formation and combustion of accidentally released fuel clouds. Process Saf. Environ. Prot. 83, 171–177. http://dx.doi.org/10.1205/psep.04242. URL http://www.sciencedirect.com/science/article/pii/S0957582005712313.

Makhviladze, G.M., Roberts, J.P., Yakush, S.E., 1998. Numerical modelling of fireballs from vertical releases of fuel gases. Combust. Sci. Technol. 132, 199–223. http://dx.doi.org/10.1080/00102209808952015. URL http://www.tandfonline.com/doi/abs/10.1080/00102209808952015#.VctJ9fITLJA.

McDermott, R., McGrattan, K., Floyd, J., 2011. A simple reaction time scale for under-resolved fire dynamics. In: Fire Safety Science – Proceedings of the 10th International Symposium. University of Maryland, College Park, Maryland, USA, pp. 809–820.

McDermott, R.J., 2014. A velocity divergence constraint for large-eddy simulation of low-Mach flows. J. Comput. Phys. 274, 413–431. http://dx.doi.org/10.1016/j.jcp.2014.06.019. URL http://www.sciencedirect.com/science/article/pii/S0021999114004264.

McGrattan, K., Hostikka, S., McDermott, R., Floyd, J., Weinschenk, C., Overholt, K., 2013a. Fire Dynamics Simulator, Technical Reference Guide. sixth ed. National Institute of Standards and Technology, Gaithersburg, Maryland, USA, and VTT Technical Research Centre of Finland, Espoo, Finland. Vol. 1: Mathematical Model; Vol. 2: Verification Guide; Vol. 3: Validation Guide; Vol. 4: Configuration Management Plan.

McGrattan, K., Hostikka, S., McDermott, R., Floyd, J., Weinschenk, C., Overholt, K., 2013b. Fire Dynamics Simulator, Technical Reference Guide, Volume 3: Validation. sixth ed. National Institute of Standards and Technology, Gaithersburg, Maryland, USA, and VTT Technical Research Centre of Finland, Espoo, Finland.

McGrattan, K., Hostikka, S., McDermott, R., Floyd, J., Weinschenk, C., Overholt, K., 2013c. Fire Dynamics Simulator, User's Guide. sixth ed. National Institute of Standards and Technology, Gaithersburg, Maryland, USA, and VTT Technical Research Centre of Finland, Espoo, Finland.

McGrattan, K., McDermott, R., Floyd, J., Hostikka, S., Forney, G., Baum, H., 2012. Computational fluid dynamics modelling of fire. Int. J. Comput. Fluid Dyn., 1–13

Milton, B., Pianthong, K., 2005. Pulsed, supersonic fuel jetsa review of their characteristics and potential for fuel injection. Int. J. Heat Fluid Flow 26, 656–671.

Muto, K., Sugano, T., Tsubota, H., Koshika, N., Suzuki, M., Ohrui, S., von Riesemann, W., Bickel, D., Parrish, R., Tachau, R., 1989. Full-scale aircraft impact test for evaluatioin of impact force: Part 2: Analysis of results. In: International Conference on Structural Mechanics in Reactor Technology vol. 10, Anaheim, Ca.

NEI 07-13, 2011. Methodology for Performing Aircraft Impact Assessments for New Plant Designs. Revision 8p. Technical Report. Nuclear Energy Institute, Washington, DC.

Pinkel, I.I., Preston, G.M., Pesman, G.J., 1952. Mechanism of Start and Development of Aircraft Crash Fires. NACA-RM-E52F06. National Advisory Committee for Aeronautics. Lewis Flight Propulsion Lab. Cleveland, OH. URL http://ntrs.nasa.gov/search.jsp?R=19930087103.

von Riesemann, W.A., Parrish, R.L., Bickel, D.C., Muto, K., Sugano, T., Tsubota, H., Koshika, N., Suzuki, M., Ohrui, S., 1989. Full-scale aircraft impact test for evaluation of impact forces. In: International Conference on Structural Mechanics in Reactor Technology 10, Anaheim, CA., pp. 285–299.

Roper, F., Arno, J., Jaggers, H.C., 1991. The effect of release velocity and geometry on burning times for non-premixed fuel gas clouds. Combust. Sci. Technol. 78, 315–338. http://dx.doi.org/10.1080/00102209108951754. URL http://www.tandfonline.com/doi/abs/10.1080/00102209108951754#.VebpUJdTLlu.

Schmehl, R., Maier, G., Wittig, S., 2000. CFD analysis of fuel atomization, secondary droplet breakup and spray dispersion in the premix duct of a LPP combustor. In: 8th International Conference on Liquid Atomization and Spray Systems, ILASS.

Siegel, R., Howell, J.R., 2002. Thermal Radiation Heat Transfer. Taylor & Francis, New York.

Sikanen, T., Vaari, J., Hostikka, S., Paajanen, A., 2013. Modeling and simulation of high pressure water mist systems. Fire Technol. 50, 483–504. http://dx.doi.org/10.1007/s10694-013-0335-8. URL http://link.springer.com/article/10.1007/s10694-013-0335-8/fulltext.html.

Silde, A., Hostikka, S., Kankkunen, A., 2011. Experimental and numerical studies of liquid dispersal from a soft projectile impacting a wall. Nucl. Eng. Des. 241, 617–624.

Sugano, T., Tsubota, H., Kasai, Y., Koshika, N., Itoh, C., Shirai, K., von Riesemann, W., Bickel, D., Parks, M., 1993. Local damage to reinforced concrete structures caused by impact of aircraft engine missiles Part 2. Evaluation of test results. Nucl. Eng. Des. 140, 407–423. http://dx.doi.org/10.1016/0029-5493(93)90121-O.

Vaari, J., Hostikka, S., Sikanen, T., Paajanen, A., 2012. Numerical simulations on the performance of water-based fire suppression systems. VTT Technology Report 54. VTT Technical Research Centre of Finland. Espoo, Finland.

Yakush, S.E., Makhviladze, G.M., 2005. Large Eddy Simulation of Hydrocarbon Fireballs. In: Proceedings of the European Combustion Meeting.

IV

Fire Safety Journal 80 (2016) 95–109

Contents lists available at ScienceDirect

Fire Safety Journal

journal homepage: www.elsevier.com/locate/firesaf

Modeling and simulation of liquid pool fires with in-depth radiation absorption and heat transfer

Topi Sikanen [a,*], Simo Hostikka [b]

[a] VTT Technical Research Centre of Finland Ltd, P.O. Box 1000, FI-02044 VTT, Finland
[b] Aalto University School of Engineering, Finland

ARTICLE INFO

Article history:
Received 14 June 2015
Received in revised form
2 December 2015
Accepted 9 January 2016
Available online 21 January 2016

Keywords:
Burning rate
Heat release rate
Pool fire
Fuel absorption
Thermal radiation

ABSTRACT

In this paper we present a computational fluid dynamics model for predicting the heat release rates of liquid pool fires. The model makes use of the one-dimensional heat transfer solver to provide the liquid surface boundary condition for the gas phase solver. The in-depth radiation transport is solved by a one-dimensional radiation transport model together with effective absorption coefficients determined from experimental data. The model accounts for the convective heat transfer in the liquid phase by modifying the thermal conductivity. The model is implemented as a boundary condition in the fire dynamics simulator (FDS). The model is validated by comparing experimental and predicted evaporation rates for water and a range of hydrocarbon fuels. The sensitivity of the results to the modelling assumptions and model input parameters is studied. The in-depth heat transfer appears to have a significant effect on the fire dynamics, except for the peak burning rates, which depend most importantly on the gas phase combustion.

1. Introduction

Pool fires are an important class of industrial fire hazards due to the large amounts of flammable liquids present in most industrial facilities, and because the rapid development of the heat release rate in such fires poses a challenge to the safety systems. Pool fires have been studied for decades and these works have been collected in several review articles [3,24,38]. The focus of the research has usually been on the steady state behavior and maximum burning rates of pools of different sizes. The results from such studies are often empirical correlations for the burning rate. A recent example is the study by Ditch et al. [13] where the authors correlated the mass burning rate with the fuel heat of gasification and smoke point.

Fire safety analyses are commonly performed using the computational fluid dynamics (CFD) type of fire simulations. The most important boundary condition for these simulations is the fire source burning rate, or liquid evaporation rate in case of the pool fires. While many of the analyses can be performed by prescribing the pool burning rate using either experimental data or empirical correlations as sources of information, there are situations where the conditions of the fire scenario are so much different from any experimental study that a reliable prediction of the pool burning rate cannot be made in advance. Examples of such conditions are the ambient temperature, radiation level, side wind and vitiation of the atmosphere. On the other hand, the heat transfer within the pool itself can be significantly different from the situation behind the empirical conditions. Furthermore, the transient nature of the analyses may require knowledge on the time-dependent burning rate, not just the peak or steady state value. It is therefore necessary to develop sub-models for the CFD fire models that can predict the pool fire dynamics and burning rate during the simulation.

Predictive CFD simulation of the pool burning rate were previously performed by Hostikka et al. [22]. In their model, the liquid evaporation rate was calculated iteratively over the course of the simulation to maintain an equilibrium fuel vapor pressure in the first gas-phase cell above the liquid boundary. The heat transfer inside the liquid layer was calculated using a one-dimensional heat conduction solver. In the results, only the steady state burning rate value was observed paying no attention to the temporal development. The main weakness of this kind of evaporation model is that the realized vapor concentration is highly sensitive to the spatial resolution. Suard et al. [40] used a more robust methodology by relating the total pool burning rate to the pool size and local oxygen concentration according to the empirical correlations. Three experiments with hydrogenated tetrapropylene fuel in a mechanically ventilated compartment were used to validate the model.

The main heat transfer mechanisms in a burning liquid pool are illustrated in Fig. 1. The heat from the flame is transported to the

* Corresponding author.
E-mail address: Topi.Sikanen@vtt.fi (T. Sikanen).

http://dx.doi.org/10.1016/j.firesaf.2016.01.002
0379-7112/

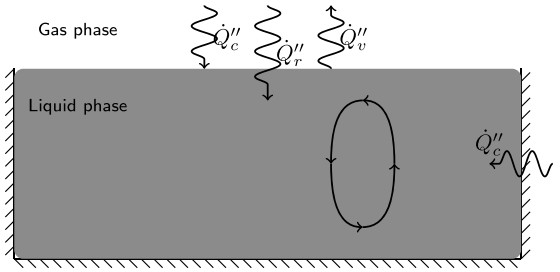

Fig. 1. Heat transfer mechanisms in pool fires.

liquid by thermal radiation and convection. Heat conduction takes place between the vessel and the liquid. The size of the pool dictates which mode of heat transfer dominates, although the type of fuel also plays a role [3,38]. For very small pool diameters, the conduction through the vessel walls dominates the heat transfer. For slightly larger pool fires, convective transport is the most important mode, and for the large pool fires, the radiative transport dominates. The exact diameters where these transitions between dominant heat transfer mechanisms occur are fuel dependent.

Studies have also been conducted to determine the spectra of emitted radiation [42] and to characterize the radiation absorption by gases within the flame [51]. The question of heat transport within the fuel has received less attention. In the liquid phase, the dominant modes of transport are convection (liquid movement) and radiation. The convection can be driven by heat transfer from the walls, unsteady burning rate, uneven surface temperature and buoyancy. Higuera [20] explored numerically the situation of a liquid layer with a cold bottom plate heated nonuniformly from above. For liquids with Prandtl numbers near unity, both thermocapillary and buoyant flows were induced.

Very little experimental data exists on the importance of liquid side convection in determining the burning rates of pool fires. In fact, steps are sometimes taken in order to minimize both convection and in-depth radiation absorption. For example, Ditch et al. [13] and Suo-anttila [41] used glass beads in the fuel bed in order to minimize in depth radiation absorption and convection. Suo-anttila and Blanchat [41] also investigated the effect of convection by removing the glass from the pools. They found that convection and in-depth radiation absorption had a small effect on the steady state burning rate. Vali et al. [50] found that there is a near constant temperature region directly below the surface of a pool fire. In this region, the heat transfer was found to be dominated by convection driven by heated pool walls. In another study, Vali et al. [49] noted that varying the temperature of the pool boundary had an effect on burning rate. The importance of the initial temperature of the liquid fuel on pool fire dynamics has been previously noted by Hayasaka et al. [18] and investigated more thoroughly by Chen et al. [11], who recorded the temperature gradient within the fuel. They found that the initial temperature did affect the temporal development of the burning rate but did not significantly affect the steady state burning rate.

To investigate the heat transfer within the liquid, we must also consider the depth over which the radiation reaching the liquid surface is absorbed. Depending on the fuel, the thickness of absorption can vary significantly, which has a great influence on how the radiation should be taken into account in numerical modelling. In fuels which are optically very thick in the infrared region, the thermal radiation is absorbed within a very thin layer on the surface, and the radiation can be taken into account as a boundary condition of the liquid's internal heat transfer problem. If the liquid is not optically thick the in-depth absorption must be taken into account as an internal source term of the heat conduction/convection problem. Additionally, the re-radiation of the fuel and vessel must be taken into account to ensure the conservation of energy in case of optically thin fuels and high temperatures. The in-depth absorption by semi-transparent fuels has been studied for PMMA [39], polymer films [48] and liquid pool fires [42]. Most of the research related to the in-depth radiation absorption in liquids considers the boil-over of liquid pool fires on water [9]. The effect of in-depth radiation absorption on evaporation of fuel droplets has also received some attention [36].

The objectives of the present study are to improve the previous model [22] by replacing the equilibrium-based vaporization model with an engineering mass transfer expression, to find an appropriate technique for the specification of the liquid phase radiation absorption coefficients, to investigate the relative importance of the internal convection to the pool burning rate dynamics, and to validate the proposed modelling approach using experimental results for different fuels.

2. Mathematical models

In this section we describe the mathematical model of liquid under consideration.

2.1. Gas phase model

The liquid model is included as a boundary condition in the CFD software Fire Dynamics Simulator [31,28,27]. FDS is a large Eddy simulation (LES) code that solves a form of the Naiver–Stokes equations appropriate for low-speed, thermally driven flow with an emphasis on smoke and heat transport from fires. The governing equations of for momentum transport are discretized by second-order central finite differences on a cartesian staggered grid. A two stage explicit Runge–Kutta method is used for time-stepping. In the present paper, gas phase combustion is treated by the single step, mixing-controlled chemical reaction scheme using three lumped species. These lumped species are air, fuel, and products. Radiative heat transfer is included in the model via the solution of the radiation transport equation (RTE) for a gray gas. In the gas phase, the RTE is solved using the finite volume method radiation. The absorption coefficients of the gas–soot mixtures are computed using the RadCal narrow-band model [17].

The gas-phase model has been validated for a wide range of fire scenarios that are relevant to the current investigation [32]. Since the evaporation in a pool fire is driven by the heat feedback from the flames, the accuracy of the heat flux predictions will propagate directly to the evaporation rate predictions. The uncertainties in the predictions can be summarized with two parameters: the bias δ and standard deviation σ. Given a model prediction M, the true value y is assumed to be normally distributed as $y \sim N(\frac{M}{\delta}, \sigma^2(\frac{M}{\delta})^2)$.

Predicted heat fluxes outside diffusion flames have bias of 0.97 and standard deviation 0.27. Heatfluxes resulting from flame impingement are predicted with standard deviation 0.37 and bias 0.93. These numbers imply that heat fluxes tend to be under predicted and that the 68% confidence interval for the predictions is $\pm$ 30%. Additionally, simulations of experiments by [43] have shown that the vertical distribution of heat release rate approaches experimentally determined values as the grid is refined. The results in this paper have been calculated with FDS version 6.2.0.

2.2. Liquid evaporation model

The rate at which liquid fuel evaporates when burning is a function of the liquid temperature and the fuel vapor pressure above the pool surface. According to the Clausius–Clapeyron

Table 1
Liquid fuel properties.

Fuel	ρ, kg/m^3 [2]	c_p, kJ/(kg K) [14]	k, W/(m K) [19]	Δh_v, kJ/kg [16]	Δh_c, kJ/kg see text	χ_r [46]	y_{CO}, g/g [46]	y_s, g/g [46]	T_b, °C [10]
Acetone	791	2.13	0.20	501	28,555	0.27	0.003	0.014	56.3
Benzene	874	1.74	0.14	393	33,823	0.60	0.067	0.181	80.3
Butane	573	2.28	0.12	385	44,680	0.31	0.007	0.029	0
Ethanol	794	2.44	0.17	837	27,474	0.25	0.001	0.008	78.5
Heptane	675	2.24	0.14	317	43,580	0.33	0.010	0.037	98.5
Methanol	796	2.48	0.20	1099	20,934	0.16	0.001	0.001	64.8

relation, the volume fraction of the fuel vapor above the surface in an equilibrium state is a function of the liquid surface temperature $T_s(0, t)$ and boiling temperature T_b

$$X_{F,\ell}(t) = \exp\left[-\frac{h_v W_F}{R}\left(\frac{1}{T_s(0,t)} - \frac{1}{T_b}\right)\right] \tag{1}$$

where h_v is the heat of vaporization and W_F is the molecular weight of the fuel gas [35]. The local evaporation rate of the fuel at time t is governed by Stefan diffusion [45]:

$$\dot{m}''(t) = h_m \frac{\bar{p}_m W_F}{R T_g(t)} \ln\left(\frac{X_{F,g}(t) - 1}{X_{F,\ell}(t) - 1}\right); \quad h_m = \frac{\mathrm{Sh} D_{\ell,g}}{L} \tag{2}$$

where h_m is the mass transfer coefficient and $\bar{p}_m$ is the pressure. T_g and $X_{F,g}$ are the gas temperature and the fuel vapor volume fraction. In the CFD model, they are given the values in the first grid cell adjacent to the pool surface.

The length scale L is the length scale of the pool surface, and is the same length scale used for the convective heat transfer calculation. According to the classical boundary layer flow theories, the most appropriate value for L would be the distance from the leading edge of the surface, which in our case could correspond to the pool edge. Unfortunately, global quantities like 'distance from an edge' are generally not defined in the CFD solvers where all the calculations should be based on the solved variables within a finite neighborhood of discrete locations. Therefore, the length scale L is treated as a model parameter rather than a true geometrical variable.

The evaporation mass flux is seen to be a logarithmic function of the current and ideal vapor pressures. The condensation of fuel is not considered in the current model, and therefore the mass flux is bounded by zero from below in the region $X_{F,g} > X_{F,l}$.

The Sherwood, Schmidt and Reynolds numbers are given by

$$\mathrm{Sh} = 0.037 \mathrm{Sc}^{1/3} \mathrm{Re}^{4/5}; \quad \mathrm{Sc} = 0.6; \quad \mathrm{Re} = \max\left(5{\cdot}10^5, \frac{\rho \|\mathbf{u}\| L}{\mu}\right) \tag{3}$$

The Reynolds number is also calculated based on the conditions in the cell adjacent to the surface. Note that the Reynolds number is bounded from below by the critical Reynolds number for flat plate flow ($\mathrm{Re} = 5{\cdot}10^5$). This implies that the boundary layer is assumed to be turbulent. Additionally the lower bound ensures a non-zero mass flux from liquid fuels and thus circumvents the need to model the ignition process when the evaporation mass flux starts to increase from zero. The Reynolds number varies over time through the gas speed dependence, and so do the Sherwood and mass transfer numbers.

The mass transfer calculation in Eq. (2) assumes that the evaporation rate is determined by diffusion of fuel vapors through a stagnant film of thickness δ. This film thickness is unknown and is therefore computed from a mass transfer correlation

$$h_m = \frac{D_{\ell,g}}{\delta} = \frac{\mathrm{Sh} D_{\ell,g}}{L} \tag{4}$$

Decreasing the Reynolds number implies an increasing film thickness. The gas phase fuel vapor volume fraction $X_{F,g}$ is again evaluated at the adjacent grid cell center. The Reynolds number must be high enough for the stagnant film thickness implied in Eq. (2) to be entirely contained within the first grid cell. Since the Sherwood number correlation used here is only valid for a turbulent boundary layer, it is natural to use the critical Reynolds number as a lower bound. Note that in laminar conditions, this results in significant overprediction of mass transfer coefficient.

An important assumption of the evaporation model is that Eq. (2) can be applied on cell-by-cell basis, not as a global dependence for the entire pool surface. This is the essential difference between the current evaporation model and that of Suard et al. [40]. The evaporation model described here also assumes that evaporation only takes place on the surface of the liquid. This assumption may be invalid if the liquid is boiling. Boiling also enhances the convective mixing within the liquid. Modeling of the heat transfer within the liquid phase is described next.

2.3. Heat transfer within the fuel

For simplicity, we treat the liquid fuel itself like a thermally thick solid for the purpose of computing the heat conduction. There is no explicit computation of the internal liquid convection within the pool. The one-dimensional heat conduction equation for liquid temperature $T_s(x, t)$ is applied in the direction x pointing into the liquid (the point $x=0$ represents the surface)

$$\rho_s c \frac{\partial T}{\partial t} = \frac{\partial}{\partial x}\left(k \frac{\partial T}{\partial x}\right) + \dot{q}_r''' \tag{5}$$

Material properties k, ρ and c are thermal conductivity, density and specific heat, respectively. Table 1 lists the properties of fuels used in this study. The evaporation is assumed to take place on the surface and no other reactions are taking place within the liquid phase. The radiative exchange term, $\dot{q}_r'''$, is explained in detail in Section 2.4.

The thermal boundary condition on the top surface of the liquid is:

$$-k \frac{\partial T}{\partial x}(0, t) = \dot{q}_c'' + \dot{q}_r'' - \Delta h_v \dot{m}'' \tag{6}$$

where $\dot{q}_c''$ is the convective heat flux and $\dot{q}_r''$ is the net radiative heat flux. In case of in-depth radiation, the surface radiation term, $\dot{q}_r''$, is set to 0.

The convective heat transfer coefficient, h, is based on a combination of natural and forced convection correlations:

$$\dot{q}_c'' = h(T_g - T_w) \quad \mathrm{W/m^2};$$
$$h = \max\left[C|T_g - T_w|^{1/3}, \ \frac{k}{L}\mathrm{Nu}\right] \quad \mathrm{W/(m^2\,K)} \tag{7}$$

where C is a empirical coefficient for natural convection (1.52 for a horizontal plate) [21], L is a characteristic length related to the size of the physical obstruction, and k is the thermal conductivity of the gas. The Nusselt number (Nu) is calculated from [21,23]

$$\mathrm{Nu} = 0.037\,\mathrm{Re}^{4/5}\,\mathrm{Pr}^{1/3};\quad \mathrm{Re} = \frac{\rho|\mathbf{u}|L}{\mu};\quad \mathrm{Pr} \approx 0.7 \tag{8}$$

Depending on the scenario, the bottom of the liquid layer can be modelled as a thermal boundary condition (either adiabatic or natural convection and radiation) or as another layer of condensed-phase material.

2.4. In-depth radiation heat transfer

A "two-flux" model based on the Schuster–Schwarzschild approximation [37] is here used to solve the transport of radiation heat inside the liquid layer. It assumes that the radiative intensity is constant inside the "forward" and "backward" hemispheres. The transport equation for the intensity in the "forward" direction is

$$\frac{1}{2}\frac{dI^{+}(x)}{dx} = \kappa_s\big(I_b(x) - I^{+}(x)\big) \tag{9}$$

where x is the distance from the material surface, κ_s is the appropriate mean absorption coefficient and I_b is the emission source term $I_b(x) = \sigma T^4(x)/\pi$. A corresponding formula can be given for the "backward" direction. Multiplying Eq. (9) by π gives us an equation for the "forward" radiative heat flux

$$\frac{1}{2}\frac{d\dot{q}_r^{+}(x)}{dx} = \kappa_s\big(\sigma T^4(x) - \dot{q}_r^{+}(x)\big) \tag{10}$$

The radiative source term in the heat conduction equation (5) is the sum of the "forward" and "backward" flux gradients

$$\dot{q}_r'''(x) = \frac{d\dot{q}_r^{+}(x)}{dx} + \frac{d\dot{q}_r^{-}(x)}{dx} \tag{11}$$

The boundary condition for Eq. (10) at the liquid surface is given by

$$\dot{q}_r^{+}(0) = \epsilon\dot{q}_{r,in} + (1-\epsilon)\dot{q}_r^{-}(0) \tag{12}$$

where ϵ is the surface emissivity, $\dot{q}_{r,in}$ is the incident radiative heat flux from the gas phase and $\dot{q}_r^{-}(0)$ is the "backward" radiative heat flux from the liquid phase at the surface. In this formulation, the surface emissivity (or reflectivity) and the internal absorption coefficient are treated as independent properties. Emissivity is assumed to be 1 for all cases.

2.5. Absorption coefficients of liquids

Most liquids are highly selective absorbers, absorbing intensively in some wavelength regions while being transparent in others. The available liquid absorption coefficient data in the open literature, such as the Coblentz Society data found on the NIST Chemistry WebBook [33], are sometimes limited to wavelengths from approximately 2.0 μm upwards. This reduces the usability of the data in fire safety applications because roughly 20% of the radiation energy in large hydrocarbon flames is on the wavelengths shorter than 2.5 μm. Absorption spectra that begin from 1 μm have been published for some liquids, including toluene [5,4,4], methanol [8], benzene [6] and water [7]. Furthermore, Ref. [42] includes spectrally resolved transmission spectra of ethanol, heptane, JP-8, and an ethanol–toluene blend. Complex refractive index spectra for a few diesel fuels and heptane were reported in Ref. [15].

Table 2 gives an overview of the absorption coefficient data used in this study. The spectral absorption coefficient is calculated from the imaginary part of the complex refractive index k_r as

$$\kappa_\lambda = 4\pi k_r/\lambda \tag{13}$$

except for Ethanol, for which the absorption coefficient is determined from Beer's law: $\kappa_\lambda = \log(I_\lambda(x)/I\lambda(0))/x$. Here x is the path length of radiation. Fig. 2 shows corresponding absorption coefficient spectra in the wavelength range 1–10 μm.

Table 2
Overview of absorption coefficient data.

Liquid	Wavelength range (μm)	Format	Ref.
Ethanol	1.5–5	Transmission	[42]
Heptane	0.2–10	Complex refractive index	[15]
Toluene	1.5–22	Complex refractive index	[4]
Methanol	1.25–5000	Complex refractive index	[8]
Water	0.66–10,000	Complex refractive index	[7]
Benzene	1.6–869	Complex refractive index	[6]

Trying to capture the wavelength dependence of in-depth absorption would be computationally too expensive and unjustified because the gas-phase radiation calculation in fire safety engineering applications usually assumes gray medium. Therefore, we need to calculate a mean absorption coefficient for each of the liquids. A number of different mean absorption coefficients have been defined in the literature but it is unclear which of the possible definitions best applies to the current situation. In this work, we want to find a mean absorption coefficient that produces an accurate prediction of the total radiative heat transport within a finite layer of liquid. For the assessment of the accuracy, we use the exact solution for the radiative flux to positive direction at distance x within a non-scattering plane layer [37]

$$\dot{q}_{\lambda,ex}^{+}(x) = E_{b,\lambda}(T_\infty)2E_3(\tau) + E_{b,\lambda}(T(x))2\int_0^\infty E_2(\tau')\,d\tau' \tag{14}$$

where $\tau = \kappa x$ is the optical thickness, T_∞ and $T(x)$ are the temperatures of the external source (flame) and liquid, and $E_n(\tau)$ are the exponential integral functions of order n. $E_{b,\lambda}(T)$ is the blackbody emissive power at wavelength λ

$$E_{b,\lambda}(T) = \frac{2\pi hc^2}{\lambda^5}\frac{1}{\exp\big[hc/k_B\lambda T\big]-1} \tag{15}$$

where h, k_B and c are the Planck constant, Boltzman constant and the speed of light respectively. The procedure for estimating the mean absorption coefficients was:

1. Start with spectrally resolved absorption coefficients κ_λ for a liquid.
2. Assume the source temperature of the incoming radiation and calculate the incoming spectrum $E_{b,\lambda}(T_\infty)$ using Eq. (15). In this paper we assume $T_\infty = 1450$ K for sooting fuels. For ethanol and methanol, the measured incoming radiation spectrum of 2 m ethanol pool fire is used [42].
3. Calculate the exact integrated radiative flux at distance x of the liquid using line by line integration of Eq. (14)

$$\dot{q}_{ex}^{+}(x) = \int_0^\infty \dot{q}_{\lambda,ex}^{+}(\tau)\,d\lambda \tag{16}$$

   The spectral dependendence of κ_λ is now introduced through τ and weighting factor $E_{b,\lambda}(T_\infty)$.
4. Find a value for the mean absorption coefficient κ_S that minimizes the error between the radiative flux obtained from solution of Eq. (10) and the flux calculated from Eq. (16).

The algorithm above requires two choices: first is the choice of characteristic flame temperature T_∞ serving a basis for wavelength weighting. The second choice is the metric of calculating the error between the line-by-line and two-flux solutions. Two alternative metrics were investigated: the first one tries to produce an accurate flux at the bottom of the liquid layer ($x = L_x$), thus giving a

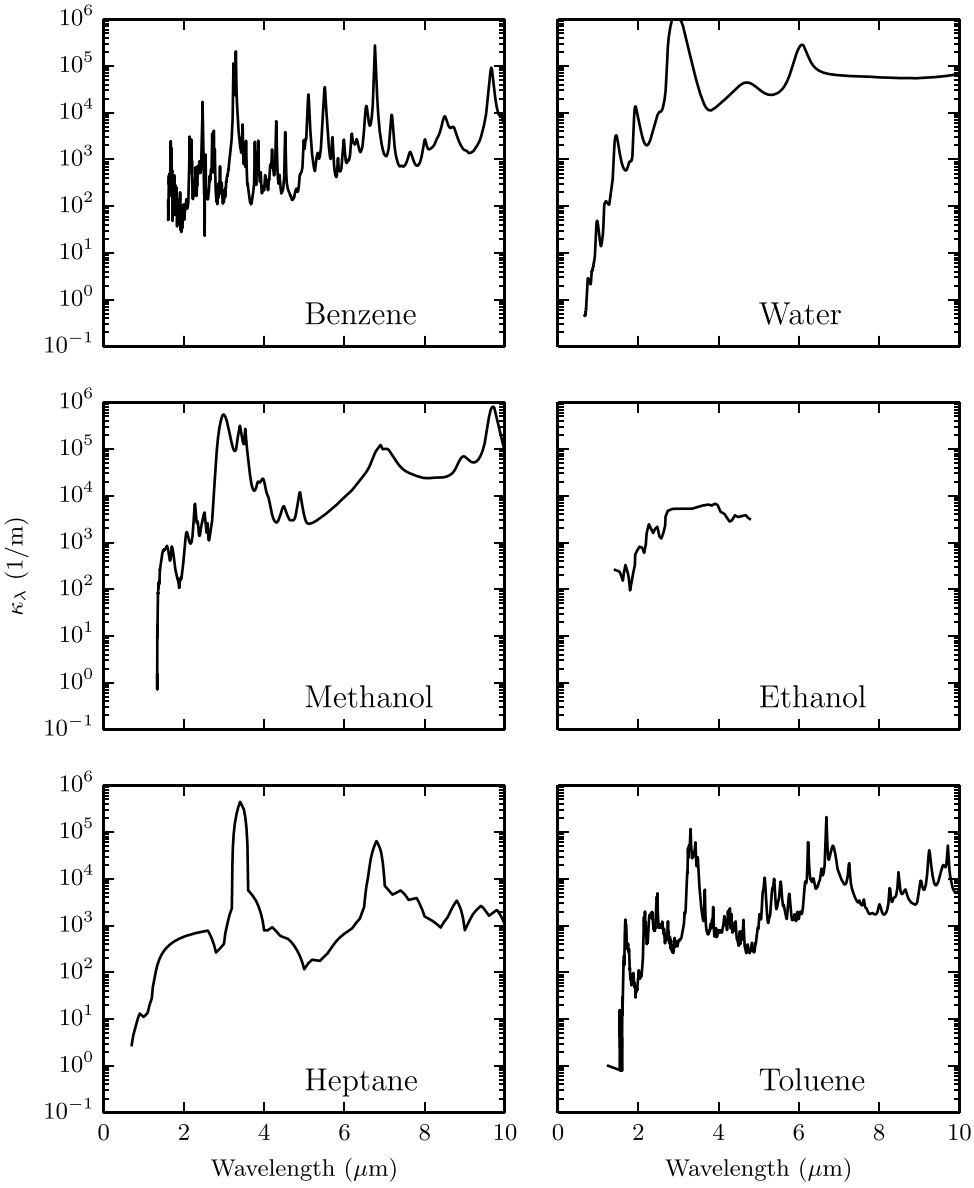

Fig. 2. Absorption coefficient spectra for liquids considered in this study.

Table 3
Effective absorption coefficients for selected liquids – M1.

Path length (mm)	1	5	10	15	50
Benzene	342	139	86	62	21
Water	1205	340	190	136	49
Ethanol	1044	303	168	116	35
Heptane	458	216	130	92	31
Toluene	456	158	90	63	21

good estimate for the amount of energy absorbed by the liquid. The absorption coefficients corresponding to this criterion were obtained as

$$\text{Method M1:} \quad \kappa = \arg\min\left[\frac{\dot{q}^+(L_x)}{\dot{q}^+(0)} - \frac{\dot{q}^+_{ex}(L_x)}{\dot{q}^+_{ex}(0)}\right] \tag{17}$$

The second, alternative criterion tries to reproduce the distribution of radiant flux over the entire thickness of liquid layer. This choice should provide more accurate distribution of temperature inside the liquid but it may not conserve the energy as well as the first criterion. The absorption coefficients corresponding to the second criterion were obtained as

$$\text{Method M2:} \quad \kappa = \arg\min\left[\int_0^{L_x}\left(\frac{\dot{q}^+(x)}{\dot{q}^+(0)} - \frac{\dot{q}^+_{ex}(x)}{\dot{q}^+_{ex}(0)}\right)^2 dx\right]. \tag{18}$$

Table 4
Effective absorption coefficients for selected liquids – M2.

Path length (mm)	1	5	10	15	50
Benzene	396	212	162	144	132
Water	1393	1336	1345	1345	1345
Ethanol	1236	1134	1140	1140	1141
Heptane	512	355	335	333	333
Toluene	537	289	227	211	207

Tables 3 and 4 show the absorption coefficients calculated with both methods. In this paper we will explore the effect of this choice on the accuracy of predicted pool burning rates.

2.6. In-depth convective heat transfer

Several authors have pointed out the possibility of convective currents in liquid fuels during pool burning, suggesting various reasons for the motion within fuel. One possible reason is the non-uniform burning rate, causing a flow towards the regions of high burning rates. Another source of motion is the temperature gradient between the liquid and the hot walls of the pool, and the resulting convective currents. Third source is the in-depth absorption that can produce a hydrodynamically unstable temperature distribution within the pool.

Accurate modeling of all these phenomena would require solving the full Naiver–Stokes equations for the liquid phase together with heat transfer modeling for the pool walls. Such approach is too time consuming for practical work and too complex for use in engineering calculations. Instead, a simplified model is sought.

We make the assumption that in large pool fires the main source of convective motions is buoyancy generated by in-depth radiation absorption. We then calculate an effective thermal conductivity that reproduces the heat flux through the liquid layer at the surface of the fuel. Abramzon and Sirignano [1] used a similar methodology in their model of droplet evaporation. They based their effective thermal conductivity on a numerical solution of liquid motion within the droplet.

The non-dimensional heat flux due to convective and conductive motions at an arbitrary plane in the liquid is given by the Nusselt number:

$$\mathrm{Nu} = \frac{\dot{q}''_{conv}}{\dot{q}''_{cond}} = \frac{\dot{q}''_{conv}}{\rho c_p k \Delta T L_x^{-1}}. \tag{19}$$

If we assume that the heat transfer by convection can be modeled by heat conduction with a effective conductivity k_{eff} Eq. (19) becomes

$$\mathrm{Nu} = \frac{k_{eff}}{k} \tag{20}$$

Several correlations have been developed for the Nusselt number in Rayleigh Benard convection. Most of them are related to the classic case of Rayleigh Benard convection with fluid heated from the bottom. We calculate the Nusselt number from a correlation for internally heated horizontal plane layer with isothermal top boundary and thermally insulated bottom boundary: [26]

$$\mathrm{Nu} = 0.338\mathrm{Ra}_i^{0.227}. \tag{21}$$

Here Ra_i is the internal Rayleigh number:

$$\mathrm{Ra}_i = \frac{g\chi\dot{q}'''_r H^5}{k\nu\alpha}, \tag{22}$$

where g is the gravitational acceleration, χ is the coefficient of thermal expansion of liquid, $\dot{q}'''_r$ is the volumetric heat source and H is a characteristic length scale. In the denominator, k is the thermal conductivity of the liquid, ν is the kinematic viscosity and α is the thermal diffusivity.

Table 5
Liquid characteristics for internal convection for various hydrocarbon fuels.

Fuel	$\chi \cdot 10^{-3}$ (1/K) [19]	$\nu \cdot 10^{-7}$ (Pa s) [19]	$Ra \cdot 10^5$	Nu
Heptane	1.24	5.5	8.99	8.4
Ethanol	1.09	5.5	0.650	4.6
Methanol	1.18	13.9	1.03	5.1
Toluene	1.08	7.1	6.52	7.8
Benzene	1.25	6.9	7.91	8.2
Water	0.214	8.9	0.02	2.1

Tasaka [44] derived the internal Rayleigh number in case of exponentially decaying heat source. The correct Rayleigh number is given by

$$\mathrm{Ra}_i = \frac{g\chi\dot{q}'''_r H^5}{k\nu\alpha}\frac{\eta^2}{Q(\eta)}\left[1 - \left(1 + \frac{1}{\eta}\right)\exp\left(-\frac{1}{\eta}\right)\right] \tag{23}$$

Here $\eta = 1/\kappa$ is the length scale associated with the source distribution. The normalization constant $Q(\eta)$ in Eq. (23) is calculated from

$$Q(\eta) = \int_0^L \exp\left(-\frac{z}{\eta}\right)dz = \eta\left[1 - \exp\left(\frac{L}{\eta}\right)\right] \tag{24}$$

The difference in convection driven by temperature differences between plates and internal heat sources is in the critical Rayleigh number Ra_C for onset of convection. Heat source concentrated near the top boundary tends to raise Ra_C.

To illustrate the influence of the absorbed internal radiation on the internal convection, we list the characteristic liquid properties in Table 5 for the case $\dot{q}''_r = 20\ \mathrm{kW/m^2}$. The Rayleigh numbers are calculated from Eq. (23) with the volumetric heat source evenly distributed over the liquid layer thickness $\dot{q}'''_r = \dot{q}''_r/H$. The characteristic length scale is taken to be 1 cm. The values of κ used in the calculations are those determined by the least squares fitting criteria defined in Eq. (18).

It can be seen that for most liquids the Rayleigh numbers are $O(10^5)$ and the Nusselt numbers are ~10. Therefore, we conclude that the heat transfer through the fuel would be greatly enhanced by convection. In this work we attempt to account for the enhanced heat transfer by replacing the thermal conductivity of the liquid by an effective value calculated from Eq. (20).

A significant source of uncertainty in calculating the effective thermal conductivity is the characteristic length scale. We take the characteristic length H to be the depth of the liquid layer L_x. However the depth of the liquid layer is constantly changing. Furthermore Eq. (21) depends also on knowing the volumetric heating rate.

The effective thermal conductivity model presented here is likely to work better for relatively thin layers of fuel. In thin layers convection can be thought to cause mixing through the whole layer. In deeper pools the convective currents are likely to involve only a part of the liquid [50].

2.7. Computational domains and boundary conditions

All the pool fires considered in this work are rectangular with side length D. The computational domain dimensions are $L \times L \times H$. The height of the computational domain is selected so that the flames are contained within the computational domain. Boundaries are open to flow with the exception of bottom boundaries, where a no slip boundary condition is used. Outside

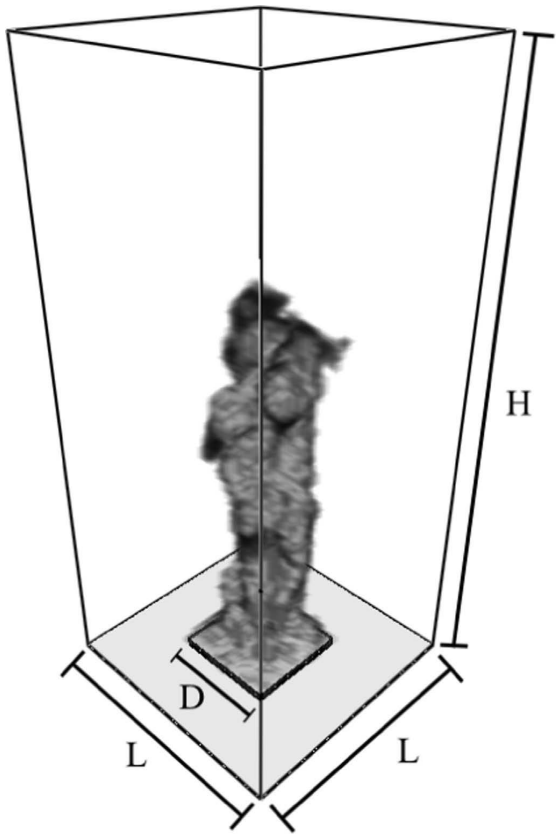

Fig. 3. Computational model of a pool fire.

the liquid pool and its walls, the floor is considered to be adiabatic. Fig. 3 shows a typical pool fire computational model.

Grid resolution is an important parameter for CFD simulations. For buoyancy dominated flows, such as flames from a pool fire, the grid resolution between two models can be compared using the Plume Resolution Index (RI) [32]. The RI is defined as

$$RI = \frac{D^*}{\delta x}, \tag{25}$$

where δx is the nominal size of a mesh cells, and D^* is a characteristic fire diameter

$$D^* = \left(\frac{\dot{Q}}{\rho_\infty c_p T_\infty \sqrt{g}} \right)^{2/5} \tag{26}$$

D^* is related to the characteristic fire power Q^* via the relation $Q^* = (D^*/D)^{5/2}$, where D is the physical diameter of the fire. The quantity, $\dot{Q}$, is the total heat release rate of the fire.

This metric is related to the resolution of the gas phase in absence of walls. The near wall grid resolution can be monitored in terms of y^+, the distance from the surface to the first grid cell center divided by the local viscous length scale, δ_ν [34]:

$$y^+ = \frac{1}{2}\frac{\delta n}{\delta_\nu}; \quad \delta_\nu = \frac{\mu/\rho}{u_\tau}; \quad u_\tau = \sqrt{\tau_w/\rho}, \tag{27}$$

where $\tau_w = \mu \partial |\mathbf{u}|/\partial n$ is the viscous stress evaluated at the wall. FDS calculates the friction velocity u_τ using the Werner–Wengle wall model [52].

3. Results

In this section we compare results from simulations, with experimental data and empirical correlations. First, we focus on the effect of the absorption coefficient and thermal conductivity.

The fuel properties used in the simulations are listed in Table 1. Note that the heats of vaporization are evaluated at the liquid boiling points. The thermal conductivities, k, are found in Ref. [19], except for butane, which is found in Ref. [16]. The heats of combustion, Δh_c, are computed in FDS based on the heats of formation of the reactants and products listed in Ref. [30]. The heats of combustion account for the presence of products of incomplete combustion, like CO and soot.

Two models, named K1 and K2, for thermal conductivity and two models, named M1 and M2, for the absorption coefficient are considered. In model K1 the thermal conductivity is equal to the molecular liquid conductivity. In model K2 the thermal conductivity is defined by Eq. (20). Absorption coefficient is calculated from Eq. (18) in model M2 and from Eq. (17) in model M1. The resulting models and the values of absorption coefficient and thermal conductivity are listed in Table 6.

After this we compare burning rate predictions with multiple empirical correlations and conduct sensitivity studies.

3.1. Evaporation of water under external heat flux

The first simulation deals with the evaporation of water in ASTM E2058 fire propagation apparatus, reported in [12]. Liquid water was placed in a 0.0072 m^2 Pyrex glass dish under 50 kW/m^2 s external heat flux, and the mass of the glass was measured. The initial mass of water in the dish was 99.6 g.

The absorption coefficient of pyrex glass is not known, but glass in general is known to be weak absorber of thermal radiation [37]. Order of magnitude estimate of 20 1/m is used for the absorption coefficient. This absorption coefficient results in transmittance of 0.7 for a 1 cm layer of pyrex. This agrees well with the values reported for various types of glass in [37]. The pyrex glass is assumed to be 1 cm thick. Density of the glass is assumed to be 2200 kg/m^3, specific heat 0.75 kJ/kg and conductivity 1.1 W/mK. The glass layer is assumed to be insulated from the bottom.

In the fire propagation apparatus, the heat flux is produced by flame-heated radiating panels. This validation case has the benefit of avoiding the model uncertainties associated with the combustion and gas-phase heat transfer by allowing the external heat flux to be prescribed instead of predicting it.

The computational model of the fire propagation apparatus is similar to the computational models used for pool fires. There is no lip around the water layer in the model. The heat flux incident on the pool is specified and the heaters are not modeled. The values of absorption coefficient and thermal conductivity used are listed in Table 6. Fig. 4 shows the measured water vaporization rate with different combinations of thermal conductivity and absorption coefficient. Fig. 4a presents models with effective thermal conductivity calculated from (20) and absorption coefficients calculated either with method M1 or M2. Both methods of calculating

Table 6
Effective thermal conductivities and absorption coefficients of water and ethanol.

Model	Water		Ethanol	
	κ	k	κ	k
M1K1	140	0.53	160	0.17
M1K2	140	2.51	160	0.89
M2K1	1345	0.53	1140	0.17
M2K2	1345	2.51	1140	0.89

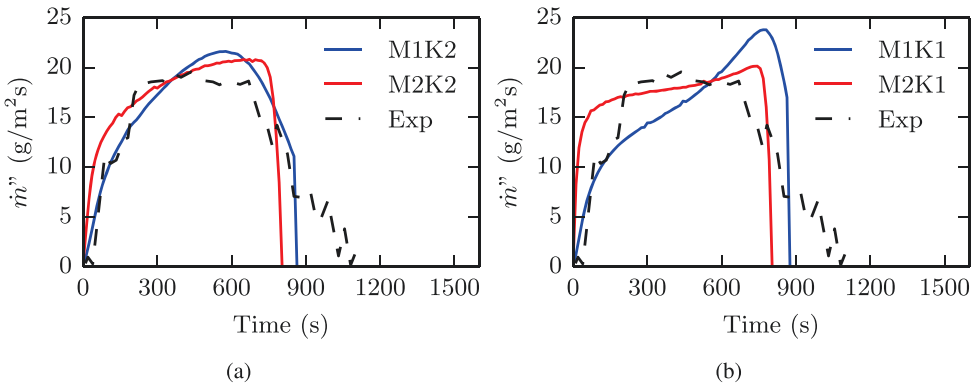

Fig. 4. Evaporation rate of water in ASTM E2058 fire propagation apparatus. Data from [12]: (a) models with effective thermal conductivity calculated from (20) and (b) models with unaltered thermal conductivity.

the absorption coefficient produce evaporation rate curves that agree reasonably well with the experimental data. Model M1K2 gives a better fit for the slow decay rate of water evaporation

Fig. 4 b shows the evaporation rates for cases where molecular values are used for thermal conductivity. When the absorption coefficient is calculated from Method M1 the evaporation rate shows a growing trend, peaking at about 20% over the measured evaporation rate. In absence of convection, lower value of absorption coefficient creates a hot zone below the surface. When absorption coefficient is calculated using method M2 the evaporation rate shows a small growing trend but remains very close to the steady state value of the measured evaporation. Since the absorption coefficient in this case is relatively high, most of the incoming radiation is absorbed near the surface.

Fig. 5 shows temperature profiles within the liquid during the simulation for all four models. The top row shows models where absorption coefficient is determined by method M2. When molecular values of thermal conductivity are used, there is a significant hot spot just beneath the liquid surface. Below this hot spot the temperatures decay quickly. When the effective thermal conductivities are used, the hot spot under the surface is diminished and temperatures throughout the liquid are more uniform. The profiles presented here are very similar to the temperature profiles measured in laboratory scale methanol pool fires in quartz containers [49].

In the bottom row, absorption coefficients are determined by

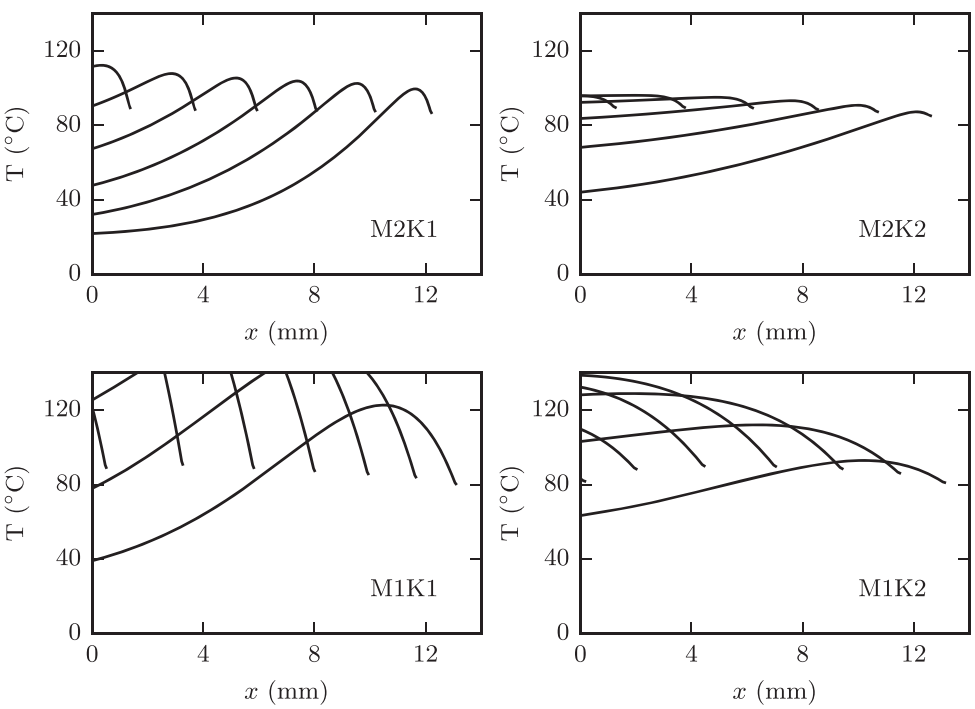

Fig. 5. Predicted temperature distributions in water evaporating in ASTM E2058 fire propagation apparatus. *Top row*: absorption coefficients determined with method M2. *Bottom row*: absorption coefficients defined by method M1.

Method M1. When molecular values of thermal conductivity are used, the hot spot in the liquid is larger and deeper in the liquid. More radiation passes through the layer, but the distribution of heat within the liquid is wrong. When the effective thermal conductivity is used, once again the hotspot is diminished and the temperature profiles are smoothed out.

When method M2 was used, the resulting temperature profiles are physically plausible. The profiles produced by method M1 are clearly unphysical. This is a direct consequence of the selection of the optimization metric. Method M2 attempts to reproduce the heat source distribution within the liquid and consequently the temperature distributions look better. Method M2 on the other hand attempts to get the right amount of radiation through the liquid layer without care for the temperature profiles.

Even though the temperature distributions from models M1K1 and M1K2 are unphysical, something can be learned from the results. These models can be seen as models of a situation, where the internal heat transfer in the liquid is greatly enhanced, e.g., by lateral convection.

The surface temperature remains relatively low in all cases. This indicates that the mass transfer coefficient predicted by Eq. (4) is likely to be too large for this situation. This point will be discussed in more detail in Section 4.

All models are unable to predict long tail of the evaporation rate. Several factors are likely to be involved. First, in reality the thin water film would form droplets, thus decreasing the projected surface area available for absorption of radiation and slowing down the evaporation rate. Second, the incoming heat flux in the experiment may be non-homogenous. The computational model retains the one-dimensional, uniform layer structure and incoming heat flux is uniform. Third, if the bottom of the pyrex dish is not exactly level, parts of the bottom may be exposed before all of the water has evaporated. This would lead to decreased surface area for evaporation and absorption of incident radiation.

3.2. Ethanol pool fires

Next we consider the time dependent burning rate of a pool fire. We test the predicted burning rates of FDS against the large ethanol pool fire case from Victoria University [47]. In this tests ethanol was burned under a hood in $0.81 \times 0.70 \times 0.05\ \mathrm{m}^3$ fuel trays constructed from steel. The computational model of the fires consists of a $0.81 \times 0.70\ \mathrm{m}^2$ surface depicting the pool and 5 cm lip around the pool (see Fig. 6). In the test under consideration there is 5 liters of ethanol in the pool. This translates to 9 mm thickness for the liquid layer. The values used for absorption coefficient and thermal conductivity are listed in Table 6. The gas phase is discretized using a 5 cm grid.

Fig. 7 shows the heat release rate of a pool fire for the four different models listed in Table 6. All models reach similar peak HRR values. The importance of internal heat transfer can be seen from results for models M1K1 and M1K2. Model M1K2 predicts a slowly growing heat release and M1K1 predicts a relatively steady and low burning rate. In both these models the incoming heat is spread deeper in to the fuel. Models M2K2 and M2K1 provide very similar results with each other. Due to the high absorption coefficient predicted by method M2, incoming radiation is absorbed near the surface, and the effect of thermal conductivity is diminished.

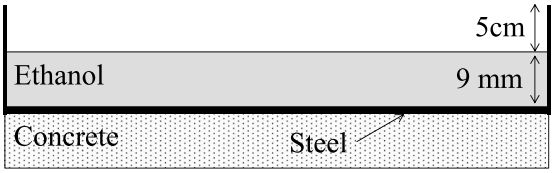

Fig. 6. Diagram of the ethanol pan.

Overall, lower absorption coefficients tend to produce lower burning rates and longer lasting fires. The effect of the thermal conductivity is tied to the value of absorption coefficient. Lower absorption coefficients lead to wider distribution of heat sources within the fuel layer which in turn increases the importance of heat transfer from within the fuel to the liquid surface.

The initial phase is too short in all cases. This is caused by over prediction of the evaporation rate in ambient conditions. This point will be discussed further in Section 4.

3.3. Maximum burning rates of hydrocarbon pool fires

Next, a series of liquid pool fires with different fuels is considered. The pool fires are assumed to burn in a 1 m by 1 m square tray, and the fuel layer is 10 cm thick. The predicted maximum burning rates are compared to several empirical correlations.

The simplest of such correlations is based on the ratio of the heat of combustion, Δh_c, and the heat of gasification, Δh_g:

$$\dot{m}'' = 0.001 \frac{\Delta h_c}{\Delta h_g}; \quad \Delta h_g = \Delta h_v + \int_{T_0}^{T_b} c_p \, dT \tag{28}$$

where Δh_v is the sensible heat of vaporization, T_0 is the initial temperature, T_b is the boiling temperature, and c_p is the specific heat of the liquid fuel. The heat of gasification, Δh_g, is the amount of energy required to raise the fuel from its initial temperature to its boiling temperature and evaporate it.

A commonly used correlation is due to Babrauskas [12]:

$$\dot{m}'' = \dot{m}''_{max} \left[1 - \exp(-k\beta D) \right]. \tag{29}$$

Here, $\dot{m}''_{max}$ and $k\beta$ are empirical parameters and D is the pan diameter. In the simulations the pans are rectangular and the side length is adjusted give the same area with a circular pool with diameter D.

Recently Ditch et al. [13] derived a empirical correlation for the heat flux incident on pool surface given by

$$\dot{q}'' = \dot{m}'' \Delta h_g = \dot{q}''_c + \dot{q}''_r Y_s^{1/4} \left\{ 1 - \exp\left(-\left[C \Delta h_g D \right]^p \right) \right\}. \tag{30}$$

Here $\dot{q}''_c = 12.5\ \mathrm{kW/m^2}$, $\dot{q}''_r = 68.3\ \mathrm{kW/m^2}$, $C = 4/3$ and $p = 3/2$ are empirical constants, D is the pool diameter (m) and Y_s is soot yield of the fuel (mass soot/mass fuel).

The grid size is 5 cm for all cases and the $D^*/\delta x$ values for these simulations range from 15 to 30.

In the preceding sections it was shown that in-depth absorption of radiation and internal convection in the liquid may affect the mass loss rate. However, since we are comparing simulation results against correlations, the layer thickness needed for absorption coefficient and thermal conductivity is not known. Furthermore, in pool fire experiments internal convection and in-depth radiation absorption are often minimized, e.g., by using glass beads or rocks in the pan. Therefore, we can assume that the effect of internal convection and absorption is not as pronounced in these pool fires. Absorption coefficients were determined using Method 2, and are listed in Table 4. The molecular values of thermal conductivity listed in Table 1 are used.

The absorption coefficients of acetone and butane could not be calculated and an order of magnitude estimate 100 1/m was used. For methanol, the absorption coefficient spectra was available, but the assumption of blackbody radiation is not applicable for low-sooting fuels such as methanol. Instead, the value for methanol is based on the absorption coefficient of ethanol.

Fig. 8 shows a comparison of predicted peak burning rates with

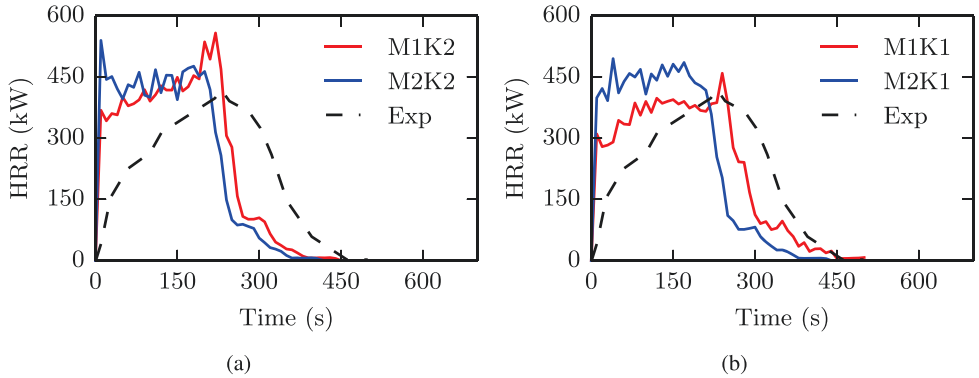

Fig. 7. Effect of absorption coefficient and thermal conductivity.

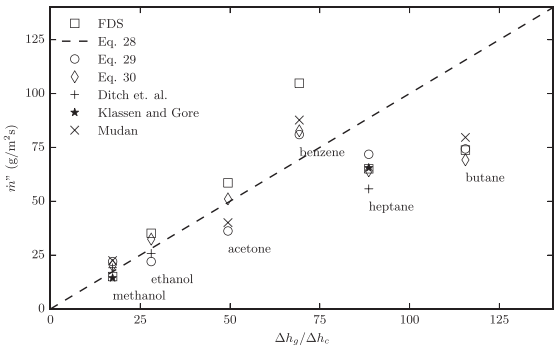

Fig. 8. Comparisons of predicted maximum burning rates of 1 m^2 square pool fires for various liquid hydrocarbon fuels with experimental data for large ($D \geq 1$ m) pool fires. Predictions with open symbols and experimental data with crosses and closed symbols.

Table 7
Empirical constants for hydrocarbon fuels considered.

Fuel	$\dot{m}''_\infty$	$k\beta$	$\dot{m}''(D = 1\text{ m})$ (kg/m^2 s)
Methanol	0.022	–	0.022
Ethanol	0.022	–	0.022
Benzene	0.085	2.7	0.081
Acetone	0.041	1.9	0.035
Heptane	0.101	1.1	0.067
Butane	0.078	2.7	0.073

experimental correlations. The circles in Fig. 8 are calculated using Eq. (29) with data listed in Table 7. The diamonds are results from Eq. (30). The squares represent results from the present work. The dashed line corresponds to Eq. (28). Experimental data is plotted with crosses and closed symbols.

Experimental data in Fig. (8) is extracted from the works of Klassen and Gore [25], Ditch et al. [13] and Mudan [29]. The data is shown for large ($D \geq 1$) poolfires. Where burning rates are available from several sources, such as for ethanol and heptane, the burning rate predictions fall within the experimental data.

The predicted and observed mass loss rates follow Eq. (28) fairly well. This highlights the importance of the thermal properties of fuels in predicting burning rates. With the exception of benzene, FDS predicts burning rates that are very close to those predicted by Eq. (30). In case of benzene, the reason for overprediction of burning rate can be found in the high radiative fraction used for the simulation.

Due to its low boiling point, butane is likely to be boiling in most experiments. The evaporation model used in this paper does not include boiling and thus is likely to lack some essential physics for predicting butane pool fires. Despite this, the burning rate predicted by FDS is very close to experimental data and correlations.

There is considerable uncertainty in the literature for mass burning rates of heptane. Several reasons for differences in reported values have been proposed, including varying lip heights, fuel level control and pan shape. The burning rate of heptane predicted by the present model is lower than predicted by either Eq. (30) or Eq. (29). Ditch et al. [13] note that in heptane pool fire experiments conducted at FM Global, burning rates over 0.07 kg/m^2 s have rarely been recorded.

3.4. Grid sensitivity studies

In this section, we investigate the effect of the gas phase grid resolution on the predicted burning rates. The gas phase solution affects the evaporation rate through the incoming radiative heat flux and the gas temperature and composition near the surface. In order to separate the sensitivity of the evaporation model from the sensitivity of the gas phase solution, we also look at grid sensitivity of the predicted radiative heat flux with fixed burning rate.

The pool fires considered in this work are rectangular. Lip was not included in the pool models because the lip height would have necessarily changed with changing grid resolution, as the grids are too coarse to resolve the lip, thus possibly adding to the grid sensitivity of the model. The dimensions and grid sizes of the models are listed in Table 8. The computational domain is discretized using N_x, N_y and N_z grid points in the x, y and z directions respectively. The domain width is set to three times the pan width and the height of the domain is set so that the flames are fully contained within the domain. The simulation time is 300 s when burning rate is predicted and 50 s when burning rate is prescribed. The burning rate is then calculated as an average of the steady state burning rate. On the finest grid, the simulations took approximately 1 month of wall clock time. Due to the increasing demands on computational time, grid resolutions finer than $D^*/\delta x = 40$ are not considered for predicting the burning rates.

Fig. 9a shows the predicted maximum burning rates for different sizes of heptane pool fires and with four grid resolutions. The expected average burning rate is based on Eq. (29). The predicted burning rates decrease as the grid is refined. On the finest grids the predicted burning rates are very close to the expected burning rates.

Fig. 9 b shows the predicted incident heat flux for different

Table 8
Mesh and computational domain dimensions for heptane pool fires and burners. See Fig. 3.

Grid no.	D (m)	L (m)	H (m)	$D^*/\delta x$	N_x	N_y	N_z
1	0.5	1.5	4	10	21	21	56
2	0.5	1.5	4	20	42	42	112
3	0.5	1.5	4	30	63	63	168
4	0.5	1.5	4	40	84	84	224
5	0.5	1.5	4	52	108	108	288
6	0.5	1.5	4	61	126	126	336
1	1	3	9	10	21	21	63
2	1	3	9	20	42	42	126
3	1	3	9	30	60	60	180
4	1	3	9	40	81	81	243
5	1	3	9	50	102	102	306
6	1	3	9	60	120	120	360
1	2	6	16	10	21	21	56
2	2	6	16	20	42	42	112
3	2	6	16	30	63	63	168
4	2	6	16	40	84	84	224
5	2	6	16	50	105	105	280
6	2	6	16	61	126	126	336
1	3	9	22	10	24	24	59
2	3	9	22	20	45	45	110
3	3	9	22	30	66	66	162
4	3	9	22	40	87	87	213
5	3	9	22	50	111	111	272
6	3	9	22	60	132	132	323

sizes of heptane pool fires and with five grid resolutions. The mass flux is calculated from Eq. (29). The incident heat flux is defined as the sum of the convective and radiative heat fluxes. The heat fluxes are calculated as a spatial average over the burner surface. The surface average is then averaged over the last 50 s of the simulation. Comparison is made with expected incident heat flux predictions derived from Eq. (29) as

$$\dot{q}''_{expected} = \dot{m}''\Delta h_g \tag{31}$$

The predicted incident heat flux decreases as the grid is refined. The predicted incident heat fluxes on the finest grid are lower than the expected value for all but the smallest pools. This behavior is in agreement with the behavior of heptane pool fires seen in Fig. 9a, which shows that higher burning rates are predicted on coarse grids. For smaller pool widths, grid convergence is reached with lower values of $D^*/\delta x$ than for large pool widths. For 0.5 m diameter pools, the results converge at about $D^*/\delta x = 30$, while for 3 m pools the resolution requirement is twice that.

Fig. 9 c shows the average y^+ values over the surface of the pool as a function of $D^*/\delta x$. Dashed lines correspond to results from simulations with predicted burning rates and continuous lines correspond to prescribed burning rates. For the smallest pool, $y^+ \approx 50$ for the coarsest mesh and $y^+ < 30$ for all other mesh resolutions (see Fig. 9c). This suggests that the boundary layer is well resolved in this case. For 3 m pools y^+ approaches 100 on the finest grid. For a given grid resolution the y^+ for pools with predicted and prescribed burning rates are very close.

The grid sensitivity analysis presented in Fig. 9 shows that the burning rates are converging. No clear rule of thumb for necessary grid resolution can be inferred. The results indicate that both the

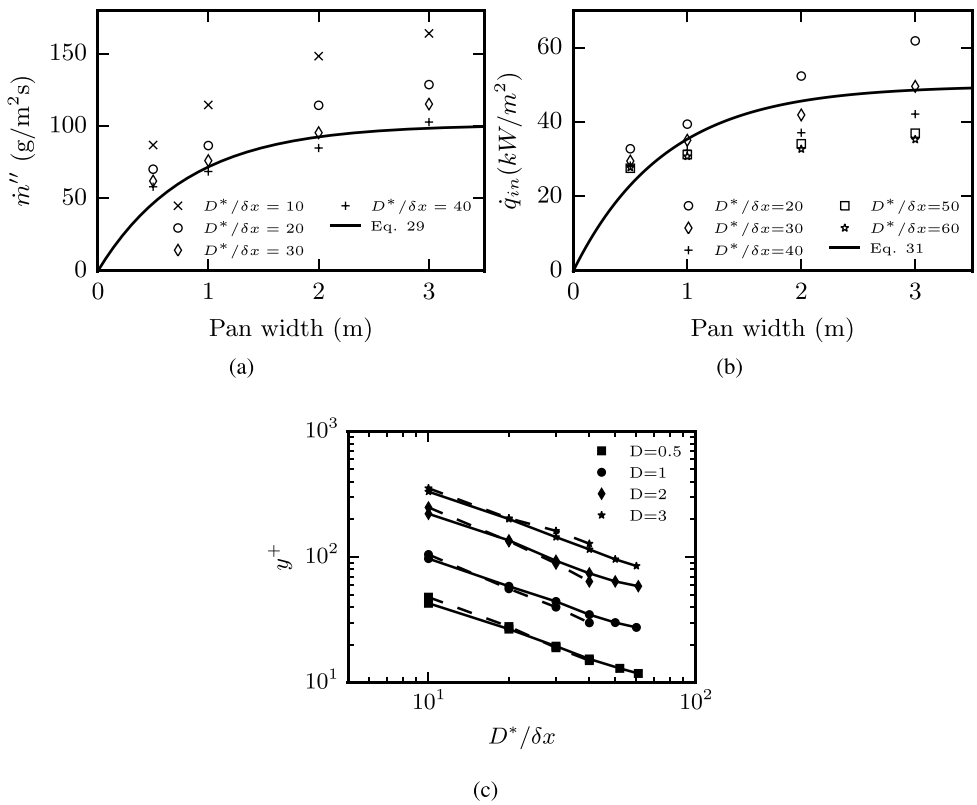

Fig. 9. Grid sensitivity for predicted mass loss rates and predicted incident heat fluxes of rectangular heptane pool fires. (a) Predicted mass loss rates, (b) predicted incident heat flux for burners with prescribed burning rates, and (c) average y^+ values on pool surface (dashed lines) and on burner surfaces (continuous lines).

flame and the boundary layer need to be adequately resolved. However relatively fine grids are needed for accurate predictions. Coarse grids produce higher burning rates than the fine grids. Possible reason for the incident heat flux and burning rate overestimation with coarse grids is the inability of the coarse grid to capture the fuel rich core of the flame. This in turn then leads to faster mixing of fuel and oxidizer. As a consequence, the source terms in the RTE are closer to the fuel surface and the blocking effect of the fuel vapors is weakened.

3.5. Sensitivity of maximum burning rates to model parameters

In this section we present the sensitivity analysis of maximum burning rate predictions on model parameters. The sensitivity study is conducted with a model of 1 m^2 heptane pool fire.

The sensitivity analysis is carried out by varying each variable θ by 10% and consequently estimating the sensitivities as

$$\Delta\dot{m}(\theta)'' = \frac{\frac{\partial \dot{m}(\theta)''}{\partial\theta}\Delta\theta}{\dot{m}(\theta)''} \times 100\%. \tag{32}$$

Variables considered were the heat of combustion h_c, radiative fraction X_r, specific heat of the fuel vapor c_g, heat of vaporization h_v, the boiling temperature T_b, specific heat of fuel liquid c_p, thermal conductivity of the fuel liquid k, soot yield ν_s, and the absorption coefficient. Fig. 10 displays the results arranged in decreasing order by their magnitude.

The most important parameters turn out to be related to gas phase properties. The heat of combustion and the radiative fraction control the source term in the radiative transfer equation and consequently the amount of radiative feedback to the fuel surface. Increasing either of these variables will increase the burning rate. The third most important variable is the specific heat of gas. Increasing the specific heat of the vapors leads to lower burning rates. This points to the importance of resolving the fuel rich core of the flame and the layer of unburnt fuel above the pool. When the specific heat is increased the fuel gases will remain cooler decreasing the convective and radiative heat transfer to the pool. In addition decreased temperatures will lead to decreased buoyant forces.

Overall the sensitivity analysis presented here corroborates the findings in this section. Fig. 9 shows that in order to reach convergence, relatively fine grids were needed. When the grid was fine enough to enable accurate prediction of heat feedback to the fuel surface, the same grid was also fine enough to predict the burning rate with similar accuracy. The findings here are also in line with Eqs. (29) and (30) which both show that the maximum burning rates of large pools are mostly related to their thermal properties, most importantly their heat of combustion and heat of gasification.

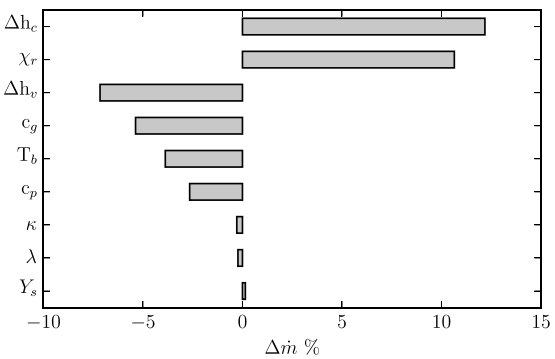

Fig. 10. Sensitivity of maximum burning rate predictions to model parameters. Results for a 1 m^2 heptane pool fire.

4. Discussion

In this paper, models for liquid evaporation at the surface and heat transfer within the liquid were presented. In this section we discuss the effects of these models on the results. We will first discuss the evaporation model and then move on to the heat transfer within a liquid. We focus on the cases where time dependent data was available: the evaporation of water under constant heat flux of Section 3.1 and the ethanol pool fire of Section 3.2.

4.1. Evaporation model

The evaporation mass flux is tied to heat transfer within the fuel through the surface temperature of the liquid. As the surface temperature increases, the fuel volume fraction at liquid surface $X_{F,\ell}$ also increases, leading to larger mass flux. As the liquid temperature approaches boiling point the mass flux predicted by Eq. (2) grows without bound. In this situation the evaporation rate is not limited by mass transfer. On the other hand, during the ignition and flame spread phase, the surface temperature is far from the boiling point and the value of the mass transfer coefficient is more important. Fig. 11 shows the behavior of evaporation rate for ethanol with various surface temperatures. The dotted line in the figure gives the limiting evaporation rate for uniform flux of $\dot{q}''_{in}$ = 30 kW. The largest value of h_m in Fig. 11 is the one predicted by Eq. (4) for ambient conditions.

For larger values of h_m the limiting mass transfer rate $\dot{q}''_{in}/h_g$ is achieved at a lower temperature. Since in the water evaporation case the incident heat flux is constant, the mass transfer coefficient mainly affects the surface temperature. The fact that the surface temperature is significantly lower than boiling point suggests that the mass transfer coefficient used in Eq. (2) is too large.

In pool fires the situation is more complicated since the incident heat flux is a function of the evaporation rate and position. Larger values of h_m lead to higher evaporation rates at ambient conditions. This in turn leads to higher incident heat flux and increase in evaporation rate. The maximum of the incident heat flux is limited by the flame geometry and eventually reaches a limiting value. The mass transfer coefficient controls the surface

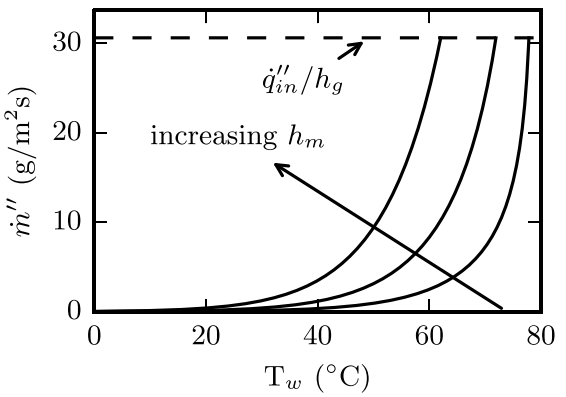

Fig. 11. Dependence of evaporation rate on mass transfer coefficient h_m and surface temperature T_w. *Full lines*: evaporation rates. *Dashed line*: limiting evaporation rate $\dot{q}''_{in}/h_g$ with $\dot{q}''_{in}$ = 30 kW.

temperature at which this equilibrium is reached. The time needed to reach equilibrium is controlled by the liquid side heat transfer together with the mass transfer coefficient.

From experiments it is known that the surface temperature of the liquid in pool fire rises quickly to a value near its boiling point [11]. During this initial phase, higher values of h_m will lead to higher evaporation rates. Since in a pool fire the heat feedback $\dot{q}''_{in}$ is strongly dependent on the evaporation rate $\dot{m}''$, higher h_m will lead to faster rise of burning rate.

After the initial phase, the effect of the mass transfer coefficient on the evaporation rate will be less pronounced. The value of the mass transfer coefficient will affect the surface temperature and therefore also the amount of surface reradiation. Higher mass transfer coefficient may lower the surface temperature and consequently lower the amount of surface reradiation. The surface reradiation by liquids at or below their boiling point is expected to be significantly lower than the incident heat flux from the flames.

The preceding analysis assumed constant values of mass transfer coefficient. When the pool fire is fully developed, the increased temperatures and gas velocities near the surface will increase the mass transfer coefficient significantly due to increased diffusivity and higher Reynolds number.

4.2. Effects of heat transfer within the liquid on heat release rates

The experimental heat release rate (HRR) curve for the Ethanol pool fire of Section 3.2 shows several stages. For the purposes of this discussion we identify the following stages:

1. *Initial phase*: In this phase the surface temperature rises quickly to a temperature near the boiling point. The duration of this stage varies but in experiments of Chen et al. [11], this stage lasted approximately 30 s.
2. *Transition phase*: In this phase the surface temperature is near the boiling point but there is still a temperature gradient within the liquid. During this stage the temperature gradient within the liquid decreases until the liquid reaches uniform temperature. During this stage the evaporation rate is slowly increasing.
3. *Bulk boiling phase*: In this phase the surface and a layer of liquid beneath the surface has reached boiling point, resulting in high evaporation rates.
4. *Decay phase*: At this point the remaining fuel layer is thin and has an almost uniform temperature close to boiling point. Sometimes this will result in a spike in burning rate as the remaining liquid boils. If the pool bottom is not completely level, the remaining liquid will flow towards the deepest parts of the pan, decreasing the pool surface area. In this case the pool will burn out more gradually.

Fig. 12 shows where these stages in relation to the HRR curve under investigation. Similar phases in burning rate have been observed in experiments on laboratory scale pool fires [18,11].

In the simulations, the initial phase was too quick. As discussed above, this is caused by the evaporation model over predicting the evaporation at low surface temperatures. This effect is especially pronounced for the ethanol poolfire case due to the low boiling point of ethanol.

In Section 3.1 it was shown that the heat transfer model M2K1 and M2K2 produced plausible temperature profiles within the liquid. On the other hand models M1K1 and M1K2 produced unphysical temperature profiles. Models M2K1 and M2K1 also matched the experimental evaporation rate better. The opposite was true for the Ethanol pool fire case, where models M1K1 and M1K2 produced a slowly rising heat release rate after initial sharp rise.

In the water evaporation case these two models were found to produce unphysical temperature distributions. These models can be seen as a surrogate for a model were the heat transfer is greatly enhanced, e.g., by lateral convection. When water is evaporated in the fire propagation apparatus, the incident heat flux on the surface is constant and reasonably homogenous. In a pool fire the incident heat flux on the liquid is neither constant nor homogenous. The resulting position dependent burning rates will drive movement of the liquid in two dimensions.

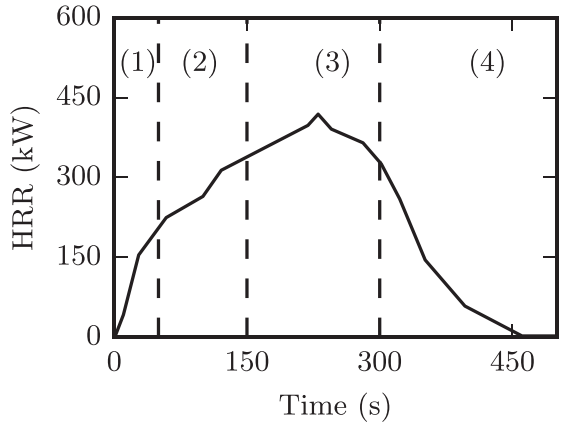

Fig. 12. Different stages in the ethanol pool fire.

Fig. 13 shows the time development of the liquid surface temperature at the pool center. In all cases the surface temperatures rise quickly to a value close to 60 °C. After this models M1K1 and M1K2 show a slow increase in the surface temperature. The surface temperatures predicted by the models M2K1 and M2K2 are virtually indistinguishable. The fact that the predicted surface temperature is significantly lower than the boiling temperature once again suggests that the mass transfer coefficient h_m is too large. Note however that for lab scale pool fires of methanol, steady surface temperatures approximately 5 °C below boiling point have been measured [49].

Due to the fast rise of HRR, the simulated ethanol pool fires burn out quicker than in the experiments. In the simulations, the pools burn out first in the middle, resulting in a long tail of decaying heat release rate.

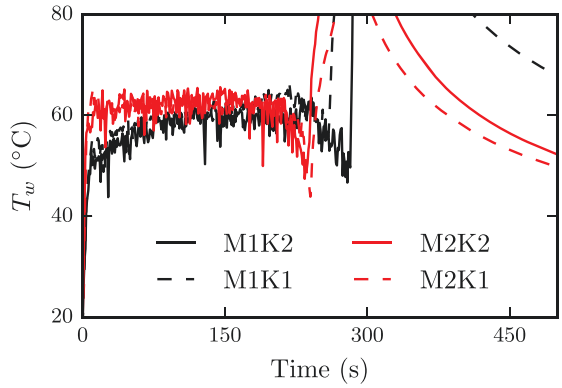

Fig. 13. Predicted surface temperatures at the center of the pool in the ethanol pool fire.

5. Conclusions

This paper considered modeling of liquid pool fires and the effect of the in-depth heat transfer on the predicted burning rates. Effective radiative absorption coefficients were determined based on spectrally resolved data, where available. The effects of the in-depth convection were modeled by an effective heat transfer coefficient in one-dimensional conduction equation.

Grid refinement studies showed that the maximum burning rates can be predicted accurately when the gas phase equations are solved on a fine enough grid. Relatively fine grids are needed for achieving grid independent predictions of pool fire burning rates. Predicting the incident heat flux on the pool surface was found to be the most important factor in predicting the maximum burning rates. These results are in agreement with the vast literature on pool fires where the maximum burning rates of pool fires have been found to mostly depended on the fire geometry and secondly on the thermophysical parameters of the fuel.

The in-depth heat transfer in the form of the in-depth radiation absorption and enhanced heat transfer in the liquid due to convective motions may be important in predicting the detailed dynamics of the fire. The models employed in this paper are not capable of accounting for all the phenomena in the liquid. The gray gas approximation of the radiation transport cannot correctly predict the transport of radiation through the liquids. This prediction could be improved by resolving the wavelength dependence of the absorption and re-radiation. In the current model, heat transfer is one dimensional. In real liquids, the heat transfer by convection in the lateral direction could play a large role. Better models for the internal heat transfer may be needed to correctly capture the dynamics of pool fires. Better evaporation model may also be needed in conjunction with the improved heat transfer models.

All pool fires considered in this paper were in open atmosphere or in large rooms, fires in compartments, spill fires and fires in elevated pressures are possible future research topics.

Acknowledgments

This work has been financed by the State Nuclear Waste Management Fund (VYR), in context of the SAFIR2014 programme and Nordic Nuclear Safety Research (NKS) in context of the POOLFIRE project.

References

[1] B. Abramzon, W.A. Sirignano, Droplet vaporization model for spray combustion calculations, Int. J. Heat Mass Transf. 32 (9) (1989) 1605–1618.
[2] V. Babrauskas, Heat release rates, in: SFPE Handbook of Fire Protection Engineering, 3rd ed., National Fire Protection Association, Quincy, MA, 2002.
[3] Vytenis Babrauskas, Estimating large pool fire burning rates, Fire Technol. 19 (4) (1983) 251–261.
[4] J.E. Bertie, R.N. Jones, Y. Apelblat, C.D. Keefe, Infrared intensities of liquids XIII: accurate optical constants and molar absorption coefficients between 6500 and 435 cm^{-1} of toluene at 25 °C, from spectra recorded in several laboratories, Appl. Spectrosc. 48 (January) (1994) 127–143.
[5] J.E. Bertie, R.N. Jones, Y. Apelblat, C.D. Keefe, Infrared intensities of liquids XXV: Dielectric constants, molar polarizabilities and integrated intensities of liquid toluene at 25 °C between 4800 and 400 cm^{-1}, J. Mol. Struct. 750 (1–3) (2005) 78–93.
[6] J.E. Bertie, R.N. Jones, C.D. Keefe, Infrared intensities of liquids XII: accurate optical constants and molar absorption coefficients between 6225 and 500 cm^{-1} of benzene at 25 °C, from spectra recorded in several laboratories, Appl. Spectrosc. 47 (7) (1993) 891–911.
[7] J.E. Bertie, Z. Lan, Infrared intensities of liquids XX: the intensity of the OH stretching band of liquid water revisited, and the best current values of the optical constants of H2O (l) at 25 °C between 15,000 and 1 cm^{-1}, Appl. Spectrosc. 50 (8) (1996) 1047–1057.
[8] J.E. Bertie, S.L. Zhang, H.H. Eysel, S. Baluja, M.K. Ahmed, Infrared intensities of liquids XI: infrared refractive indices from 8000 to 2 cm^{-1}, absolute integrated intensities, and dipole moment derivatives of methanol at 25 °C, Appl. Spectrosc. 47 (August) (1993) 1100–1115.
[9] B. Broeckmann, H. Schecker, Heat transfer mechanisms and boilover in burning oil–water systems, J. Loss Prev. Process Ind. 8 (3) (1995) 137–147.
[10] R.L. Brown, S.E. Stein, Boiling point data, in: NIST Chemistry WebBook, NIST Standard Reference Database Number 69, National Institute of Standards and Technology, Gaithersburg, MD. ⟨http://webbook.nist.gov⟩, (retrieved 23.05.14).
[11] Chen Bing, Shou-Xiang Lu, Chang-Hai Li, Quan-Sheng Kang, Vivien Lecoustre, Initial fuel temperature effects on burning rate of pool fire, J. Hazard. Mater. 188 (1-3) (2011) 369–374.
[12] P.J. DiNenno (Ed.), SFPE Handbook of Fire Protection Engineering, 3rd ed., National Fire Protection Association, Quincy, MA, 2002.
[13] Benjamin D. Ditch, John L. de Ris, Thomas K. Blanchat, Marcos Chaos, Robert G. Bill Jr., Sergey B. Dorofeev, Pool fires an empirical correlation, Combust. Flame 160 (12) (2013) 2964–2974.
[14] E.S. Domalski, E.D. Hearing, Condensed phase heat capacity data, in: NIST Chemistry WebBook, NIST Standard Reference Database Number 69, National Institute of Standards and Technology, Gaithersburg, MD. ⟨http://webbook.nist.gov⟩, (retrieved May 23, 2014).
[15] L.A. Dombrovsky, S.S. Sazhin, S.V. Mikhalovsky, R. Wood, M.R. Heikal, Spectral properties of diesel fuel droplets, Fuel 82 (2003) 15–22.
[16] M.O. McLinden E.W. Lemmon, D.G. Friend, Thermophysical Properties of Fluid Systems, ⟨http://webbook.nist.gov⟩, (retrieved 23.05.14).
[17] W. Grosshandler, RadCal: A Narrow Band Model for Radiation Calculations in a Combustion Environment. NIST Technical Note TN 1402, National Institute of Standards and Technology, Gaithersburg, MA, 1993.
[18] H, Hayasaka, Unsteady burning rates of small pool fires, in: 5th Symposium on Fire Safety Science, 1997, pp. 499–510.
[19] W.M. Haynes (Ed.), Thermal conductivity of liquids, in: CRC Handbook of Chemistry and Physics, 95th ed., CRC Press/Taylor and Francis, Boca Raton, FL (Internet Version 2015).
[20] F.J. Higuera, Steady thermocapillary-buoyant flow in an unbounded liquid layer heated nonuniformly from above, Phys. Fluids (1994–present) 12 (9) (2000) 2186–2197.
[21] J.P. Holman, Heat Transfer, 7th ed., McGraw-Hill, New York, 1990.
[22] S. Hostikka, K.B. McGrattan, A. Hamins, Numerical modeling of pool fires using large eddy simulation and finite volume method for radiation, in: Fire Safety Science—Proceedings of the Seventh International Symposium, International Association for Fire Safety Science, 2002, pp. 383–394.
[23] F.P. Incropera, D.P. De Witt, fundamentals of Heat and Mass Transfer, 4th ed., John Wiley and Sons, New York, 1996.
[24] Pierre Joulain, The behavior of pool fires: state of the art and new insights, in: Symposium (International) on Combustion, vol. 27(2), 1998, pp. 2691–2706.
[25] M. Klassen, J.P. Gore, Structure and radiation properties of pool fires, NIST GCR 94-651, National Institute of Standards and Technology, 1994. Final Report: Grant No. 60NANB1D1169.
[26] F.A. Kulacki, A.A. Emara, Steady and transient thermal convection in a fluid layer with uniform volumetric energy sources, J. Fluid Mech. 83 (02) (1977) 375–395.
[27] R.J. McDermott, A velocity divergence constraint for large-eddy simulation of low-mach flows, J. Comput. Phys. 274 (2014) 413–431.
[28] K.B. McGrattan, R. McDermott, J. Floyd, S. Hostikka, G. Forney, H. Baum, Computational fluid dynamics modelling of fire, Int. J. Comput. Fluid Dyn. (2012) 1–13.
[29] K.S. Mudan, P.A. Croce, Fire hazard calculations for large open hydrocarbon fires, in: SFPE Handbook of Fire Protection Engineering, 2nd ed., National Fire Protection Association, Quincy, MA, 1995.
[30] M.W. Chase Jr., NIST-JANAF thermochemical tables, 4th ed., J. Phys. Chem. Ref. Data, Monograph No. 9, 1998.
[31] National Institute of Standards and Technology, Gaithersburg, Maryland, USA, and VTT Technical Research Centre of Finland, Espoo, Finland. Fire Dynamics Simulator, Technical Reference Guide, 6th ed., April 2013. Vol. 1: Mathematical Model; Vol. 2: Verification Guide; Vol. 3: Validation Guide; Vol. 4: Configuration Management Plan.
[32] National Institute of Standards and Technology, Gaithersburg, MD, USA, and VTT Technical Research Centre of Finland, Espoo, Finland. Fire Dynamics Simulator, Technical Reference Guide, Vol. 3: Validation, 6th ed., April 2013.
[33] P.J. Linstrom, W.G. Mallard, Evaluated Infrared Reference Spectra. Webpage. NIST Chemistry WebBook, NIST Standard Reference Database Number 69. ⟨http://webbook.nist.gov⟩, (retrieved May 23.05.14).
[34] S.B. Pope, Turbulent Flows, Cambridge University Press, Cambridge, 2000.
[35] K. Prasad, C. Li, K. Kailasanath, C. Ndubizu, R. Ananth, P.A. Tatem, Numerical modelling of methanol liquid pool fires, Combust. Theory Model. 3 (1999) 743–768.
[36] S.S. Sazhin, P.A. Krutitskii, W.A. Abdelghaffar, E.M. Sazhina, S.V. Mikhalovsky, S.T. Meikle, M.R. Heikal, Transient heating of diesel fuel droplets, Int. J. Heat Mass Transf. 47 (14–16) (2004) 3327–3340.
[37] R. Siegel, J.R. Howell, Thermal Radiation Heat Transfer, 4th ed., Taylor & Francis, New York, 2002.
[38] T. Steinhaus, S. Welch, R.O. Carvel, J.L. Torero, Large-scale pool fires, Thermal Sci. 11 (2) (2007) 101–118.
[39] S.I. Stoliarov, S. Crowley, R.E. Lyon, G.T. Linteris, Prediction of the burning rates of non-charring polymers, Combust. Flame 156 (2009) 1068–1083.
[40] S. Suard, M. Forestier, S. Vaux, Toward predictive simulations of pool fires in mechanically ventilated compartments, Fire Saf. J. 61 (2013) 64.

[41] J.M. Suo-Anttila, T.K. Blanchat, Hydrocarbon Characterization Experiments in Fully Turbulent Fires: Results and Data Analysis, Technical Report SAND2010-6377, Sandia National Laboratory, Albuqueque, NM, 2011.
[42] J.M. Suo-Anttila, T.K. Blanchat, A.J. Ricks, A.L. Brown, Characterization of thermal radiation spectra in 2 m pool fires, Proc. Combust. Inst. 32 (2) (2009) 2567–2574.
[43] F. Tamanini, Direct measurement of the longitudinal variation of burning rate and product yield in turbulent diffusion flames, Combust. Flame 51 (1983) 231–243.
[44] Y. Tasaka, Y. Takeda, Effects of heat source distribution on natural convection induced by internal heating, Int. J. Heat Mass Transf. 48 (6) (2005) 1164–1174.
[45] R. Taylor, R. Krishna, Multicomponent Mass Transfer, Wiley-Interscience, New York, 1993.
[46] A. Tewarson, Generation of heat and gaseous, liquid, and solid products in fires, in: SFPE Handbook of Fire Protection Engineering, 4th ed., National Fire Protection Association, Quincy, MA, 2008.
[47] I.R. Thomas, K.A.M. Moinuddin, I.D. Bennetts, The effect of fuel quantity and location on small enclosure fires, J. Fire Protect. Eng. 17 (May (2)) (2007) 85–102.
[48] P.T. Tsilingiris, Comparative evaluation of the infrared transmission of polymer films, Energy Convers. Manag. 44 (2003) 2839–2856.
[49] A. Vali, D.S. Nobes, L.W. Kostiuk, Effects of altering the liquid phase boundary conditions of methanol pool fires, Exp. Thermal Fluid Sci. 44 (2013) 786–791.
[50] A. Vali, D.S. Nobes, L.W. Kostiuk, Transport phenomena within the liquid phase of a laboratory-scale circular methanol pool fire, Combust. Flame 161 (4) (2014) 1076–1084.
[51] K. Wakatsuki, G. Jackson, J. Kim, A. Hamins, M. Nyden, S. Fuss, Determination of planck mean absorption coefficients for hydrocarbon fuels, Combust. Sci. Technol. 180 (2008) 616–630.
[52] H. Werner, H. Wengle, Large-eddy simulation of turbulent flow over and around a cube in a plate channel, in: 8th Symposium on Turbulent Shear Flows, Munich, Germany, 1991. Technische University Munich, pp. 155–168.

Fire Safety Journal 91 (2017) 266–275

Contents lists available at ScienceDirect

Fire Safety Journal

journal homepage: www.elsevier.com/locate/firesaf

IAFSS 12th Symposium 2017

Predicting the heat release rates of liquid pool fires in mechanically ventilated compartments

Topi Sikanen[a,*], Simo Hostikka[b]

[a] VTT Technical Research Centre of Finland Ltd., Espoo, Finland
[b] Aalto University, Espoo, Finland

ARTICLE INFO

Keywords:
Pool fire
Compartment fires
Industrial fires
Modelling

ABSTRACT

In this paper we perform predictive simulations of liquid pool fires in mechanically ventilated compartments. We show that steady state burning rates are accurately predicted using a detailed model for the liquid phase heat transfer. The effect of lowered oxygen vitiation on the burning rate of pool fires is correctly captured. Simulations were done using the Fire Dynamics Simulator and the experiments considered were conducted in the OECD PRISME project. The main difference between the present study and previous simulation studies is the use of a detailed liquid evaporation model and the direct calculation of the vitiation and thermal environment interactions through the CFD solver.

1. Introduction

Liquid pool fires are a significant hazard to industrial facilities. The liquids could originate e.g. from leaking transformers, generators or other machinery. Knowing the fire burning rate is the starting point of any fire safety analysis. The factors affecting the burning rates of liquid pool fires in open atmosphere are well known for a wide variety of liquids. However, many fire scenarios, especially in nuclear facilities, involve fires in confined spaces.

The burning rates in confined spaces, possibly coupled with mechanical ventilation, can be significantly different from the ones measured in open atmosphere. These differences are caused by e.g. air vitiation and heat radiation from hot walls and the hot gas layer. An international research program PRISME was conducted between January 2006- June 2011 to study fires in air-tight mechanically ventilated compartments. Results from this program have been previously used in validation of CFD codes for compartment fire scenarios [1–5]. For the purposes of this paper the studies of Wahlqvist and Van Hees [1,3] are of interest. In [3] they showed that the Fire Dynamics Simulator (FDS) and especially the HVAC model in it were able to accurately predict the temperatures and pressures in a mechanically ventilated compartment. In this paper, we build upon their model of the PRISME experimental facility.

Relatively few attempts have been made of predicting rather than prescribing the burning rates in compartments. The proposed models vary in complexity. The simplest model is a correlation such as the one by Peatross and Beyler [6]. Suard et al. [4] implemented this model as a boundary condition for ISIS-CFD code. Pretrel et al. [5] used a simple heat balance at the liquid surface to predict the burning rates.

Wahlqvist and Van Hees [3] combined the empirical correlation of Peatross and Beyler and added a term to account for enhanced vaporization due to heat flux from hot walls and the gas layer. Their model takes as an input the mass loss rate of the pool fire in open atmosphere. This may come from correlations or from a experimentally determined mass loss curve. If a mass loss curve is used, it is simplified and the steady state burning rate is assumed to continue indefinitely. This predetermined mass loss rate is reduced according to the correlation or enhanced based on the radiative heat feedback from the walls. Their model was implemented as an boundary condition for FDS and the oxygen concentration near the flame base was obtained from the gas phase solution. They added an output quantity to extract the external radiation without any influence from the flame radiation.

In this study, we will not rely on such an “engineering” approach but try to model the liquid evaporation rate from the first principles. The benefit of our approach is that the burning rates can also be predicted for fuels for which the experimental data is not available. On the other hand, much more detailed information about the thermophysical properties of the fuels is needed.

In this paper we investigate the capability of the detailed liquid evaporation model in the FDS to predict the pool fire burning rates in a series of compartment fire experiments. We focus on 0.4 m^2 pool fires. First the model predictions are compared against experimental data from open air experiments. We look at both the burning rate predictions and the temperatures within the liquid. After this we turn to

* Corresponding author.
E-mail address: topi.sikanen@vtt.fi (T. Sikanen).

http://dx.doi.org/10.1016/j.firesaf.2017.03.060
Received 14 February 2017; Accepted 15 March 2017
Available online 25 April 2017

Nomenclature

c	heat capacity (kJ/kg/K)
$D_{l,q}$	binary diffusion coefficient (m/s)
g	gravitational acceleration (m/s^2)
h	heat transfer coefficient (W/m^2/K)
h_m	mass transfer coefficient (m/s)
Δh_v	latent heat of vaporization (kJ/kg)
k	thermal conductivity (W/m/K)
L	length scale (m)
$\dot{m}''$	mass flux (kg/m^2/s)
$\dot{m}$	burning rate (kg/s)
p	Pressure (Pa)
$\dot{q}''$	heat flux (kW/m^2)
$\dot{q}'''$	volumetric heat source (kW/m^3)
R	universal gas constant (J/mol/K)
T	temperature (K)
t	time (s)
u	velocity (m/s)
X	Species volume fraction (dimensionless)
x	dimension into the liquid (m)

Greek

δx	grid cell size (m)
ϵ	emissivity (dimensionless)
κ	absorption coefficient (1/m)
σ	Stefan-Boltzman constant (kg/s^3/K^4)
μ	viscosity (kg/m/s)
ρ	density (kg/m^3)

subscripts

c	convective part of heat flux
g	gas phase conditions
r	radiative part of heat flux
s	surface conditions
0	ambient conditions

under-ventilated fires. We look at predicted burning rates and extinction times as function of the ventilation rate.

2. Simulation methods

2.1. Gas-phase

The simulations considered in this paper were conducted using Fire Dynamics Simulator. The details of the physical and numerical models can be found in [7]. In this section a brief overview of the relevant models and methods is given. FDS is a Large Eddy Simulation (LES) code that solves a form of the Navier-Stokes equations appropriate for low-speed, thermally-driven flow with an emphasis on smoke and heat transport from fires. The governing equations for momentum transport are discretized by second order central finite differences on a cartesian staggered grid. A two stage explicit Runge-Kutta method is used for time-stepping. Radiative heat transfer is included in the model via the solution of the radiation transport equation (RTE) for a gray gas. In the gas phase, the RTE is solved using the finite volume method radiation. The absorption coefficients of the gas-soot mixtures are computed using the RadCal narrow-band model. The RTE solution method for condensed phase will be described below.

In the present paper, gas phase combustion is treated by the single step, mixing-controlled chemical reaction scheme using three lumped species. These lumped species are air, fuel, and products. All simulations in this study were performed by using dodecane as the fuel. The combustion reaction was assumed to yield 1.5% soot and 0.6% carbon monoxide [3]. The radiative fraction of the combustion reaction is assumed to be 0.35 and the heat of combustion Δh_c is set to 42 MJ/kg.

FDS contains a simple extinction model based on the concept of critical flame temperature. For each computational cell, the extinction is determined by two criteria: The first criterion suppresses the combustion if the temperature in the computational cell does not exceed a user defined auto ignition temperature. The second criterion considers a stoichiometric pocket of fuel, air and products in a computational cell. If the combustion energy of this fuel is not sufficient to raise the temperature of the gas mixture over the critical flame temperature, the combustion reaction is again suppressed. Both the critical flame temperature T_{CFT} and auto ignition temperature T_{AIT} are user defined constants. For the simulations in this paper, these temperatures are 1650 K and 373 K, respectively. The former is the default value for the FDS extinction model and is a typical value for hydrocarbon fuels. Since the temperature field of a LES is not fully resolved, the measured value of auto ignition temperature cannot be used as an input. The value of 373 K for the auto ignition temperature was chosen by experimenting.

FDS has a dedicated module for modelling Heating, Ventilation and Air-conditioning (HVAC) systems connected to the gas space of the fire simulation [8]. The ventilation network is described as a series of ducts and nodes. The nodes are placed at points where the ducts intersect each other or the CFD computational domain. The ducts are uninterrupted domains of fluid flow which can encompass elbows, expansion/contraction fittings and various other fittings. The losses due to friction and various other duct fittings are assigned as dimensionless loss numbers to the ducts. The node losses are attached to the ducts as loss terms only appear in the duct equations. The module does not presently store any mass. Therefore, mass flux into a duct is equal to the mass flux out of the duct.

2.2. Liquid evaporation

The rate at which liquid fuel evaporates when burning is a function of the liquid temperature and the fuel vapor pressure above the pool surface. According to the Clausius-Clapeyron relation, the volume fraction of the fuel vapor above the surface in an equilibrium state is a function of the liquid surface temperature T_s and boiling temperature T_b

$$X_{F,\ell} = \exp\left[-\frac{h_v W_F}{R}\left(\frac{1}{T_s} - \frac{1}{T_b}\right)\right] \tag{1}$$

where h_v is the heat of vaporization and W_F is the molecular weight of the fuel gas (170.3 g/mol for dodecane). The local evaporation rate of the fuel at time t is governed by Stefan diffusion:

$$\dot{m}'' = h_m \frac{\bar{p}_m W_F}{R T_g} \ln\left(\frac{X_{F,g} - 1}{X_{F,\ell} - 1}\right); \quad h_m = \frac{Sh\, D_{\ell,g}}{L} \tag{2}$$

where h_m is the mass transfer coefficient and $\bar{p}_m$ is the pressure. T_g and $X_{F,g}$ are the gas temperature and the fuel vapor volume fraction. They are given the values in the first grid cell adjacent to the pool surface. The diffusivity calculated from gas viscosity: $D_{\ell,g} = \nu_g/Sc$. The molecular viscosity is obtained from the gas phase solution. The Schmidt number is given a constant value of 0.6. A model with variable and fuel dependent Schmidt number is under preparation. However for the simulations in this paper the effect is negligible.

The liquid fuel itself is treated like a thermally-thick solid for the purpose of computing the heat conduction. There is no computation of the internal liquid convection within the pool. The one-dimensional

heat conduction equation for liquid temperature T is applied in the direction x pointing into the liquid (the point x=0 represents the surface)

$$\rho c \frac{\partial T}{\partial t} = \frac{\partial}{\partial x}\left(k\frac{\partial T}{\partial x}\right) + \dot{q}_r''' \tag{3}$$

Material properties k, ρ and c are thermal conductivity, density and specific heat, respectively. Table 2 lists the properties of fuels used in this study. The evaporation is assumed to take place on the surface and no other reactions are taking place within the liquid phase. Calculation of the radiative exchange term, $\dot{q}_r'''$, is explained later in this section.

The thermal boundary condition on the top surface of the liquid is:

$$-k\frac{\partial T}{\partial x}(0, t) = \dot{q}_c'' + \dot{q}_r'' - \Delta h_v \dot{m}'' \tag{4}$$

where $\dot{q}_c''$ is the convective heat flux and $\dot{q}_r''$ is the net radiative heat flux. In case of in-depth radiation, the surface radiation term, $\dot{q}_r''$, is set to 0.

The convective heat transfer coefficient, h, is based on a combination of natural and forced convection correlations:

$$\dot{q}''_c = h\,(T_g - T_s) \quad \mathrm{W/m^2};\ h = \max\left[\ C\ |T_g - T_s|^{\frac{1}{3}}\ ,\ \frac{k}{L}\,\mathrm{Nu}\right] \quad \mathrm{W/(m^2.\ K)} \tag{5}$$

where C is an empirical coefficient for natural convection (1.52 for a horizontal plate), L is a characteristic length related to the size of the pool, and k is the thermal conductivity of the gas. The Nusselt number (Nu) is calculated from Incropera and Witt [9].

$$\mathrm{Nu} = 0.037\,\mathrm{Re}^{\frac{4}{5}}\,\mathrm{Pr}^{\frac{1}{3}};\quad \mathrm{Re}=\frac{\rho|\mathbf{u}|L}{\mu};\quad \mathrm{Pr}\approx 0.7 \tag{6}$$

The Sherwood and Schmidt numbers are given by

$$\mathrm{Sh} = 0.037\mathrm{Sc}^{\frac{1}{3}}\mathrm{Re}^{\frac{4}{5}};\quad \mathrm{Sc} = 0.6 \tag{7}$$

For calculation of the Sherwood number, the Reynolds number is bounded from below to be greater than $5{\cdot}10^5$. The evaporation model (Eq. (2)) is applied on cell-by-cell basis, not as global dependence for the entire pool surface. This model does not consider boiling.

A "two-flux" model is used to solve the transport of radiation heat inside the liquid layer. The transport equation for the intensity in the "forward" direction is

$$\frac{1}{2}\frac{\mathrm{d}I^+(x)}{\mathrm{d}x} = \kappa_s(I_b(x) - I^+(x)) \tag{8}$$

where x is the distance from the liquid surface, κ_s is the appropriate mean absorption coefficient and I_b is the emission source term $I_b(x) = \sigma\,T^4(x)/\pi$. A corresponding formula can be given for the "backward" direction. Multiplying Eq. (8) by π gives us an equation for the "forward" radiative heat flux

$$\frac{1}{2}\frac{\mathrm{d}\dot{q}_r^+(x)}{\mathrm{d}x} = \kappa_s(\sigma\,T^4(x) - \dot{q}_r^+(x)) \tag{9}$$

The radiative source term in the heat conduction Eq. (3) is the sum of the "forward" and "backward" flux gradients

$$\dot{q}_r'''(x) = \frac{\mathrm{d}\dot{q}_r^+(x)}{\mathrm{d}x} + \frac{\mathrm{d}\dot{q}_r^-(x)}{\mathrm{d}x} \tag{10}$$

The boundary condition for Eq. (9) at the liquid surface is given by

$$\dot{q}_r^+(0) = \epsilon\dot{q}_{r,\mathrm{in}} + (1-\epsilon)\dot{q}_r^-(0) \tag{11}$$

where ϵ is the surface emissivity, $\dot{q}_{r,\mathrm{in}}$ is the incident radiative heat flux from the gas phase and $\dot{q}_r^-(0)$ is the "backward" radiative heat flux from the liquid phase at the surface. In this formulation, the surface emissivity (or reflectivity) and the internal absorption coefficient are treated as independent properties.

Eq. (3) is discretized by finite differences. The size of the smallest cell size in each layer of material is selected automatically and is smaller than $\sqrt{k/\rho c_p}$. The mesh cells are smallest on the boundaries of the layer. For liquid fuels the mesh is regenerated each time step to avoid large errors in approximation of the temperature gradient at the surface.

3. Description of the experiments

In this paper we simulate a set of experiments conducted in open atmosphere and in mechanically ventilated compartment. These experiments were carried out by the French "Institut de Radioprotection et de Sûreté Nucléaire" (IRSN) within the OECD PRISME project [10]. The PRISME SOURCE program consisted of a series of experiments with hydrogenated tetra-propylene ($C_{12}H_{26}$, isomer of dodecane), in open atmosphere and in a mechanically ventilated compartment [11].

Single room of a larger experimental facility was used for the compartment experiments considered in this paper. The room size was 5 m wide, 6 m deep and 4 m high. The walls of the compartment are made of concrete and insulated by stone wool (Thermopan). The position of the pool was always in the middle of the room and slightly elevated to allow insulation of the pool. The pools were constructed of steel and were circular in shape. Tests with pool sizes 0.4 m^2 and 0.2 m^2 were conducted, but only the 0.4 m^2 pools were considered in the present study.

Ventilation to the room was provided by rectangular inlet and exhaust ducts connected to the ceiling. The dimensions of the inlet and exhaust openings were 0.3 m and 0.6 m. For each experiment the ventilation system was tuned to provide a certain nominal ventilation rate in absence of the fire. The inlet duct can be in either "high" position or in a "low" position. Lowering the inlet duct causes increased mixing in the compartment and disturbs the two layer structure. Table 1 shows the inlet positions and nominal air renewal rates (RR) in all the experiments.

3.1. Computational models of the experiments

The model of the liquid pool is the same in both the open atmosphere simulations and the compartment simulations. Fig. 1c shows a drawing of the pool model. The condensed phase model takes care of the heat and mass transfer within the liquid layer and the insulation below. The liquid pool boundary condition consists of three layers. On top there is 5 cm layer of TPH. This layer changes size during the simulation. Below the TPH, there is a thin, 3 mm thick, steel layer. On the bottom there is a 20 cm layer of rock wool. The bottom boundary of the rock wool is taken to be perfectly insulated.

The simulation models include a model of the pool rim. This rim is one grid cell thick. In the experiments, the free rim height was approximately 5 cm in the beginning of the tests and increased as the fuel level decreased. In the compartment fire simulations, including the rim in the model reduces the noise within the predicted steady state burning rates. For fires in open atmosphere, including the rim decreased the burning rates on coarse grids. Square shaped pools are used in the simulations. The computational models of the pools are square and their physical size is 0.36 m^2. The mass loss rates are scaled so that the effective size of the pools matches the experiments.

Table 1
Nominal air renewal rates and inlet positions in the experiments.

Experiment	RR (1/h)	Inlet position
PRS-SI-D1	4.7	High
PRS-SI-D2	8.4	High
PRS-SI-D3	1.5	High
PRS-SI-D4	4.7	High
PRS-SI-D6	4.7	Low
PRS-SI-D6a	1.7	Low

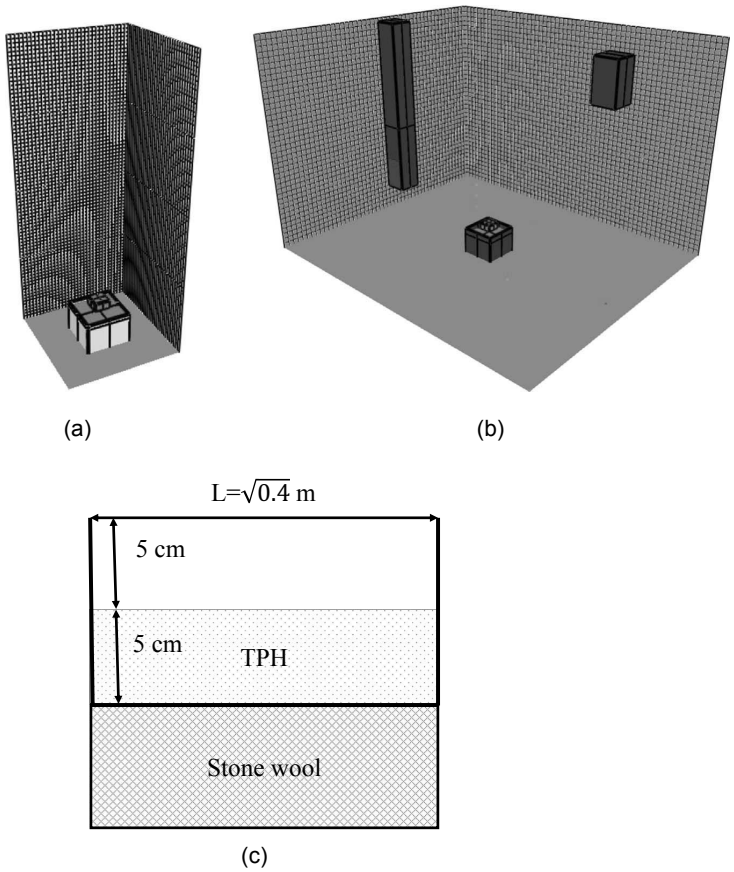

Fig. 1. Simulation geometries: (a) Model of the pool fires in open atmosphere. (b) Model of the room in DIVA facility. (c) Layered model of the liquid pool.

Table 2
Material properties used in the simulations.

Property	TPH	Steel	Concrete	Stone wool
ρ (kg/m^3)	749	2430	7850	140
c_p (kJ/kg K)	2.4	0.736	0.46	0.84
k (W/m K)	0.18	1.5	45.8	0.102
ϵ	1.0	0.7	1.0	0.95
κ (1/m)	300	–	–	–
Δh_v (kJ/kg)	380	–	–	–
Δh_c (MJ/kg)	42	–	–	–

Fig. 1a illustrates the computational domain for open pool fires. The computational domain for the open atmosphere calculations is 6 m high and 2.4 m wide. The sides and the top of the simulation domain are open to flow.

The computational model for the compartment fires is the same as the one used by Wahlqvist and Hees [1]. The model includes a single room with rectangular inlet and exhaust channels. The room is 5 m wide, 6 m deep and 4 m high. The walls of the compartment are made of 30 cm thick concrete. The ceiling of the compartment has a 5 cm layer of stone wool on top of the concrete. The position of the pool was always in the middle of the room and 40 cm from the floor. The pool rim is made of 5 mm thick steel. Fig. 1b illustrates shows the simulation model for DIVA experiments, with the inlet branch in "low" position. A one dimensional heat transfer calculation is conducted on all boundary cell faces.

The room contains a ventilation system model developed by Walquist and van Hees [1]. They created a simplified model of the ventilation network. The loss coefficients for the network nodes were calculated based on initial pressure data in the room. Room leakage rates are based on experimental measurements. Details may be found in [1]. The room models and the ventilation network models for the DIVA experiments (PRS_SI_Dx) are also available from the "fire-models" github repository (https://github.com/firemodels/fds/).

In the experiments, the liquid fuel was ignited using a gas burner. In the simulations, ignition source is a heated cubical block with 20 cm side. The surface of this block is set to 1000 °C. The block is removed after 20 s of simulation. The time needed for ignition was decided by trial and error. Too long application of the heating block leads to large initial spikes in burning rate. Too short prevents sustained combustion.

Table 2 lists the thermophysical properties of the fuel and all other materials used in the model. The thermal properties of the materials used in the DIVA facility were experimentally determined by IRSN. The absorption coefficient of TPH is estimated using the methodology described in [12] based on spectral absorption data of DTE medium oil. The absorption coefficient is of similar magnitude to the absorption coefficient of N-heptane determined in [12]. The radiative fraction of the fuel is assumed to be 0.35 (Table 3).

The model of the ventilated compartment includes a full model of the ventilation network developed by Wahlqvist and Hees [1]. A uniform grid with 10 cm cell size is used for both open fires and fires

Table 3
Parameters for the McCaffrey's plume correlations (Eq. (13)).

Region	$z/\dot{Q}^{2/5}$	η	κ
Continuous	<0.08	1/2	6.8
Intermittent	0.08 – 0.2	0	1.9
Plume	>0.2	−1/3	1.1

in compartments unless otherwise stated. This grid size selected based on grid convergence study of compartment fires. The grid convergence study is presented at the end of this paper.

4. Results and discussion

4.1. Open fires

Fig. 2a shows a comparison of predicted and observed burning rates of a 0.4 m^2 TPH pool fire in open atmosphere. Gas phase grid size is 10 cm.

The experimental mass loss rate curve shows a growing trend with a sharp spike at the end of the experiment. This trend is not captured in the simulations. Instead, the simulated burning rate quickly reaches a steady state and stays there until the fuel is consumed. The burnout is more gradual in the simulations than in the experiments because the liquid is treated as a solid and the evaporation model is applied on a cell by cell basis. This kind of modelling allows the pool to burn out in the middle, before all fuel is consumed. In the experiments, the flowing liquid would remain as a large burning surface until the very end.

Predicted and measured liquid temperatures at the center of the pool are compared in Fig Fig 2b. The predicted liquid temperatures stay almost constant before rising quickly to a temperature near the boiling point. This indicates that the thermal penetration depth in the simulations is significantly shorter than that observed in the experiments. In the simulations, a hot zone is formed under the surface of the liquid where temperatures are higher than on the surface of the liquid. In the experiments the layer just below the liquid surface is at uniform temperature near the boiling point. This can be seen as plateaus in the experimental temperature curves. In the simulations, the surface temperature remains below the boiling point. This is caused by over prediction of the mass transfer coefficient as was discussed in [12].

The one-dimensional heat transfer model with a gray radiation transfer does not seem to accurately predict the temperatures within the liquid. Convective motions within the liquid are likely to be important in explaining the experimental temperature profiles. Also, the possible benefits of spectrally resolved radiation should be examined, because the gray absorption coefficient cannot be accurate for both overall energy balance and absorption gradients, as pointed out in [12].

4.2. Compartment fires

Predicted and simulated burning rates for the compartment fires are shown in Figs. 3a–f. The overall dynamics of the pool fires are predicted well, except for the strong fluctuations in some simulations, and the high initial spikes.

In fires PRS_SI_D1 - D4, the inlet ventilation was in the “high” position. In the simulations of these experiments, the steady state burning rates and the extinction times are predicted accurately. The exaggerated initial spikes are a consequence of the ignition modelling and flame radiation challenges. In the experiments, the pools were ignited using a gas burner. The heated obstruction in the simulations cannot reproduce exactly the experimental ignition system. The second issue is that in the beginning of the simulations, before the smoke layer descends to the level of the pool surface, the burning rate prediction depends on the heat feedback from an open flame. The gas phase flame resolution will in these simulations limit the model's capability to predict the flame radiation. After the smoke layer descends below the level of the pool surface, the problem is transformed to a much easier one of predicting the heat feedback from a hot gas layer.

Wahlqvist and Van Hees [3] simulated experiments PRS_SI_D1 - D3 using their engineering model. They used a simplified version of the experimentally determined open atmosphere burning rate as an input for their model. Their results for experiments PRS_SI_D1 - D2 were similar to ours. They slightly over predicted the steady state burning rate in PRS_SI_D2 and good agreement between simulation and experiment for the steady burning rate in PRS_SI_D1. Their model was not able to predict extinction in PRS_SI_D3. Because they used the experimental burning rate curves as an input, they did not have to model the ignition process. Their simulations did not show the exaggerated spikes in the beginning of the simulation.

Figs. 3d and f show results for cases where the air inlet is in “low” position. In the experiments, this position was found to increase the mixing in the compartment, providing more oxygen to the flame base. This resulted in higher burning rate (cf. Figs. 3c and d). The simulations reproduced the burning rate enhancement between PRS_SI_D1 and PRS_SI_D6, but the predicted burning rate started to oscillate in PRS_SI_D6. Similar oscillations have been observed in other pool fire experiments in the same experimental facility for similar sized pool fires [5]. They had a period of 150–200 s, while the period of the

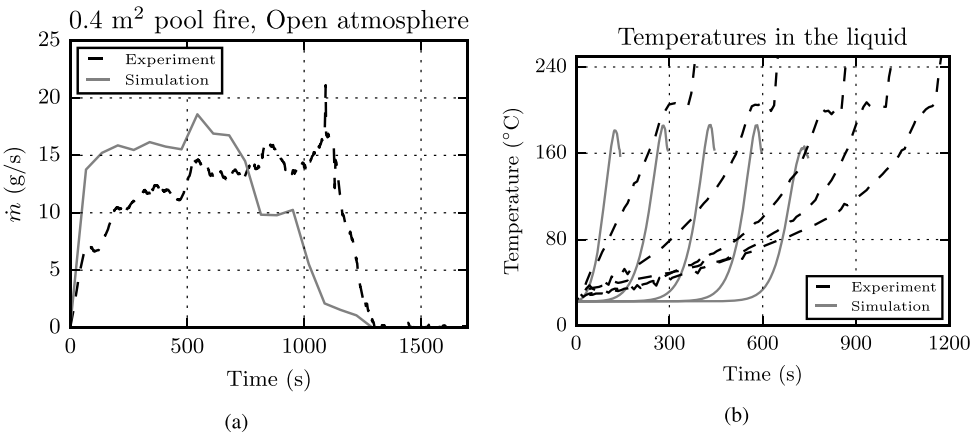

Fig. 2. (a) Burning rate of a 0.4 m^2 TPH pool fire. (b) Liquid temperatures within the liquid measured at 0,1,2,3,4 and 5 cm from the pool bottom.

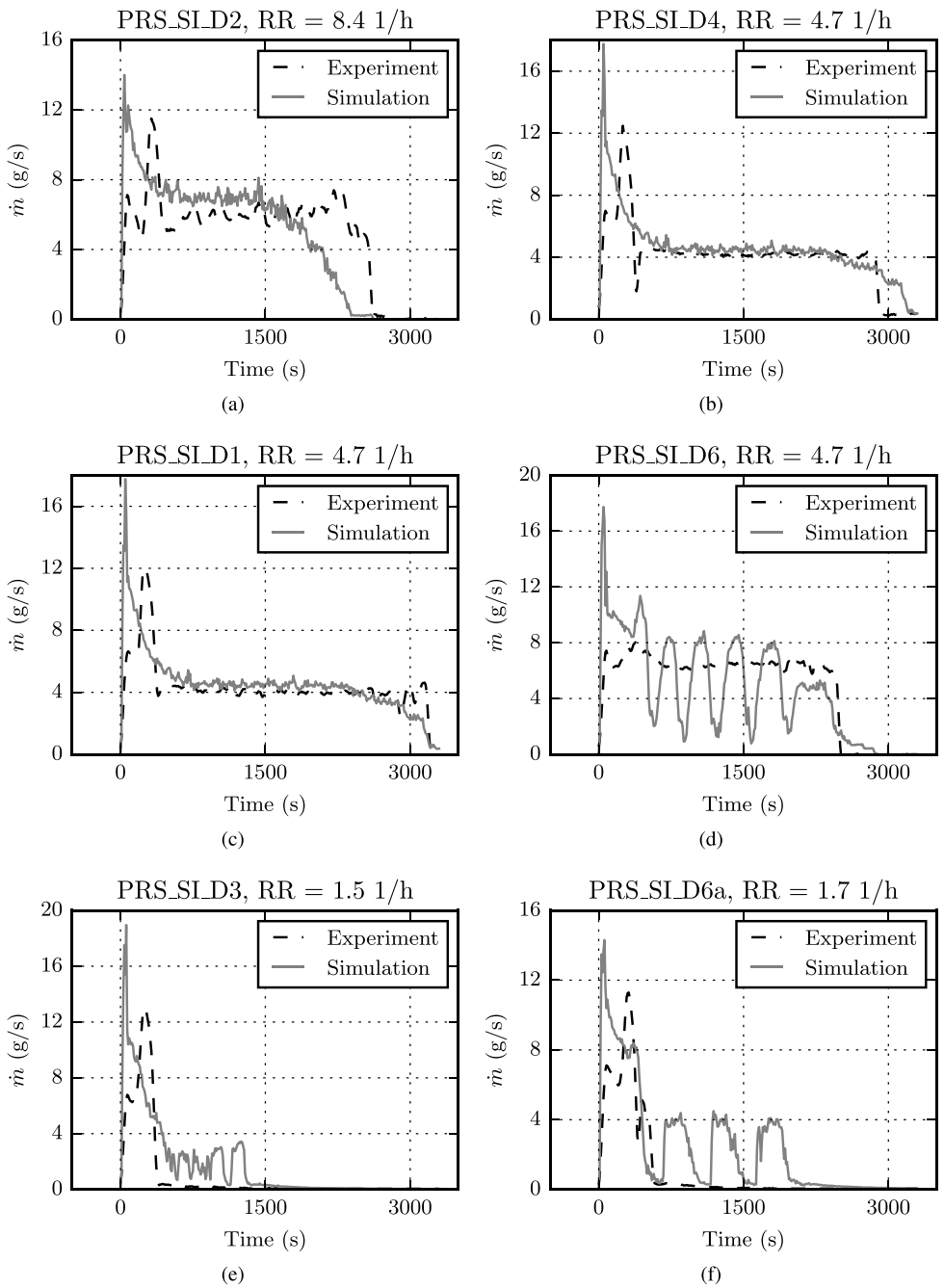

Fig. 3. Comparison of predicted and simulated burning rates for a 0.4 m^2 TPH pool fire. (a) highest air renewal rate in the compartment. Air renewal rates 4.7 h^{-1}: (b) and (c) inlet in high position and (d) inlet in low position. Air renewal rates 1.7 h^{-1}: (e) inlet in high position and (f) inlet in low position.

simulated oscillations here is about 300 s.

Despite the oscillations, the extinction time of PRS_SI_D6 was predicted fairly well because the extinction happened due to fuel burning out. For PRS_SI_D6a, the simulation predicts that the fire continues the oscillatory burning, while in the experiment it was suppressed due to the low oxygen concentration before a steady state was reached. However, extinction time is well predicted if one takes the beginning of the oscillatory burning phase as the time of extinction.

Fig. 4 shows a closer look at the oscillating burning rate period in the PRS_SI_D6 simulation. The oscillations were preceded by a short spike in the burning rate. This caused a rapid increase of the compartment pressure. The pressure variations in the current com-

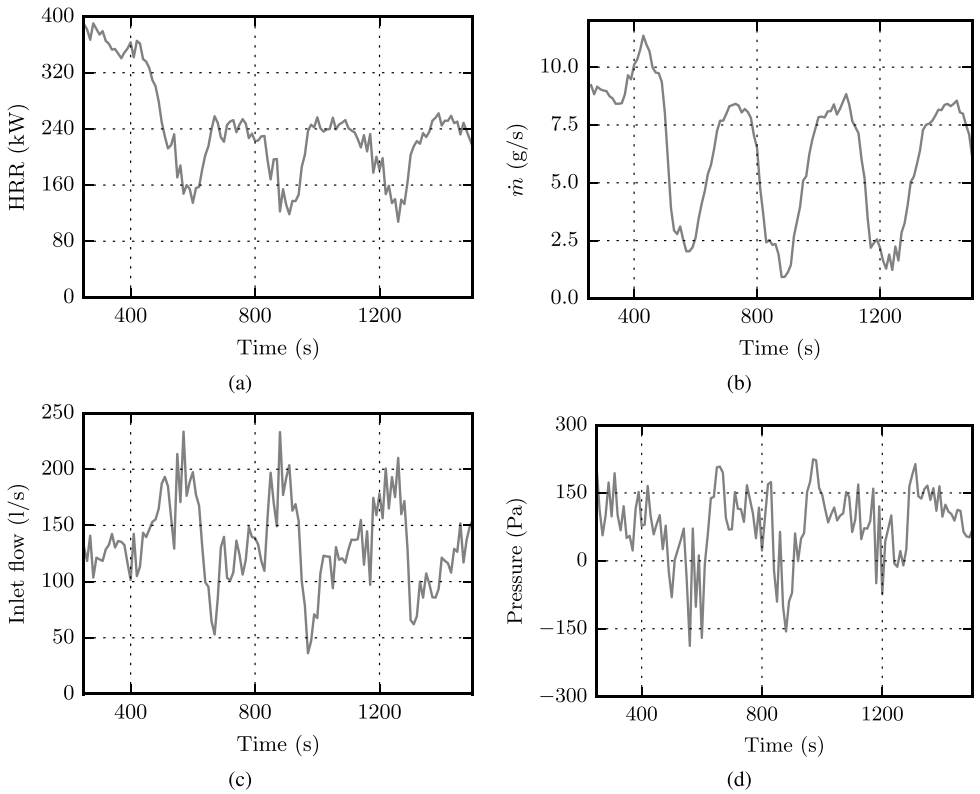

Fig. 4. Closer look at the oscillatory phase of PRS_SI_D6 simulation. (a) heat release rate (b)) mass loss rate (c) volume flow through the inlet. (d) Compartment pressure.

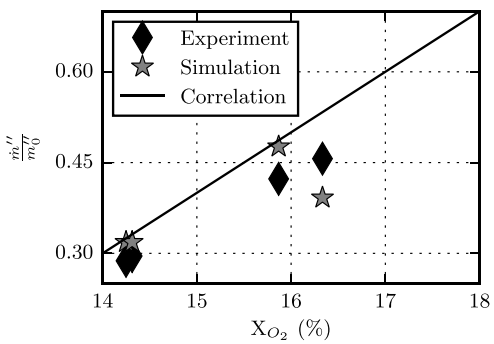

Fig. 5. Correlation between oxygen concentration near the pool surface and the burning rate.

partment have been found to be sufficiently high to counteract the pressure of the ventilation inlet branch. This was the case here as well; the pressure spike resulted in a reduced air inflow, again, very quickly. With some delay, the reduced air supply lead to reduced oxygen concentration and flame moving away from the pool towards the air inlet. The reduced heat feedback lead to reduced fuel evaporation rate, HRR and pressure, enabling higher inflow, flame returning over the pool and increased burning rate, making the oscillation cycle complete. Similar cycle takes place in PRS_SI_D6a, where the burning rate recovery from almost zero level seems clearly unphysical.

The oscillations were caused by an interplay of the combustion model, evaporation model and the ventilation. The oscillations did not appear in the simulations without the evaporation model and the extinction model. Removing either model also removed the oscillations in the burning rate. However, removing the extinction model lead to a significant over prediction of the burning rate. The appearance and amplitude of the oscillations was affected by the grid resolution (see Fig. 7c): Running the simulations on a coarse (δx = 200 mm) grid the oscillations disappeared, and on a finer grid their amplitude and frequency increased. These findings indicate a relation between the oscillations and the gas phase combustion dynamics.

To our understanding, the erroneous oscillations are, at least partially, caused by the simplifications in the combustion modelling. The model assumes that combustion occurs whenever fuel and oxidizer mix. This causes the fuel vapors in the compartment to reignite as soon as enough oxygen is supplied by the mechanical ventilation. The re-ignition behaviour could be prevented by specifying a fuel auto ignition temperature higher than 373 K. However, there is no generally applicable method for choosing the value to be used. If the temperature is set too low, the ignition-extinction cycle seen in Fig. 3f will continue until the fuel runs out. If the value is set too high, e.g, at auto-ignition temperature of dodecane), extinction will occur too soon. The value of 373 K was chosen after experimenting.

In their study of oscillatory behaviour of hydrocarbon pool fires Pretrel et al [5] concluded that the oscillatory phenomena is explained as a coupling process between the fuel evaporation rate and inlet flow rate. These two variables are coupled through the compartment pressure. They postulated that the oscillation is caused by phenomenon of “ghosting flame” where the flame moves away from the pool and towards the air inlet. The prerequisites for the oscillatory phenomenon are under-ventilated conditions and high enough temperatures to allow combustion at low oxygen concentrations.

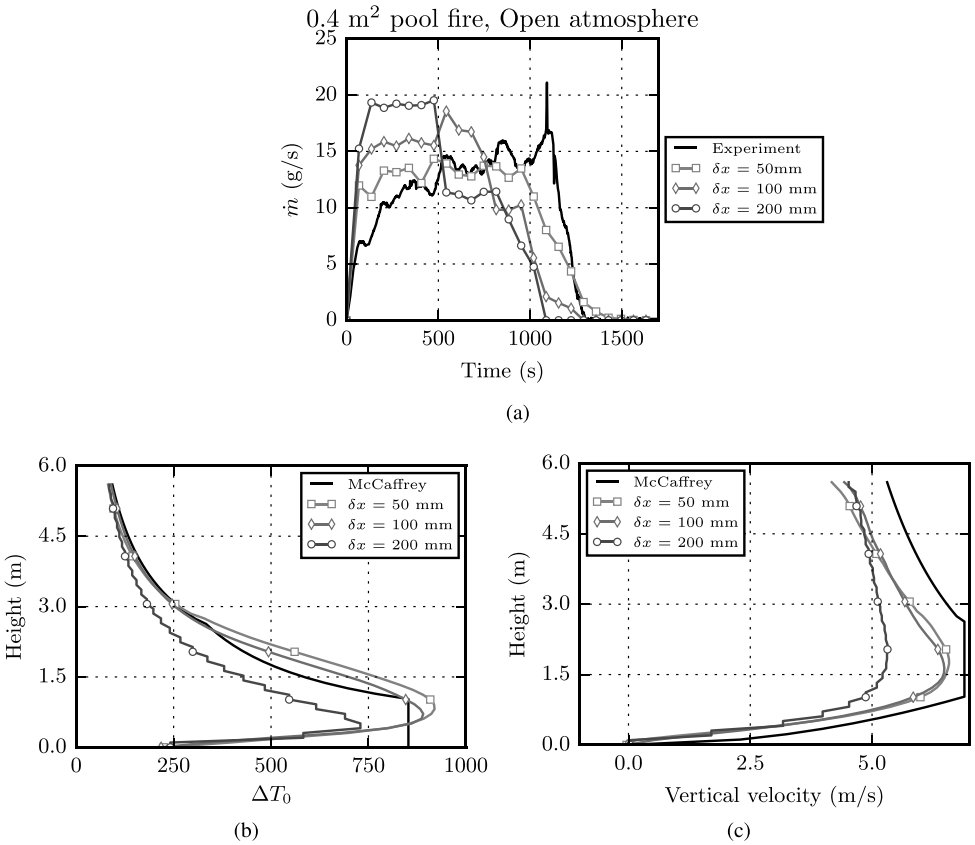

Fig. 6. Grid sensitivity study for 0.4 m^2 TPH pool fire in open atmosphere. (a) Burning rate. (b) Temperatures on plume centerline. (c) Vertical velocity on the plume centerline.

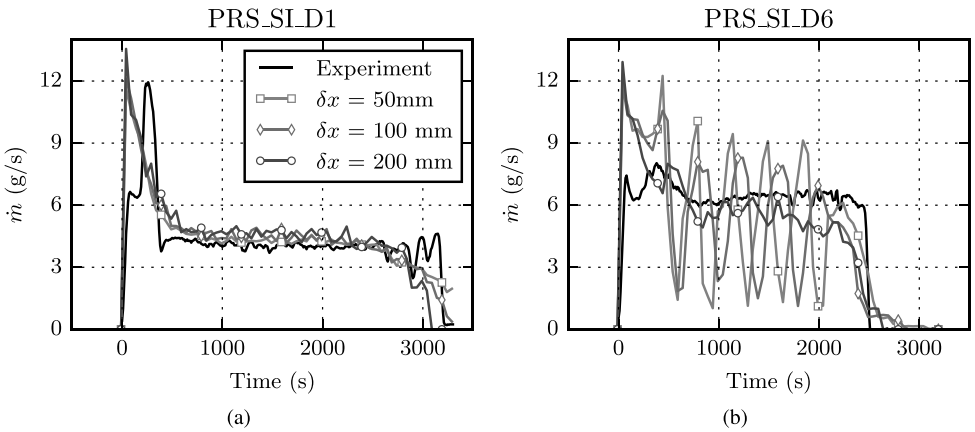

Fig. 7. Grid sensitivity studies for fires in a compartment with air renewal rate 4.7 h^{-1}. (a) High inlet position. (b) Same as (a) but low inlet position.

The above explanation of the oscillations closely matches the results from our simulations. However, it is not clear why the oscillations occurred in the simulations when the experimental results show no oscillation. Pretrel et al. noted that there is still a lack of knowledge for complete understanding of the oscillatory phenomenon but conjectured that issues involved are evaporation, local extinction phenomena and gas phase mixing. In our simulations the oscillatory phenomena was triggered by a change in the ventilation inlet position from high to low. Lowering the inlet position changes the gas phase mixing in the compartment.

Based on the pool fire experiments in a ventilated compartment, Peatross and Beyler developed a correlation to relate the mass loss rate to the oxygen concentration inside the compartment [6]. According to their correlation, the ratio of pool mass loss rates determined at low

oxygen concentration ($\dot{m}''$) and open air ($\dot{m}_{0''}$) is given by

$$\frac{\dot{m}''}{\dot{m}_{0''}} = 10X_{O_2} - 1.1. \tag{12}$$

where X_{O_2} is the volume fraction of oxygen.

Fig. 5 compares the predicted steady state burning rates with the experimental results and Eq. (12). The oxygen volume fractions were obtained by averaging the oxygen concentration near the pool surface over the period of steady burning. Good agreement is obtained between the correlation, experiments and simulations for all cases except the simulation of PRS_SI_D6. In this simulation, the averaged burning rate is decreased by the oscillations during the averaging period.

Finally, Figs. 6 and 7 show the results of the grid sensitivity studies for fires in open atmosphere and in a compartment. Fig. 6a shows that in open atmosphere, there is a tendency to over predict burning rates on coarse grids. However, as the grid is refined, the burning rates start to be underpredicted. Furthermore, the resolution of 50 mm is not enough to reach grid convergence. These findings are in agreement with the results in [12].

The structure of the open pool fires is checked by comparing against the McCaffrey plume correlations [13]:

$$\Delta T_c = \left(\frac{\kappa}{0.9\sqrt{2g}}\right)^2 \left(\frac{z}{\dot{Q}^{2/5}}\right)^{(2\eta-1)} \quad ; \quad u_c = \kappa \left(\frac{z}{\dot{Q}^{2/5}}\right)^{(2\eta-1)} \tag{13}$$

Here $\dot{Q}$ is the total heat release rate of the fire in kW, u_c is the vertical velocity on the centerline and z is the height above the fuel surface. ΔT_c is the temperature rise compared to ambient on the plume centerline. For the open pool fire the total heat release rate is taken to be 630 kW.

Fig. 6b shows that for 100 mm and 50 mm grid the centerline plume temperatures are slightly over predicted incontinuous and intermittent flame zones. In the plume zone, good agreement is found with the correlations. This indicates that the flame heights are correctly predicted. For 200 mm grid the temperatures are-under predicted everywhere, but the overall shape of the temperature curve is correct.

Fig. 6b compares the predicted centerline velocities with Eq. (13). Here velocities are under predicted everywhere. In the intermittent zone, the predicted vertical velocities are within 10% of the correlation for the two finest grids. The overall shape of the vertical velocity dependence on height is qualitatively correct.

The differences between velocity and temperature profiles for the two finest grid sizes is small (see Fig. 6b and c). Near the pool surface, the temperatures and velocities on the centerline increase as the mesh is refined, while the predicted burning rates decrease. This most likely a numerical artefact: The temperatures and velocities obtained from the simulation represent volume averages. On coarser grids the quantities of interest are averaged over the larger grid cell leading to lower values. On the other hand, Eq. (13) suggests that the centerline temperature and velocity are only weakly related to the heat release rate, especially near the surface. Therefore, the relatively large differences in burning rate should result in fairly small differences in centerline values. In the plume region finer grids produce slightly smaller temperatures and velocities, consistent with the decreasing heat release rate.

The grid resolution can be compared with earlier works using the ratio of hydraulic diameter to grid size, $D^*/\delta x$, where $D^* = (\dot{Q}/\rho_0 c_p T_0 \sqrt{g})^{2/5}$. The ratio $D^*/\delta x$ for pool fires in open atmosphere is 4, 8 or 16 for 200 mm, 100 mm and 50 mm discretizations respectively. In [12] it was found that for a pool fire with 1 m diameter ratios $D^*/\delta x$ in excess of 30 were needed for convergence. Therefore grid convergence could be seen between 25 mm and 12.5 mm grid ($D^*/\delta x$ between 30 and 60). Due to limitations in computational capacity these grid sizes could not be achieved. However, these convergence results allow us to compare the grid convergence behaviour of fires in the open and in compartments.

Fig. 7 shows that inside the compartment, grid size has a much smaller effect on the burning rate. The ratios $D^*/\delta x$ for the compartment fires during steady state combustion are 3, 5 and 11 for 200 mm, 100 mm and 50 mm grid sizes respectively. The reasonable burning rate predictions on such coarse grids indicate that resolving the fire plume is not as important in compartment fire cases. This can be attributed to the fact that the compartment quickly fills with smoke, reducing the relative importance of the direct flame heat flux prediction. The layered structure in a compartment fire can be resolved using significantly fewer grid points compared to the structure of the flame. The 10 cm grid size used in the compartment fire simulations is adequate.

5. Conclusions

Predictive simulations of liquid pool fires were conducted using a CFD solver coupled with a detailed model for liquid evaporation. The results showed that code is capable of predicting the steady state burning rates of the TPH pool fires in compartments within 15% of the experimental value. The characteristic dependence between the ventilation rate and the burning rate was correctly captured.

In some simulations, the predicted burning rate showed strong oscillations that were not observed in the experiments. Similar oscillations have been observed in other experiments conducted in the same enclosure, though. The appearance of the oscillations was found to depend on the details of the geometry, grid resolution and the combustion modelling options.

The 1-d heat transfer model employed in this work could not reproduce the temperature gradient in the liquid phase. It is possible, that the gradual rise seen in burning rates of open atmosphere pool fires could be explained by enhanced heat transfer within the liquid phase by, e.g., lateral convection. The effect of non-gray radiation transport should also be investigated in the future.

Acknowledgements

We would like to thank the IRSN for providing the experimental data for our use. The current work was carried out within the Finnish research programmes for the safety of nuclear power plants (SAFIR), funded by the State Nuclear Waste Management Fund (VYR).

References

[1] Jonathan Wahlqvist, Patrick van Hees, Validation of FDS for large-scale well-confined mechanically ventilated fire scenarios with emphasis on predicting ventilation system behavior, Fire Saf. J. 62 (November) (2013) 102–114 (ISSN 03797112. URL ⟨http://www.sciencedirect.com/science/article/pii/S0379711213001185⟩).

[2] T. Beji, F. Bonte, B. Merci, Numerical simulations of a mechanically-ventilated multi- compartment fire, Fire Saf. Sci. 11 (2014) 499–509 (URL ⟨http://www.iafss.org/publications/fss/11/499⟩).

[3] Jonathan Wahlqvist, Patrick van Hees, Implementation and validation of an environmental feedback pool fire model based on oxygen depletion and radiative feedback in FDS, Fire Saf. J. 85 (October) (2016) 35–49 (ISSN 03797112. URL ⟨http://www.sciencedirect.com/science/article/pii/S0379711216301047⟩).

[4] S. Suard, M. Forestier, S. Vaux, Toward predictive simulations of pool fires in mechanically ventilated compartments, Fire Saf. J. 61 (October) (2013) 54–64 (ISSN 03797112. URL ⟨http://www.sciencedirect.com/science/article/pii/S0379711213001306⟩).

[5] Hugues Pretrel, Sylvain Suard, Laurent Audouin, Experimental and numerical study of low frequency oscillatory behaviour of a large-scale hydrocarbon pool fire in a mechanically ventilated compartment, Fire Saf. J. 83 (July) (2016) 38–53 (ISSN 03797112. URL ⟨http://www.sciencedirect.com/science/article/pii/S0379711216300492⟩).

[6] M.J. Peatross, C.L. Beyler, Ventilation effects on compartment fire characterization, Fire Saf. Sci. 5 (1997) 403–414 (URL http://www.iafss.org/publications/fss/5/403⟩).

[7] K. McGrattan, S. Hostikka, R. McDermott, J. Floyd, C. Weinschenk, K. Overholt. Fire Dynamics Simulator, Technical Reference Guide. National Institute of Standards and Technology, Gaithersburg, Maryland, USA, and VTT Technical Research Centre of Finland, Espoo, Finland, sixth edition, September 2013. Vol. 1: Mathematical Model; Vol. 2, Verification Guide; Vol. 3: Validation Guide; Vol. 4: Configuration Management Plan.

[8] J. Floyd, Coupling a network HVAC model to a computational fluid dynamics

model using large eddy simulation, Fire Saf. Sci. 10 (2011) 459–470 (URL http://www.iafss.org/publications/fss/10/459)).
[9] F.P. Incropera, D.P. de Witt, Fundamentals of Heat and Mass Transfer, 4th ed., John Wiley and Sons, New York, 1996.
[10] L. Audouin, L. Rigollet, H. Prétrel, W. le Saux, M. Röwekamp, OECD PRISME project: fires in confined and ventilated nuclear-type multi-compartments - Overview and main experimental results, Fire Saf. J. 62 (November) (2013) 80–101 (ISSN 03797112. URL ⟨http://www.sciencedirect.com/science/article/pii/S0379711213001197⟩).
[11] H. Pretrel, P. Querre, M. Forestier, Experimental study of burning rate behaviour in confined and ventilated fire compartments, Fire Saf. Sci. 8 (2005) 1217–1228 (URL ⟨http://www.iafss.org/publications/fss/8/1217⟩).
[12] Topi Sikanen, Simo Hostikka, Modeling and simulation of liquid pool fires with in-depth radiation absorption and heat transfer, Fire Saf. J. 80 (February) (2016) 95–109 (ISSN 03797112. URL ⟨http://www.sciencedirect.com/science/article/pii/S0379711216300030⟩).
[13] Bernard J. McCaffrey, Purely Buoyant Diffusion Flames: Some Experimental Results, NBSIR 79-1910, National Bureau of Standards, Washington, D.C., 1979.

Aalto-DD 254/2017
VTT SCIENCE 169

ISBN 978-952-60-7784-0 (printed)
ISBN 978-952-60-7785-7 (pdf)
ISSN-L 1799-4934
ISSN 1799-4934 (printed)
ISSN 1799-4942 (pdf)

978-951-38-8599-1 (printed)
978-951-38-8598-4 (pdf)
2242-119X
2242-119X (printed)
2242-1203 (pdf)

Aalto University
School of Engineering
Department of Civil Engineering
www.aalto.fi

BUSINESS + ECONOMY

ART + DESIGN + ARCHITECTURE

SCIENCE + TECHNOLOGY

CROSSOVER

DOCTORAL DISSERTATIONS